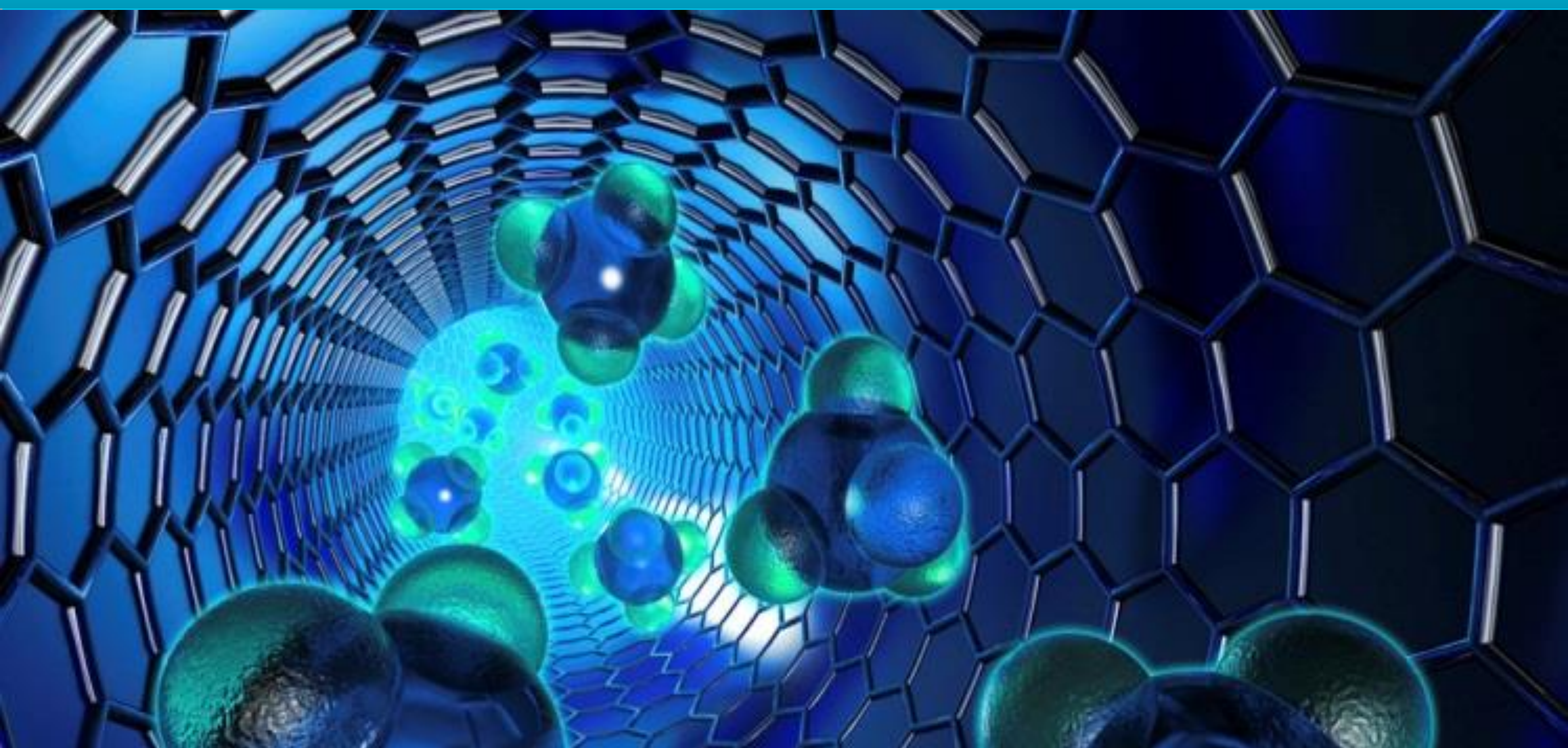


e-ISSN: 2602-277X

International Journal of Chemistry and Technology



Volume:2, Issue:2

28 December 2018

E - Journal

<http://dergipark.gov.tr/ijct>



International Journal of Chemistry and Technology

JOURNAL INFO

Journal Name	International Journal of Chemistry and Technology
Journal Initial	IJCT
Journal Abbreviation	Int. J. Chem. Technol.
ISSN (Online)	2602-277X
Year of Launching	2017, August
Editor-in-Chief and Managing Editor	Prof. Dr. Bilal Acemioğlu
Manager of Publication	Assist. Prof. Mehmet Akyüz
Scope and Focus	Chemistry, Material Science, Technology
Review Type	Peer Review Double-Blinded
Ethical Rules	Plagiarism check, copyright agreement form, conflict of interest, ethics committee report
Access Type	Open Access
Publication Fee	Free
Article Language	English
Frequency of Publication	Biannually
Publication Issue	June, December
Publisher	Prof. Dr. Bilal Acemioğlu
Web Page	http://dergipark.gov.tr/ijct
Contact E-mail address	ijctsubmission@gmail.com, ijctsubmission@yahoo.com
Contact Address and Executive address	Kilis 7 Aralik University, Faculty of Science and Arts, Department of Chemistry, 79000, Kilis
Contact Telephone	90 5535983054 (Editor-in-Chief), 90 530 3645222 (Manager of Publication), 90 532233 17 38 (Secretary)
Publication Date	28/12/2018
Technical Editor	Assist. Prof. Dr. Evrim Baran Aydın
Spelling Editor	Dr. Oğuzhan Koçer, MSc. Rabia Acemioğlu
Language (Grammar) Editor	Doç. Dr. Gülcihan Güzeldağ, Assist. Prof. Dr. Muhammet Karaman, English Expert. Abdulkadir Doğan, Dr. Muhittin Kulak
Secretary	Dr. Oğuzhan Koçer, MSc. Rabia Acemioğlu

All detailed information including instructions for authors, aim and scopes, ethical rules, manuscript evaluation, indexing info, and manuscript template etc. can be found on the main web page of IJCT (<http://dergipark.gov.tr/ijct>).



International Journal of Chemistry and Technology

Volume: 2, Issue: 2, 28 December 2018

Founder of IJCT

Prof. Dr. Bilal Acemiođlu

EDITORIAL BOARD

Editor-in-Chief

Prof. Dr. Bilal Acemiođlu

(Physical Chemistry, Kilis 7 Aralık University, Kilis, Turkey)

Associate Editors

Prof. Dr. İbrahim Demirtaş
(Organic Chemistry and Phytochemistry,
Çankırı Karatekin, University, Çankırı, Turkey)

Prof. Dr. M. Hakkı Alma
(Material Science and Technology,
K.Maraş Sütçü İmam/Iğdır University, Turkey)

Prof. Dr. Metin Bülbül
(Biochemistry, Dumlupınar University,
Kütahya, Turkey)

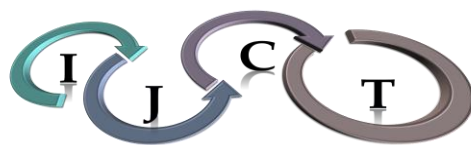
Prof. Dr. Fevzi Kılıçel
(Analytical Chemistry, Karamanođlu Mehmet
Bey University, Karaman, Turkey)

Prof. Dr. Yuh-Shan Ho
(Chemical and Environmental Engineering,
Asia University, Taichung City, Taiwan)

Prof. Dr. Yahya Güzel
(Theoretical Chemistry and Polymer Chemistry,
Erciyes University, Kayseri, Turkey)

Prof. Dr. Mustafa Arık
(Physical Chemistry, Atatürk University,
Erzurum, Turkey)

Prof. Dr. Mehmet Sönmez
(Inorganic Chemistry, Gaziantep University,
Gaziantep, Turkey)



International Journal of Chemistry and Technology

Advisory Editorial Board

Prof. Dr. Harun Parlar
(Technical University of Munich, München,
Germany)

Prof. Dr. Shaobin Wang
(Curtin University, Perth, Australia)

Prof. Dr. Gelu Bourceanu
(Alexandru Ioan Cuza University, Romania)

Prof. Dr. Jon-Bae Kim
(College of Health Sciences, South Korea)

Prof. Dr. Rashid Ahmad
(University of Malakand, Chakdara, Pakistan)

Prof. Dr. Guang-Jie Zhao
(Beijing Forestry University, Beijing, China)

Prof. Dr. Jaine H. Hortolan Luiz
(Federal University of Alfenas, Unifal-MG, Brazil)

Prof. Dr. Papita Das
(Jadavpur University, Jadavpur, India)

Prof. Dr. Vagif Abbasov
(Nef-Kimya Prosesleri Institutu, Baku, Azerbaijan)

Prof. Dr. Atiqur Rahman
(Islamic University, Kushita, Bangladesh)

Prof. Dr. Mika Sillanpää
(LUT Lappeenranta University of Technology,
Lappeenranta, Finland)

Prof. Dr. Salah Akkal
(University of Mentouri Consatntine,
Consatntine, Algeria)

Prof. Dr. Gilbert Kapche Deccaux
(University of Yaounde I, Yaounde, Cameroon)

Prof. Dr. Anatoli Dimoglu
(Düzce University, Düzce, Turkey)

Prof. Dr. Ahmet Çakır
(Kilis 7 Aralık University, Kilis, Turkey)

Prof. Dr. M. Salih Ağırtaş
(Yüzüncü Yıl University, Van, Turkey)

Prof. Dr. Seyithan Taysi
(Gaziantep University, Gaziantep, Turkey)

Prof. Dr. Rahmi Kasımoğulları
(Dumlupınar University, Kütahya, Turkey)

Prof. Dr. Ahmet Baysar
(Inonu University, Malatya, Turkey)

Prof. Dr. Hamdi Temel
(Dicle University, Diyarbakır, Turkey)

Prof. Dr. Ö. İrfan Küfrevioğlu
(Atatürk University, Erzurum, Turkey)

Prof. Dr. Ömer Şahin
(Siirt University, Siirt, Turkey)

Prof. Dr. Mehmet Çiftçi
(Bingöl University, Bingöl, Turkey)

Prof. Dr. Mehmet Uğurlu
(Sıtkı Kocman university, Muğla, Turkey)

Prof. Dr. Şükrü Beydemir
(Anadolu University, Eskişehir, Turkey)

Prof. Dr. Ramazan Solmaz
(Bingol University, Bingöl, Turkey)

Prof. Dr. Mahfuz Elmastaş
(Health Sciences University, İstanbul, Turkey)

Prof. Dr. Mehmet Doğan
(Balıkesir University, Balıkesir, Turkey)

Prof. Dr. Giray Topal
(Dicle University, Diyarbakır, Turkey)

Prof. Dr. Birgül Yazıcı
(Cukurova University, Adana, Turkey)



International Journal of Chemistry and Technology

Advisory Editorial Board

Prof. Dr. Mehmet Muhtar Kocakerim
(Çankırı University, Çankırı, Turkey)

Prof. Dr. Murat Alanyalıoğlu
(Atatürk University, Erzurum, Turkey)

Prof. Dr. T. Abdulkadir Çoban
(Erzincan University, Erzincan, Turkey)

Prof. Dr. İsmet Kaya
(18 Mart University, Çanakklae, Turkey)

Prof. Dr. Barbaros Nalbantoğlu,
(Yıldız Technical University, İstanbul, Turkey)

Prof. Dr. Ömer Işıldak
(Gaziosmanpaşa University, Tokat, Turkey)

Prof. Dr. Nurullah Saraçoğlu
(Atatürk University, Erzurum, Turkey)

Prof. Dr. Ahmet Tutar
(Sakarya University, Sakarya, Turkey)

Prof. Dr. Duygu Ekinci
(Atatürk University, Erzurum, Turkey)

Prof. Dr. Ekrem Köksal
(Erzincan University, Erzincan, Turkey)

Assoc. Prof. Dr. Mahjoub Jabli
(University of Monastir, Monastir, Tunisia)

Assoc. Prof. Dr. Şenay Şimşek
(North Dakota State University, Fargo, USA)

Assoc. Prof. Niyaz M. Mahmoodi,
(Institute for Color Science and Technology,
Tehran, Iran)

Assoc. Prof. Dr. Murat Sadıkoğlu
(Gaziosman Paşa University, Tokat, Turkey)

Assoc. Prof. Dr. Ali Kara
(Uludağ University, Bursa, Turkey)

Assoc. Prof. Dr. Metin Açıkyıldız
(Kilis 7 Aralık University, Kilis, Turkey)

Assoc. Prof. Dr. Muhammet Köse
(Sütçü İmam University, K.Maraş, Turkey)

Assoc. Prof. Dr. Mustafa Karataş
(Aksaray University, Aksaray, Turkey)

Assoc. Prof. Dr. Serhan Uruş
(Sütçü İmam University, K.Maraş, Turkey)

Assoc. Prof. Dr. Murat Saraçoğlu
(Erciyes University, Kayseri, Turkey)

Assoc. Prof. Dr. Halim Avcı
(Kilis 7 Aralık University, Kilis, Turkey)

Assoc. Prof. Dr. Mustafa Özdemir
(Süleyman Demirel University, Isparta, Turkey)

Assist. Prof. Dr. Mutasem Z. Bani-Fwaz
(King Khalid University, Asir-Abha, Saudi Arabia)

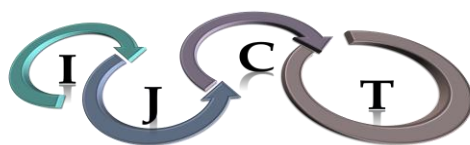
Assist. Prof. Masood Ayoub Kaloo
(Govt. Degree College Shopian, J &K, India)

Dr. Zineb Tribak
(Sidi Mohamed Ben Abdellah University, Fez
Morocco)

Assist. Prof. Dr. Bakhtiyor Rasulev
(North Dakota State University, Fargo, USA)

Dr. Ramadan E. Ashery
(Damanhour University, Egypt)

Dr. Sameer Ahmed Awad
(University of Anbar, Ramadi, Iraq)



International Journal of Chemistry and Technology

Reviewers for December 2018, Vol: 2, Issue: 2

Prof. Dr. Hamdi Karaoğlu
(Sıtkı Koçman University, Muğla, Turkey)

Prof. Dr. Yahya Güzel
(Erciyes University, Kayseri, Turkey)

Prof. Dr. Şükrü Karataş
(Sütçü İmam University, K.Maraş, Turkey)

Prof. Dr. Anatoli Dimoglo
(Düzce University, Düzce, Turkey)

Prof. Dr. Ömer Işıldak
(Gazi Osman Paşa University, Tokat, Turkey)

Prof. Dr. Mehmet Tunç
(Yüzüncü Yıl University, Van, Turkey)

Prof. Dr. İbrahim Ender Mülazımoğlu
(Necmettin Erbakan University, Konya, Turkey)

Prof. Dr. Ömer Şahin
(Siirt University, Siirt, Turkey)

Prof. Dr. Hüseyin Köksal
(Sütçü İmam University, K.Maraş, Turkey)

Prof. Dr. Abdulkadir Levent
(Batman University, Batman, Turkey)

Prof. Dr. Mehmet Uğurlu
(Sıtkı Koçman University, Muğla, Turkey)

Assoc. Prof. Dr. Muharrem İnce
(Munzur University, Tunceli, Turkey)

Assoc. Prof. Dr. Micah Green
(Texas AM University, College Station, USA)

Assoc. Prof. Dr. Rafet Yılmaz
(Yüzüncü Yıl University, Van, Turkey)

Assoc. Prof. Dr. Ebru Çubuk Demiralay
(Süleyman Demirel University, Isparta, Turkey)

Assoc. Prof. Dr. Mahmut Toprak
(Bingöl University, Bingöl, Turkey)

Assoc. Prof. Dr. Murat Sadıkoğlu
(Gazi Osman Paşa University, Tokat, Turkey)

Assoc. Prof. Dr. Bülent Sarı
(Çukurova University, Adana, Turkey)

Assoc. Prof. Dr. Oğuzhan Çalışkan
(Mustafa Kemal University, Hatay, Turkey)

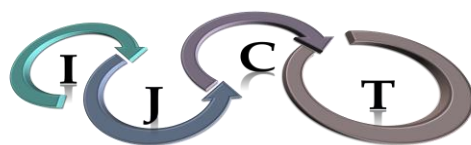
Assist. Prof. Dr. Meltem Kızılca Çoruh
(Atatürk University, Erzurum, Turkey)

Assist Prof. Dr. Mutasem Z. Bani-Fwaz
(King Khalid University, Saudi Arabia)

Assist. Prof. Dr. Adem Koçyiğit
(İğdir University, Iğdır, Turkey)

Assist. Prof. Dr. Neşe Keklikçioğlu Çakmak
(Cumhuriyet University, Sivas, Turkey)

Assist Prof. Dr. Ali Özkan
(Gaziantep University, Gaziantep, Turkey)



International Journal of Chemistry and Technology

TABLE OF CONTENTS

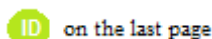
Research Articles	Pages
1. Evaluation of fatty acid compositions and physicochemical quality parameters of ancient and recent olive (<i>Olea europaea</i> L.) oil varieties of Southeast Anatolia (Güneydoğu Anadolu'nun eski ve yeni zeytin (<i>Olea europaea</i> L.) yağı çeşitlerinin yağ asiti bileşimleri ve fizikokimyasal kalite parametrelerinin değerlendirilmesi) Halim Avci, Yılmaz Uğur, Selim Erdoğan	76-88
2. Investigation of different reactor configurations for electrochemical ferrate (VI) synthesis (Elektrokimyasal ferrat (VI) sentezi için farklı reaktör konfigürasyonlarının araştırılması) Sibel Barışçı	89-94
3. Adsorption of safranin-O dye by peanut shell-based polyurethane type foam (Yerfıstığı kabuğu esaslı poliüretan tipi köpük ile safranin-O boyasının adsorpsiyonu) Bilal Acemioğlu, Melike Hilal Bilir, Mehmet Hakkı Alma	95-104
4. Theoretical approach using DFT and muscle relaxant effects of 5-Chloroisatin Derivatives (5-Kloroizatin türevlerinin DFT kullanarak teorik yaklaşımı ve kas gevşetici etkileri) Zineb Tribak, Alae Chda, Mohammed Khalid Skalli, Amal Haoudi, Youssef Kandri Rodi, Omar Senhaji, El Mokhtar Essassi, Rachid Ben Cheikh, Kaouakib El Abida	105-115
5. Electrical characteristics of Au/Ti/HfO ₂ /n-GaAs metal-insulator-semiconductor structures with high-k interfacial layer (Yüksek <i>k</i> -arayüzey tabakalı metal-yalıtken yarıiletken Au/Ti/HfO ₂ /n-GaAs yapıların Elektriksel Karakteristikleri) Abdulkerim Karabulut, İkrâm Orak, Abdülmecit Türüt	116-122
6. Optimization of dissolution of ulexite by pure CO ₂ gas in aqueous medium under pressure and production of sodium pentaborate (Basınç altında üleksitin saf CO ₂ gazı ile sulu ortamda çözünürleştirilmesinin optimizasyonu ve sodyum pentaborat elde edilmesi) Veysel Selimoğlu, M. Muhtar Kocakerim	123-128
7. Investigation of improvement of thermal and mechanical properties of polypropylene / nano clay composites (Polipropilen/nanokil kompozitlerinin termal ve mekanik özelliklerinin iyileştirilmesinin incelenmesi) Sameer A. Awad, Eman M. Khalaf	129-134
8. Flow analysis of highly concentrated xhantan gum fluid (Yüksek derişimli ksantan gam sıvısının akış analizleri) Guler Bengusu Tezel	135-140

9. Molecular structure of Zn (II) compound containing 8-hydroxyquinoline and 2- picoline ligands [I], theoretical HF and DFT studies [II] 141-152
(8-hidroksikinolin ve 2-pikolin ligandları içeren Zn (II) bileşiminin moleküler yapısı [I], teorik HF ve DFT çalışmaları [II])
Kani Arıcı
10. Determination of aflatoxin and some trace element contents in black pepper samples 153-160
(Karabiber örneklerinde aflatoxin ve bazı eser element içeriklerinin belirlenmesi)
Fevzi Kiliçel, Hacer Sibel Karapinar
11. Promising bay laurel (*Laurus nobilis* L.) genotypes for fruit production 161-167
(Meyve üretimi için ümitvar defne (*Laurus nobilis* L.) genotipleri)
Filiz Ayanoğlu, Durmuş Alpaslan Kaya, Oğuzhan Koçer
12. Development of calcium-selective potentiometric electrode using 10,19- 168-172
Bis[(octadecylcarbamoyl)methoxyacetyl]-1,4,7,13,16-pentaoxa-10,19-diazacyclo-
heneicosane compound as ionophore
(İyonofor olarak 10,19-Bis [(oktadesilkarbamoil) metoksiasetil]- 1,4,7,13,16-pentaoksa-
10,19-diazasikloheniikosan bileşimini kullanarak kalsiyum seçici potensiyometrik
elektrotun geliştirilmesi)
Omer Isildak



Evaluation of fatty acid compositions and physicochemical quality parameters of ancient and recent olive (*Olea europaea* L.) oil varieties of Southeast Anatolia

Halim AVCI^{1,*}, Yilmaz UGUR², Selim ERDOGAN³



¹Kilis 7 Aralık University, Faculty of Science and Art, Department of Chemistry, Kilis, Turkey

²Apricot Research Institute, Malatya, Turkey

³Inonu University, Faculty of Pharmacy, Department of Analytical Chemistry, Malatya, Turkey

Received: 28 August 2018, Revised: 14 September 2018; Accepted: 17 September 2018

*Corresponding author e-mail: halimavci77@gmail.com

Citation: Avci, H.; Ugur, Y.; Erdogan, S. *Int. J. Chem. Technol.* 2018, 2 (2), 76-88.

ABSTRACT

Upper Mesopotamia is known to be the homeland of olive, spanning over Mardin, Hatay, Kilis and the western shores of Syria and Palestine. Having earliest habitation in the Southeastern Anatolia region, olive lies down along the Western Anatolia. The goal of the present study is to evaluate the fatty acid compositions of the olive oils obtained from the olive trees which are the kinds of Kilis yağlık (KY), Halhalı (H), Gemlik-Kilis (GK), and Gemlik-Gemlik (GG). While GG variety has the lowest total saturated fatty acids (SFAs), KY, GK and H varieties show similarity in respect to the total SFAs levels, and these have the higher SFAs levels. While GG variety has the lowest total SFAs and polyunsaturated fatty acids (PUFAs), KY contains the highest total SFAs and PUFAs. While mean docosahexaenoic acid (DHA) values in KY and GK varieties are minor levels, it is found below the detection limit of GC-FID method for all of H and GG samples.

Keywords: Olive oil, fatty acid composition, genotype, physicochemical quality parameters.

Güneydoğu Anadolu'nun eski ve yeni zeytin (*Olea europaea* L.) yağı çeşitlerinin yağ asiti bileşimleri ve fizikokimyasal kalite parametrelerinin değerlendirilmesi

ÖZ

Zeytinin anavatanının Mardin, Hatay, Suriye'nin ve Filistin'in batı kıyılarını içerisine alan yukarı Mezopotamya olduğu bilinmektedir. Güneydoğu Anadolu bölgesinde ilk yerleşime sahip olan zeytin Batı Anadolu'ya kadar uzanmıştır. Bu çalışmanın amacı, Kilis yağlık (KY), Halhalı (H), Gemlik-Kilis (GK) ve Gemlik-Gemlik (GG) çeşitleri olan zeytin ağaçlarından elde edilen zeytinyağlarının yağ asidi bileşimlerini değerlendirmektir. GG türü en düşük doymuş yağ asidine (SFAs) sahip iken, KY, GK and H türleri toplam SFAs seviyelerine benzerlik gösterir ve bunlar daha yüksek SFAs seviyelerine sahiptir. GG türü en düşük toplam SFAs ve çoklu doymamış yağ asitlerine (PUFAs) sahip iken KY en yüksek toplam SFAs ve PUFAs içermektedir. KY ve GG türlerinde ortalama docosahexaenoic asit (DHA) düşük seviyelerde iken, H ve GG örneklerinin hepsi için GC-FID metodunun gözlenebilme sınırı değerinin altında bulunmuştur.

Anahtar Kelimeler: Zeytinyağı, yağ asidi bileşeni, genotip, fizikokimyasal kalite parametreleri.

1. INTRODUCTION

Olive farming has a history and may be as old as human kind itself, and on the other hand olive is said to be “the father of all trees”. The importance of olive is cited in all religious texts and in myths of creation and origin. The Archeological and geological finds also reveal that olive has been used since 6000 BC.^{1, 2} Upper

Mesopotamia is known to be the homeland of olive, spanning Mardin, Hatay, Kilis and the western shores of Syria and Palestine. This judgment is reached by means of the subspecies of olive tree seen on the across strips of these provinces, recently. Olive, having earliest habitation in the Southeastern Anatolia region, is lies down along the Western Anatolia, and continuous from there to Greece, Italy, France and Spain through the

Aegean islands. At the same time, it reaches North Africa through Sicily, and merges with the second stripe that comes from the Southeastern Anatolia region and moves through Syria and Egypt and finally spread over all southern coasts of the Mediterranean.^{2,3}

Olive farming is carried out along the shores in Mediterranean, Southeastern Anatolia, Marmara, Aegean and Black Sea regions of Turkey and in most provinces reaching up to Mardin in the Southeastern Anatolia. Within this ecological environment, olive has various species in Turkey, its homeland.^{2,3} The Turkish Agriculture Ministry has recorded total 88 assortment of native olives (include 26 foreign olive varieties) derived from both pomological and morphological variables in 1990 year.⁴ Gemlik variety, the dominant olive variety in the Marmara Region, particularly in the Gemlik Gulf, has also been grown in other parts of Turkey since 40 years. On the other hand, the most widely known and grown olive varieties in South Anatolia Region are Kilis Yağlık (KY) and Halhalı (H).^{5,6}

The most important factor that affects the chemical composition of olive is its variety. Other factors are the environmental conditions that the olive trees are grown. In determination of the quality of the olive, the big difficulty is encountered due to olive variety grown in different geographic region, and environment. While the environmental factors can be said as soil and climate, the agronomic factors are mentioned as irrigation and fertilization. Harvesting and ripeness which form cultivation factors have important effects as well as the technological factors such as post-harvest storage and extraction system. Geographical indication about olive variety informs about the authenticity of the extra-virgin olive oils in Europe.⁷⁻¹⁰

In this study, olive oil samples of ancient (native) and recent varieties obtained from the local producers were extracted by three-phase continuous centrifugation process. The chemical compositions of all extracted olive oil samples (Kilis Yağlık (KY), Gemlik-Kilis (GK), Gemlik-Gemlik (GG) and Halhalı (H)) were determined. Moreover, the physicochemical quality parameters including peroxide value (PV), free fatty acid (FFA) content, UV-spectrophotometric characteristics, refractive index and the viscosity were also determined in all the olive oil samples.

2. MATERIALS AND METHODS

2.1. Study area

Saline-sodic soils are known to covering 1.5 million ha in Turkey. The soils in Southeastern Anatolia are highly calcareous with high pH. Calcium carbonate is abundant in regional soils.¹¹ The soil in Kilis is generally geologically with limestone, and it contains high

amounts of lime, generally in the range of 30-60 % CaCO₃.

The olive (*Olea europaea* L.) oil samples of KY, GK, GG, and H (İskenderun-Hatay) were obtained from the local producers in Kilis, Gemlik and İskenderun, respectively (Figure 1).



Figure 1. The map showing three regions where the olive tree varieties grown in Gemlik (G), İskenderun (I) and Kilis (K).

2.2. Plant material

The most significant type of olive oil in the Southeastern Anatolia is KY olive oil. This type is widespread in Gaziantep, Kilis, Şanlıurfa, Kahramanmaraş, and Mardin provinces. Its fruits are very small compared to its bigger seeds. The fruits of KY olive contain oil up to 31.8%. When considered as one of the most known olive types in terms of oil containment, the KY olive is a significant olive type of the Southeastern Anatolia region with its strength, fertility and adaptable nature to the region.¹² The GG olive cultivar is originated from Gemlik Gulf at Marmara region and it is the major olive variety of the Marmara and Aegean region. Gemlik is a typical olive variety in the Marmara Region. More than 80% of the olives in the region are composed of Gemlik variety. The shell of Gemlik olive is thin and attached to the flesh, the kernel is small, round, and smooth. An important feature of the Gemlik variety is the being very aromatic. Its oil ratio is about 25-28%. Although it is generally regarded as black table olive, it can sometimes be processed as fat. Gemlik, in Turkey's various regions, has been grown intensively since the last 30-40 years.¹³ Halhalı olive variety which is belong to Eastern Mediterranean and Southeastern Anatolia Regions widely grows in Hatay, Gaziantep, Kahramanmaraş, Kilis, Mardin, and their surroundings. In addition to being considered more fat, it is also regarded as green or black table olive. Its fruit is small and round. The Fat percentage is very high, about 30-32%.¹³

2.3. Olive oils

Monovarietal virgin olive oils of Kilis yağlık (KY), Gemlik-Kilis (GK) and Halhalı (H) samples used in this study were collected from the commercial small or medium-scale olive oil producers in 2014 year. 100 ml of olive oil samples were placed in dark glass bottles and were stored in a refrigerator at 4°C until the samples were brought to analyze. The dominant olive variety grown in Kilis is Kilis yağlık, but Gemlik variety has been also cultivated in Kilis region for 20-30 years. The original growing area of Gemlik variety is the North Marmara Region. Growing area of Halhalı is East Mediterranean and Southeast Anatolia. Growing area of Kilis yağlık is Southeast Anatolia.

The olive (*Olea europaea* L.) oil of KY (n = 18), GK (n = 10), GG (n = 10), and H (İskenderun) (n = 18) samples were obtained from the local producers in Kilis, Gemlik, and İskenderun, respectively and all samples were extracted by three-phase continuous centrifugation process. The temperature was less than 40°C in all processing stages. The olive cultivars were identified according to the morphological properties.

Oil Extraction Systems: The centrifugation system, called “the three-phase system decanter”, is the most popular extraction system in Turkey. In the three-phase system decanter, water was added to the system. As the centrifuge rotates at a high speed (3500-3600 rpm), the non-miscible liquids (olive oil and vegetation water) were separated by proper nozzles from oil pomace due to specific weight differences. This liquid is then taken to a vertical centrifuge where the olive oil is separated from the fruit’s vegetable water.¹⁴

2.4 Sample preparation and analysis of fatty acids

The olive oil samples were prepared as described in the official journal of the European Official Method. The vials were stored at -20 °C in a deep freeze until the moment of chromatographic analysis. 37 fatty acid methyl esters (FAME), mix certified reference material (18919-1 AMP SUPELCO) containing C4–C24 (1.343–6.640 wt. % relative concentration) was used as a reference, and the results were expressed in relative percentages of each fatty acid. Three replicate measurements were performed for each sample.

Chromatographic analyses were achieved on a Shimadzu 2010 gas chromatography (GC) (Shimadzu Technologies, Kyoto, Japan) consisting of autosampler, in-line degasser and a flame ionization detector (FID). The instrumental configuration and analytical conditions were summarized in the following; Shimadzu 2010 GC-FID instrument equipped with a RT-2560 capillary column (100 m x 0.25 mm x 0.20 µm, RESTEK Scientific) under the following temperature program: 140 °C for 5 min followed by an increase to 240 °C at a rate of 20 °C/min for 45 min. The injector and flame ionization detector temperatures were set at 240 °C. The

instrumental configuration for analysis of fatty acid methyl esters from all samples are summarized below.

Column: Rt-2560, 100 m x 0.25 mm I.D., 0.20 µm, **Oven:** 140 °C (5 min), 4 °C/min to 240 °C (at 4 °C min), hold 15 min, **Injection:** 1 µl, split 1:80, **Inj. Temp.:** 240 °C, **Carrier Gas:** Helium, 20 cm/sec., 150 °C, **Detector:** FID, 240 °C. **Liner:** 4 mm I.D split, cup design.

The fatty acids mentioned in section 2.3 were analyzed by GC-FID after the olive oil samples were digested (extracted). The fatty acid composition is a quality parameter and authenticity indicator for virgin olive oils. Typical chromatograms are shown in Figure 2.

The determinations of fatty acid methyl esters (FAME) was carried out by comparing the retention time with those of the 37 components’ reference standard mixture (37-Component FAME Mix, Supelco) analyzed under the same analytical conditions.

2.4. Physicochemical parameters of olive oils

Analysis of peroxide values (PV), fatty acids (FAs) and UV absorption characteristics were performed according European Community (EC) methods (European Economic Community, EEC/2568/91 and European Economic, EE/1429/92).¹⁵

The PV (meq O₂/kg oil) was determined by reacting oil and 3:2 chloroform/acetic acid with potassium iodide in darkness. Free fatty acid (FFA; as oleic acid %) was determined by volumetric method. K232 and K270 extinction coefficients were calculated by means of UV-Vis spectrophotometer.¹⁶ In addition, the refractive index and the viscosity of the oil samples were also determined by a refractometer and a viscosimeter, respectively. The results of FFA, PV, and UV absorption characteristics (K232, K270), the refractive index, and the viscosity are shown in Table 1.

3. RESULTS AND DISCUSSION

3.1. Fatty acids composition of olive oils

A proportionally small amount of polyunsaturated fatty acids (PUFAs) and large amount of monounsaturated fatty acids (MUFAs) determine fatty acid components which have a total up to 98% in oil constituents. The largest amount (98% to 99%) of the fatty acid structure composes of triglycerides, whereas diglycerides and monoglycerides constitute very small amounts; 1% to 1.5% and below 1%, respectively. The different amounts of saturated palmitic (C16:0; 7.5–20%) and stearic fatty acids (C18:0; 0.5–3.5%) as well as monounsaturated palmitoleic (C16:1; 0.3–3.5%) and oleic fatty acids (C18:1; 56.0–85.0%); with polyunsaturated linoleic (C18:2; 3.5–20%) and linolenic fatty acids (C18:3; 0–1.5%), an acid that humans do not amalgamate, constitute nearly all of fatty acid component.¹⁷

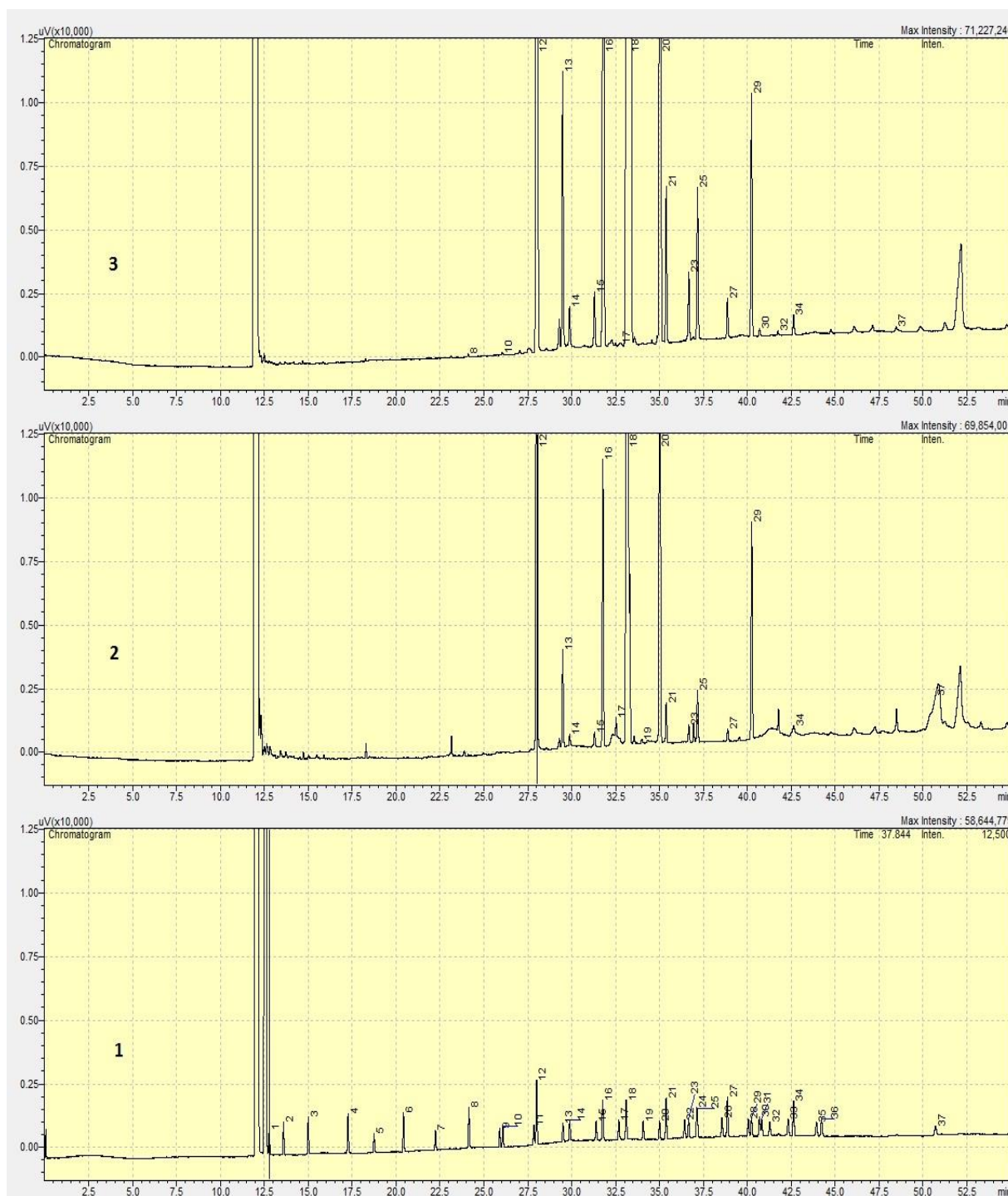


Figure 2. Typical GC-FID chromatograms for (1) composition of 37 components FAME mix standart, (2) GK and (3) KY olive oil.

1: C4:0 (Butyric), **2:** C6:0 (Caproic), **3:** C8:0 (Caprylic), **4:** C10:0 (Capric), **5:** C11:0 (Undecanoic), **6:** C12:0 (Lauric), **7:** C13:0 (Tridecanoic), **8:** Myristic acid C14:0, **9:** Myristoleic acid C14:1, **10:** Pentadecanoic acid C15:0, **11:** cis-10-pentadecanoic acid C15:1, **12:** Palmitic acid C16:0, **13:** Palmitoleic acid C16:1, **14:** Heptadecanoic acid C17:0, **15:** cis-10 heptadecanoic acid C17:1, **16:** Stearic acid C18:0, **17:** Elaidic acid C18:1n9t, **18:** Oleic acid C18:1n9c, **19:** Linolelaidic acid C18:2n6t, **20:** Linoleic acid C18:2n6c, **21:** Arachidic acid C20:0, **22:** gamma-linolenic acid C18:3n6, **23:** cis-11-eicosenoic acid C20:1, **24:** Linolenic acid C18:3n3, **25:** Henoicosanoic acid C21:0, **26:** cis-11,14-eicosadienoic acid C20:2, **27:** Behenic acid C22:0, **28:** cis-8,11,14-eicosatrienoic acid C20:3n6, **29:** Erucic acid C22:1n9, **30:** cis-11,14,17-eicosatrienoic acid C20:3n6, **33:** cis-13,16-docosadienoic acid C22:2, **34:** Lignoceric acid C24:0, **35:** cis-5,8,11,14,17- eioxapentaenoic C20:5n3 (EPA), **36:** Nervonic acid C24:1, **37:** cis-4,7,10,13,16,19-docosahexaenoic acid C22:6n3 (DHA).

The big difficulty is encountered in qualifying the olive oil in terms of varieties and geographic derivation due to how it is composed of different factors. While the environmental factors are soil and climate, irrigation and fertilization form the agronomic factors. Harvesting and ripeness which form cultivation factors have effects as well as the technological factors do, such as post-harvest

storage and extraction system. How chemically vegetable oils are formed is mostly affected by climate the impact of which on monovarietal features is a widely examined subject in research.⁹ Several studies are conducted on fatty acid compositions of the virgin olive oils of KY, H, and Gemlik varieties (Table 2).

Table 1. The determined physicochemical quality parameters of olive oils and the European Regulation Standard limit values for olive oil quality parameters¹⁵

Olive Oil Species and Quality Indexes	Free acidity (oleic acid; %)		Peroxide value (meq O ₂ /kg oil)		K232		K270		Refractive index		Viscosity (cp)	
	Range	Mean± SD	Range	Mean± SD	Range	Mean± SD	Range	Mean± SD	Range	Mean± SD	Range	Mean± SD
Kilis yağlık (Kilis)	1.0-7.8	3.9±1.9	9.6-46.6	27.8±10.5	1.9-3.3	2.6±0.4	0.09-0.41	0.25±0.1	1.467-1.469	1.468±0.00	74.6-81.4	79.0±1.5
Gemlik (Kilis)	0.4-5.9	2.5±1.9	8.6-28.8	18.0±7.3	1.5-2.0	1.8±0.1	0.17-0.32	0.22±0.0	1.468-1.470	1.469±0.00	77.0-80.4	78.1±1.1
Gemlik (Gemlik)	0.3-3.7	1.4±1.1	2.0-27.3	14.8±7.1	1.4-2.0	1.8±0.2	0.15-0.27	0.20±0.0	1.468-1.469	1.469±0.00	76.1-79.3	78.1±0.9
Halhalı (Iskenderun)	0.3-4.8	1.7±1.1	3.3-29.2	15.6±7.2	1.8-2.1	2.0±0.1	0.15-0.76	0.25±0.13	1.467-1.469	1.467±0.00	74.7-82.6	79.0±1.9
Extra virgin OO	≤ 1.0		≤ 20		≤ 2.5		≤ 0.20					
Virgin OO	≤ 2.0		≤ 20		≤ 2.6		≤ 0.25					
Ordinary virgin OO	≤ 3.3		≤ 20		≤ 2.6		≤ 0.25					
Lampante OO	> 3.3		> 20		≤ 3.7		> 0.25					
Refined OO	≤ 0.5		≤ 5		≤ 3.4		≤ 1.20					

Arslan and Ozcan¹⁰ studied on the monovarietal virgin olive oils of four Turkish varieties which are quite common in Turkey: Ayvalık, Gemlik, Kilis yağlık, and Sarulak from Mediterranean and the Southeastern Anatolia Regions of Turkey. In Gemlik and KY olive oils among these varieties, high oleic acid levels were observed up to 70%. Çolakoğlu¹⁸ researched fatty acid levels in the various olive oils collected from the different parts of West and Southeast Anatolia, Mediterranean, Aegean, and Marmara. These varieties were reported according to the oleic, palmitic, linoleic, stearic, palmitoleic, and linolenic acid levels in ranges of 61.0-79.3, 9.0-19.7, 4.7-16.5, 1.4-4.2, 0.3-1.5, and 0.5-1.2%, respectively.

In this study, olive (*Olea europaea* L.) oil samples of KY, GK, GG, and H (Iskenderun-Hatay) (Figure 1) were collected from commercial small or medium-scale olive oil producers. The dominant olive variety grown in Kilis is KY, but Gemlik variety has also been cultivated in Kilis region for 30-40 years. The fatty acid profiles of the olive oils are submitted in Table 3. As can be seen in Table 3, the range for individual fatty acid determined for different varieties virtually are covered the full range of International Olive Council (IOC)¹⁹ and

the Turkish Food Codex standards.²⁰ Generally, the fatty acids levels in each variety of olive oil samples are similar to the same variety samples collected from different regions.

Olive oils are divided into two types according to their fatty acid composition. The first type of olive oil has low linoleic and palmitic content but also high oleic acid content. In the second type of olive oil, it has high linoleic and palmitic content and low oleic acid content. According to this group; Turkish virgin olive oil (such as Spanish, Italian and Greek) is the first type, and Tunisian oils are the second type.⁸ The most important major fatty acid in olive oils is oleic acid. The highest average level of oleic acid (72.6%) is determined for GG in Marmara Region. The oleic acid levels in all varieties are different with a confidence level of 0.05, but at higher confidence level (lower α values), significant differences is not found between KY and GK, and between KY and H ($p < 0.1$). At a confidence level of 0.2, there are three groups according to oleic acid levels; (a) KY and H, (b) GK, and (c) GG. Arslan and Ozcan¹⁰ studied on the monovarietal virgin olive oils of four Turkish varieties: Ayvalık, Gemlik, Kilis yağlık, and Sarulak from Mediterranean and the Southeastern Anatolia Regions of Turkey.

Table 2. Reported fatty acids contents (m/m %) of virgin olive oil of KY, GK, GG, and H (İskenderun), and some varieties of different parts of Turkey
¹Gemlik variety olives grown in three different districts (Gemlik, Nilüfer and Orhangazi) of Bursa. ²Turkish virgin olive samples of five groups from the Aegean Region (n = 64)

Variety	Location	C16:0	C16:1	C17:0	C17:1	C18:0	C18:1n9c	C18:2n6c	C18:3	C20:0	C20:1	C18:3n3	C21:0	C22:0	C24:0	Literature
Kilis yağlık	Kilis	13.4-15.0	0.9-1.7			2.7-3.6	66.8-70.6	7.6-11.2		0.40-0.70		1.0-1.60		0.30-0.50		10
Kilis yağlık	Kilis-Agdere	14.9	1.0	0.12	0.17	3.1	70.1	9.1		0.46	0.23	0.65		0.11	0.06	22
Kilis yağlık	Kilis-Besenli	15	1.1	0.13	0.18	3.2	70.4	8.3		0.53	0.26	0.66		0.14	0.07	22
Nizip yağlık	Nizip	14.2-16.8	1.2-1.3	0.12-0.16	0.17-0.23	3.1-3.2	66.4-73.4	6.3- 10.5		0.44-0.50	0.20-0.21	0.63- 0.68		0.09-0.12	0.04-0.06	22
Nizip yağlık	Nizip	15.4	1.2	0.12	0.16	3.7	68.8	9		0.59	0.24	0.58		0.15	0.09	32
Gemlik	Kilis	14.7	1.6	0.12	0.22	2.9	70.7	8.2		0.40	0.21	0.78		0.09	0.04	22
Gemlik	Gemlik	14	0.9	-	-	2.9	70.7	10.1		0.78	-	0.39		0.15	-	9
Gemlik	İzmir	8.6-16.8	0.9-1.4	0.01-0.13	nd	2.3-3.3	61.9- 65.3	12.8-16.0		0.33-0.56	0.51-0.60	0.19-0.27		0.00-0.12	0.00- 0.10	31
Gemlik ¹	Bursa	12.8-16.9	1.1- 1.3		0.10- 0.16	3.1 -4.0	68.6- 74.4	6.8- 8.7		0.36- 0.50	0.20- 0.25	0.54- 0.60		0.05- 0.13	0.03-1.18	21
Gemlik	Bursa	12.5	1.2	-	-	2.3	72.3	7.9		0.36	0.25	-		0.04	-	23
Gemlik	İzmit	13.9	1.6	0.1	0.2	2.2	72.6	8.1		0.32	0.22	0.6		0.13	0.02	22
Gemlik	Edremit	13.7	1.1	-	-	3.2	72.1	8.9		0.59	-	0.37		0.14	-	9
Gemlik	Mediterranean	14.1-15.8	1.2-1.6			2.3-3.1	67.2-70.2	6.4-10.3		0.50-0.50		0.6-1.5		0.30-0.50		10
Gemlik	İzmir-Torbalı	12.8	1.1	0.12	0.19	2.9	73.4	8.1	0.67	0.38	0.24	0.75		0.09	0.06	22
Gemlik	Karlıdağ	13.9	1.6	0.11	0.23	2.8	69.8	10.0	0.91	0.38	0.23	0.67		0.08	0.06	22
Gemlik	Hatay	9.05	1.9	0.07	0.22	1.3	75.4	10.8		0.17	0.24	0.8		0.05	0.01	22
Gemlik	Antakya	15.6-16.3	1.5-2.2	0.11-0.13	0.21-0.23	2.8-3.0	69.8-71.8	5.6-7.1		0.42-0.46		0.21-0.62	0.14-0.28	0.11-0.11	0.06-0.10	13
Halhali	Antakya	14.4-16.4	0.9-1.3	0.11-0.14	0.15-0.17	3.2-4.2	70.9-71.6	5.8-6.8		0.58-0.69		0.53-0.59	0.18-0.32	0.10-0.19	0.10-0.11	13
Halhali	Reyhanlı. Kırıkhan	11.7-15.4	0.8-1.11	0.10-0.15	0.17-0.18	2.2-4.2	71.1-75.0	6.3-8.3	0.55-0.56	0.61-0.69	0.21-0.23	0.55		0.08-0.16	0.04-0.09	22
Halhali	Nizip	15.1	0.9	0.06	0.05	3.9	63.4	15.3		0.43	0.2	0.59		0.09	0.03	22
Five groups ²	Aegean	12.1	0.78	0.1	0.16	2.5	73.1	9.7		0.40	0.31	0.56		0.12	0.05	29
Different varieties	N.Aegean	12.9	1.04	0.11	0.19	0.2	71.5	10.6	0.69	0.36	0.26			0.10	0.04	22
Different varieties	S.Aegean	12.7	1.06	0.06	0.11	2.1	73.8	8.7	0.74	0.33	0.26			0.09	0.03	22
Different varieties	Mediterranean	13.1	1.77	0.13	0.23	2.5	69.3	11.	0.72	0.38	0.25			0.11	0.04	22
Different varieties	S.Anatolia	15.2	1.12	0.13	0.18	3.2	70.1	8.6	0.65	0.48	0.22			0.11	0.05	22
Different varieties	Bursa. Akhisar	9.0-13.9	0.73-	0.03-0.20	0.04-0.29	1.6-3.6	68.6-76.4	6.9-11.4		0.24-0.57		0.48-0.71		0.06-0.16	0.03-0.07	6
Different varieties	N.Aegean	11.6-13.9	0.7-1.3	0.05-0.17		1.6-3.5	70.0-77.1	7.47-11.0		0.24-0.47	0.22-0.37	0.45-0.71		0.09-0.13	0.03-0.06	32
Different varieties	Different regions	13.7-18.2	1.2-1.7	0.1-0.1	0.16-0.21	2.6-4.3	64.9-72.9	6.8-11.0		0.4-0.6	0.21-0.27	0.53-0.77		0.10-0.15	0.06-0.1	6

Table 3. Fatty acids (FAs) contents (m/m %) of virgin olive oil varieties from different geographic regions of Turkey*. Suggested or regulatory levels thresholds from relevant sources are also provided

Types of FAs	Formula of FAs	IUPAC name of FAs	Kilis Yağlık (KY) n= 18		Gemlik-Kilis, (GK) n = 10		Gemlik-Gemlik (GG) n = 10		Halhali (H) (İskenderun) n = 18		Turkish Food Codex, IOC
			Range	Mean±SD	Range	Mean±SD	Range	Mean±SD	Range	Mean±SD	
SFAs	C 14:0	Myristic	0.000-0.05	0.012±0.014	0.000-0.013	0.006±0.006	0.000-0.014	0.007±0.005	0.01-0.016	0.012±0.001	≤ 0.05
	C15:0	Pentadecanoic	0.000-0.016	(0.005±0.005)ab	0.000-0.017	(0.004±0.06)ab	0.000-0.017	(0.005±0.005)ab	0.006-0.009	(0.008±0.001)b	
	C16:0	Palmitic	12.93-14.98	(13.946±0.511)a	12.41-16.56	(13.740±1.373)a	10.9-13.081	(11.820±0.78)b	12.160-15.00	(14.040±0.810)a	7.5-20
	C17:0	Heptadecanoic	0.11-0.141	(0.126±0.009)a	0.113-0.268	(0.144±0.047)a	0.094-0.18	(0.138±0.025)a	0.114-0.168	(0.141±0.013)a	≤ 0.3
	C18:0	Stearic	3.409-4.08	(3.716±0.181)b	3.133-3.851	(3.507±0.242)a	2.873-3.909	(3.402±0.310)a	2.995-3.815	(3.516±0.241)a	0.5-5.0
	C20:0	Arachidic	0.401-0.58	(0.568±0.049)c	0.401-0.594	(0.496±0.059)b	0.415-0.546	(0.457±0.037)a	0.462-0.634	(0.543±0.043)c	≤ 0.6
	C21:0	Henoicosanoic	0.546-0.637	(0.590±0.049)a	0.561-0.776	(0.631±0.059)b	0.447-0.660	(0.557±0.070)a	0.561-0.735	(0.632±0.046)b	
	C22:0	Behenic	0.127-0.178	(0.152±0.025)b	0.091-0.233	(0.152±0.041)b	0.106-0.150	(0.127±0.014)a	0.120-0.176	(0.141±0.016)ab	≤ 0.2
	C24:0	Lignoceric	0.069-0.409	(0.150±0.0130)a	0.00-0.989	(0.234±0.298)a	0.000-1.168	(0.270±0.465)a	0.063-0.117	(0.081±0.014)a	≤ 0.2
	ΣSFA (%)		19.256		18.904		16.787		19.114		
MUFAs	C14:1	Myristoleic	0.000-0.000	-	0.000-0.000	-	0.000-0.000	-	0.000-0.000	-	
	C15:1	cis-10-pendacanoic	0.000-0.458	(0.0459±0.134)a	0.000-0.000	0.000a	0.000-0.000	0.000 a	0.006-0.013	(0.009±0.002)a	
	C16:1	Palmitoleic	0.799-1.060	(0.913±0.090)ab	0.940-1.193	(1.057±0.095)a	0.601-1.176	(0.826±0.169)ab	0.515-1.276	(0.988±0.252)b	0.3-3.5
	C17:1	cis-10-pendacanoic	0.161-0.213	(0.187±0.012)a	0.165-0.240	(0.192±0.020)ab	0.147-0.275	(0.230±0.037)c	0.165-0.238	(0.206±0.020)b	≤ 0.3
	C18:1n9c	Oleic	64.40-70.25	(68.436±1.507)ab	60.35-72.96	(67.059±4.971)a	70.37-74.73	(72.564±1.655)c	64.596-72.07	(69.426±1.760)b	55.0-83.0
	C20:1	cis-11-eicosenoic	0.209-0.274	(0.258±0.015)a	0.160-0.266	(0.224±0.036)a	0.229-0.306	(0.250±0.022)a	0.251-0.340	(0.269±0.028)a	≤ 0.4
	C22:1n9	Erucic	0.713-5.453	(1.686±1.198)ab	0.694-3.990	(2.029±1.340)b	0.694-2.269	(1.189±0.571)a	0.672-1.421	(0.950±0.212)a	
		ΣMUFA (%)		71.523		70.561		73.870		70.897	
	MUFA/PUFA		6.92		6.98		8.65		7.77		

*Results of statistical analyses (Duncan Multiple Test) of fatty acid levels in olive oil varieties are indicated in the "Mean" columns of this table. Values with the same letter are not statistically different ($p < 0.05$) for that element across the species.

SD: standard deviation; **FA:** fatty acid, **SFA:** saturated fatty acid, **MUFA:** monounsaturated fatty acid, **PUFA:** polyunsaturated fatty acid, **USFA:** unsaturated fatty acid, **O/L:** oleic/linoleic, **PA/L:** palmitic/linoleic; **DHA:** Cis-4,7,10,13,16,19-docosahexaenoic acid.

DOI: 10.32571/ijct.455519

E-ISSN:2602-277X

Table 3's continuation

PUFAs	C18:2n6c	Linoleic**	7.372-9.879	(8.755±0.837)b	6.304-9.838	(8.511±1.131)ab	6.575-10.58	(7.915±1.284)a	6.449-10.930	(8.557±1.313)ab	3.5-21.0
	C20:3n6	cis-8.11.14- eicosatrienoic	0.000-0.012	(0.001±0.0030)a	0.000-0.000	0.000a	0.000-0.027	(0.016±0.009)b	0.000-0.000	0000a	
	C20:3n6	cis-11.14.17- eicosatrienoic	0.021-0.209	(0.034±0.044)a	0.000-0.028	(0.013±0.013)a	0.047-0.327	(0.096±0.085)b	0.023-0.032	(0.026±0.003) a	
	C22:6n3	DHA	0.000-1.253	(0.287±0.368)a	0.000-3.140	(0.937±1.200)b	0.000-0.00	0.000a	0.006-0.061	(0.020±0.016)a	
		∑PUFA (%)		10.332		10.101		8.542		9.122	
	∑USFA (%)		81.855		80.662		82.412		80.019		
	∑(MUFA+PUFA)										
	O/L		6.73-9.47	(7.89±0.83)a	6.180-10.03	(8.073±1.388)a	7.116-1.340	(9.321±1.426)b	6.206-11.176	(8.279±1.485)a	

*Results of statistical analyses (Duncan Multiple Test) of fatty acid levels in olive oil varieties are indicated in the "Mean" columns of this table. Values with the same letter are not statistically different (p < 0.05) for that element across the species.

**p < 0.1.

SD: standard deviation; FA: fatty acid, SFA: saturated fatty acid, MUFA: monounsaturated fatty acid, PUFA: polyunsaturated fatty acid, USFA: unsaturated fatty acid, O/L: oleic/linoleic, PA/L: palmitic/linoleic; DHA: Cis-4,7,10,13,16,19-docosahexaenoic acid.

They reported that Gemlik and KY olive oil samples had high oleic acid levels rising to 70%, but KY had low linoleic and palmitic acids levels which made it superior to Gemlik.

The other major fatty acids (FAs) are palmitic, stearic, and linoleic acids. The mean levels of palmitic and linoleic acids in KY, GK, and H varieties are similar and higher than those in GG (Table 3). In our study, olive oil of GG variety has the lowest mean linoleic and palmitic acid levels. However, Arslan and Ozcan¹⁰ reported lower linoleic and palmitic acids levels in olive oil samples of Kilis yağlık than those reported in Gemlik variety from Mediterranean Region.

In this study, mean oleic and linoleic acids in KY, Gemlik, and H varieties are generally similar to the mean levels of FAs in the same varieties reported by some authors (Table 3).^{9,13,21-23} The levels of palmitic and oleic acids in GK and GG olive oil samples cultivated in different regions show significant differences at a confidence level of 0.05, but significant differences are found for stearic and linoleic acids levels in the same varieties and at the same confidence level. At lower confidence levels (higher α values), significant differences are found for palmitic ($p < 0.1$) and oleic acids ($p < 0.1$) (Table 3). The ratios of oleic to linoleic acid and MUFAs to PUFAs are important indicators of oxidative stability. KY, GK, and H varieties had similar oleic/linoleic acid ratios (O/L) while GG variety had higher O/L ratio. The O/L ratios did not show a significant difference at a confidence level of 0.05 among KY, GK, and H varieties, but differences appeared at confidence levels of 0.1 and 0.2. These O/L ratios are in agreement with the findings of Arslan and Ozcan¹⁰ and Pinelli et al.²⁴

Negative relationships between oleic and linoleic acid levels in the South Anatolian Region varieties were determined from coefficient of determination, H ($R^2 = -0.66$), GK ($R^2 = -0.65$), and KY ($R^2 < -0.30$). Oleic acid may have been transformed into linoleic acid especially in olive oils produced from these varieties.

Brescia et al.²⁵ reported that fatty acid content did not present any particular trend with ripening, however, the oil fraction sensibly enriched in longer-chain fatty acids with ripening. It has been reported that the contents of mono- and polyunsaturated fatty acids are reduced with olive ripening and this can be expressed by the conversion of enzyme activity to oleic acid and linoleic acids. Baccouri et al.²⁶ reported that the oleic acid level decreased with ripeness or harvest time. However, some authors^{27,28} reported that the increase in linoleic acid content was due to the fact that besides the continuing biosynthesis of triglycerides, with the formation of oleic acid, the enzyme oleate desaturase was active, transforming oleic acid into linoleic acid.

The mean levels of palmitoleic, arachidic, henoicosanoic, behenic and erucic acid being minor FAs in KY, GK, and H are similar, while the mean levels of the FAs in GG is lower. Hepta decanoic acid mean levels in four varieties are near to each other. However, mean levels of cis-10-pendacanoic and cis-11,14,17-eicosatrienoic acid considered as minor fatty acids in GG are higher than the those of the other varieties. On the other hand, it cannot be made generalizations among four varieties in terms of the mean levels of the other minor fatty acids such as heptadecanoic, cis-10-pendacanoic, cis-11-eicosenoic, linolenic, cis-8.11.14-eicosatrienoic acid, and docosahexaenoic acid (DHA) (Table 3).

Some minor FAs, heptadecanoic, lignoceric, cis-11-eicosenoic acids levels in GK and GG olive oil samples as being the same varieties but cultivated in different regions did not show significant differences at a confidence level of 0.05, but significant differences were found for arachidic, henoicosanoic, behenic palmitoleic, and linolenic acids levels at the same confidence level in the same samples (Table 3).

Minor FAs, heptadecanoic, lignoceric, and cis-11-eicosenoic acids levels were not different at a confidence level of 0.05, but significant differences were found at a confidence level of 0.05 for arachidic, henoicosanoic, beheni, palmitoleic, cis-10-pendacanoic, erucic, and linolenic acids levels between olive oil samples of KY and GK varieties cultivated in the same region.

Significant differences ($p < 0.05$) are present between KY and GK varieties cultivated in the same region, minor SFAs such as arachidic and henoicosanoic, minor MUFAs such as palmitoleic, cis-10-pendacanoic, and erucic, and minor PUFA and DHA. However, significant differences ($p < 0.05$) were not found for the levels of some minor SFAs such as heptadecanoic, behenic, and lignoceric acids and a minor MUFA, cis-11-eicosenoic acids. The differences between levels of major FAs in KY and GK varieties cultivated in the same region can be primarily attributed to genotype. The differences and/or similarities between levels of FAs between GK and GG olive oil samples being the same varieties but cultivated in different regions can be attributed to the physicochemical properties of soils and the other ecological factors. Genotype, clearly affects the composition of the fatty acid. The fatty acid profile of an olive oil is genotype dependent in terms of unsaturated/saturated fatty acids ratio.⁷

KY variety contains the highest percentage of total SFAs (19.3%) and PUFAs (10.3%) while GG variety has the lowest total SFAs (16.8%) and PUFAs (8.5%). Because linoleic acid includes the major fatty acid in the fraction, generally, the varieties including higher linoleic acid levels have high total PUFA. GG variety has the lowest total SFAs (16.8%) essentially due to the lowest palmitic acid content, which represents the major fatty

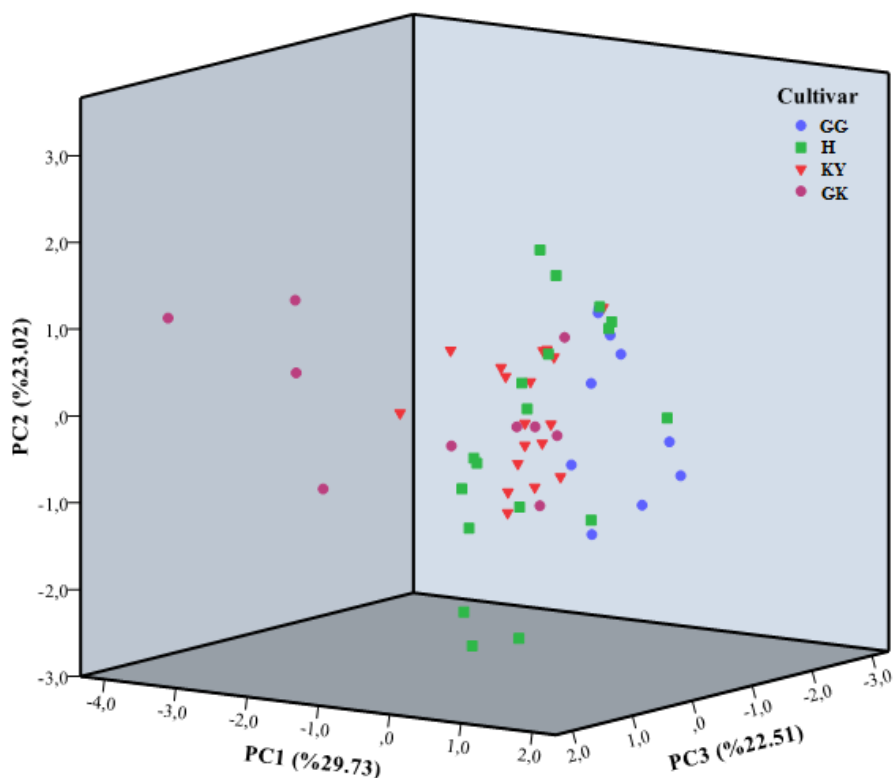


Figure 3. Principal component analyses showing the natural interposition of olive oils of Gemlik-Gemlik (GG), Halhalı (H), Kilis yağlık (KY), and Gemlik-Kilis (GK) varieties.

acid in the SFA fraction. KY, GK, and H varieties may accept similar in respect to the total SFAs levels as 19.3, 18.9 and 19.1%, respectively. SFAs levels between GK and GG olive oil samples as being the same varieties show significant differences at a confidence level of 0.05, except for minor SFAs, heptadecanoic, and lignoceric acids levels among all varieties (Table 3).

In general, SFAs are found at greater levels in the varieties cultivated in the Southeast and Mediterranean Regions. However, significant differences are not seen clearly among mean SFAs levels reported in Gemlik varieties cultivated in Marmara^{9,21-23}, in Aegean^{9,22,29}, in Mediterranean^{13,22} and in Southeastern Anatolia²² Regions (Table 3). GG variety contains the highest percentage (73.9%) of total MUFAs due to the highest oleic acid (C18:1n9c) content (72.6%), which represents the major fatty acid in the MUFA fraction. The total MUFAs of KY, GK, and H are 71.5, 70.6, and 70.9%, respectively. While the mean levels of DHA in KY and GK varieties are minor, it is at trace levels in all of H variety and below the detection limit of GC-FID method in all samples of GG variety. In vitro studies have suggested that PUFAs are more proinflammatory than

monounsaturated FAs (MUFAs) and saturated FAs (SFAs). In fact, linoleic acid has more oxidative and inflammatory stress induction capacity than other fatty acids.³⁰

The levels of minor FAs such as arachidic, henoicosanoic, beheni, palmitoleic, cis-10-pendacanoic, and erucic acids are significantly ($p < 0.05$) different among olive oil samples of four varieties, but the levels of heptadecanoic, lignoceric, and cis-11-eicosenoic are not different among the same samples at the same confidence level. The variations in FAs composition observed in olive oils analyzed (Table 3) are probably related to both genetic factors and environmental conditions during the development and the progress in maturity of the fruit.

3.2. Principal component analyses

There are formed 8 factors, and the total variance ratio is 84.796% when all components are examined together (Figure 3). Fatty acids analyzed in olive oil samples of GG, H, KY, and GK were separated into three components;

Major components (> 1.0%): Major fatty acids are oleic (C18:1n9c), linoleic (C18:2n6c), palmitic (C 16:0), stearic (C18:0), and erucic (C22:1n9). Varimax vertical rotation method is applied after factor loadings are calculated for major components. Eigenvalue have two factors greater than 1. The explained variance rate is 65.732%. The factor loadings of each component are as follows. The variance ratio for PC1 explained by the first component is 34.15% while the variance ratio for PC2 explained by the second component is 31.58%. C18:1n9c, and C22:1n9 acids were the most important factors for PC1 whereas C18:2n6c, C16:0, and C18:0 were the most important factors for PC2 (Figure 3). According to PCA values, GG, H, and GK species seem to be clearly separated. KY olive oil type is mixed partially with GG and H.

Minor components (0.01-1%): Minor components of fatty acids in olive oils are arachidic (C20:0), cis-10-pendacanoic (C17:1), behenic (C22:0), cis-11-eicosenoic (C20:1), palmitoleic (C16:1), henoicosanoic (C21:0), lignoceric (C24:0), linolenic (C18:3n3), and heptadecanoic (C17:0). There are formed 4 factors above Eigen Value 1. The total variance ratio explained is 72.74%. The explained variances for the first three components (PC1, PC2, and PC3) are 22.19%, 17.48%, and 17.26%, respectively. The most important factors are C20:0, C22:0, C20:1, and C17:1 for PC1, C16:1 and C21:0 for PC2, and C24:0 and C18:3n3 for PC3.

Trace components (< 0.01%): Trace components of fatty acids in olive oils are pentadecanoic (C15:0), lignoceric acid (C24:0), cis-10-pendacanoic (C15:1), cis-11.14.17-eicosatrienoic (C20:3n6), and DHA (C22:6n3). There are formed 3 factors above Eigen Value 1. The explained variances for the first three components (PC1, PC2, and PC3) are obtained as 29.73%, 23.02%, and 22.51%, respectively. The most important factors are C15: 0 and C24: 0 for PC1, C15: 1 and C20: 3n6. for PC2.

4. CONCLUSIONS

The present study provide information regarding the fatty acid composition of Kilis yağlık (KY), Gemlik-Kilis (GK), Gemlik-Gemlik (GG), and Halhalı (H) (İskenderun) varieties that are collected from commercial olive oil producers. Individual fatty acid determined for different varieties has covered with the range of the IOC and the Turkish Food Codex standards.

The levels of oleic and palmitic acids in GK and GG showed significant differences at a confidence level of 0.05, but significant differences were found for stearic and linoleic acids levels in the same varieties and at the same confidence level. However, at a confidence level of 0.2, there were three groups according to oleic acid levels; (a) KY and H, (b) GK and (c) GG. Also, KY, GK, and H varieties had similar oleic/linoleic acid ratios (O/L) while GG variety had higher O/L ratio than the

other varieties' O/L ratios. The mean levels of other major FAs such as palmitic, stearic, and linoleic acids in KY, GK, and H varieties were similar, but higher than those in GG. GG variety had both the lowest mean of linoleic and palmitic acid levels. Negative relationships between oleic and linoleic acid levels in the South Anatolian Region varieties were determined from coefficient of determination, H ($R^2 = -0.66$), GK ($R^2 = -0.65$), and KY ($R^2 < -0.30$). The results could be attributed to oleic acid having been transformed into linoleic acid in olive oils produced from these varieties.

The mean levels of palmitoleic, arachidic, henoicosanoic, behenic, and erucic acids being minor FAs in KY, GK, and H were similar, while the mean levels of the FAs in GG was lower. Also, the mean levels of cis-10-pendacanoic and cis-11,14,17-eicosatrienoic acids as minor fatty acids in GG were higher than of other varieties. On the other hand, it cannot be made generalizations among four varieties in terms of the mean levels of the other minor fatty acids such as heptadecanoic, cis-10-pendacanoic, cis-11-eicosenoic, linolenic, cis-8.11.14-eicosatrienoic acid, and DHA.

There were significant differences ($p < 0.05$) between KY and GK in terms of minor SFAs such as arachidic and henoicosanoic, minor MUFAs such as palmitoleic, cis-10-pendacanoic, erucic, and minor PUFA and DHA. However, significant differences were not found for the levels of some minor SFAs such as heptadecanoic, behenic, and lignoceric acids, and a minor MUFA, cis-11-eicosenoic acids. The differences between levels of major FAs in KY and GK varieties cultivated in the same region can be primarily attributed to genotype. It was seen that KY variety contained the highest percentage of total SFAs (19.3%) and PUFAs (10.3%), while GG variety had the lowest total SFAs (16.8%) and PUFAs (8.5%). Because linoleic acid had the major fatty acid in fraction, generally the varieties having higher linoleic acid levels had high total PUFAs. While DHA mean levels in KY and GK were minor, it was at trace levels in all of H and below the detection limit of GC-FID method in all samples of GG variety.

ACKNOWLEDGMENTS

Authors thank to the Laboratory of Apricot Research Institute in Malatya for required analyses, and to the Institute authorities for fatty acid analyses, and especially, the people who contributed to the collection of olive oil samples from Kilis, İskenderun and Gemlik.

Conflict of interest

Authors declare that there is no a conflict of interest with any person, institute, company, etc.

REFERENCES


1. Cavusoglu, A.; Cakir, M. *Modern olive farming (Modern Zeytincilik)*. Ministry of Agriculture and Village Affairs, 1998; pp 303.
2. Efe, R.; Soykan, A.; Curebal, I.; Sonmez, S. *Olive and olive oil in edremit region*. Edremit Municipality Cultural Publication, Edremit. 2013; pp 9.
3. Vossen, P. *Hortscience* **2007**, 42, 1-8.
4. The Official Gazette of Republic of Turkey, No: 20507, Ankara, 1990.
5. Canozar, O. *The catalogue of standard olive cultivars*. Ministry of Agriculture and Rural Affairs, The General Directorate of Agricultural Production and Development, No: 334, Professional publications, Ankara, 1991.
6. Diraman, H.; Dibeklioglu, H. *J. Am. Oil. Chem. Soc.* **2009**, 86, 663-674.
7. Inglese, P.; Famiani, F.; Galvano, F.; Urbani, U. *Hortic. Rev.* **2011**, 38, 83-147.
8. Boskou, D. *Olive oil chemistry and technology*. AOCS Press, Champaign, Illinois. 1996.
9. Gurdeniz, G.; Ozen, B.; Tokatli, F. *Eur. Food Res. Technol.* **2008**, 227, 1275-1281.
10. Arslan, D.; Ozcan, M.M. *J. Food Agric. Environ.* **2011**, 9, 53-59.
11. Kaplan, M.; Orman, S.; Kadar, I.; Koncz, J. *Agric. Ecosyst. Environ.* **2005**, 111, 41-46.
12. Gozel, H. Study on determine rates of seed germination and rooting cuttings on Kilis yağlık and Nizip yağlık olive varieties. MSc Thesis, University of Kahramanmaraş Sutcu İmam, 2006.
13. Konuskan, D.B. Determination of some properties of solvent extracted oils of olive oil Halhalı, Sari hasebi and Gemlik varieties grown in Hatay and comparison with olive oils obtained by mechanical method. PhD Thesis, University of Çukurova, 2008.
14. Gurdeniz, G. Chemometric studies for classification of olive oils and detection of adulteration. MSc Thesis, Izmir Institute of Technology University, 2008.
15. European Union Commission, Regulation EEC 2568/91 on the characteristics of olive oil and olive residue oil and on the relevant methods of analysis, Official Journal of European Communities L248, 1991.
16. Diraman, H.; Dibeklioglu, H. *J. Am. Oil Chem. Soc.* **2009**, 86, 663-674.
17. Montedoro, G.F.; Servili, M.; Pannelli, G. Le caratteristiche del prodotto e le relazioni con le variabili agronomiche, In: P. Fiorino (ed.), *Olea-Trattatodi olivicoltura*, Edagricole-Edizioni Agricole de Il Sole 24 ORE Edagricole, Bologna, 2003, pp 263-289.
18. Colakoğlu, M. Analytical characters of Turkish olive oil obtained from 1966-1967 Campaign, Aegean University, Faculty of Agriculture, İzmir, 1969.
19. International olive oil council, trade standard applying to olive oils and olive: pomace oils, COI/T.15/NC No: 3 Rev.1, 2008.
20. Turkish Food Codex Communique on olive oil and pomace oil, The Official Gazette of Republic of Turkey, No: 26602, Ankara, 2007.
21. Uylaser, V.; Tamer, C.E.; Incedayi, B.; Vural, H.; Copur, O.U. *J. Food Agric. Environ.* **2008**, 6, 26-30.
22. Yavuz, H. Determination of some quality and genuineness of Turkish olive oils. MSc Thesis, Ankara University, 2008.
23. Uylaser, V.; Yıldız, G. *Not. Bot. Horti Agrobot. Cluj Napoca.* **2013**, 41, 518-523.
24. Pinelli, P.; Galardi, C.; Mulinacci, N.; Vincieri, F.F.; Cimato, A.; Romani, A. *Food Chem.* **2003**, 80, 331-336.
25. Brescia, M.A.; Pugliese, T.; Hardy, E.; Sacco, A. *Food Chem.* **2007**, 105, 400-404.
26. Baccouri, O.; Guerfel, M.; Baccouri, B.; Cerretani, L.; Bendini, A.; Lercker, G.; Zarrouk, M.; Miled, D.D.B. *Food Chem.* **2008**, 109, 743-754.
27. Gutierrez, F.; Arnaud, T.; Albi, A.M. *J. Am. Oil Chem. Soc.* **1999**, 76, 617-621.
28. Cossignani, L.; Simonetti, M.S.; Damiani, P. *Eur. Food Res. Technol.* **2001**, 212, 160-164.
29. Diraman, H.; Saygi, H.; Hisil, Y. *J. Am. Oil Chem. Soc.* **2010**, 87, 781-789.
30. Akoh, C.C.; Min, D.B. *Food Lipids Chemistry, Nutrition, and Biotechnology*. Second Edition, Revised and Expanded, Marcel Dekker, Inc. New York, Basel. 2002.
31. Aktas, A.B.; Ozen, B.; Tokatli, F.; Sen, I. *Food Chem.* **2014**, 161, 104-111.


DOI: 10.32571/ijct.455519


E-ISSN:2602-277X

32. Diraman, H.; Dibekoglu, H. *Int. J. Food Prop.* **2014**, 17, 1013-1033.

ORCID

 ID 0000-0002-6252-1819 (H. Avci)

 ID 0000-0002-9040-4249 (Y. Uğur)

 ID 0000-0002-9169-9771 (S. Erdoğan)



Investigation of different reactor configurations for electrochemical ferrate (VI) synthesis

Sibel BARISCI*

on the last page

Environmental Engineering Department, Faculty of Engineering, Gebze Technical University, 41400, Gebze, Kocaeli, Turkey

Received: 09 August 2018, Revised: 22 September 2018; Accepted: 24 September 2018

*Corresponding author e-mail: sbarisci@gtu.edu.tr

Citation: Barisci, S. *Int. J. Chem. Technol.* 2018, 2 (2), 89-94.

ABSTRACT

There are numerous methods used for wastewaters treatment. The agents to be used in those methods should be harmless and degraded to non-hazardous byproducts. Ferrate (VI) has high oxidation capability and is reduced to a non-toxic byproduct, Fe (III), during the degradation of pollutants. Thus, ferrate (VI) is one of the most influential and eco-friendly chemical for water and wastewater treatment. This study aimed to investigate electrochemical ferrate (VI) synthesis, using two different reactor configurations using pure iron plates (R1) and cast-iron flakes (R2) as electrode. In this study, the optimum conditions have been determined experimentally for electrochemical synthesis of ferrate (VI). Ferrate (VI) yield and current efficiency are leading parameters for this purpose. The most appropriate electrolyte concentration is found as 16 M, and the applied current of 1 A is the optimum value with the highest determined current efficiency for both reactor configurations. In comparison with reactor configurations, R2 with iron flakes provided higher ferrate (VI) yield and current efficiency providing higher surface area and higher dissolution rates.

Keywords: Ferrate (VI), reactor design, electrochemical synthesis method, optimum conditions.

Elektrokimyasal ferrat (VI) sentezi için farklı reaktör konfigürasyonlarının araştırılması

ÖZ

Atık suların arıtılmasında kullanılan çok sayıda yöntem bulunmaktadır. Bu proseslerde kullanılan kimyasalların zararsız olması ve tehlikesiz ürünlere parçalanması gerekmektedir. Ferrat (VI), yüksek yükseltgeyici yeteneğe sahiptir ve kirleticilerin parçalanması sırasında toksik olmayan bir yan ürüne, Fe (III)' e indirgenir. Bu sebeple, ferrat (VI) su ve atık su arıtım için en etkili ve çevre dostu kimyasallarından biridir. Bu çalışma elektrot olarak saf demir plaka (R1) ve sert 2) demir pullar (R2) kullanarak elektrokimyasal ferrat (VI) sentezini incelemeyi amaçlamıştır. Bu çalışmada, ferrat (VI)'ın elektrokimyasal sentezi için optimum şartlar deneysel olarak belirlenmiştir. Ferrat (VI) verimi ve akım verimliliği bu amaç için önde gelen parametrelerdir. En uygun elektrolit konsantrasyonu 16 M olarak bulunmuştur ve uygulanan 1 A akım, her iki reaktör konfigürasyonu için en yüksek belirlenen akım verimliliğine sahip optimum değerdir. Reaktör konfigürasyonlarına kıyasla, demir pullu R2 daha yüksek ferrat (VI) verimi ve daha yüksek yüzey alanı ve çözünme oranları sağlayan akım verimliliği sağlamıştır.

Anahtar Kelimeler: Ferrat (VI), reaktör tasarımı, elektrokimyasal sentez metodu, optimum şartlar.

1. INTRODUCTION

Iron has wide variety of valence states ranging from 2- to 8+. All those valence states have different electron structures, co-ordination numbers and geometries. However, apart from metallic iron, only two ions of iron are stable in aqueous medium, namely, iron (II) and iron (III). However, 6+ valence state of iron which is known as ferrate (VI), is also stable at alkaline pH values.

Ferrate (VI) with characteristic purple color is powerful oxidant. At acidic conditions, its redox potential is more than that of ozone (2.2 V). For this reason, the synthesis of ferrate (VI) has been considered by many researchers and ferrate has been used for water and wastewater treatment agent for years.

Commonly, there are three ferrate (VI) synthesis methods, i.e., (1) wet oxidation, by oxidizing a Fe (III) salt at an extremely alkaline medium by hypochlorite or

chlorine, (2) dry oxidation, by heating or melting several iron-oxide-containing minerals at the conditions of robust alkaline and oxygen flow, and (3) an electrochemical method, by anodic oxidation of iron or its alloys in strong alkaline media using NaOH or KOH as electrolyte. Among those methods, electrochemical method has numerous advantages for instance safety, simplicity and cost-effectiveness.¹ The electrochemical ferrate (VI) synthesis is noticeably affected by many factors, mainly, the electrolyte type²⁻³ and its concentration, current density⁴⁻⁵, temperature⁶, anode type⁷ and anode structure.⁸

This study focuses on the determination of optimum operating conditions for the electrochemical ferrate (VI) synthesis using two different reactor configurations. High purity iron plates and iron flakes as anode were used for the first (R1) and second (R2) reactor configuration, respectively. NaOH concentration and applied current were considered as key parameters that impact ferrate (VI) synthesis in each electrochemical reactor. Current efficiency and ferrate (VI) yield were considered for the determination of optimum conditions for each reactor, and the comparison of reactor configurations was presented in this paper.

2. MATERIALS AND METHODS

2.1. Materials

Potassium ferrate (K_2FeO_4 , purity of 97%) and sodium hydroxide (pellets, anhydrous, purity of $\geq 98\%$) were supplied from Sigma Aldrich. All solutions were prepared with high quality pure water using Millipore Water Purification System. High purity iron plate electrodes with iron content of 99.195% and cast-iron flakes were provided by Artı Makina, Turkey. The electrodes were appropriate for the EN 10025-2 standards.

2.2. Experimental set-up

2.2.1. Reactor configuration using pure iron plates (R1)

The electrochemical synthesis of ferrate (VI) was conducted in an electrochemical cell made of plexiglass material. The dimensions of the cell are 15.5 x 14 x 16 cm, and the wall thickness is 1 cm. Two anodes and two cathodes (iron plates) were used and they were connected by way of monopolar mode for each experiment. Electrolyte solution was mixed using magnetic stirrer. The experimental set-up for R1 can be seen in Figure 1.

2.2.2. Reactor configuration using iron flakes (R2)

The electrosynthesis was conducted in a plexiglass electrochemical cell with the dimensions of 22 x 14 x 10 cm,

and the wall thickness is 0.4 cm. As seen in Figure 2, plexiglass material with 20 holes which have 1 cm in diameter was placed to the bottom of the reactor over 1 cm above. These holes provided input of the electrolyte to the reactor. Then iron flakes as anode were located on this perforated material. Pure iron plate as cathode with the same shape and dimensions of plexiglass material was situated to top part of the reactor, and insulant plastic with the same dimensions was placed between the cathode and iron flakes to prevent short circuit. To allow stirring the electrolyte, air from air compressor was provided with silicon pipe. The R2 set-up can be seen in Figure 2.

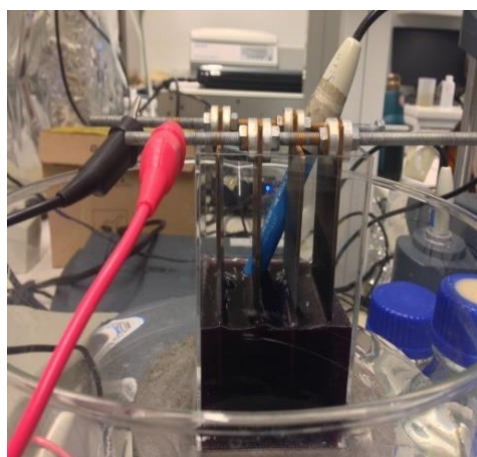


Figure 1. First reactor configuration with pure iron plates (R1).

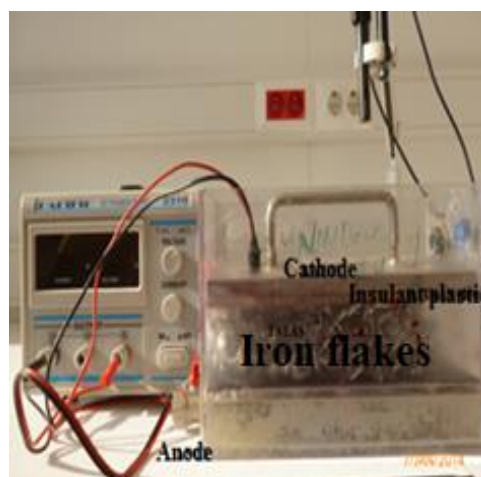


Figure 2. Second reactor configuration with iron flakes (R2).

2.3. Methods

The concentration of ferrate (VI) was measured by HACH DR-5000 UV/VIS Spectrophotometer at 505 nm of wavelength. Calibration curves were prepared for each NaOH concentration according to the experiments. For this purpose, NaOH solutions at various concentrations

(15 M, 16 M, 18 M and 20 M) were prepared, and various amounts of potassium ferrate were added to each solution. After that 0.10; 0.20; 0.25; 0.5; 1.0; 1.5; 2; 2.5 mM potassium ferrate solutions in NaOH were obtained. The absorbance values were measured at $\lambda = 505$ nm. R^2 values of calibration curves were found more than 0.99. The calibration curve and UV spectrum of ferrate (VI) can be found in Figure 3.

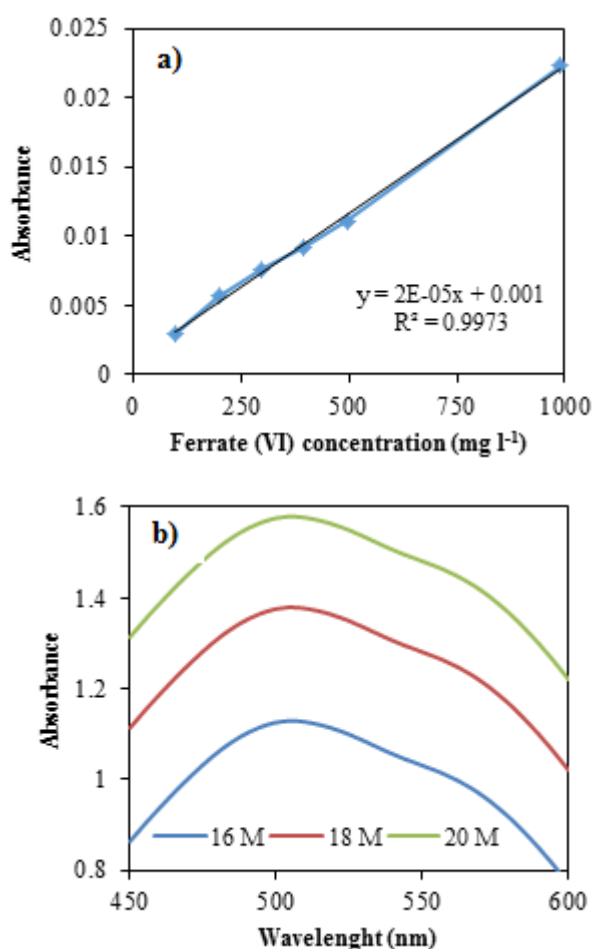


Figure 3. (a) Calibration curve for ferrate (VI) analysis and (b) the wavelength scan of ferrate (VI) at different NaOH concentrations.

After reactor set-up, the procedure was followed: before electrochemical synthesis, electrodes were washed with 0.5 N H₂SO₄ solution for 5 minutes and rinsed with deionized water, then they were dehydrated in the oven and located in a desiccator to turn cold. The same process was applied after each experiment. At that point the electrodes were weighed before and after the experiments to notice total amount of dissolved iron experimentally. As it is seen in Eq. (1), current efficiency (CE) was determined considering the ratio of the experimental ferrate (VI) concentration, [Fe (VI)]_e to the amount of ferrate(VI) which was calculated theoretically, [Fe (VI)]_t,

according to the Faraday's Law in Eq. (2).

$$\text{Current Efficiency (CE) (\%)} = \frac{[\text{Fe (VI)}]_e}{[\text{Fe (VI)}]_t} \times 100 \quad (1)$$

$$[\text{Fe (VI)}]_t = \frac{M_w \times i \times t}{z \times F} \quad (2)$$

Where M_w is the molecular weight of ferrate (VI) (120 g mol⁻¹), i is applied current (A), t is electrolysis time (sec); z is electron number in the reaction, F is a constant of Faraday's Law (96485 Coulomb/mol).

All experiments were conducted at room temperature. Continual current (DC) was provided by GW Instek PSP-405 Programmable power source. The electrolytic voltage was noted through the electrolysis. Different alkaline concentrations were used to evaluate the effect of NaOH concentration on the ferrate (VI) synthesis yield. Besides, different applied current values (1, 3 and 5 A) were applied to see the effect. Electrolysis period was 3 hours for all applied current values. Samples were analysed using UV-Vis spectrophotometer. Measurements were repeated, and the average value was presented. The optimum conditions were determined considering ferrate (VI) yield and CE.

3. RESULTS AND DISCUSSION

3.1. Effect of parameters for reactor configuration-R1 (pure iron plates)

One of the key factors that affects the electrochemical ferrate (VI) synthesis is the type of electrolyte and its concentration.⁹ The electrolyte type determines the dissolution rate of iron anode and the formation of oxo-hydroxide layers occurring on the anode surface.¹⁰ NaOH is the principal electrolyte for electrochemical synthesis of ferrate (VI).¹¹ Figure 4 presents the ferrate (VI) yield at different electrolyte concentrations and applied current values.

As seen from Figure 4, the maximum ferrate (VI) yield was obtained with 16 M NaOH media at applied current of 5 A (1.28 g l⁻¹). 20 M NaOH media also provided high ferrate (VI) yield (1.278 g l⁻¹). It can be said that increasing electrolyte concentration provided higher ferrate (VI) yield. Increasing electrolyte concentration provides higher dissolution rates of iron electrode and prevents formation of oxo-hydroxide layer on the anode surface. Furthermore, increasing alkalinity enhances produced ferrate (VI) stability. In other words, ferrate (VI) stability decreases with decreasing NaOH concentration. While ferrate (VI) formation takes place in a reactor, it simultaneously reduces to Fe (III). In this case, only 18 M NaOH media provided less ferrate (VI) yield.

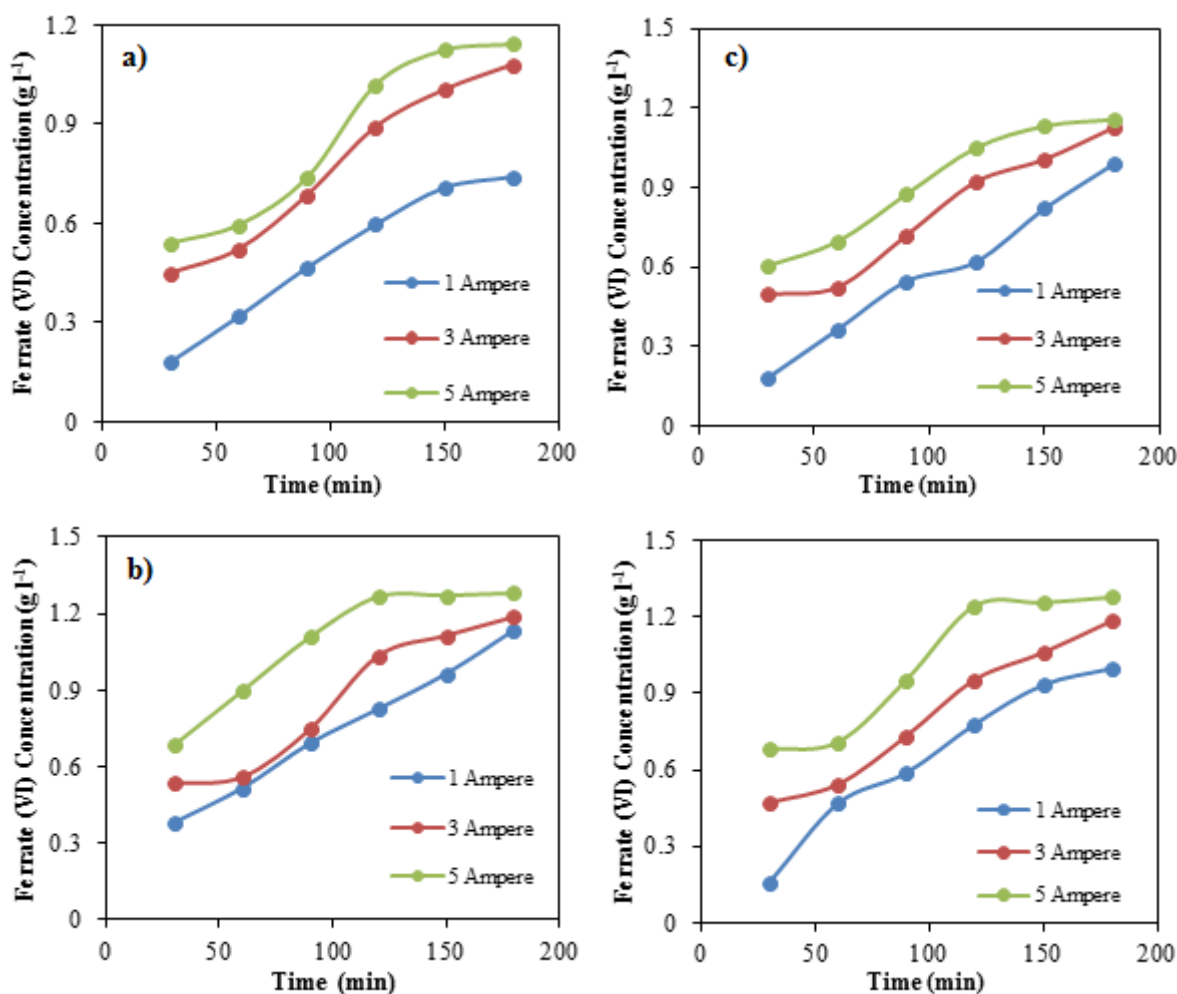


Figure 4. Ferrate (VI) yield in terms of different applied current values and NaOH concentrations: a) 15 M, b) 16 M, c) 18 M and d) 20 M for reactor design, R1.

Applied current is another important parameter which affects ferrate (VI) formation yield. As seen from Figure 4, increasing applied current provided higher ferrate (VI) concentration independent from NaOH concentration. Figure 5 shows current efficiency values in terms of applied current and NaOH concentrations. As seen, current efficiencies were found as 71.5%, 55.9% and 68.3% for applied current values of 1, 3 and 5 A at 16 M NaOH media, respectively. Similar trends were observed at other mentioned NaOH concentrations. It can be said that the lowest applied current value provided the highest current efficiency. This may be due to the competition between produced ferrate (VI) and oxygen evolution on the anode surface. Increasing current and potential causes more participation of this adverse reaction to the mechanism and this lowers current efficiency.¹² Besides, the formation of H₂ gas on the cathode side increases with increasing current and this may lower electron transfer area due to hydrogen bubbles.¹³ Consequently, in the case of reactor design-R1, applied current of 1 A can be chosen for optimal

point providing the highest current efficiency and reasonable ferrate (VI) yield (1.14 g l⁻¹).

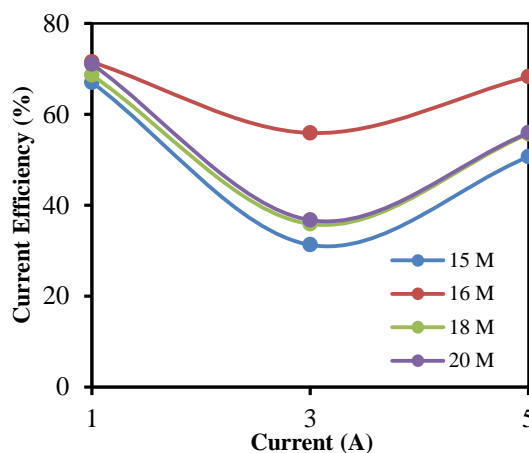


Figure 5. Current efficiencies and in terms of applied current and NaOH concentration for reactor design, R1.

3.2. Effect of parameters for the second reactor configuration-R2 (iron flakes)

To determine the effect of anode type and reactor configuration on the electrochemical ferrate (VI) synthesis, the experiments were conducted at the same electrolyte concentrations and applied current values and [Figure 6](#) represents ferrate (VI) yields at those conditions. As seen from [Figure 6](#), the highest ferrate (VI) yield was gained under the applied current of 5 A with 16 M NaOH media (2.28 g l^{-1}) after 3 h. This is

similar with the results for R1. While ferrate (VI) yield increased with increasing NaOH concentration from 15 M to 16 M, further increase in NaOH concentration did not provide higher ferrate (VI) yield. Also, increasing applied current provided higher efficiency for all NaOH concentration except 20 M NaOH media. Beyond applied current of 3 A, ferrate (VI) yield significantly reduced in 20 M NaOH media.

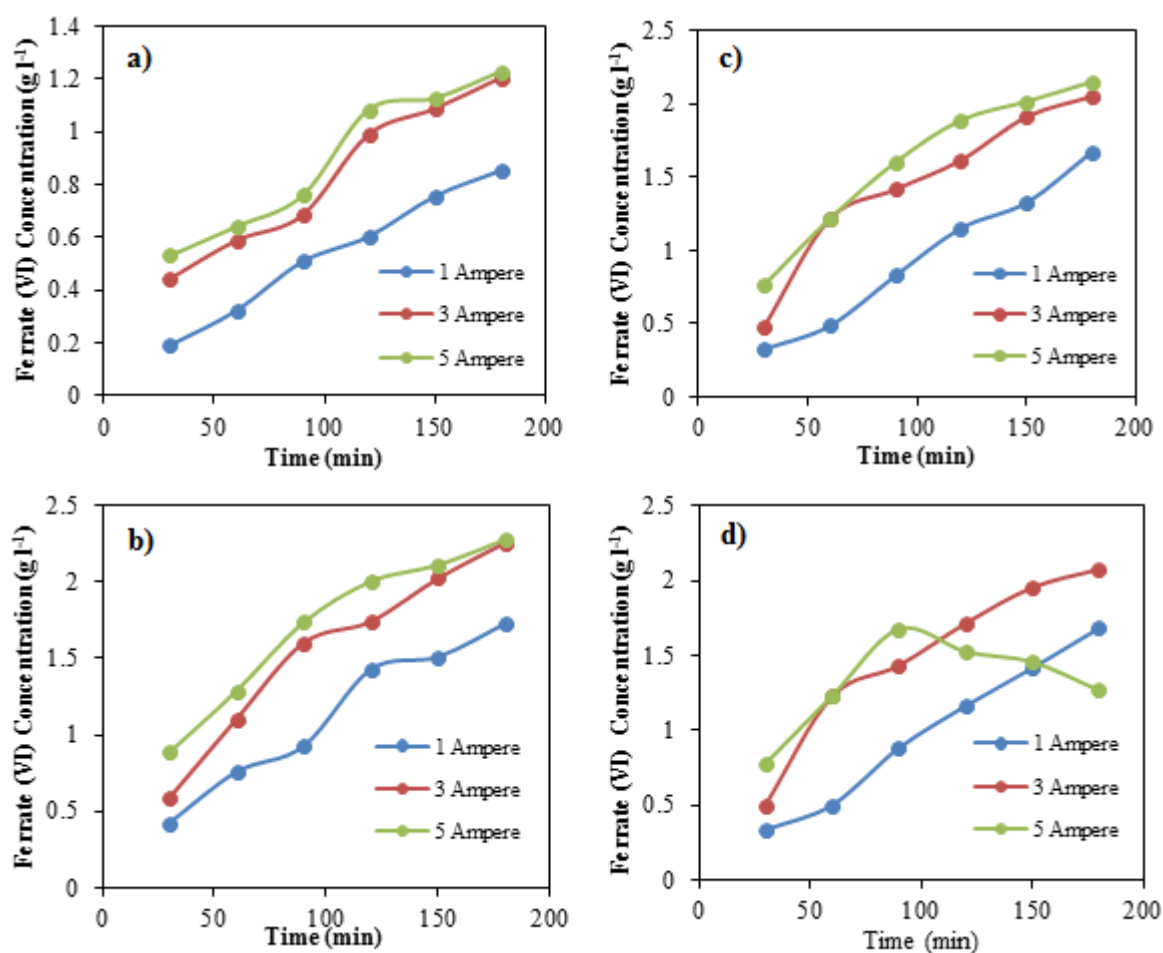


Figure 6. Ferrate (VI) yield in terms of different applied current values and NaOH concentrations: a) 15 M, b) 16 M, c) 18 M and d) 20 M for reactor design, R2.

When current efficiencies are considered (see [Figure 7](#)), the highest efficiency was observed with applied current of 1 A, and the efficiency reduced with increasing applied current values for all NaOH concentrations. Increasing applied current provides higher dissolution of iron anode. However, oxygen evolution also increases with increasing applied current which may affect ferrate (VI) yield negatively. When ferrate (VI) starts to form in the anode surface with dissolving iron anode, oxygen evolution also participates to the mechanism as

mentioned above. Besides, electrical energy affects the electrochemical reactions by the generation of H₂ gas. The domination of these situations determines ferrate (VI) yield. In this case, applied current of 5 A provided the highest yield. However, current efficiency was the lowest. Consequently, in this case, applied current of 1 A can be chosen for optimal condition with 1.73 g l^{-1} ferrate (VI) yield and 169.9% current efficiency in 16 M NaOH media. In the overall assessment, where the most suitable electrolyte concentration was 16 M, applied current of 1

A was the optimum value with the highest provided current efficiency for both reactor configurations.

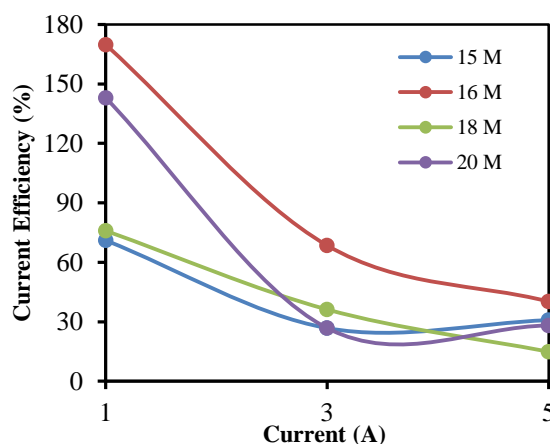


Figure 7. Current efficiencies in terms of applied current and NaOH concentration for reactor design, R2.

When reactor configurations were compared, R2 with iron flakes provided higher ferrate (VI) yield and current efficiency. This may be due to higher surface area of iron flakes and high dissolution rates.

4. CONCLUSIONS

Ferrate (VI) was produced using different reactor configurations with iron plates and cast-iron flakes in this study. Optimum conditions such as electrolyte concentration and applied current were determined for both reactor configurations considering the ferrate (VI) yield and the highest current efficiency. Using cast-iron flakes with high surface area provided higher ferrate (VI) yields with the highest current efficiency.

ACKNOWLEDGEMENTS

The authors are grateful to The Scientific and Technological Research Council of Turkey (TUBITAK) for their financial support (Project number: 112Y258).

Conflict of interest

I declare that there is no a conflict of interest with any person, institute, company, etc.

REFERENCES

1. Alsheyab, M.; Jiang, J.Q.; Stanford, C. *Journal of Environmental Management*, **2009**, 90, 1350-1356.

2. Bouzek, K.; Roušar, I. *Journal of Applied Electrochemistry*, **1993**, 23, 1317-1322.

3. Bouzek, K.; Roušar, I. *Journal of Applied Electrochemistry*, **1997**, 27, 679-684.

4. Yu, X.; Licht, S. *Journal of Applied Electrochemistry*, **2008**, 38, 731-742.

5. He, W.; Wang, J.; Yang, C.; Zhang, J. *Electrochimica Acta*, **2006**, 51, 1967-1973.

6. Barisci, S.; Ulu, F.; Sarkka, H.; Dimoglo, A.; Sillanpaa, M. *International Journal of Electrochemical Science*, **2014**, 9, 3099-3117.

7. Sun, X.; Zu, K.; Liang, H.; Sun, L.; Zhang, L.; Wang, C.; Sharma, V. K. *Journal of Hazardous Materials*, **2018**, 344, 1155-1164.

8. Liu, C.; Zhou, Z.; Yuan, B.; Liu, S. *Journal of Environmental Engineering*, **2018**, 144, 1-7.

9. Macova, Z.; Bouzek, K.; Sharma, V.K. *Journal of Applied Electrochemistry*, **2010**, 40, 1019-1028.


10. Macova, Z.; Bouzek, K. *Journal of Applied Electrochemistry*, **2012**, 42, 615-626.

11. Sun, X.; Zhang, Q.; Liang, H.; Ying, L.; Xiangxu, M.; Sharma, V.K. *Journal of Hazardous Materials*, **2016**, 313, 130-136.

12. Hives, J.; Gal, M.; Kerekes, K.; Kubinakova, E.; Mackulak, T. *ACS Symposium Series: Ferrites and Ferrates: Chemistry and Applications in Sustainable Energy and Environmental Remediation*, **2016**, 1238, Chapter 8, 221-240.

13. Vogt, H.; Aras, O.; Balzer, J. *International Journal of Heat and Mass Transfer*, **2004**, 47, 787-795.

ORCID

 0000-0003-4229-0408 (S. Barisci)



Adsorption of safranin-O dye by peanut shell-based polyurethane type foam

Bilal ACEMİOĞLU^{1,*}, Melike Hilal BİLİR¹, Mehmet Hakkı ALMA²

on the last page

¹Department of Chemistry, Faculty of Science and Arts, Kilis 7 Aralık University, 79000, Turkey

²Rectorate of Iğdır University, Iğdır, 76000, Turkey

Received: 18 August 2018, Revised: 27 September 2018; Accepted: 01 October 2018

*Corresponding author e-mail: bilacem@yahoo.com

Citation: Acemioğlu, B.; Bilir, M. H.; Alma, M. H. *Int. J. Chem. Technol.* 2018, 2 (2), 95-104.

ABSTRACT

The adsorption of safranin-O dye was performed in batch and continuous column systems by polyurethane-type rigid foam produced from peanut shell. In batch system, effects of contact time, initial dye concentration, solution pH and temperature on the adsorption were investigated. In column system, solution flow rate and initial dye concentration effect were studied. Under conditions studied, the adsorption of safranin-O was 95-99% for batch system, and 93-99% for column system. Adsorption isotherm best followed the Langmuir model ($R^2 = 0.986$). Adsorption kinetics was in consistent with best the pseudo-second order model (R^2 values ≥ 0.998). Adsorption was of spontaneous nature and in favor of increasing temperature (i.e. endothermic nature). For example, when the temperature was increased from 20 to 60°C, standard Gibbs free energy change (ΔG°) decreased regularly from -5303 to -8170 J mol⁻¹. The values of standard enthalpy (ΔH°) and standard entropy (ΔS°) were estimated as 13.35 kJ mol⁻¹ and 0.64 kJ mol⁻¹ K⁻¹, respectively. Moreover, FTIR and SEM analyses were done, and the results were interpreted in detail.

Keywords: Peanut shell, polyurethane foam, safranin-O, adsorption.

Yerfıstığı kabuğu esaslı poliüretan tipi köpük ile safranin-O boyasının adsorpsiyonu

ÖZ

Safranin O boyasının adsorpsiyonu yerfıstığı kabuğundan üretilen poliüretan tipi sert köpük ile kesikli ve sürekli kolon sisteminde gerçekleştirilmiştir. Kesikli sistemde adsorpsiyon üzerine temas süresi, başlangıç boyar madde konsantrasyonu, çözelti pH'sı ve sıcaklığın etkileri araştırıldı. Kolon sisteminde çözelti akış hızı ve başlangıç boyar madde konsantrasyonunun etkisi incelendi. İncelenen şartlar altında Safranin O'nun adsorpsiyonu kesikli sistem için %95-99, ve kolon sistemi için %93-99 idi. Adsorpsiyon izotermi en iyi Langmuir modelini ($R^2 = 0.986$) takip etti. Adsorpsiyon kinetiği en iyi yalancı ikinci dereceden model ile (R^2 values ≥ 0.998) uyumluydu. Adsorpsiyon spontan tabiatlıydı ve artan sıcaklığın lehindeydi (yani endotermik tabiatlıydı). Örneğin, sıcaklık 20 den 60°C'ye artırıldığında standart Gibbs serbest enerji değişimi (ΔG°), -5303 den -8170 J mol⁻¹'e düzenli olarak azaldı. Standart entalpi (ΔH°) and standart entropi (ΔS°) değerleri sırasıyla 13.35 kJ mol⁻¹ ve 0.64 kJ mol⁻¹ K⁻¹ olarak belirlendi. Ayrıca FTIR ve SEM analizleri yapıldı ve sonuçlar ayrıntılı olarak yorumlandı.

Anahtar Kelimeler: Yerfıstığı kabuğu, poliüretan köpük, safranin-O, adsorpsiyon.

1. INTRODUCTION

Recently, various low cost adsorbent materials have been used as an alternative to activated carbon to remove dyes from environment by using adsorption technique. These inexpensive materials can be listed as organic (poly(N-isopropylmethacrylamide-acrylic acid) microgels¹, polydopamine microspheres², inorganic (fly ash³, perlite⁴, clay^{5,6}, and biological materials (fungus^{7,8}, yeast⁹, and alge¹⁰). Besides these, lignocellulosic

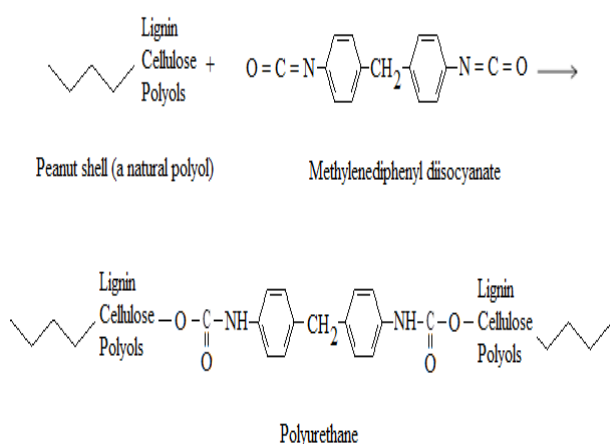
materials such as wood apple¹¹, tree barks^{12,13}, fruit peels¹⁴, banana^{15,16}, orange peel^{15,17}, and peanut hull¹⁸ are mostly used, also.

On the other hand, new adsorbents produced from lignocellulosic materials are also utilized as adsorbent the removal of dyes, metal ions, and organic contaminants. For example, phenolated wood resin¹⁹ have been used for the adsorption of various metals. Polyurethane cross-linked pine cone biomass²⁰ has been utilized for 2-nitrophenol adsorption.

Lignin-based hydrogels²¹ has been utilized for dye adsorption.

In the present work, as an alternative to activated carbon, the polyurethane type rigid foam produced from peanut shell was used as an adsorbent for the removal of safranin-O dye from aqueous solution. In our another work, the sorption of Remazol brilliant blue R using peanut shell-based polyurethane type foam is studied²², but any work has been not meet for the sorption of safranin-O dye by this foam in the literature. Thus, this paper is an original work. The formation of the peanut shell-based polyurethane-type foam is explained in the following.

The peanut shell-based polyurethane foam has been produced from a reaction between peanut shell and methylenediphenyl diisocyanate (MDI) via polyaddition polymerization by us (Scheme 1).



Scheme 1. The formation of polyurethane-type rigid foam from the chemical reaction between peanut shell and MDI.

Lignin and cellulose groups including OH groups in the structure of the peanut shell-based polyurethane-type rigid foam can adsorb the positively charged safranin-O dye.

In this study, therefore, effects of initial dye concentration, contact time, temperature, and pH on safranin-O dye adsorption were investigated. Moreover, adsorption isotherm, kinetics and thermodynamic studies were also done.

2. MATERIALS AND METHODS

2.1. Materials

Safranin-O dye was received from Carlo Erba. Some physical properties and chemical structure of safranin-O dye are given in Table 1.^{23,24} Peanut shell was provided from Osmaniye province located in the east

Mediterranean region of Turkey. The ingredients used in the making of foam was received from Ispol company in Turkey. These ingredients are polyethylene glycol (PEG-400, commercial polyol), monoethylene glycol (MEG, polyol), triethylenediamine (TEDA-D33LV, foaming catalyst), and polymeric diphenylmethane diisocyanate (PMDI-TED-31, crosslinking agent). On the other hand, for the elemental analysis, a LECO CHNS-932 analyzer device was used. For FT-IR spectra, a FTIR RX-1 Perkin Elmer brand ATR spectrophotometer was used. For SEM analyses, it was used a LEO 435 VP SEM brand device. For Specific surface area and porosity measurements, a nitrogen adsorption device was used.

2.3. Methods

Peanut shell powders with 100 micron size were utilized as a natural polyol to produce the polyurethane-type rigid foam. Peanut shell-based polyurethane type foam shell is prepared as described in our another work.²² The resulting foam exhibited very little adsorption capacity. With aim to improve the adsorption capacity, the foam was pretreated with 0.1 N HCl for 5 min, then the mixture was filtered and washed well with pure water, and finally dried for 12 h at 103°C. Thus, the foam was become ready for use in adsorption experiments.

The reason for pretreated with HCl of the foam can be interpreted in 2 different ways:

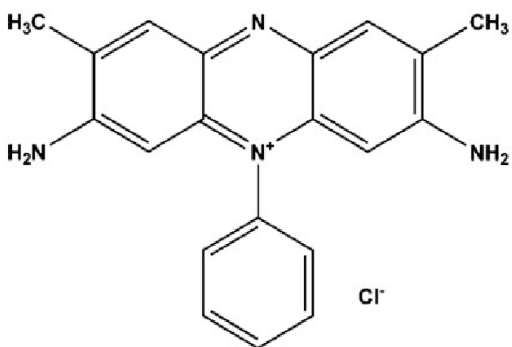
1) It is thought that HCl is effective in the modification, leading to the elimination of some impurities that may be present in the foam during foam formation,

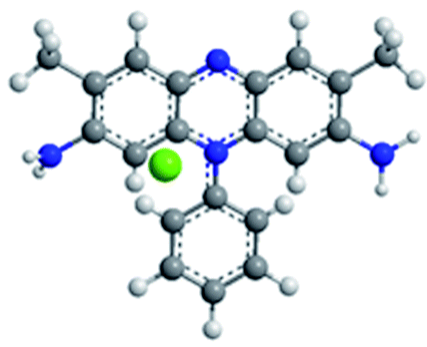
2) When the foam is washed with HCl, functional groups on the surface (i.e. end groups such as -OH groups) give rise, and these groups cause to the adsorption of positively charged safranin dye.

On the other hand, the stock solution of 500 mg l⁻¹ of safranin-O dye was prepared with distilled pure water. Desired solutions were prepared from the stock solution. Adsorption experiments were done by shaking 0.125 g of peanut shell-based polyurethane type rigid foam with 25 ml-dye solution at 130 rpm. Shaking process was performed in a temperature-controlled water bath at various initial dye concentrations (10, 20, 50, 75, 100 and 150 mg l⁻¹), pH values (3, 5, 7 and 9) and temperatures (20, 30, 40, 50, and 60°C) at early specified times, respectively. After shaking times, the mixtures were then centrifuged at 5000 rpm for 5 min. For aim of the determination of the concentrations of unadsorbed dye in the solutions, the supernatants were analyzed by an UV-Vis spectrophotometer (T80 UV-Vis spectrophotometer). The pH values of the dye solutions were regulated by dropping diluted HCl or NaOH solutions. The amounts of dye adsorbed per gram of the foam (*q_t*) and percent adsorption values were estimated using following Equations, respectively.

Table 1. Some physical properties of safranin-O dye

Common name	Safranin-O
C.I. name	Basic red 2
IUPAC name	3,7-Diamino-2,8-dimethyl-5-phenylphenazinium chloride
C.I. number	50240
Ionization	Basic
Solubility in water (%)	5.45
Solubility in ethanol (%)	3.41
Max. wavelength (nm)	517
Color	Red
Molecular weight (g mol ⁻¹)	350.85
Molecular formula	C ₂₀ H ₁₉ N ₄ Cl
Chemical structure	3D model structure





$$q_t = \frac{(C_0 - C_t)}{m}$$

$$\text{Adsorption \%} = \frac{(C_0 - C_t)}{C_0} \times 100$$

where C_0 is initial dye concentration (mg l⁻¹). C_t points to the concentration of the unadsorbed dye in the solution at any time (mg l⁻¹). The q_t indicates the amount of the dye adsorbed per unit mass of the foam at any time (mg g⁻¹). m indicates adsorbent mass (g), and V is dye solution volume (l). At the equilibrium time, q_t and C_t can be expressed as q_e and C_e .

3. RESULTS AND DISCUSSION

3.1. Characterization of the foam

Specific BET surface area, porosity, density, and color of the foam pretreated with HCl have been determined as 2.824 m² g⁻¹, 0.00215 cm³ g⁻¹, and 0.0341 g cm⁻³, and brownish, respectively. According to elemental analysis results, the foam pretreated with HCl includes 61.98% C, 5.832% H, 67.478% N, 0.231% S.

SEM image shows the surface morphology of the peanut shell-based polyurethane typ rigid foam (see Figure 1). As seen in Figure 1, the surface of the foam has a porous, rough and heterogeneous structure which may adsorb dye molecules.

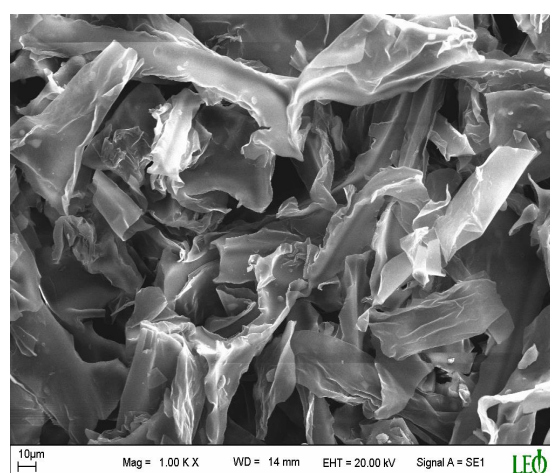


Figure 1. SEM image of the peanut shell-based polyurethane foam pretreated with HCl.

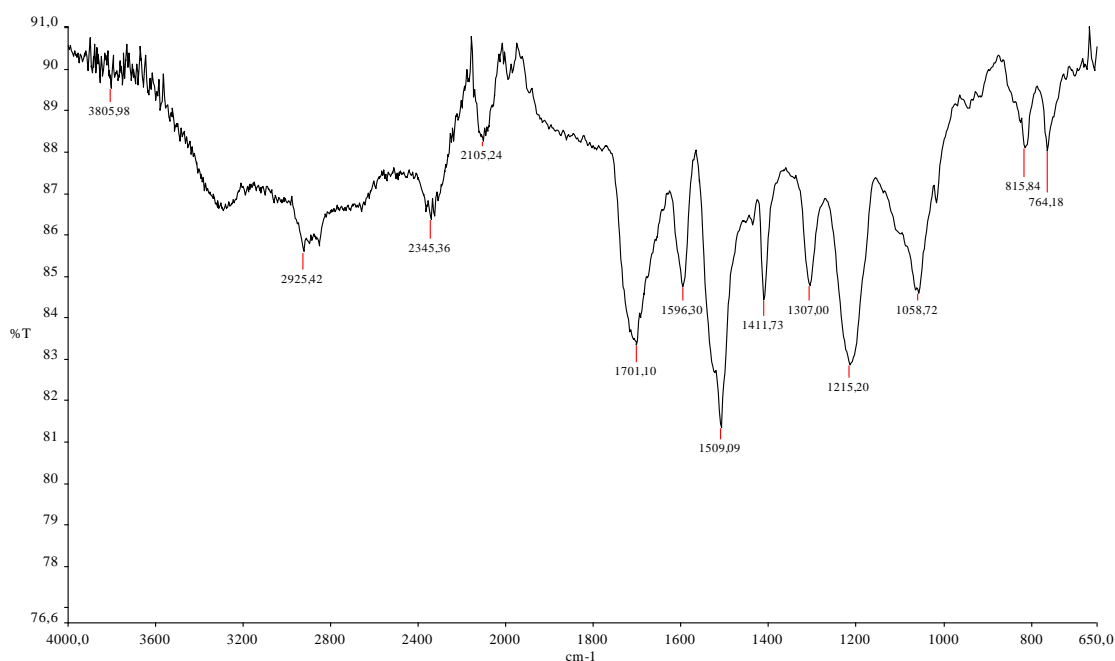


Figure 2. FT-IR spectrum of the peanut shell-based polyurethane foam pretreated with HCl.

FT-IR spectrum of the peanut shell-based polyurethane foam pretreated with HCl for Safranin-O adsorption is shown in Figure 2.

This spectrum can be interpreted as follows. In FT-IR spectrum, the broad band at 3293.58 cm^{-1} indicates the vibration of $-\text{NH}$ and $-\text{NH}_2$ groups and $-\text{OH}$ groups of cellulose.²⁵ The band at 2925.42 points to $-\text{CH}$ stretching of carboxyl groups.²⁶ Very robust bands at 1701.10 and 1509.09 cm^{-1} denote the amide I and amide II bonds.²³ The robust peaks at 1411.73 and 1596.30 cm^{-1} indicate phenyl fragment in the structure of the foam.²⁵ The strong band at 1307.00 cm^{-1} points to the stretching of $\text{C}-(\text{CH}_3)_2$.²⁶ Peaks at around $1200\text{--}1000\text{ cm}^{-1}$ indicate C-O single bond in carboxylic acids, alcohols, phenols, and esters. Herein, the strong peak at 1058.72 and the weak band at 1018.02 cm^{-1} might be assigned to C-O and C-O-C stretching bonds in the structure of the foam.²⁶ A robust band observed at 1215.20 cm^{-1} indicates the C=O stretching band of carboxylic groups.²⁷ The bands at 815.84 and 764.18 cm^{-1} denotes the vibrations of aromatic skeleton in the structure of the polyurethane foam.²⁶ All these findings indicate that the dye molecules may be adsorbed by functional groups in the structure of the foam. When compared according to bands in raw foam without pretreated with HCl²², the intensity decrease and spectral shifts in bands obtained here are occurred with the effect of HCl.

3.2. Initial dye concentration effect

Figure 3 shows effect of initial dye concentration on safranin-O adsorption by the foam. As can be seen that

the adsorption is strongly influenced by the initial concentration of the dye.

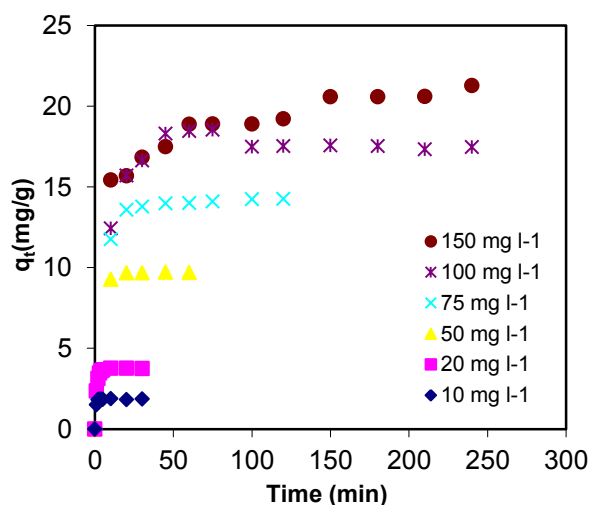


Figure 3. Effect of initial dye concentration on the adsorption of safranin-O by the foam ($T: 60^\circ\text{C}$, $\text{pH}: 9$, $w/v: 0,125\text{ g}/25\text{ ml}$, 130 rpm).

While maximum adsorption occurs at lower times for lower concentrations, it occurs at longer periods for higher concentrations. For example, the time of the maximum adsorption is determined, as 10 min for low concentrations such as 10 and 20 mg l^{-1} , as 45 min for 50 mg l^{-1} , as 120 min for 75 and 100 mg l^{-1} , and as 240 min for 150 mg l^{-1} , respectively. These different times denote the different equilibrium time for each concentration. Different equilibrium times for different

concentrations probably indicate an equilibrium shift. The maximum adsorption and percentages are determined as 1.87 mg g^{-1} (93.83%), 3.76 mg g^{-1} (94.18%), 9.71 mg g^{-1} (97.14%), 14.25 mg g^{-1} (95.03%), 17.53 mg g^{-1} (87.67%) and 21.28 mg g^{-1} (70.94%) for the initial dye concentrations of 10, 20, 50, 75, 100 and 150 mg l^{-1} , respectively. If it is paid attention to these values, it can be seen that as the amount of adsorbed dye increases with increasing concentration, the adsorption percent decreases. This situation denotes the saturation of the surface of the adsorbent as the adsorbent surface is covered with more dye molecules with effect of increasing dye concentration. Thus the decrease of active sites on the adsorbent leads the decrease of percent adsorption. A similar trend has been obtained for malachite green adsorption by orange peel.¹⁷

3.3. pH effect

Solution pH in an adsorption process affects the ionization of a dye molecule and the charge of an adsorbent surface. Herein, pH values of dye solutions are selected as 3, 5, 7 and 9. The results obtained are graphed in Figure 4.

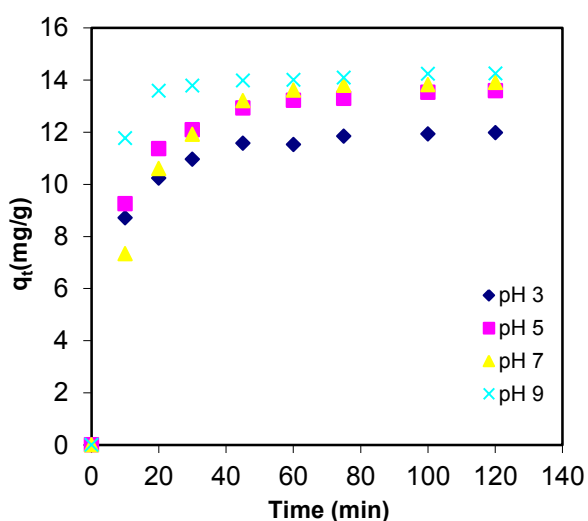


Figure 4. Effect of pH on the adsorption of safranin-O by the foam ($T: 60^\circ\text{C}$, $C_0: 75 \text{ mg l}^{-1}$, w/v: 0,125 g/25 ml, 130 rpm).

As seen in Figure 4, it is seen that the adsorption increases with a rise in pH from 3 to 9. The adsorption equilibrium is reached at 120 min for all pHs. The reason for the increase in adsorption with increasing pH indicates that the adsorbent surface becomes more negative due to the excess hydroxyl ions released at higher pH, and therefore electrostatically attracted between the foam and positively charged safranin-O molecules. This situation comes to a rise in adsorption. While the maximum adsorption is 14.25 mg g^{-1} (95.03%) at pH 9, it determined as 11.94 mg g^{-1} (79.82%) at pH 3. A similar result has been obtained for safranin adsorption

onto coal fly ash.²⁸

3.4. Temperature effect

Figure 5 demonstrates the effect of temperature on safranin-O adsorption by the foam. As seen from Figure 5, the adsorption is strongly influenced by temperature. While maximum adsorption occurs at higher times for lower temperatures, it occurs at longer periods for higher temperatures.

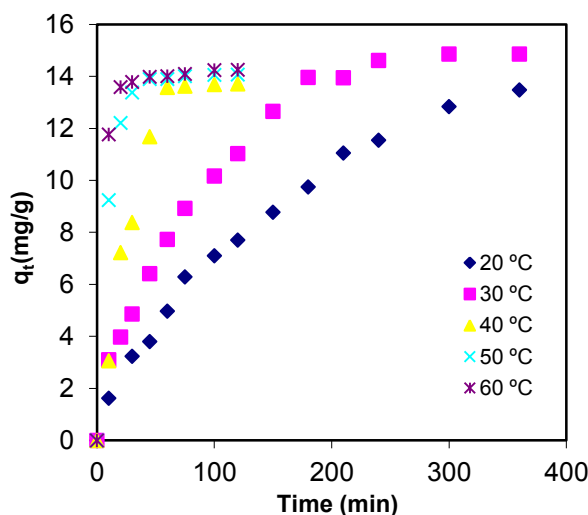


Figure 5. Effect of temperature on the adsorption of safranin-O by the foam ($C_0: 75 \text{ mg l}^{-1}$, pH: 9, w/v: 0,125 g/25 ml, 130 rpm).

For example, the adsorption proceeds slowly by starting from first minutes at 20 and 30°C and reaches a maximum with gradual increases at 360 min. It progresses quickly and reaches a maximum value in 120 min time at the temperature of 40, 50 and 60°C . Namely, it is observed that the maximum adsorption occurs at 360 min at temperatures of 20 and 30°C , it occurs at 120 min at temperatures of 40, 50 and 60°C . Why of this can ascribable the swelling of the adsorbent particles at high temperatures and the faster act of the dye molecules. The maximum adsorption and percentages are found as 13.47 mg g^{-1} (89.81%) ve 14.85 mg g^{-1} (99.04%), 13.70 mg g^{-1} (91.39%) 14.06 mg g^{-1} (93.79%), and 14.25 mg g^{-1} (95.03%) for the temperatures of 20, 30, 40, 50 and 60°C , respectively.

3.5. Column adsorption study

Column with a diameter of 1 cm and a length of 20 cm was used for continuous adsorption system. The foam particles (dry weight 1 g) were packed between two layers of glass wool in column. 50 ml of dye solutions with desired concentrations (10, 20, 50, 75, 100 ve 150 mg l^{-1} solutions) were fed through the top of the column. Column height is 10 cm. The flow rate of feed solutions

was regulated as 0.35 ml min^{-1} (21 ml h^{-1}). The system was operated at 25°C and pH 9. The dye samples passed through column were collected from the bottom of column at specific times. The concentrations of dye unadsorbed within samples in the outlet of the column were estimated as described as before. The amounts of dye calculated from the analysis of the samples taken at the outlet of the column at all residence times are shown in Figure 6.

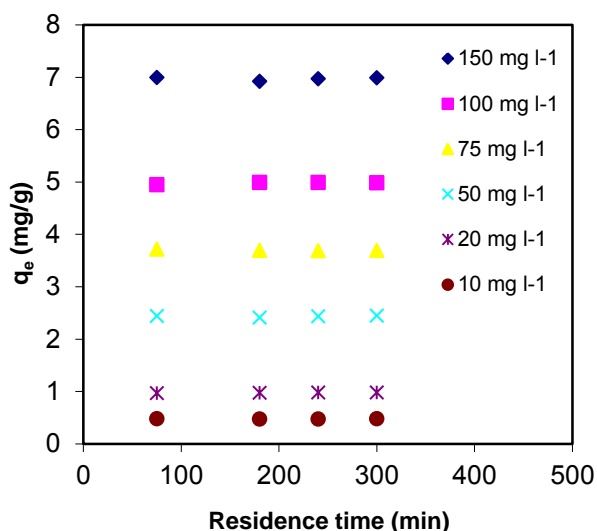


Figure 6. Effect of initial concentration on the column adsorption of safranin-O by the foam (pH: 9, T: 25°C , flow rate: 21 ml h^{-1}).

As seen from this figure, it is seen that the amounts of dye uptaken per unit gram of the foam in the column (i.e. column capacity) rise with an increase in initial dye concentration. For instance, while the initial dye concentration increases from 10 to 150 mg l^{-1} , maximum column capacity is determined to increase from 0.475 to 6.987 mg g^{-1} . On the other hand, while the percentage of column adsorption among the initial dye concentrations of 10 and 100 mg l^{-1} was determined to be between 94.90% and 99.79% between 60 and 300 min residence times. The percentage of column adsorption was estimated to be between 92% and 93% between 60 and 300 min residence times for the initial dye concentration of 150 mg l^{-1} . It is seen that the outlet samples of 99% are colourless and cleared off the red colour of safranin-O. This situation points to be a strong interaction between the functional groups of safranin-O dye and foam packed in column. Column exhaustion time was determined as 5 h.

3.6. Isotherm study

Isotherm studies of the adsorption of safranin-O by the foam were investigated according to commonly given the Langmuir and Freundlich models.²⁹ The Langmuir isotherm is shown in Figure 7.

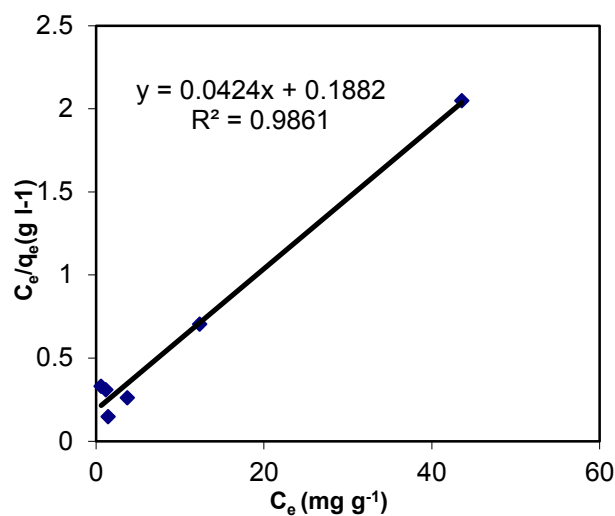


Figure 7. The Langmuir isotherm of safranin-O adsorption by the foam (C_0 : 10 – 150 mg l^{-1} , pH: 9, T: 60°C , w/v: $0.125 \text{ g}/25 \text{ ml}$, 130 rpm).

The adsorption is observed to obey best the Langmuir isotherm model (with $R^2 = 0.986$). The compatibility with the Langmuir isotherm indicates a monolayer adsorption on the foam surface. A similar trend has been reported for safranin O adsorption onto carbonized spent coffee ground.³⁰ The Correlation coefficient value (R^2 value) obtained from Freundlich isotherm model is found as 0.744. Due to this low R^2 value, the Freundlich plot is not given here. The k value indicating the Freundlich adsorption capacity and n value indicating adsorption intensity are found as 4.38 and 1.97, respectively. It is determined that Langmuir adsorption capacity (Q_0 value) is 23.58 mg g^{-1} , and the adsorption energy (b value) is 0.225 mg^{-1} . In safranin-O adsorption, the Langmuir adsorption capacity of the foam are compared with other some sorbents (see Table 2).

3.7. Kinetic study

Adsorption kinetics of dye adsorbed by the foam was studied in terms of the pseudo-first and-second order kinetics, and intra-particle diffusion models. The linearized equations of these kinetic models are given in Table 3.³¹⁻³⁴ At the same time, Table 3 shows all of kinetic parameters obtained. As seen from this table, the R^2 values obtained for the pseudo-second order kinetics are the highest than the pseudo-first order and intra-particle diffusion models. The R^2 values for the pseudo-second order kinetics are found between 0.998 and 0.999. On the other hand, the theoretical q_2 values are close to the values of the experimental q_e . (see Table 3). Therefore, both the high correlation coefficients and the compliancy of the theoretical and experimental adsorption capacities indicate that the adsorption follows the pseudo-second order kinetic model.

Table 2. Comparison of the Langmuir adsorption capacity (Q_o) of the foam to some other adsorbents for the adsorption of safranin-O

Adsorbent/Biosorbent	Q_o (mg g ⁻¹)	References
Peanut shell-based polyurethane foam	23.58	This study
Coal fly ash	1.76	(28)
Coffee spent grounds	3.76	(30)
Magnetic clay	18.48	(38)
Kaolinite clay	16.23	(39)
Pineapple peels	26.08	(40)
Rice husk	35.65	(41)
Activated red mud	894	(42)
NaOH treated bambusa tulda	32.26	(43)
Untreated Sugarcane Bagasse	1.80	(44)
H ₂ SO ₄ Sugarcane Bagasse	1.39	(44)
NaOH Sugarcane Bagasse	2.64	(44)

Similar results have been found for safranin-O adsorption onto carbonized spent coffee ground²⁸ and safranin-O adsorption onto Miswak.³⁵

Plots for the pseudo-second order kinetic model are illustrated in Figure 8. Because the R^2 values for the pseudo-first order and intra-particle diffusion kinetic models are low, it is not possible to mention for fit to these models. Therefore, these plots kinetics are not shown.

3.8. Thermodynamics study

Thermodynamics of safranin-O adsorption by the foam was by means of thermodynamic equations given elsewhere.^{36,37} From the thermodynamic parameters, standard The equilibrium constant of the adsorption (K_c), Gibbs free energy change (ΔG°), standard enthalpy (ΔH°) and standard entropy (ΔS°) values were determined. All of thermodynamic parameters obtained are given in Table 4.

As seen from Table 4, the values of ΔG° were determined as negative at all temperatures. These values indicate the spontaneous nature of dye adsorption. The fact that the values of ΔG° decrease with increasing temperature denotes the increase of spontaneous tendency of the adsorption. The values of ΔH° and ΔS° are estimated as 13.35 kJ mol⁻¹ and 0.64 kJ mol⁻¹ K⁻¹ from Van't Hoff equation respectively. The low value of ΔH°

indicates a physical adsorption. The positive value of ΔS° points to a randomness adsorption of dye molecules onto the foam surface. Similar results for ΔG° , ΔH° and ΔS° have also been reported for the adsorption of magnetic mesoporous clay.³⁸

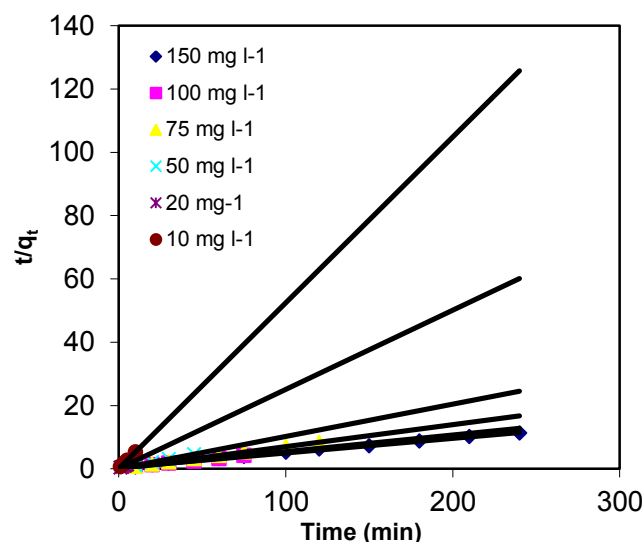


Figure 8. The pseudo-second order plots of safranin-O adsorption by the foam (C_o :10-150 mg l⁻¹, pH: 9, T: 60°C, w/v: 0,125 g/25 ml, 130 rpm).

4. CONCLUSIONS

Peanut shell-based polyurethane type rigid foam produced was used as a new adsorbent material for the removal of safranin-O dye from aqueous solution. The adsorption of dye onto the foam increased with rises in initial dye concentration, pH and temperature. The maximum percent adsorption was determined to be between 95% and 99% for batch system and 93% and 99% for column system under studied conditions. Adsorption isotherm was in consistent with best the Langmuir model. The Langmuir adsorption capacity was determined as 23.58 mg g⁻¹. Adsorption kinetics followed the pseudo-second order model. The negative ΔG° values indicated the spontaneous tendency of dye adsorption onto the foam. The spontaneous tendency increased with increasing temperature. The values of ΔG° were determined as -5.303, -6.513, -6.146, -7.291, and -8.170 kJ mol⁻¹ for 20, 30, 40, 50, and 60°C, respectively. The adsorption of dye was physical with a low ΔH° value of 13.35 kJ mol⁻¹. Adsorption entropy was estimated as 0.64 kJ mol⁻¹ K⁻¹. Peanut shell-based polyurethane type rigid foam could be preferably used as a new adsorbent, as an alternative to activated carbon, in dye removal due to its low cost.

Table 3. Kinetic parameters for safranin-O adsorption by the foam at initial dye concentrations.

Pseudo-Second order					Pseudo-Second order			Intra-particle Difussion		
$\frac{t}{q_t} = \frac{1}{k_2 q_2^2} + \frac{1}{q_2} t$					$\log(q_e - q_t) = \log q_1 - \frac{k_1}{2.303} t$			$q_t = k_i x t^{1/2}$		
C _e ^a	q ₂ ^b	k ₂ ^c	h ^d	r ₂ ^{2e}	q ₁ ^f	k ₁ ^g	r ₁ ^{2h}	k _i ⁱ	r _i ^{2j}	q _e ^k
10	1.91	3.419	12.47	0.999	0.309	0.614	0.652	0.129	0.480	1.87
20	4.01	0.466	7.49	0.998	2.46	0.670	0.984	0.588	0.689	3.76
50	9.90	0.217	21.26	0.999	0.857	0.112	0.701	0.111	0.706	9.71
75	14.49	0.039	8.18	0.999	2.529	0.043	0.908	0.236	0.616	14.25
100	20.40	0.008	3.32	0.999	9.484	0.087	0.977	1.072	0.863	18.55
150	21.73	0.004	1.88	0.998	6.309	0.011	0.927	0.472	0.941	21.28

^aInitial dye concentration (mg l⁻¹),^bEquilibrium adsorption capacity obtained from the pseudo-second order equation (mg g⁻¹),^cThe rate constant of the pseudo-second order reaction (g mg⁻¹ min⁻¹),^dThe initial adsorption rate from the pseudo-second (mg g⁻¹ min⁻¹),^eCorrelation coefficient from the pseudo-second-order kinetics order kinetics (mg g⁻¹ min⁻¹),^fEquilibrium adsorption capacity of the pseudo-first order reaction (mg g⁻¹),^gThe rate constant of the pseudo-first order reaction (min⁻¹), ^hCorrelation coefficient from the pseudo-first order kineticsⁱIntra-particle diffusion rate (mg g⁻¹ min^{-1/2}),^jCorrelation coefficient from intra-particle diffusion equation,^kEquilibrium adsorption capacity obtained as experimental (mg g⁻¹).**Table 4.** Thermodynamic parameters of the adsorption of safranin-O by the foam

Temperature (in K)	K _c	ΔG° (J mol ⁻¹)	ΔH° (kJ mol ⁻¹)	ΔS° (kJ mol ⁻¹ K ⁻¹)
20	8,820	-5303		
30	13,274	-6513		
40	10,617	-6146	13.35	0.64
50	15,111	-7291		
60	19,139	-8170		

ACKNOWLEDGEMENTS

This study was supported by The Scientific and Technical Research Council of Turkey (TUBITAK), project number: 107Y043.

Conflict of interest

We declare that there is no a conflict of interest with any person, institute, and company, etc.

REFERENCES

- Naseem, K.; Farooqi, Z. H.; Begum, R.; Ghufuran, M.; UrRehman, M. Z.; Najeeb, J.; Irfan, A.; .Al-Sehemi, A.G. *J. Mol. Liq.* 2018, 268, 229-238.
- Fu, J.; Xin, Q.; Wu, X.; Chen, Z.; Yan, Y.; Liu, S.; Wang, M.; Xu, Q. *J. Colloid Interf. Sci.* 2016, 461, 292-304.
- Acemioğlu, B. *J. Colloid Interf. Sci.* 2004, 274, 371-379.

4. Acemioğlu, B. *Chem. Eng. J.* **2005**, 106, 73-81.
5. Uğurlu, M. *Microporous Mesoporous Mater.* **2009**, 119, 276-283.
6. Vanaamudan, A.; Pathan, N.; Pamidimukkala, P. *Desalin. Water Treat.* **2014**, 52 (7-9) 1589-1599.
7. Bankole, P.O.; Adekunle, A.A.; Govindwar, S.P. *J. Environ. Chem. Eng.* **2018**, 6(2), 1589-1600.
8. Acemioğlu, B.; Kertmen, M.; Digrak, M.; Alma, M.H.; Temiz, F. *Asian J. Chem.* **2010**, 22(2), 1394-1402.
9. Martorell, M. M.; Pajot, H. F.; de Figueroa, L. I. C. *J. Environ. Chem. Eng.* **2017**, 5987-5993.
10. Errgene, A.; Ada, K.; Tan, S.; Katircioğlu, H. *Desalination* **2009**, 249, 1308-1314.
11. Sartape, A.S.; Mandhare, A.M.; Jadhav, V.V.; Raut, P.D.; Kolekar, S.S. *Arabian J. Chem.* **2017**, 3229-3238.
12. Şen, A.; Pereira, H.; Olivella, M. A.; Villaescusa, I. *Int. J. Environ. Sci. Technol.* **2015**, 12, 391-404.
13. Acemioğlu, B.; Alma, M. H.; Demirkıran, A. R. *J. Chem. Soc. Pak.* **2004**, 26(1), 82-89.
14. Ning-chuan, F.; Xue-yi, G. *Trans. Nonferrous Met. Soc. China* **2012**, 22, 1224-1231.
15. Temesgen, F.; Gabbiye, N.; Sahu, O. *Surfaces Interfaces* **2018**, 12, 151-159.
16. Amela, K.; Hassen, M. A.; Kerroum, D. *Energy Proced.* **2012**, 19, 286-295.
17. Kule, L.; Acemioğlu, B.; Baran, E. *Int. J. Chem. Technol.* **2017**, 1, 58-66.
18. Tanyildizi, M.Ş. *Chem. Eng. J.* **2011**, 168(3), 1234-1240.
19. Kara, A.; Acemioğlu, B.; Alma, M.H.; Cebe, M. *J. Appl. Polym.* **2006**, 101, 2838-2846.
20. Kupeta, A. J. K.; Naidoo, E. B.; Ofomaja, A. E. *J. Clean. Prod.* **2018**, 179, 191-209.
21. Domínguez-Robles, J.; Peresin, M.S.; Tamminen, T.; Rodríguez, A.; Jääskeläinen, A.S. *Int. J. Biol. Macromol.* **2018**, 115, 1249-1259.
22. Bilir, M. H.; Sakalar, N.; Acemioğlu, B.; Baran, E.; Alma, M. H. *J. Appl. Polym. Sci.* **2013**, 6, 4340-4350.
23. Sakalar, N.; Bilir, M. H.; Acemioğlu, B.; Hakkı Alma, M. H. *Asian J. Chem.* **2010**, 22(7), 5649-5662.
24. Sahu, M.K.; Patel, R.K. *RSC Adv.* **2015**, 5, 78491-78501.
25. Dmitrienko, S. G.; Siviridova, O. A.; Pyatkova, L. N.; Senyamin, V. M. *Anal. Bioanal. Chem.* **2002**, 374(3), 361-368.
26. Hameed, B. H.; Mahmoud, D. K.; Ahmad, A.L.; *J. Hazard. Mater.* **2008**, 158(2-3) 499-506.
27. Bayramoğlu, G.; Arica, M. Y. *J. Hazard. Mater.* **2007**, 143(1-2), 135-143.
28. Dwivedi, M. K., Neeraj Jain, Pragati Sharma and Chanchala Alawa, *J. Appl. Chem.* **2015**, 8, 27-35.
29. Liu, R.; Zhang, B.; Mei, D.; Zhang, H.; Liu, J. *Desalination* **2011**, 268, 111-116.
30. Lakshmi Prasanna, M.; Sumithra, S.; Madakka, M. *Int. J. Recent Scientific Research* **2016**, 7 (4), 10401-10405.
31. Weber, W.J.; Morris, J.C. *J. Sanit Eng. Div.* **1963**, 89, 31-59.
32. Lagergren, S. *Kung. Sven. Vetén. Hand.* **1898**, 24, 1-39.
33. Y. S. Ho, G. Mckay, *Chem. Eng. J.* **1998**, 70(2), 115-124.
34. Azizian, S.; Haerifar, M.; Bashiri, H. *Chem. Eng. J.* **2009**, 146, 36-41.
35. Moawed, E.A.; Abulkibash, A.B. *J. Saudi Chem. Soc.* **2016**, 20, S178-S185.
36. Acemioğlu, B. *Bioresour. Technol.* **2004**, 93, 99-102.
37. Hema M.; Arivoli, S. *Int. J. Phys. Sci.* **2007**, 2, 10-17.
38. Fayazi, M.; Afzali, D.; Taher, M.A.; Mostafavi, A.; Gupta, V.K. *J. Mol. Liq.* **2015**, 212, 675-685.
39. Adebowale, K. A.; Olu-Owalabi, B. I.; Chigbundu, E. C. *J. Encapsulation Adsorption Sci.* **2014**, 4, 89-104.
40. Yusuf, M.; Elfghi, F. M.; Mallak, S. K. *Iranica J. Energy Environ.* **2015**, 6, 173-180.
41. Kumar, K.V.; Sivanesan, S. *Dyes Pigment.* **2007**, 72, 130-133.

DOI: 10.32571/ijct.454516


E-ISSN:2602-277X


42. Dehury, K. K. MSc. Thesis, Removal of Safranin-O dye from aqueous solution using acid activated red mud. National Institute of Technology, Rourkela, 2014.


43. Laskar, N.; Kumar, U. *IOP Conf. Ser. Mater. Sci. Eng.* 2017, 225, 012105.

44. Farahani, M.; Kashisaz, M.; Abdullah. S.R.S. *Inter. J. Ecol. Sci. Environ. Eng.* **2015**, 2(3), 17-29.

ORCID

 ID 0000-0002-0728-2747 (B. Acemioğlu)

 ID 0000-0001-9987-1882 (M. H. Bilir)

 ID 0000-0001-6323-7230 (M. H. Alma)



Theoretical approach using DFT and muscle relaxant effects of 5-Chloroisatin Derivatives

Zineb TRIBAK^{1*}, Alae CHDA⁴, Mohammed Khalid SKALLI¹, Amal HAOUDİ¹, Youssef Kandri RODİ¹, Omar SENHAJİ², El Mokhtar ESSASSI³, Rachid Ben CHEIKH⁴, Kaouakib EL ABIDA⁴

on the last page

¹ Laboratory of Applied Chemistry, Faculty of Sciences and Technology, B.P. 2202, Sidi Mohamed Ben Abdellah University, Fez Morocco

² Laboratory of Applied Physical Chemistry, Moulay Ismail University, Faculty of Sciences and Technology of Errachidia, Morocco.

³ Laboratory of Heterocyclic Organic Chemistry, Pole of Competences Pharmacochemistry, Mohammed V University in Rabat, BP 1014, Avenue Ibn Batouta, Rabat, Morocco

⁴ Laboratory of Bioactive Molecules, Faculty of Sciences & Technology, B.P. 2202, Sidi Mohamed Ben Abdellah University, Fez Morocco

Received: 21 July 2018, Revised: 27 September 2018; Accepted: 06 October 2018

*Corresponding author e-mail: tribak.zineb@gmail.com

Citation: Tribak, Z.; Chda, A.; Skalli, M. K.; Haoudi, A.; Rodi, Y. K.; Senhaji, O.; Essasi, M.; Cheikh, R. B.; El-Abida, K. *Int. J. Chem. Technol.* 2018, 2 (2), 105-115.

ABSTRACT

A new series of 5-Chloroisatin derivatives were synthesized and characterised with different characterization methods such as ¹H-NMR and ¹³C-NMR spectroscopy, and then tested for their myorelaxant activity. Computational investigations of the compounds **1a-3a**, **2b** and **4b** on the muscle-relaxing effects performance were performed by using the DFT method with B3LYP functional. The result of descriptors calculation revealed that the theoretical approach was in good agreement with the reported experimental data.

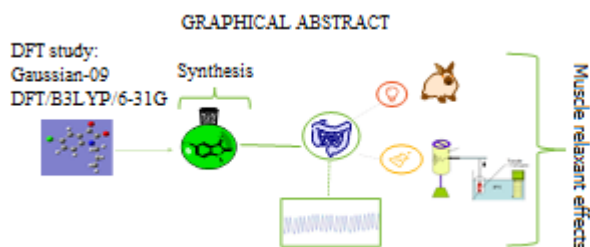
Keywords: 5-Chloroisatin derivatives, B3LYP functional and DFT method, synthesis, myorelaxant effects.

5-Kloroizatin türevlerinin DFT kullanarak teorik yaklaşımı ve kas gevşetici etkileri

ÖZ

Yeni bir 5-Kloroizatin türevleri serisi sentezlendi ve ¹H-NMR ve ¹³C-NMR spektroskopisi gibi farklı karakterizasyon yöntemleri ile karakterize edildi ve daha sonra miyorelaks aktiviteleri için test edildi. Bileşik **1a-3a**, **2b** ve **4b**'nin kas gevşetici etki performansı üzerindeki hesaplamalı incelemeleri, B3LYP fonksiyonelli DFT yöntemi kullanılarak gerçekleştirildi. Tanımlayıcıların hesaplanması sonucu, teorik yaklaşımın rapor edilen deneysel verilerle iyi bir uyum içinde olduğu ortaya kondu.

Anahtar Kelimeler: 5-Kloroizatin türevleri, B3LYP işlevselliği ve DFT metodu, sentez, myorelaxant etkileri.



1. INTRODUCTION

In order to view the extended applications of isatin derivatives¹ in various fields of biology, medicine, industry and because of their anti-fungal properties², antibacterial³, anticonvulsant⁴, anti HIV⁵, antidepressants⁶, anti-inflammatory⁷ and anticorrosive⁸⁻¹⁰, we have synthesized new heterocyclic compounds derived from 5-Chloroisatin as active candidates. The synthesis and the characterizations have been a subject of intense interest in many disciplines of chemistry. In addition, the results of quantum chemical calculations are obtained without laboratory measurements, thus saving time and equipment and alleviating safety and disposal concerns.^{11,12} Density functional theory (DFT) has been used intensively and proved as an efficient approach.^{13,14} We report here the synthesis, characterization and myorelaxant activity of some new 5-Chloroisatin derivatives and the Optimization of the structure using DFT method with B3LYP functional.

2. EXPERIMENTAL METHODS

2.1. Computational details

The DFT calculations were done with Gaussian 09 program package¹⁵ using 6-31G+ basis set and the B3LYP Density Functional. Then, several related structural parameters were selected from the quantum computation results: highest occupied molecular orbital energy E_{HOMO} (eV), lowest unoccupied molecular orbital energy E_{LUMO} (eV), energy gap (ΔE), ionisation potential (IP) and electron affinity (EA), hardness (η), softness (σ), absolute electronegativity. The previous parameters can be explained in terms of the energy of the HOMO and the LUMO.^{16,17}

$$\text{IP} = -E_{\text{HOMO}} \quad (1)$$

$$\text{EA} = -E_{\text{LUMO}} \quad (2)$$

$$\chi = \frac{\text{IP} + \text{EA}}{2} \quad (3)$$

$$\eta = \frac{\text{IP} - \text{EA}}{2} \quad (4)$$

$$\sigma = \frac{1}{\eta} \quad (5)$$

Electron charge distribution on the surfactant molecules were determined which could be used to calculate Fukui indices (f^+ and f^-) for local nucleophilic and electrophilic attacks and s^+ , s^- local softness.^{18,19}

$$f^+ = q_{(N+1)} - q_N \quad \text{For nucleophilic attack} \quad (6)$$

$$f^- = q_N - q_{(N-1)} \quad \text{For electrophilic attack} \quad (7)$$

$$S_k^+ = S [q_{k(N+1)} - q_{k(N)}] = S f_k^+ \quad (8)$$

$$S_k^- = S [q_{k(N)} - q_{k(N-1)}] = S f_k^- \quad (9)$$

Where, $q_{k(N)}$, $q_{k(N+1)}$ and $q_{k(N-1)}$ are the natural populations

for the atom k in the neutral, anionic and cationic species, respectively.

2.2. Chemicals and devices

The melting points were taken with the help of an open capillary tube and were uncorrected. The ^1H and ^{13}C -NMR (75 MHz) spectra were recorded on a Bruker 300 NMR spectrometer (with TMS for ^1H and CDCl_3 for ^{13}C as internal references). The purity of the compounds was checked by TLC on pre-coated SiO_2 gel (230-400 mesh) aluminium plates (E-Merck) using ethyl acetate: hexane and visualized in a UV chamber.

2.2.1. General method of N-alkylated 5-Chloroisatin derivatives

0.2 g (1.1 mmol) of 5-chloro-1*H*-indole-2,3-dione, (0.23 g, 1.16 mmol) of potassium carbonate and (0.035 g, 0.10 mmol) of BTBA were dissolved in 15 ml of *N,N*-dimethylformamide, then, the brominated reagent was added slowly, the mixture was left at room temperature for 48 hours under magnetic stirring, during this period, the progress of the reaction was monitored by TLC (thin layer chromatography). After the reaction was complete, the salts were removed by filtration, the solvent (DMF) was evaporated under reduced pressure. The product obtained was purified on a column of silica gel eluent (ethyl acetate / hexane).²⁰

Compound 1a: 5-chloro-1-octylindoline-2,3-dione

Yield: 88% ; m.p: 68-70°C ; $R_f = 0.85$; ^1H NMR (CDCl_3 ; 300MHz) : δ (ppm) 7.54-7.55(d, H, H_{Ar} , $^4J_{\text{H-H}} = 3\text{Hz}$) ; 7.50-7.51 (d, H, H_{Ar} , $^4J_{\text{H-H}} = 3\text{Hz}$) ; 6.84 (d, H, H_{Ar} , $^3J_{\text{H-H}} = 9\text{Hz}$) ; 3.68 (t, 2H, CH_2 , $^3J_{\text{H-H}} = 6\text{Hz}$) ; 1.71-1.53 (m, 2H, CH_2) ; 1.24-1.31 (m, 10H, CH_2), 0.85 (t, 3H, CH_3 , $^3J_{\text{H-H}} = 6\text{Hz}$). ^{13}C NMR (CDCl_3 ; 75MHz): δ (ppm) 183.20 (C=O); 160.73 (N-C=O); 144.60, 137.60, 125.37 (Cq); 129.45, 115.79, 111.42 (CH_{Ar}); 40.47, 31.73, 29.19, 27.20, 26.88, 22.60(CH_2); 14.04 (CH_3).

Compound 2a: 5-chloro-1-nonylindoline-2,3-dione

Yield: 87% ; m.p: 67-68°C ; $R_f = 0.82$; ^1H NMR (CDCl_3 ; 300MHz): δ (ppm) 7.58-7.59 (d, H, H_{Ar} , $^4J_{\text{H-H}} = 3\text{Hz}$) ; 7.54-7.55 (d, H, H_{Ar} , $^4J_{\text{H-H}} = 3\text{Hz}$) ; 6.85 (d, H, H_{Ar} , $^3J_{\text{H-H}} = 9\text{Hz}$) ; 3.70 (t, 2H, CH_2 , $^3J_{\text{H-H}} = 9\text{Hz}$) ; 1.65-1.75(m, 2H, CH_2) ; 1.28 (m, 12H, CH_2), 0.89 (t, 3H, CH_3 , $^3J_{\text{H-H}} = 6\text{Hz}$). ^{13}C NMR (CDCl_3 ; 75MHz): δ (ppm) 181.84 (C=O); 167.00 (N-C=O); 147.07, 137.63, 129.39 (Cq); 141.28, 116.10, 110.29 (CH_{Ar}); 42.53, 32.42, 29.49, 29.27, 29.21, 27.21, 26.89, 23.18 (CH_2); 15.83 (CH_3).

Compound 3a: 1-allyl-5-chloroindoline-2,3-dione

Yield: 89% ; m.p: 140-142°C ; $R_f = 0.78$. ^1H NMR (CDCl_3 ; 300MHz) δ ppm 7.52-7.58 (m, 2H, H_{Ar}); 6.89 (d,

H, H_{Ar}, ³J_{H-H} = 9Hz); 5.77-5.90 (m, 1H, CH); 5.30-5.35 (m, 2H, CH₂); 4.38 (d, 2H, CH₂, ⁴J_{H-H}=3Hz). ¹³C NMR (CDCl₃; 75MHz) δppm: 182.18 (C=O); 157.34 (N-C=O); 149.07, 129.67, 118.93 (Cq); 137.64, 130.02, 112.00 (CH_{Ar}); 125.25 (C=CH); 118.41 (C=CH₂); 42.63 (CH₂).

Compound 2b: 5-chloro-1-(prop-2-yn-1-yl)indoline-2,3-dione

Yield: 88% ; m.p: 166-170°C; R_f= 0.78; ¹H NMR (CDCl₃) δppm 7.57-7.62 (m, 2H, H_{Ar}); 7.12 (d, H, H_{Ar}, ³J_{H-H} = 6Hz); 4.54 (s, 2H, CH₂); 2.34 (t, H, ⁴J_{H-H} = 3Hz); ¹³C NMR (CDCl₃) δppm: 181.55 (C=O); 156.60 (N-C=O); 147.87, 130.07, 118.50 (Cq); 137.80, 125.24, 112.75 (CH_{Ar}); 73.72 (C≡C); 71.21 (CH); 29.59 (CH₂).

2.2.2. General produces of copper-catalyzed 1,3-dipolar cycloaddition reaction

0.2 g of 5-chloro-1- (prop-2-ynyl) indoline-2,3-dione and 1.2 equiv of azide were reacted in the presence of Cu (I) catalyst with the addition of sodium ascorbate (10⁻³ mol) in excess as a reducing agent in the presence of 0.5.10⁻³ mol of a copper (II) salt (CuSO₄), in a medium composed of a mixture (1:1) of water and ethanol. This procedure made it possible to selectively obtain the disubstituted 1,4-triazole regioisomer.²¹

Compound 4b: 1-((1-benzyl-1H-1,2,3-triazol-4-yl)methyl)- 5-chloroindoline-2,3-dione

Yield: 80%; m.p : 140-145°C; R_f=0.55; ¹H NMR (CDCl₃, 300MHz) δppm 7.32-7.29 (m, 2H, H_{Ar}); 7.26 (d, H, H_{Ar}, ⁴J_{H-H} = 3Hz); 7.08 (d, 2H, H_{Ar}, ⁴J_{H-H} = 3Hz); 6.99-7.03 (m, 1H, CH); 6.71-6.73 (d, 2H, H_{Ar}, ⁴J_{H-H} = 3Hz); 6.47-6.49 (m, H, H_{Ar}); 5.23 (s, 2H, CH₂); 4.89 (s, 2H, CH₂); ¹³C NMR (CDCl₃;75MHz) δppm: 186.50 (C=O); 165.30 (N-C=O); 149.82, 143.25, 135.62, 130.53, 117.81 (Cq); 132.65, 131.15, 129.47, 127.66, 123.11 (CH_{Ar}); 125.65 (CH); 56.54, 43.82 (CH₂).

2.3. Pharmacology

2.3.1. Animals

The animals used in the experiments were placed in an animal house, subjected to a natural photoperiod alternating illumination and darkness. Experiments on smooth jejunum muscle were performed using rabbits of both sexes of 1.5 kg. The present study was performed according to international and institutional rules regarding animal experiments (NIH Publication No. 85-23, revised 1996).

2.3.2. Tissue preparations

Rabbits of both sexes (1.8-2.5 kg) were kept in a standard environmental condition of humidity,

temperature and light. The animals had free access to water and food until the experiment. However, the food was withdrawn 24 hours prior the experiment. The rabbits were killed by exsanguinations, segments of jejunum about 2-3 cm were quickly isolated and transferred in 50 mL organ bath chamber filled with tyrode solution containing (in mM): 136 NaCl, 2.7 KCl, 1.4 CaCl₂ 2H₂O, 0.5 MgCl₂ 6H₂O, 11.9 NaHCO₃, 0.42 NaH₂PO₄ and 5.56 glucose (bubbled continuously with 95% O₂-5% CO₂, pH 7.4 at 37°C).²²

3. RESULTS AND DISCUSSION

3.1. Computational Study

It is generally accepted that the values of E_{HOMO} indicate the electron donating ability of the molecule and the inhibition efficiency increases with increasing E_{HOMO} value. High E_{HOMO} values indicate that the molecule has a tendency to donate electrons to the unoccupied orbitals of the metal with low energy empty orbital.²³ An increase in E_{HOMO} values facilitates the relaxation of the isolated intestine of the rabbit. The E_{LUMO} indicates the ability of the molecules to accept electrons; with lower E_{LUMO} values, greater relaxation ability can be expected.²⁴ The optimized structures of all four 5-Chloroisatin bases, namely **1a**, **2a**, **3a**, **2b** and **4b** with numbering schemes are depicted in Figures 1, 3, 5, 7 and 9. The value of E_{HOMO} of **2a** and **4b** are the highest which correlates with the experimentally determined muscle relaxant effect and the values of E_{LUMO} favour **2a**. The compound **1a** shows also highest value of E_{HOMO} .

The separation energy, $\Delta E = (E_{\text{LUMO}} - E_{\text{HOMO}})$, is an important parameter and it is a function of reactivity of the molecules towards the muscle-relaxing activity on the isolated intestine of the rabbit.

As ΔE decreases, the reactivity of the molecule increases leading to increase in the myorelaxant effects of the compounds.

The calculations given in Table 1 shows the decreasing trend for the ΔE : 3.6125 (4b) > 3.5480 (2a) > 3.5146 (2b) > 3.4781 (3a) > 3.4391 (1a) which follows the same order of the myorelaxant effects of the compound obtained experimentally. The calculations show an obvious correlation between the molecular area of the molecules and the myorelaxant effects. It is clear from Table 1 that the compound **2a** has the highest molecular area that probably increases its muscle relaxant effect.

The values of the global hardness and global softness of the molecules **1a**, **2a**, **3a**, **1b** and **2b**, shown in Table 1 are important properties to measure stability and reactivity of molecules.

The dipole moment (μ) provides information about the polarity of the whole molecule. High dipole moment means greater molecular polarity, which probably gives rise to high chemical reactivity.²⁵ It relates to the dipole-dipole interaction of molecule and the isolated intestine

of the rabbit. Table 1 shows that **2a** has the highest dipole moment.

As we know, frontier orbital theory is useful in predicting the relaxation centers of the molecules responsible for the interaction with the isolated intestine of the rabbit. Figures 2, 4, 6, 8 and 10 show the HOMO and LUMO orbital contributions for the neutral species of the studied molecules **1a**, **2a**, **3a**, **2b** and **4b**. For all the molecules, the HOMO densities were concentrated on

both rings, Cl atom > C=N group, and O-atom of methoxy group. This means that these are active sites of the molecules responsible for interaction with the isolated intestine of the rabbit. The LUMO molecular orbital is uniformly distributed over rings as well as on > C=N group, while contribution from Cl atom is negligible. Due to the presence of an iminic (> C=N-) group and rings, these molecules could have good relaxant effects.

Table 1. The calculated quantum chemical parameters of the studied molecules **1a**, **2a**, **3a**, **2b** and **4b**

Parameters	1a	2a	3a	2b	4b
$-E_{\text{HOMO}}$ (ev)	-6.3709	-6.5768	-6.6598	-6.7608	-6.3260
$-E_{\text{LUMO}}$ (ev)	-2.8228	-3.1377	-3.1818	-3.2463	-2.7135
ΔE gap (ev)	3.5480	3.4391	3.4781	3.5146	3.6125
μ (debye)	6.1043	6.1371	5.9192	5.6945	9.6572
IP= $-E_{\text{HOMO}}$	6.3709	6.5768	6.6599	6.7608	6.3260
EA= $-E_{\text{LUMO}}$	2.8228	3.1377	3.1818	3.2463	2.7135
$\chi = \frac{\text{IP} + \text{EA}}{2}$	4.5968	4.8572	4.9208	5.0036	4.5197
$\eta = \frac{\text{IP} - \text{EA}}{2}$	1.7740	1.7195	1.7391	1.7573	1.8063
$\sigma = \frac{1}{\eta}$	0.5636	0.5815	0.5750	0.5691	0.5536

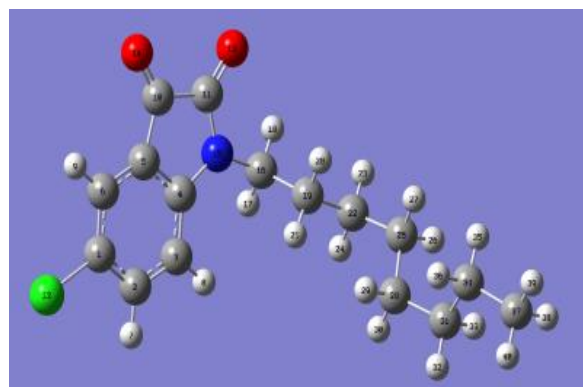


Figure 1. Optimized structure of compound 1a.

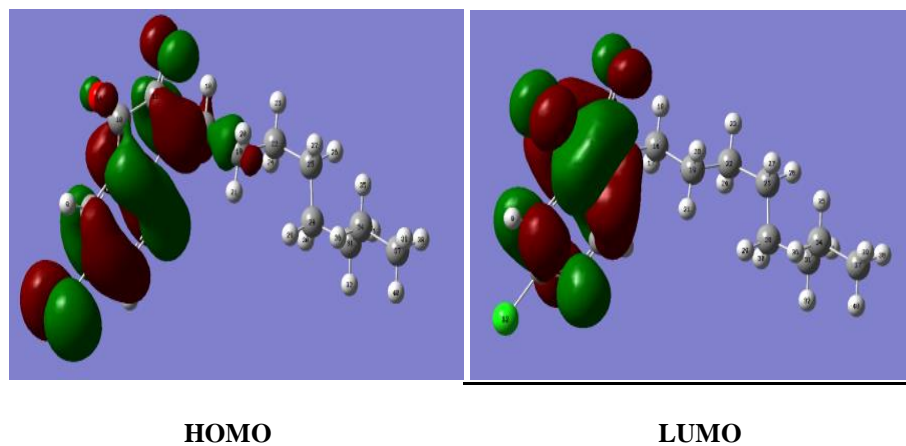


Figure 2. FMO of compound 1a.

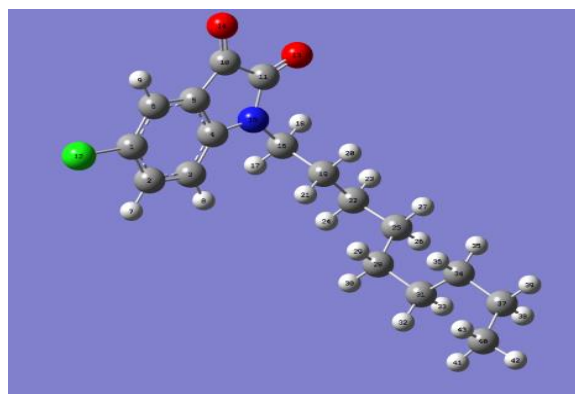


Figure 3. Optimized structure of compound 2a.

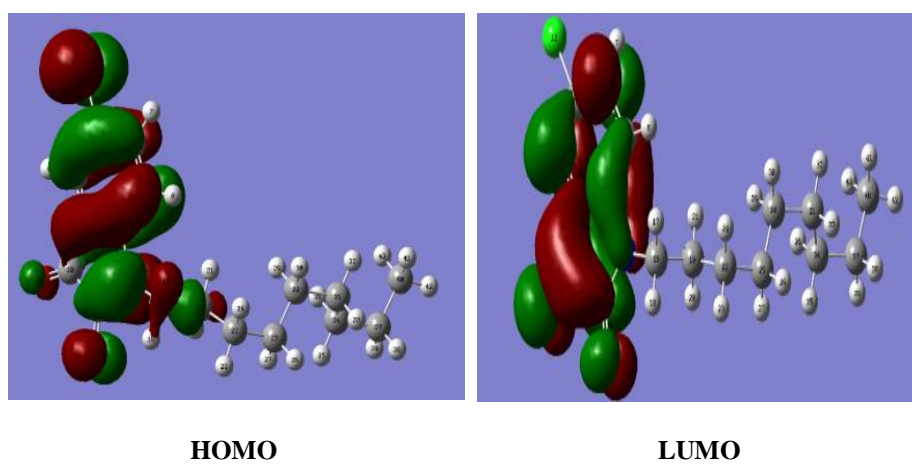


Figure 4. FMO of compound 2a.

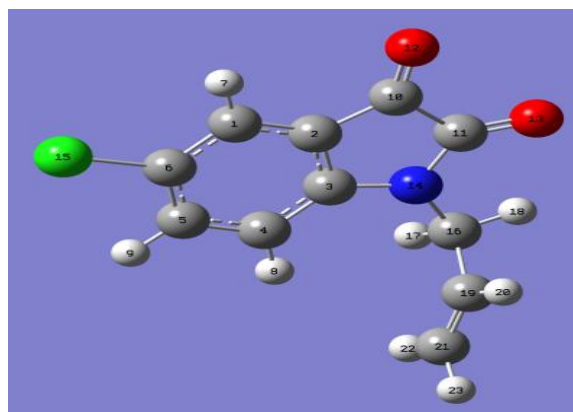


Figure 5. Optimized structure of compound 3a.

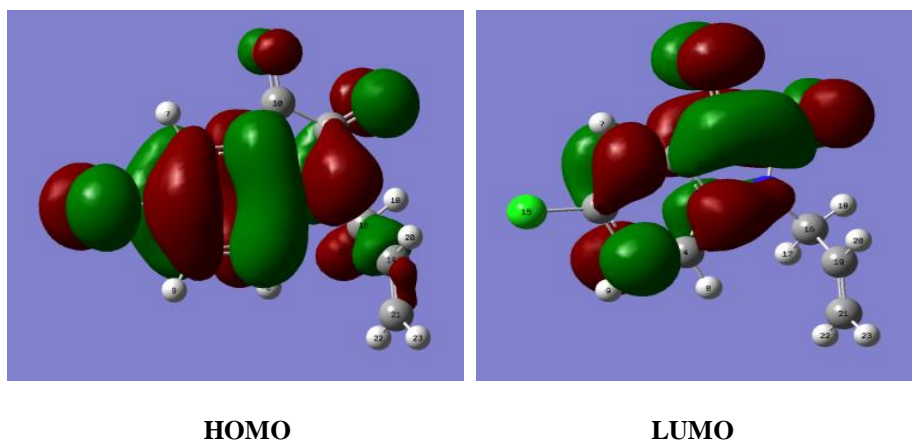


Figure 6. FMO of compound 3a.

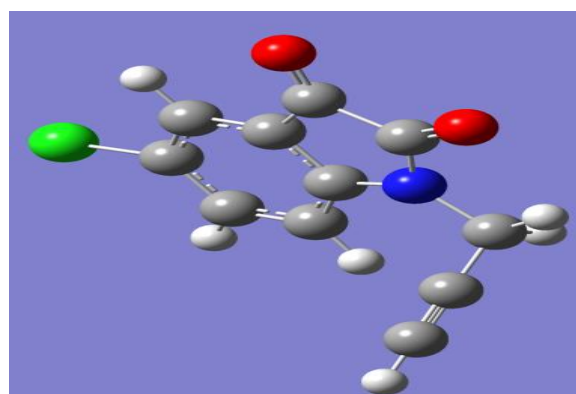


Figure 7. Optimized structure of compound 2b.

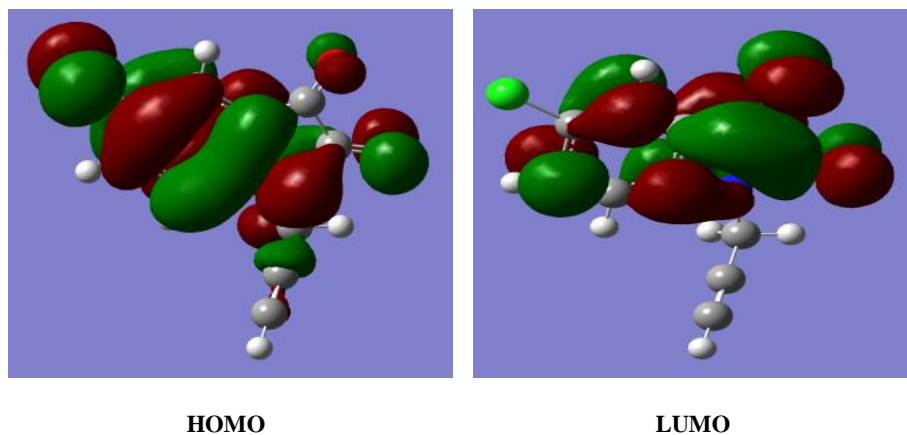


Figure 8. FMO of compound 2b.

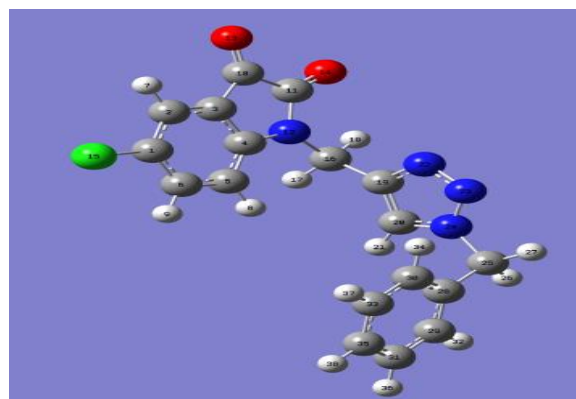


Figure 9. Optimized structure of compound 4b.

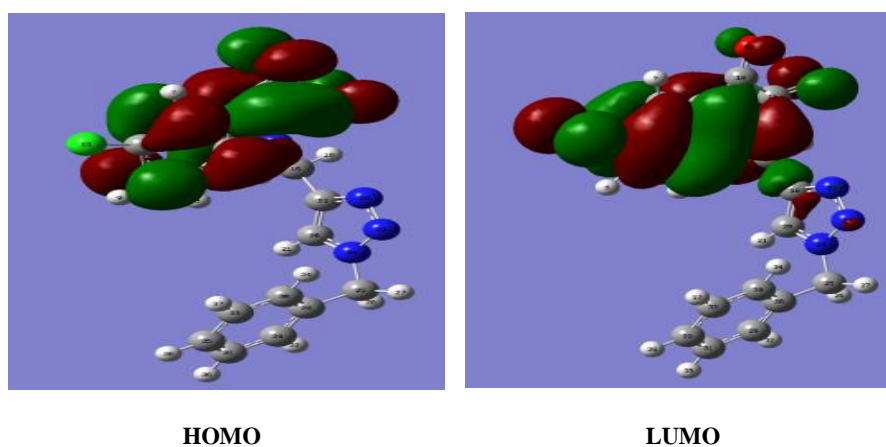


Figure 10. FMO of compound 4b.

Local charges are important in many chemical reactions and physicochemical properties of compound.²⁶ Table 2 shows that most of the carbon atoms (C1, C2, C3, C4, C5, C12, C20, C21, C22, C23, and C25), oxygen atom (O11), nitrogen atom (N18), and chlorine atom Cl12 possess the excess of negative charge. Among them, highest negative charge is located on the nitrogen (N15) and (O13) for **2a** and oxygen atom (O13) for the **1a**, O13 for the **3a** then C20 for **1b** then the N22, N24 for the **4b**. It confirmed that electron donation ability of atoms to the unoccupied orbital of metal is directly related to negative atomic charges of relaxation sites. Therefore, these atoms should be the active relaxation sites.

The preferred site for nucleophilic attack is the atom in the molecule where Fukui function (f^+) has the highest value as it is associated with the LUMO and measures the reactivity towards a donor reagent.

The preferred site for electrophilic attack is the atom in the molecule where the value of Fukui function (f^-) is the highest as it is associated with the HOMO and measures reactivity toward an acceptor reagent.²⁷⁻³⁰ An analysis of Fukui functions depicted in Table 2 shows that the atoms Cl12, O14, C11, C20, Cl15, are preferred sites for electrophilic attack, as these sites have higher values of Fukui function (f^-). The atoms C9, Cl12, O13, C20 and Cl15 are most susceptible sites for nucleophilic attack. For the simplest transfer of electrons, muscle relaxant effect can occur at the part of the molecule, where local softness (s) has the highest value. A high value of s^+ indicates high nucleophilicity, and a high value of s^- indicates high electrophilicity. The results shown in Table 2 indicate that the condensed local softness indices s^+ and s^- follow the same trend as that of Fukui functions.³¹

Table 2. Pertinent natural populations and Fukui functions of the studied compounds calculated at B3LYP/6-31G

	Atom k	q(N)	q(N+1)	q(N-1)	f_k^+	f_k^-	s^+	s^-
1a	C9	0.0022	0.1880	-0.0215	0.1858	0.0238	0.1047	0.0134
	C6	0.0516	0.2015	0.0116	0.1499	0.0400	0.0845	0.0225
	Cl12	-0.0086	0.2928	-0.0639	0.3014	0.0553	0.1699	0.0312
	O13	-0.4680	-0.2722	-0.5312	0.1958	0.0632	0.1104	0.0356
2a	Cl12	0.0849	0.2924	-0.0638	0.2075	0.1486	0.1207	0.0864
	O13	-0.3937	-0.2723	-0.2303	0.1214	-0.1634	0.0706	-0.0950
	O14	-0.3490	-0.2654	-0.5312	0.0835	0.1822	0.0486	0.1059
	N15	-0.7078	-0.6598	-0.5276	0.0479	-0.1802	0.0279	-0.1048
	C37	0.0089	0.0243	-0.0042	0.0153	0.0131	0.0089	0.0076
C40	-0.0090	0.0028	-0.0195	0.0118	0.0105	0.0069	0.0061	
3a	C11	0.1970	0.3038	0.0231	0.1068	0.1739	0.0438	0.0713
	O13	-0.1013	0.0734	-0.2303	0.1747	0.1290	0.0717	0.0529
	C19	0.1174	0.1162	0.1191	-0.0012	-0.0018	-0.0007	-0.0010
	C21	-0.0269	0.0629	-0.1073	0.0898	0.0803	0.0516	0.0462
2b	C16	0.2385	0.3262	0.1818	0.0877	0.0566	0.0499	0.0322
	C19	0.1829	0.1366	0.2151	-0.0463	-0.0322	-0.0264	-0.0183
	C20	-0.1626	-0.0511	-0.2648	0.1115	0.1022	0.0635	0.0581
4b	C151	-0.0121	0.1648	-0.1294	0.1769	0.1174	0.0979	0.0650
	N22	-0.3218	-0.3458	-0.3158	-0.0240	-0.0060	-0.0133	-0.0033
	N23	-0.0682	-0.0393	-0.0896	0.0289	0.0213	0.0160	0.0118
	N24	-0.2493	-0.2459	-0.2697	0.0034	0.0204	0.0019	0.0113

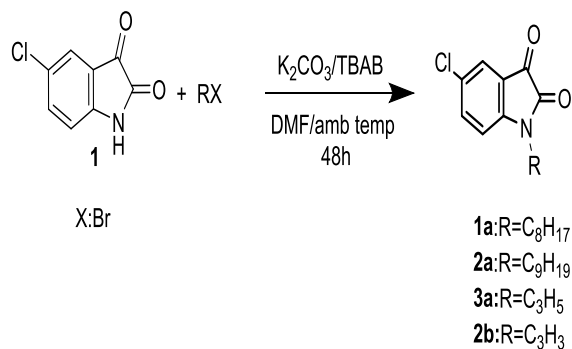
3.2. Synthesis of 5-Chloroisatin derivatives

In our laboratory, Tribak and co-workers³²⁻³⁵ carried out the alkylation reaction of 5-Chloroisatin with allyl and propargyl bromides and other brominated reagent under the conditions of liquid-solid phase transfer catalysis. It was able to isolate a single N-alkylated product **1a-3a** and **2b** in good yield (Scheme 1 and 2).

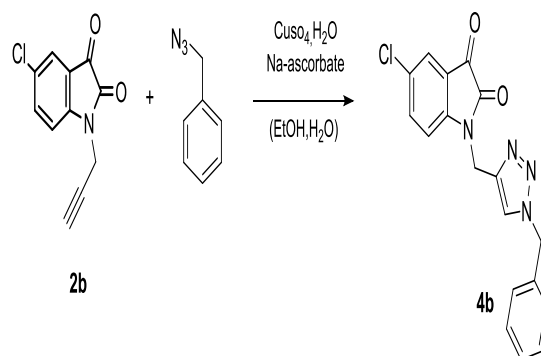
Also, Tribak and co-workers³⁶ studied the condensation of N-propargylchloroisatin with benzyl azide at the reflux of ethanol, for 24 hours, led to the formation of a single regioisomer **4b** resulting from the attack of the most nucleophilic nitrogen of the dipole on the most electrophilic sp^3 carbon of the dipolarophile.

3.3. Muscle relaxant effect of 5-Chloroisatin derivatives

In this study, we investigated the muscle-relaxing activity on the isolated intestine of the rabbit of our molecules containing the 5-Chloroisatin molecule, which possesses an indole nucleus having both the keto and lactam parts, aroused an enormous curiosity due to its various biological and pharmacological studies.^{37,38}



Scheme 1



Scheme 2

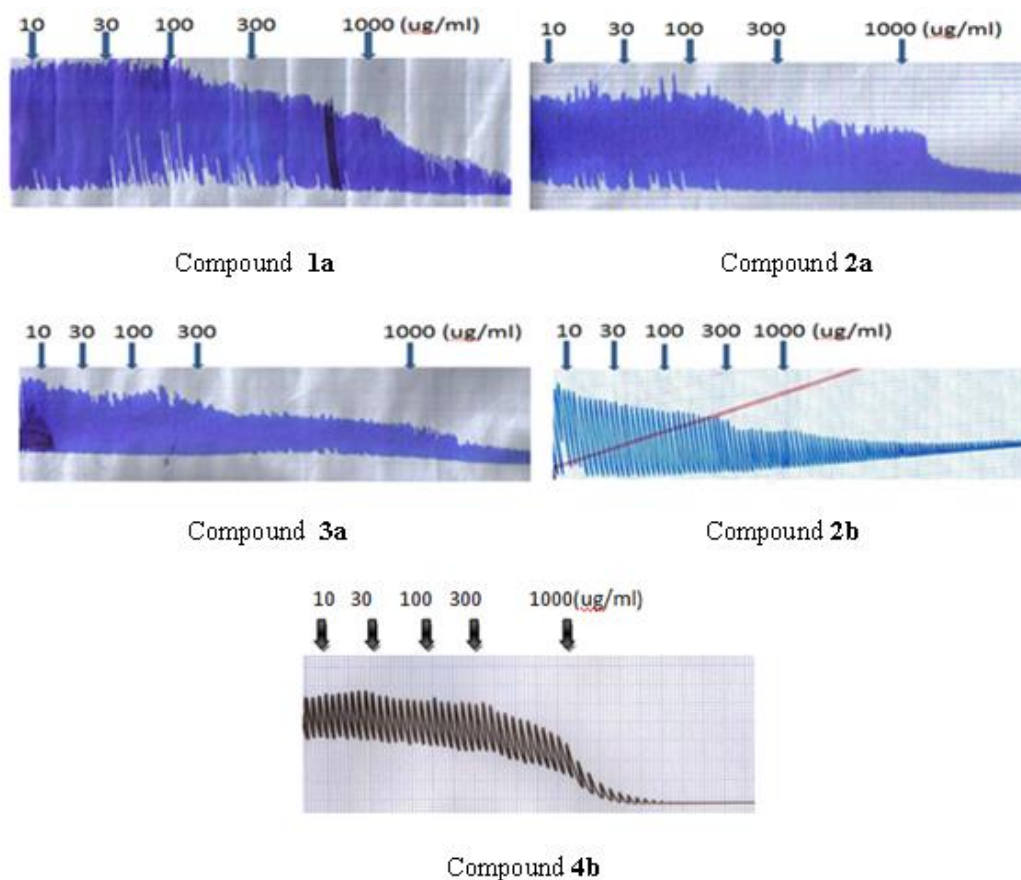


Figure 11. The original plot shows a significant muscle relaxant effect of the compounds 1a-3a, 2b and 4b above on the contractile activity of the rabbit jejunum.

The present study aims at the in vitro research of possible muscle relaxant effect of new heterocyclic molecules derived from 5-Chloroisatin. Once the preparation is mounted on the insulated organ vessel, we wait for its stabilization (about 30 min). Once stable, spontaneous contractions of the rabbit jejunum are recorded. After pharmacological screening of the samples studied, we were able to demonstrate that products **1a-3a**, **2b** and **4b** belonging to the family of 5-Chloro-1*H*-indole-2,3-dione are endowed with muscle-relaxing activity in the segments isolated from the jejunum. The amplitude of contractions of the segments of the jejunum isolated from the base rabbit was reduced in a concentration-dependent manner (Products: **1a-3a**, **2b** and **4b**).

The compounds (**1a-3a**, **2b** and **4b**) were tested on isolated rabbit jejunum to determine its myorelaxant effect. As shown in Figure 12, the cumulative concentrations of 5-Chloroisatin derivatives altered the spontaneous contractions of the isolated rabbit jejunum in a concentration-dependent manner since the percentage of contraction decreased to 97% for the lowest concentration and was almost totally inhibited at the highest concentration to 3%. The effects of the products tested are very close and in this case it is adequate to say that the products have a similar effect (Figure 12).

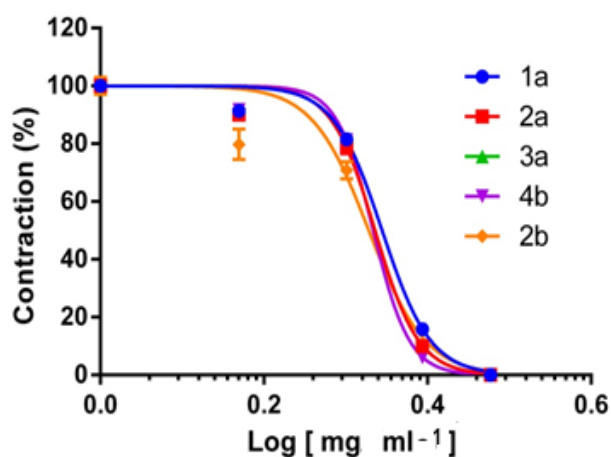


Figure 12. Myorelaxant effects of cumulative concentrations of 5-Chloroisatin derivatives (**1a-3a**, **2b** and **4b** (mg ml^{-1})) on the spontaneous contraction of isolated rabbit jejunum.

4. CONCLUSIONS

Some new 5-Chloroisatin derivatives **1a-3a**, **2b** and **4b** were synthesized and identified in good yields. The myorelaxant activity performed for all the compounds, which were effective relaxant on isolated rabbit jejunum. Most of the studied quantum chemical descriptors

correlated well with the available experimental observations.

ACKNOWLEDGEMENTS

The authors would like to thank all the people who helped to carry out this work such as ^1H NMR, ^{13}C NMR and Muscle relaxant effects.

Conflict of interest

Authors declare that there is no a conflict of interest with any person, institute, company, etc.

Ethical Report: For the Ethical report, the present study was performed according to international and institutional rules regarding animal experiments (NIH Publication No. 85-23, revised 1996).

REFERENCES

1. Tribak, Z.; Skalli, M. K.; Haoudi, A.; Rodi, Y. K.; Senhaji, O.; Essassi, E. M. *IMedPub Journals*. **2018**, *3*, 1–4.
2. Pandeya, S. N.; Sriram, D.; Nath, G.; De Clercq, E. *Pharm. Acta Helv* **1999**, *74* (11).
3. Sarangapani, M.; Reddy, V. M.. *Indian J. Pharm. Sci.* **1996**, *58* (4), 147.
4. Popp, F. D.; Parson, R.; Donigan, B. E. *J. Heterocycl. Chem.* **1980**, *17* (6), 1329–1330.
5. Pandeya, S. N.; Smitha, S.; Jyoti, M.; Sridhar, S. K. *Acta Pharm* **2005**, *55* (1), 27–46.
6. Singh, G. S.; Singh, T.; Lakhan, R. *ChemInform* **1998**, *29* (17).
7. Bhattacharya, S. K.; Chakrabarti, A. *Indian J. Exp. Biol.* **1998**, *36* (1), 118–121.
8. Tribak, Z.; Kharbach, Y.; Haoudi, A.; Skalli, M. K.; Rodi, Y. K.; El Azzouzi, M.; Aouniti, A.; Hammouti, B.; Senhaji, O. *J. Mater. Environ. Sci.* **2016**, *7* (6), 2006–2020.
9. Tribak, Z.; Kandri Rodi, Y.; Elmsellem, H.; Abdel-Rahman, I.; Haoudi, A.; Skalli, M. K.; Kadmi, Y.; Hammouti, B.; Ali Shariati, M.; Essassi, E. M. *J. Mater. Environ. Sci* **2017**, *8* (3), 1116–1127.
10. Tribak, Z.; Haoudi, A.; Skalli, M. K.; Rodi, K. Y.; El Azzouzi, M.; Aouniti, A.; Hammouti, B.; Senhaji, O. *J. Mater. Environ. Sci.* **2017**, *8* (1), 299–309.

11. Obot, I. B.; Obi-Egbedi, N. O.; Umoren, S. A. *Int. J. Electrochem. Sci* **2009**, 4 (6), 863–877.
12. Zhang, S. G.; Lei, W.; Xia, M. Z.; Wang, F. Y. *J. Mol. Struct. THEOCHEM* **2005**, 732 (1–3), 173–182.
13. Irfan, A.; Al-Sehemi, A. G.; Asiri, A. M.; Nadeem, M.; Alamry, K. A. *Comput. Theor. Chem.* **2011**, 977 (1–3), 9–12.
14. Irfan, A.; Hina, N.; Al-Sehemi, A. G.; Asiri, A. M. *J. Mol. Model.* **2012**, 18 (9), 4199–4207.
15. Frisch, M.; Trucks, G. W.; Schlegel, H. B.; Scuseria, G. E.; Robb, M. A.; Cheeseman, J. R.; Scalmani, G.; Barone, V.; Mennucci, B.; Petersson, G. A. *Inc., Wallingford, CT*, **2009**, 200.
16. Chattaraj, P. K.; Roy, D. R. *Chem. Rev.* **2007**, 107 (9), PR46-PR74.
17. Wang, H.; Wang, X.; Wang, H.; Wang, L.; Liu, A. *J. Mol. Model.* **2007**, 13 (1), 147–153.
18. Siaka, A. A.; Edd, N. O.; Idris, S. O.; Magaji, L. *Res. J. Appl. Sci.* **2011**, 6 (7–12), 487–493.
19. Eddy, N. O.; Stoyanov, S. R.; Ebenso, E. E. *Int. J. Electrochem. Sci* **2010**, 5, 1127–1150.
20. Tribak, Z.; Haoudi, A.; Rodi, Y. K.; Elmsellem, H.; Skalli, M. K. *Mor. J. Chem.* **2016**, 4, 1157–1163.
21. Tribak, Z.; Skalli, M. K.; Senhaji, O.; Rodi, Y. K.; Haoudi, A.; Essassi, E. M. *Am. Inter. J. Res. Formal. Appl. Nat. Sci.* **2017**.1, 41–50.
22. Chda, A.; El Kabbaoui, M.; Chokri, A.; El Abida, K.; Tazi, A.; Cheikh, R. Ben. *Eur. J. Med. Plants* **2016**, 11 (2), 1–13.
23. Obi-Egbedi, N. O.; Obot, I. B.; El-Khaiary, M. I.; Umoren, S. A.; Ebenso, E. E. *Int. J. Electrochem. Sci* **2011**, 6, 5649–5675.
24. Özcan, M.; Solmaz, R.; Kardaş, G.; Dehri, I. *Colloids Surfaces A Physicochem. Eng. Asp.* **2008**, 325 (1–2), 57–63.
25. Kikuchi, O. *Mol. Inform.* **1987**, 6 (4), 179–184.
26. Khaled, K. F. *Appl. Surf. Sci.* **2010**, 256 (22), 6753–6763.
27. Tribak, Z.; Rodi, Y. K.; Haoudi, A.; Skalli, M. K.; Mazzah, A.; Ouzidan, Y.; Senhaji, O.; Essassi, E. M.; *J. Mar. Chim. Heterocycl.* **2017**, 16, 110–118.
28. Tribak, Z.; R. Ghibate.; Skalli, M. K.; Senhaji, O.; Rodi, Y. K. *Inter. J. Sci. Tech. Eng.* **2016**, 3 (06), 257–262.
29. Tribak, Z.; Skalli, M. K.; Senhaji, O.; Rodi, Y. K. *Inter. J. Adv. Chem.* **2017**, 5 (2), 91–95.
30. Tribak, Z.; Skalli, M. K.; Senhaji, O.; Rodi, Y. K. *Inter. J. Adv. Chem.* **2017**, 4 (5), 2–7.
31. Tribak, Z.; Skalli, M. K.; Senhaji, O.; Rodi, Y. K. *Inter. J. Sci. Res.* **2017**, 6 (7), 1069–1074.
32. Tribak, Z.; Kandri Rodi, Y.; Haoudi, A.; Essassi, E. M.; Capet, F.; Zouihri, H. *IUCrData* **2016**, 1 (6), x160913.
33. Tribak, Z.; Kandri Rodi, Y.; Haoudi, A.; Essassi, E. M.; Capet, F.; Zouihri, H. *IUCrData* **2016**, 1 (6), x160854.
34. Tribak, Z.; Kandri Rodi, Y.; Haoudi, A.; Essassi, E. M.; Capet, F.; Zouihri, H. *IUCrData* **2016**, 1 (6), x160862.
35. Tribak, Z.; Kandri Rodi, Y.; Haoudi, A.; Essassi, E. M.; Capet, F.; Zouihri, H. *IUCrData* **2016**, 1 (6), x160971.
36. Tribak, Z.; Skalli, M. K.; Senhaji, O.; Rodi, Y. K. *Inter. J. Adv. Eng. Manag. Sci.* **2017**. 3(8) 837-841
37. Tribak, Z.; Amin, O. El; Skalli, M. K.; Senhaji, O.; Rodi, Y. K.; Iraqui, M. H. *Int. J. Eng. Res. Appl.* **2017**, 7 (6), 21–24.
38. Tribak, Z.; Amin, O. El; Skalli, M. K.; Senhaji, O.; Rodi, Y. K.; Iraqui, M. H. *Int. J. Eng. Res. Appl.* **2017**, 7 (6), 66–70.

ORCID

-  0000-0002-2169-9856 (Z. Tribak)
-  0000-0001-8508-8678 (A. Chda)
-  0000-0002-1620-0619 (M.K. Skalli)
-  0000-0002-0949-4428 (A. Haoudi)
-  0000-0002-4527-9258 (Y.K. Rodi)
-  0000-0003-3253-3955 (O. Senhaji)
-  0000-0002-1490-7522 (El.M. Essassi)
-  0000-0001-6341-6677 (R.B. Cheikh)
-  0000-0003-0660-4967 (K. El-Abida)



Electrical characteristics of Au/Ti/HfO₂/n-GaAs metal-insulator-semiconductor structures with high-*k* interfacial layer

Abdulkerim Karabulut^{1,*}, Ikram Orak²⁻³, Abdülmecit Türüt⁴

on the last page

¹Department of Electrical and Electronics Engineering, Faculty of Engineering, Sinop University, Sinop, TR-57000, Turkey

²Vocational School of Health Services, Bingöl University, Bingöl, TR-12000, Turkey

³Department of Physics, Faculty of Sciences and Arts, Bingöl University, Bingöl, TR-12000, Turkey

⁴Department of Physics Engineering, Faculty of Sciences, Istanbul Medeniyet University, Istanbul, TR-34730, Turkey

Received: 04 September 2018, Revised: 16 October 2018; Accepted: 19 October 2018

*Corresponding author e-mail: akerimkara@gmail.com

Citation: Karabulut, A.; Orak, I.; Turut, A. *Int. J. Chem. Technol.* 2018, 2 (2), 106-112.

ABSTRACT

We have fabricated, metal-insulator-semiconductor (MIS) structures, the Au/Ti/HfO₂/n-GaAs. Metal rectifying contacts were made by DC magnetron sputtering technique, and hafnium dioxide (HfO₂) interfacial insulating layer with 3, 5 and 10 nm thickness has been formed by the atomic layer deposition (ALD) technique. The series resistance values from the forward bias current-voltage (*I-V*) curves of 3 nm and 5 nm MIS structures has reduced very slightly with a decrease in the measurement temperature. The diode potential barrier height value from *I-V* characteristics increased with increasing HfO₂ layer thickness. Thus, the diode potential barrier height was changed using the interfacial layer of the hafnium dioxide. Barrier height increment is an important and desirable feature in the field effect transistors (FET) and microwave mixers.

Keywords: Metal-oxide-semiconductor structures, GaAs semiconductor, Hafnia HfO₂, Atomic layer deposition (ALD) technique.

Yüksek *k*-arayüzey tabakalı metal-yalıtkan yarıiletken Au/Ti/HfO₂/n-GaAs yapıların Elektriksel Karakteristikleri

ÖZ

Au/Ti/HfO₂/n-GaAs metal-yalıtkan-yarıiletken (MIS) yapılar oluşturduk. Metal doğrultucu kontakları DC magnetron sputtering tekniğiyle yapıldı ve 3, 5 ve 10 nm kalınlıklı hafnium dioksit (HfO₂) arayüzey yalıtım tabakası atomic layer deposition (ALD) tekniğiyle oluşturuldu. 3 ve 5 nm MIS diyotların doğru besleme akım-gerilim eğrilerinden seri direnç değerleri, ölçüm sıcaklığındaki bir azalma ile çok hafif bir şekilde azaldı. *I-V* karakteristiklerinden diyot potansiyel engel yüksekliği değeri artan HfO₂ tabaka kalınlığıyla arttı. Böylece, hafnium dioksit arayüzey tabakası kullanılarak diyot potansiyel engel yüksekliği değiştirildi. Bariyer yükseklik artırma, alan etkili transistörler (FET) ve mikrodalga karıştırıcılarında önemli ve istenen bir özelliktir.

Anahtar Kelimeler: Metal-oksit-yarıiletken yapılar, GaAs yarıiletkeni, Hafnia HfO₂, Atomic tabakalı depolama (ALD) tekniği.

1. INTRODUCTION

The Metal-semiconductor (MS) rectifying and ohmic contacts are of huge importance in fabricating modern electronic device applications such as bipolar transistor, field effect transistor (FET) and metal-oxide-semiconductor (MOS) FET (i.e. MOSFET). MS

rectifying current and admittance theory serve in understanding the foundation of the semiconductor device physics.¹⁻⁶ The metal-insulator-semiconductor (MIS) or MOS capacitors are the most useful devices in semiconductor surface physics studies since most practical problems in the reliability and stability of all semiconductor devices are closely related to their surface

conditions.¹⁻¹⁰ We have prepared the Au/Ti/HfO₂/n-GaAs MIS structures. The metal oxide interfacial layer with 3, 5 and 10 nm thickness, the hafnium dioxide (HfO₂) thin film, was grown by the ALD technique. Ti (10 nm) Schottky contacts have been produced on HfO₂/n-GaAs structure by DC magnetron sputtering technique, and Au (50 nm) was evaporated as a top layer on the Ti/n-GaAs structure under 10⁻⁶ Torr vacuum. We have described the current-voltage (*I-V-T*) characteristics of these MIS diodes.

Hafnium oxide (HfO₂) known as hafnia is a colourless solid and is an inorganic insulating compound. Also, HfO₂ is one of the most common and stable compounds of hafnium. It is a material with high dielectric constant, i.e. high-*k* dielectric. As it is well-known, the insulating or oxide interfacial layer is one of the most critical MOSFET components. It is an electrical insulator with a band gap of nearly 6 eV and a high dielectric constant value of 22, which is utilized to increase the interfacial layer capacitance without generating excess gate current in a MOSFET and thus to achieve a large current.^{1,4-10} Therefore, the oxide film growth technique is a very important issue. The ALD technique is one of the most important methods for preparing high quality high-*k* dielectric thin metal-oxide layers. The layer-by-layer nature of the deposition kinetics of the ALD process allows surface-controlled nearly perfect thin films with excellent electrical characteristics.⁵⁻¹⁰

Generally, the SiO₂ is the main dielectric gate oxide material in the semiconductor electronic industry owing to its excellent compatibility with Si semiconductors. However, the main disadvantage of SiO₂ is its high power consumption and large leakage currents which limits its technological applications. For instance, the improved performance of complementary CMOS transistors requires the high *k*-metal oxides such as HfO₂ the substitution of the SiO₂ gate oxide.⁴⁻⁷ Therefore, the high *k*-metal oxides such as HfO₂ can be selected for the GaAs MOSFETs, MOS high-electron-mobility transistors (MOS-HEMTs) and high voltage power switching devices.⁵⁻¹⁰

2. EXPERIMENTAL PROCEDURES

The Au/Ti/HfO₂/n-GaAs structures were produced utilizing *n*-type GaAs wafer with (100) crystal orientation, having 300 μm thickness, 2 inch diameter and 1.2 Ω cm resistivity (the manufacturer data) and 6.8 x 10¹⁵ cm⁻³ carrier concentration. Before the SBD fabrication process, the experimental procedure was first performed by a cleaning procedure which is sonicated for 2 minutes in acetone and propanol, and then rinsed in deionized water thoroughly and dried under nitrogen gas flow. After cleaning of n-GaAs's surface, Indium metal (purity of 99.999%) which has a thickness of nearly 2000

Å was deposited for back-side ohmic contact at a reactor pressure approximately 10⁻⁶ Torr in a high-vacuum thermal evaporation system. In order to form the low-resistance ohmic contact, In-deposited n-GaAs wafer was annealed at 385°C for 3 min under the nitrogen gas atmosphere. After this process, HfO₂ thin films were deposited on the cleaned top surface of GaAs samples using standard thermal ALD system (Savannah S100 ALD reactor, Cambridge Nanotech Inc.). Deposition was carried out at 200°C using tetrakis (dimethylamido) hafnium [Hf(NMe₂)₄] and water (H₂O) as the organometallic precursor and oxygen source, respectively. Hf(NMe₂)₄ was preheated to 75°C and stabilized at this temperature before the deposition. Carrier gas (N₂) with a flow rate of 20 sscm was utilized. Pulse times of the Hf precursor and oxygen source were 0.2 and 0.015 s, respectively. Purging was done after each step. Deposition rate for this recipe was determined about 1 Å per cycle. The total number of ALD cycles was used to precisely control the thickness of deposited hafnia layer. Afterwards, for Schottky diode fabrication, the hafnia coated and Indium-back-contacted GaAs sample was patterned via standard lithography process. After development process, the sample was rinsed entirely in de-ionized water. On the top of the ALD-grown HfO₂ insulating layer, Au (90nm)/Ti(10nm) Schottky contacts were formed using DC magnetron sputtering technique. Figure 1 shows the schematical representation of experimentally produced MIS devices.

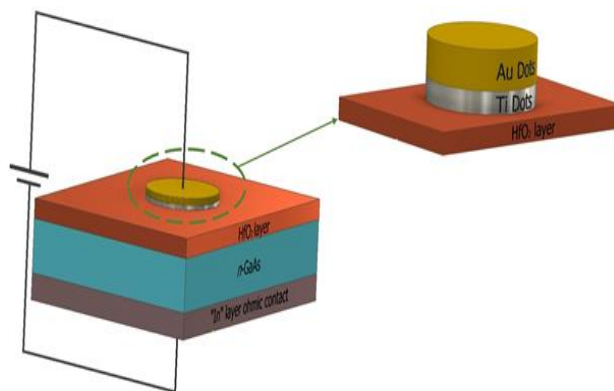


Figure 1. Schematical representation of experimentally produced MIS devices.

After fabrication process, the current-sample temperature-voltage (*I-T-V*) characteristics were measured using a Leybold Heraeus closed-cycle helium cryostat and a Keithley 487 Picoammeter Voltage Source in dark conditions. The sample temperature was always monitored by a copper-constantan thermocouple and by a Windaus MD850 electronic thermometer which has better sensitivity than ± 0.1 K.

3. RESULTS AND DISCUSSION

Figure 2 illustrates 3D for the surface morphology of deposited 3 nm HfO₂ on substrate, the RMS value is 1.09 nm. Figure 3 shows 3D for the surface morphology of deposited 5 nm HfO₂ on substrate, the RMS value is 1.20 nm. Figure 4 shows 3D for the surface morphology of deposited 10 nm HfO₂ on *n*-type GaAs substrate, the RMS value is 1.19 nm.

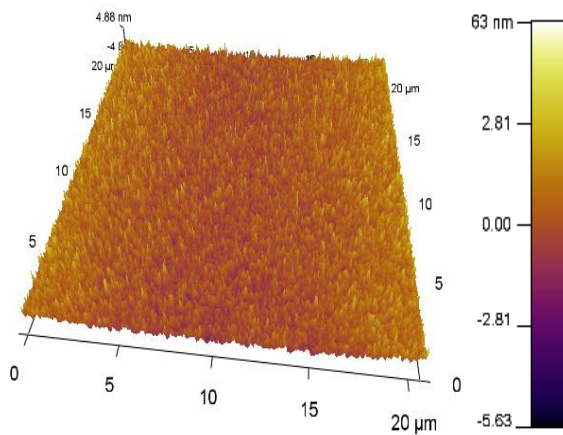


Figure 2. 3D for the surface morphology of 3 nm HfO₂ deposited on *n*-GaAs substrate, the RMS value is 1.09 nm.

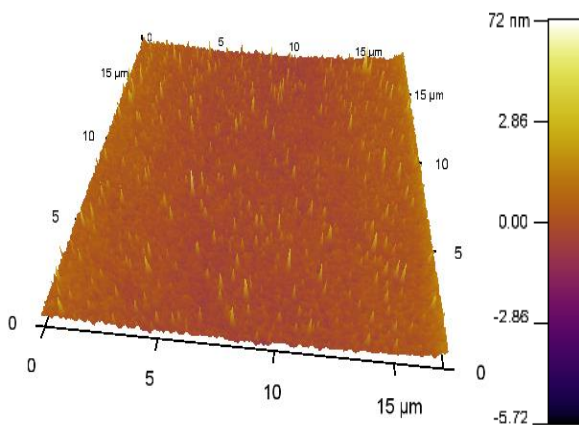


Figure 3. 3D for the surface morphology of 5 nm HfO₂ deposited on *n*-GaAs substrate, the RMS value is 1.20 nm.

The experimental *I-V* characteristics at 60, 200, 300 and 400 K of the MIS diodes structures are given in Figures 5 and 6. The current by the carriers across the diode is supplied by the thermionic emission (TE) given in Eq. (1).¹⁻⁴

$$I = I_0 \left[\exp \left(\frac{q(V - IR_s)}{nkT} \right) - 1 \right] \quad (1)$$

where *I*₀ indicates the saturation current, and it is expressed by Eq. (2).

$$I_0 = AA^*T^2 \exp \left(- \frac{q\Phi_{b0}}{kT} \right) \quad (2)$$

Φ_{b0} and *n* indicate the effective barrier height (BH) at zero bias and ideality factor calculated from the intercept and slope of the linear portion of the semi-log forward bias *lnI-V* characteristics, respectively. *A** shows the effective Richardson constant of 8.16 Acm⁻²K⁻² for *n*-type GaAs. *A* is the diode area. *R_s* indicates the series resistance from the neutral region of the semiconductor substrate and the interfacial layer HfO₂. The *IR_s* is the voltage drop across the series resistance, respectively.¹²⁻²⁴ The *R_s* value was calculated using Cheung's method arranged from Eq. (1).¹¹

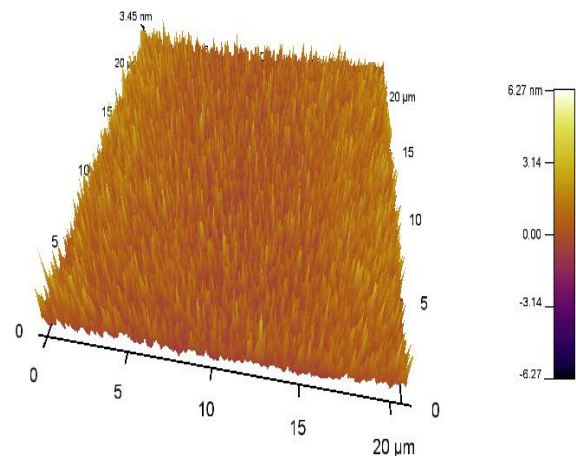


Figure 4. 3D for the surface morphology of 10 nm HfO₂ deposited on *n*-type GaAs substrate, the RMS value is 1.19 nm.

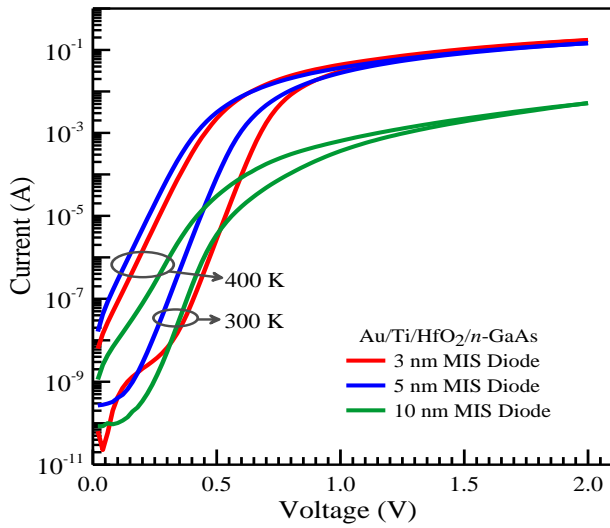


Figure 5. Experimental forward bias I - V characteristics for MIS structures with 3, 5 and 10 nm HfO_2 interfacial layer thicknesses at 300 and 400 K.

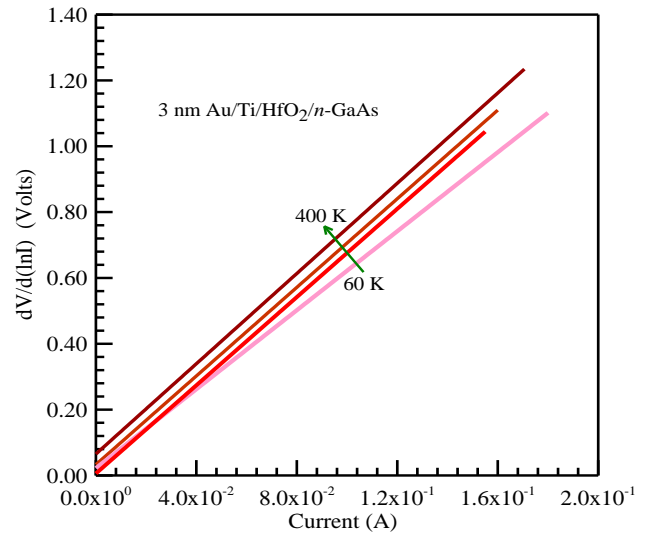


Figure 7. $dV/d(\ln I)$ versus current plots by Cheung's Model for determining the series resistance for the 3 nm MIS diode at different temperatures.

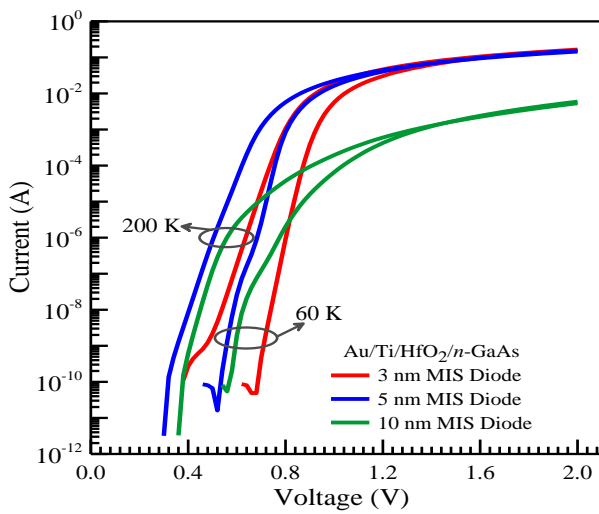


Figure 6. Experimental forward bias I - V characteristics at 60 and 200 K for the MIS structures with 3, 5 and 10 nm HfO_2 interfacial layer thicknesses.

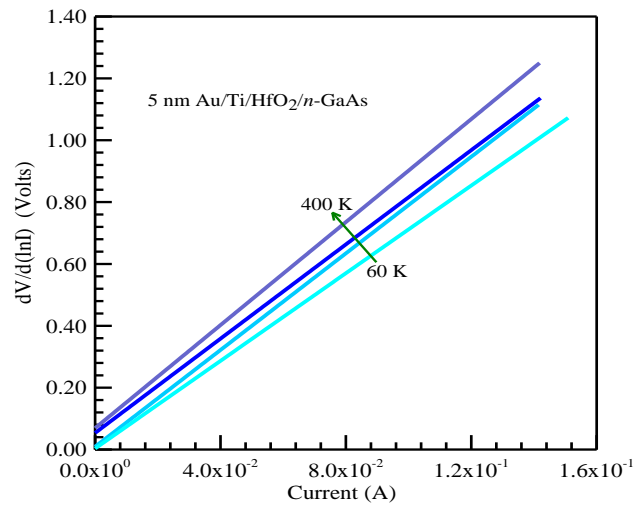


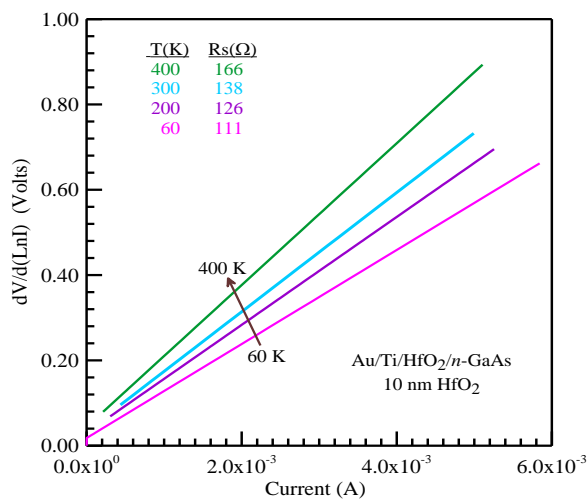
Figure 8. $dV/d(\ln I)$ versus current plots by Cheung's Model for determining the series resistance at different temperatures for the MIS structure with 5nm HfO_2 interfacial layer thickness.

The plots by Cheung's method are given in Figures 7, 8 and 9. The calculated R_S , Φ_{b0} and n values for the diodes are given in Table 1. The R_S value for the MIS diodes of 3 and 5 nm very has slightly reduced from 60 K to 400 K, and ranged from 7.26 Ω at 400 K to 6.30 Ω and 60 K for the MIS diode of 3 nm and from 8.33 Ω to 7.10 Ω for

the MIS diode of 5 nm and from 166 Ω to 111 Ω for 10 nm MIS diode, respectively. This extreme value for the MIS diode of 10 nm comes from the contribution of the HfO_2 interfacial layer and imperfect ohmic contact to the semiconductor substrate.¹²⁻²⁴

Table 1. The experimental parameters from the forward bias I - V characteristics at some measurement temperatures for the MIS diodes with different HfO_2 interfacial layer thickness fabricated by us

T (K)	3 nm Au/Ti/ n -GaAs			5 nm Au/Ti/ HfO_2 / n -GaAs			10 nm Au/Ti/ HfO_2 / n -GaAs		
	n	Φ_b (eV)	R_S (Ω)	n	Φ_b (eV)	R_S (Ω)	n	Φ_b (eV)	R_S (Ω)
400	1.03	0.99	7.26	1.04	0.94	8.33	1.20	1.06	166
300	1.09	1.02	6.76	1.09	0.93	7.98	1.06	1.00	138
200	1.25	0.89	6.70	1.24	0.78	7.81	2.20	0.90	126
60	2.72	0.40	6.30	2.58	0.37	7.10	6.88	0.20	111

**Figure 9.** $dV/d(\ln I)$ versus current plots by Cheung's Model for determining the series resistance at different temperatures for the MIS structure with 10 nm HfO_2 interfacial layer thickness.

This behavior of the R_S in high-bias region arises from strongly dependent on the semiconductor substrate mobility increasing with an increase in temperature.^{25,26} Similarly, Osvald and Horvath²⁶ have resulted from the theoretical study of the temperature dependence of Schottky diodes that the cross-point independent of measurement temperature at certain voltage depends on the doping concentrations and thickness of the doped near-surface layer of semiconductor substrate.

The BH Φ_{b0} and n calculated using Equations (1) and (2) are provide to understand the contribution from other current mechanisms through the devices such as generation recombination and tunneling. The additional contributions other than TE can cause significant

deviation in the extraction of these characteristic parameters.^{8,27}

As seen in Table 1, the BH decreased with a decrease in the temperature because the current preferentially flows through the lowest BH with a decrease in temperature due to the BH inhomogeneity.²⁷⁻³⁵ It can be seen from Figures 6 and 7 that the current value of the 5 nm MIS diode at a given bias is larger than that of the MIS diode of 3 nm up to the starting point of the downward curvature region of the I - V curve for all temperatures. The use of very thin interfacial layer increases the interfacial layer capacitance without generating excess gate current in a MOSFET and thus causes a large current through device.^{1,4-10}

As seen in Table 1, the BH values for the MIS diode of 3 nm range from 0.99 eV at 400 and 0.40 eV at 60 K, and n values range from 1.03 at 400 and 2.72 at 60 K. The BH values for the 5 nm MIS diode range from 0.94 eV at 400 and 0.37 eV at 60 K, and n values range from 1.04 at 400 and 2.58 at 60 K. Moreover, the BH values for the 10 nm MIS diode range from 1.06 eV at 400 and 0.20 eV at 60 K, and n values range from 1.20 at 400 and 6.88 at 60 K. The BH and the n values for the 10 nm MIS diode at 400 K are larger than those for the other two diodes. It can be said that the case is supplied from the more thickness interfacial layer. An increased high barrier height-diode is useful for the gates of MESFETs and can supply a sufficient barrier height for FET operation and be used in the microwave rectifier applications with the DC offset voltage.^{3-10,35} As can be seen from Figures 5 and 6, the reducing the diode current, the additional barrier increasing and the non-ideality in the forward bias I - V characteristics for the 10 nm MIS diode comes from the interface state charge change and the potential change across the interfacial layer as a result of the voltage applied.^{1-4,36}

4. CONCLUSIONS

The value of R_S has decreased with a decrease in the temperature. It has been expressed that this behavior of the series resistance arises from strongly dependent on the semiconductor substrate mobility increasing with an increase in temperature and the thickness of the counter-doped near-surface layer of semiconductor substrate. The increase in the BH due to insulating layer between metal-GaAs substrate is useful for the gates of MESFETs and can provide an adequate BH for FET operation and be used in the microwave rectifier applications with the DC offset voltage.

Conflict of interest

We declare that there is no a conflict of interest with any person, institute, company, etc.

REFERENCES

- Rhoderick, E.H.; Williams, R.H. *Metal-Semiconductor Contacts*, Clarendon Press, Oxford University Press, 1988.
- Mönch, W. *Electronics Properties of Semiconductor Interfaces*, Springer-Verlag, Berlin Heidelberg, 2004.
- Sze, S.M. *Physics of Semiconductor Devices*, Second Ed. Wiley, New York, 1981.
- Colinge, J.P., Colinge, C.A. *Physics of Semiconductor Devices*, Kluwer Academic Publishers, New York, 2002.
- Mo Wu, Alivov, Y.I.; Morkoc, H. *J. Mater. Sci-Mater. El.* **2008**, 19, 915–951.
- Missoum, I.; Ocak, Y.S., Benhaliliba, M., Benouis, C.E., Chaker, A. *Synthetic Met.* **2016**, 214, 76.
- Cheong, K.Y.; Moon, J.H.; Kim, H.J., Bahng, W.; Kim, N.K. *J. Appl. Phys.* **2008**, 103, 084113.
- Reddy, V.R.; Manjunath, V.; Janardhanam, V.; Kil, Y.H.; Choi, C-J. *J. Electron. Mater.* **2014**, 43(9) 3499.
- Turut, A. Karabulut, A.; Ejderha, K.; Bıyıklı, N. *Mater. Res. Express* **2015**, 2, 046301.
- Pan, T.M.; Lee, J.D.; Shu, W-H.; Chen, T.T. *Appl. Phys. Lett.* **2006**, 89, 232908.
- Cheung, S.K.; Cheung, N.W. *Appl. Phys. Lett.* **1986**, 49, 85.
- Kumar, R.; Chand, S. *J. Electron. Mater.* **2015**, 44(1), 194.
- E. E. Tanrıku, D. E. Yıldız, A. Günen, Ş. Altındal, *Phys. Scripta* **2015**, 90, 095801.
- Huang, W.C.; Linb, T.C.; Horng, C.T., Li, YH. *Mat. Sci. Semicon. Proc.* **2013**, 16, 418-423
- A. Gümüş and Ş. Altındal, *Mat. Sci. Semicon. Proc.* **2014**, 28, 66-71.
- Martens, K.; Wang, W.F.; Dimoulas, A.; Borghs, G.; Meuris, M.; Groseneken, G.; Maes, H.E. *Solid State Electron.* **2007**, 51, 1101.
- Korucu, D., Duman, S. *Thin Solid Films* **2013**, 531, 436.
- Jyothi, I.; Janardhanam, V.; Hong, H.; Choi, C.J. *Mat. Sci. Semicon. Proc.* **2015**, 39, 390.
- Özden, Ş.; Tozlu C.; Pakma, O. *Int. J. Photoenergy* **2016**, 2016, 6157905.
- Chen J., Wang, Lv, Q. J.; Tang H.; Li, X.; *J. Alloy. Compd.* **2015**, 649, 1220-1225.
- Guzel, A.; Duman, S.; Yıldırım, N.; Turut, A. *J. Electron. Mater.* **2016**, 45(6), 2808.
- Kaushal, P.; Chand, S. *Intern. J. Electron.* **2016**, 103(6), 937.
- Asubay, S.; Genisel M.F.; Ocak, Y.S. *Mater. Sci. Semicon. Proc.* **2014**, 28, 94.
- Zizeng, L.; Mingmin, C.; Shengkai, W.; Qi, L.; Gongli, X.; Honggang L.; Haiou, L. *J. Semicond.* 2016, 37, 026002.
- Morrison, D.J.; Wright, N.G.; Horsfall, A.B.; Johnson, C.M.; O'Neill, A.G.; Knights, A.P.; Hilton, K.P.; Uren, M.J. *Solid State Electron.* 2000, 44, 1879.
- Osvald, J.; Horvath, Zs.J. *Appl. Surf. Sci.* **2004**, 234, 349.
- Kavasoglu, N.; Kavasoglu, A.S.; Metin, B. *Mater. Res. Bull.* **2015**, 70, 804.
- Rahmatallahpur Sh.; Yegane, M. *Physica B: Conden.Matter.* **2011**, 406, 1351-1356.
- Sekhar, M.C.; Reddy, N.N.K.; Verma, V.K., Uthanna, S. *Ceram. Int.* **2016**, 42, 18870.

DOI: [10.32571/ijct.456902](https://doi.org/10.32571/ijct.456902)

E-ISSN:2602-277X

30. Sani, N.; Wang, X.; Granberg, H.; Ersman, P.A.; Crispin, X.; Dyreklev, P.; Engquist, I.; Gustafsson, G.; Berggren, M. *Sci. Rep.* **2016**, 6, 28921.

31. Duman, S.; Turgut, G.; Ozcelik, F.S.; Gurbulak, B. *Philos. Mag.* **2015**, 95, 1646-1655.

32. Deniz, A.R.; Çaldıran, Z.; Metin, Ö.; Meral, K.; Aydoğan, Ş.; *J. Colloid Interf. Sci.* **2016**, 473, 172.


33. Mönch, W. *Mat. Sci. Semicon. Proc.* **2014**, 28, 2–12.


34. Turut, A.; Ejderha, K.; Yildirim, N.; Abay, B. *J. Semicond.* **2016**, 37(4), 044001.


35. Eglash, S.J.; Newman, N.; Pan, S.; Mo, D.; Shenai, K.; Spicer, W.E.; Ponce F.A.; Collins, D.M. *J. Appl. Phys.* **1987**, 61, 5159.

36. Turut, A.; Bati, B.; Kökçe, A.; Sağlam, M.; Yalçın, N. *Phys. Scripta* **1996**, 53, 118.

ORCID

 ID 0000-0003-1694-5458 (A.Karabulut)

 ID 0000-0003-2318-9718 (I. Orak)

 ID 0000-0002-4664-4528 (A. Türüt)



Optimization of dissolution of ulexite by pure CO₂ gas in aqueous medium under pressure and production of sodium pentaborate

Veysel SELIMOGLU^{1,*}, M. Muhtar KOCAKERIM²

on the last page

¹Ministry of Environment and Urbanization, 6510, Ankara, Turkey

²Department of Chemical Engineering, Faculty of Engineering, Cankiri Karatekin University, 18100, Çankırı, Turkey

Received: 03 October 2018, Revised: 27 October 2018, Accepted: 30 October 2018

*Corresponding author e-mail: v.selimoglu@hotmail.com

Citation: Selimoglu, V. ; Kocakerim, M. M. *Int. J. Chem. Technol.* 2018, 2 (2), 123-128.

ABSTRACT

The obtain of the boron compounds from Ulexite which is one of the most important ores of Turkey is important. In this study, optimization of dissolution of ulexite by pure CO₂ was investigated in aqueous media under pressure in according to Taguchi method. Temperature, particle size, solid-to-liquid ratio, reaction time and pressure were chosen as parameters for the studies carried out in a high pressure-high temperature reactor. After dissolution experiments, optimum conditions for the dissolution of ulexite were found as 75 g/300 g water (A₁) for solid-to-liquid ratio, 15 bar (B₃) for CO₂ pressure, 80 °C (C₁) for temperature, 60 min (D₃) for time and -150µm (E₁) for particle size. The solutions obtained under optimum conditions were dried using a spray drier. Further, after the solution was concentrated, it was crystallized by cooling, and the crystals were filtered and dried. Chemical analyzes exhibited that the products obtained in both cases are sodium pentaborate (Na₂B₁₀O₁₆) with different water contents.

Keywords: Ulexite, carbon dioxide, sodium pentaborate, Taguchi method.

Basınç altında üleksitin saf CO₂ gazı ile sulu ortamda çözünürleştirilmesinin optimizasyonu ve sodyum pentaborat elde edilmesi

ÖZ

Türkiye'nin en önemli cevherlerinden biri olan Ulexitten bor bileşiklerinin elde edilmesi önemlidir. Bu çalışmada, basınç altında sulu ortamda saf CO₂ ile üleksitin çözünmesinin optimizasyonu Taguchi metoduna göre araştırıldı. Bir yüksek sıcaklık ve basınç reaktöründe gerçekleştirilen çalışmalarda sıcaklık, tane boyutu, katı/sıvı oranı, reaksiyon süresi ve basınç parametreleri olarak seçildi. Çözünme denemeleri sonunda üleksitin çözünmesi için optimum şartlar; katı/sıvı oranı için 75 g/300 g su (A₁), CO₂ basıncı için 15 bar (B₃), sıcaklık için 80 °C (C₁), süre için 60 dak (D₃) ve tane boyutu için -150 µm (E₁) olarak bulundu. Optimum şartlarda elde edilen çözeltiler bir püskürtmeli kurutucu kullanılarak kurutuldu. Ayrıca, çözelti konsantre edildikten sonra soğutulmuş kristallendirildi. Kristaller süzülde ve kurutuldu. Kimyasal analizler her iki halde de elde edilen ürünlerin farklı su içerikli sodyum pentaborat (Na₂B₁₀O₁₆) olduğunu gösterdi.

Anahtar Kelimeler: Üleksit, karbon dioksit, sodyum pentaborat, Taguchi metodu.

1. INTRODUCTION

The boron is one of the most important natural sources of Turkey. Turkey holds %73 of the world boron reserves in addition to the ore deposits of colemanite, tincal and ulexite. In Turkey, boric acid and borax hydrate are produced. Boron components have significant role in today's ultimate technologies and are

notably consumed in areas in Europe and Northern America. Ever-increasing level of use and utilization in diverse fields have further increased the importance of boron. Today, boron components plays great role in our daily life. Additionally, mankind have used boron for thousands of years without realizing it.

In some countries boric acid is produced by dissolving ulexite with sulphuric acid. Also, studies on

kinetic, optimization and mechanism of dissolution of ulexite in various acids have been performed. The dissolution kinetic of ulexite with mineral acids like H_2SO_4 , H_3PO_4 , with organic acids like acetic acid and acidic gases has been elaborated.¹⁻⁵ In addition, dissolution kinetics of ulexite mineral in some different solutions were subject to the studies.⁶⁻⁸ However, any process study that encompasses the direct production of sodium pentaborate from ulexite has been encountered so far.

Increasing uses of fossil fuels in the world causes fluctuations of CO_2 . However existing natural mechanisms remain inadequate to eliminate these emissions. In the end, this circumstance gives rise to the global warming and climate change.⁹ Carbondioxide is a gas produced by the animals in the course of the respiration through putrefaction of the biomass and benefitted by the plants during the photosynthesis. Although carbondioxide constitutes solely 0.04% of the atmosphere, it is actually one of the most important greenhouse gases. Uses of fossil fuels have been shown to be the causes of the increased concentration of carbondioxide in the atmosphere, which is believed to result in the global warming. Therefore, CO_2 emission has become a considerable environment problem. Natural balance mechanisms to dispose CO_2 emissions in the world fall short and this situation causes global warming and desertification. Hence, methods and measures to decrease the CO_2 emission should be developed. Besides, Europe and global society has made a commitment of decreased carbon future as an aim that should be achieved until the mid-century. In 2009, the European Council set a goal to reduce EU-wide greenhouse gases emission until 2050, which was around 80%-95% in the 1990s.¹⁰

Some countries and international organizations take diverse measures and develop various methods in order to reduce CO_2 emission. One of those methods is to withhold the CO_2 by natural rocks.¹¹ Many studies have been carried out regarding the retention of the CO_2 . However, in the most of these studies, acquired products subsequent to the CO_2 retention process are unvaluable;¹¹⁻¹⁴ dissolution kinetic of the lizardite - which was partly de-hydroxided with the CO_2 under unstable conditions - was examined in 30-120 °C warmth and 0,1-2 bar partial pressure conditions and a model based on surface complex formation to define specific dissolution velocities was developed.¹⁵

In this study, sodiumpentaborate, which is an important boron product, has been obtained through using ulexite ore in CO_2 retention. Sodium pentaborate is a crucial boron compound that is used in several fields particularly agriculture and yet has no production in our

country. In existing patents, this compound is obtained from boric acid and borax.¹⁶ In the present study, the optimization of dissolution of ulexite with pure CO_2 in aqueous medium and under pressure is scrutinized. Consequently, CO_2 is held in the form of Ca and $CaCO_3$ within the ulexite, and sodium pentaborate is obtained by the crystalization of the attained dissolution after concentrated.

2. MATERIALS AND METHODS

2.1. Procurement and preparation of the materials

For the study, the ulexite which was obtained from Bigadiç, Balıkesir and its XRD is given in the Figure 1 was used. 40.49% B_2O_3 , 16.6% CaO , 5.59% Na_2O , 33.81% H_2O , 1.33% MgO , 0.03% Al_2O_3 , 0.02% Fe_2O_3 , 2.11% SiO_2 and 0.02% SO_4^{2-} were found in the chemical analysis. The samples were milled with a laboratory type grinder. The milled sample was sieved to -250,-180,-150, -125, -75 ve -45 μm with standard sieves. The CO_2 gas used in the experiments has 99.9% purity grade and procured from the Linde Company.

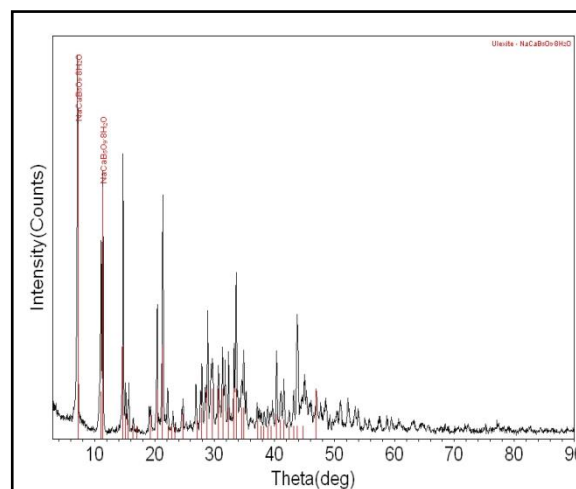


Figure 1. XRD pattern of the used ulexite.

Moreover, water-dissolving B_2O_3 , acid-dissolving B_2O_3 and humidity analyses for the solid wastes acquired by the experiment as well as B_2O_3 , CaO and MgO analyses for the solutions were conducted. Also, B_2O_3 , CaO and MgO analyses were carried out in solid products from solutions. ICP appliance was used for the CaO and MgO analyses. Humidity analyses were carried out gravimetrically while B_2O_3 analyses were volumetrically performed.

2.2. Parameters used in the experiments and their levels

The parameters used in the tests and their levels are specified according to the previously conducted pre-tests and these parameters are determined as solid-liquid ratio, pressure, particle size, temperature and time. Parameters and their levels are shown in the Table 1.

Table 1. Parameters used in experiments and their values

Parameters	Parameter Levels			
	1	2	3	4
A Solid/Liquid Ratio (g/300 g)	75	99	120	150
B Pressure (bar)	5	10	15	20
C Temperature (°C)	80	90	100	110
D Time (min)	20	40	60	90
E Particle size (µm)	-150	-125	-75	-45

2.3. Experiment design and its analysis

Along with the present study, it was aimed to determine the optimum conditions for the dissolution of ulexite with CO₂ in gas under pressure. Parameters used in the studies which were conducted with ulexite samples and CO₂ gas under pressure were pressure, temperature, solid to liquid ratio, stirring speed and time. The firstly, it was planned to examine four different level of each parameter and thereby L₁₆ (4⁵) Taguchi factorial fractional experiment design plan was used.¹⁷

2.4. Implementing dissolution experiments

During the tests, after adding 300 g water and adequate amount of ore into the reactor, the cover of the reactor was closed. Afterward, desired pressure was achieved by transferring CO₂ into the reactor through CO₂ cylinder. The reactor content was heated until the convenient temperature was reached. In the end of the test duration, the reactor was cooled, its cover was opened, solid and liquid constituents were separated by filtrating the reactor's contents. Solid waste was weighed as wet and dry and humidity content of the wet waste was detected. Later, B₂O₃ ratios that passed into the solution were calculated by means of the B₂O₃ analyses, which could be dissolved in both water and acid, carried out on the solid waste. Additionally, XRD of the solid waste was taken. Liquid part was also weighed, its density was detected and B₂O₃, CaO, MgO analyses were carried out. The reactor seen in the Figure 2, had 1 liter volume and made of stainless steel. Its operating pressure and temperature could be controlled.



Figure 2. Experiment system used in the studies under pressure.

2.5. Crystallization studies

Sodium pentaborate is extracted from the solutions that were acquired in the end of the dissolution studies. In these studies, two methods were used:

In the first method, sodium pentaborate is acquired by drying the solution obtained from the high temperature and pressure reactor in a spray drier. In this study, a spray drier, Yamato ADL311 model was used. In the other alternative, the density of the solution was brought to 1250 kg m⁻³ by evaporating and then it re-cooled down to 25°C so that the crystallization was actualized. B₂O₃, Na₂O, MgO and CaO analyses made for the solid products obtained in both methods besides the XRDs of the samples were obtained.

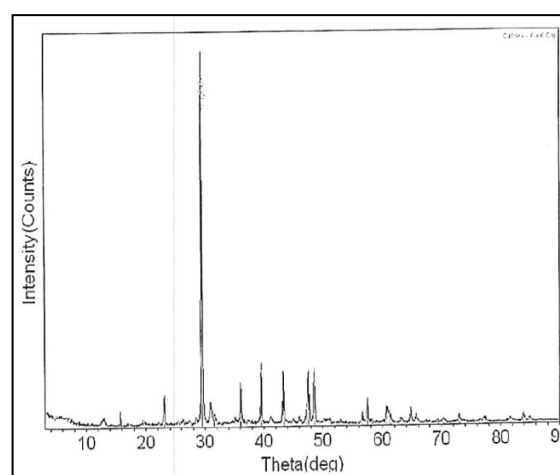


Figure 3. XRD of the solid obtained from dissolving ulexite with pure CO₂ in aqueous medium under pressure.

3. FINDINGS

3.1. Dissolving ulexite with pure CO₂ in aqueous medium under pressure

The parameters used in the tests were solid/liquid ratio (A), pressure (B), temperature (C), time (D) and particle size (E). Experimental data regarding the B₂O₃ ratios which passed into the solution by the end of the dissolution process are given in the Table 2. As can be seen on the table, all dissolution values exceeded 95%. On the other hand, the XRD of the solid waste obtained by filtration of the reaction mixture was also given in the Figure 3. Figure 3 exhibits that CaCO₃ occurred during the dissolving process.

Table 2. B₂O₃ ratios passed into the solution in dissolving the ulexite with pure CO₂ in aqueous medium and under pressure

Test No	Parameters					1. Series Experiment %	2. Series Experiment %	Average
	A	B	C	D	E			
1	1	1	1	1	1	99.8	98.93	99.3
2	1	2	2	2	2	98.87	98.96	98.9
3	1	3	3	3	3	98.83	98.80	98.8
4	1	4	4	4	4	99.43	99.24	99.3
5	2	1	2	3	4	99.35	98.81	99.0
6	2	2	1	4	3	99.05	99.00	99.0
7	2	3	4	1	2	99.12	99.03	99.0
8	2	4	3	2	1	99.31	98.28	98.8
9	3	1	3	4	2	98.38	97.63	98.0
10	3	2	4	3	1	99.08	98.31	98.7
11	3	3	1	2	4	98.62	99.19	98.9
12	3	4	2	1	3	97.90	97.58	97.7
13	4	1	4	2	3	95.08	96.94	96.0
14	4	2	3	1	4	96.75	99.15	97.9
15	4	3	2	4	1	98.74	98.79	98.7
16	4	4	1	3	2	99.39	98.97	99.1

4. RESULTS

4.1. Experimental results of ulexite dissolved with CO₂ under Pressure

4.1.1 Observed and estimated dissolved B₂O₃ amounts

It is seen that the levels of the parameters that maximize the performance statistics are, B₃, C₁, D₃ ve E₁. Using these values of the parameters, estimated values are calculated and in order to determine the confidence

interval and the adequacy of the model, two verifications experiments are conducted. The experimental results and the additional studies conducted under the optimum conditions with different parameter levels are presented in Table 3. The amount of B₂O₃ passing into the solution is estimated as 100% and measured as 97.45% at the optimum conditions.

Table 3. Estimated and observed amounts of %B₂O₃ passing into the solution

Parameters	Value	Level
Solid/liquid ratio (g/500 g)	75	1
Pressure, bar	15	3
Temperature, °C	80	1
Time, min	60	3
Particle size, µm	-150	1
Observed B ₂ O ₃ (mean value of 2 experiments) (%)	97.45	
Estimated value B ₂ O ₃ , (%)	100	
Confidence interval	100±8	

Table 4. Chemical analysis of the product from spray drier

Components, %			Impurities, ppm			
B ₂ O ₃	Na ₂ O	H ₂ O	CaO	MgO	CO ₃ ²⁻	SiO ₂
66.63	12.02	20.93	263	107	135	180

4.2. Crystallization of sodium pentaborate with the obtained solutions

In this study, the solutions obtained under pressure with CO₂ along with the solutions obtained under atmospheric pressure are used. These studies are conducted in two ways.

4.2.1. Drying of the solutions with Spray Drier

71 g of dry content out of 640 g solution is obtained in the studies conducted with 170°C inlet and 10°C outlet at constant flow rate in the spray drier. The chemical and XRD analysis of the dry content is given in Table 4 and Figure 4, respectively. Table 5 shows CaO, MgO, CO₃²⁻

and SiO₂ impurity contents are 263, 107, 135, 180 ppm, respectively. In addition to this, XRD analysis in Figure 4 shows that the product has lost its crystal structure. The 66.63% content of B₂O₃ shows that approximately 4 moles of water in Na₂B₁₀O₁₆·10H₂O is separated by the heating effect and creates an amorphous structure in Na₂B₁₀O₁₆·6H₂O.

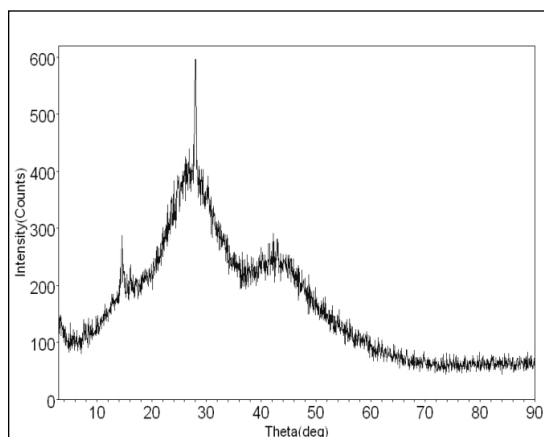


Figure 4. XRD pattern of the solid product from spray drier for the dissolution of ulexite with CO₂ under pressure in aqueous medium.

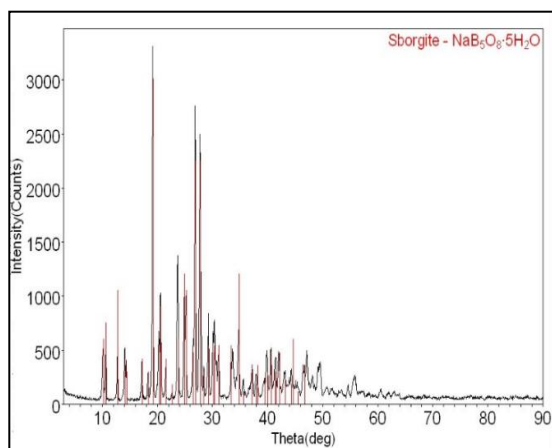


Figure 5. XRD pattern of the solid product from evaporation and then crystallization.

4.2.2. Evaporation of the solutions and crystallization from concentrated solution

In this study, 600 g of solution with 1.10 g ml⁻¹ density obtained with CO₂ under pressure is concentrated to 1.25 g ml⁻¹ and then cooled down to crystallize and the crystal solution suspension is filtered from the solution and dried.

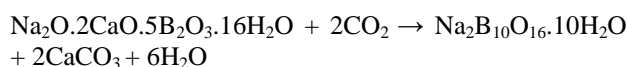
The chemical and XRD analysis of the obtained dry content is given in Table 5 and Figure 5, respectively. Table 5 shows that CaO, MgO, CO₃²⁻ and SiO₂ impurity contents are 185, 38, 114, 150 ppm, respectively. Figure 5 shows that all of the formed crystals are sodium pentaborate decahydrate. The impurity content here is lower than the ones obtained in the spray drier.

Table 5. Chemical analysis of the crystals from evaporation and then crystallization

Components, %			Impurities, ppm			
B ₂ O ₃	Na ₂ O	H ₂ O	CaO	MgO	CO ₃ ²⁻	SiO ₂
58.19	10.31	29.98	185	38	114	150

In this study, the solubility optimization and for original ulexite ore samples with different particle sizes under pressure using pure CO₂ and the production of sodium pentaborate are investigated and the following results are obtained.

The reaction between ulexite and CO₂ in the aqueous medium, which forming sodium pentaborate is as follows:



The studies in the aqueous medium under pressure result in 99% solubility. This shows that the optimum conditions to dissolve ulexite ore under pressure in aqueous medium and to produce sodium pentaborate decahydrate or other pentaborate hydrates are 75 g ulexite / 300 g water for solid / liquid ratio, 15 bars for pressure, 80 °C for temperature, 60 minutes for the time and -150 μm for the particle size. The spray drying of the solutions obtained by dissolving ulexite resulted in an amorphous sodium pentaborate in the form of Na₂B₁₀O₁₆·6H₂O, concentration of the solution at 90 °C and cooling down to 25°C resulted in sodium pentaborate decahydrate in the form of Na₂B₁₀O₁₆·10H₂O.

ACKNOWLEDGEMENTS

Authors thank to Çankırı Karatekin University for continuous motivation.

Conflict of interest

Authors declare that there is no a conflict of interest with any person, institute and company, etc.

DOI: [10.32571/ijct.467098](https://doi.org/10.32571/ijct.467098)

E-ISSN:2602-277X

REFERENCES

1. Abalı, Y.; Bayca, S. U.; Mıstıncık, E. *Physicochem. Probl. MI.* **2011**, 47, 139-148.
2. Demirkıran, A.E.; Erpek, H.; Çakır, C.; Kozacı, D.; Tunçyürek, P. *Hydrometallurgy* **2009**, 93(3-4),198-202.
3. Ekmekyapar, A.; Demirkıran, N.; Künkül, *Chem. Eng. Res. Des.* **2008**, 86, 1011-1016.
4. Tunç, M.; Yapıcı, S.; Kocakerim, M.; Yartaşı, A. *Chem. Biochem. Eng. Q.* **2001**, 15(4), 175-180.
5. Küçük, Ö.; Kocakerim, M. M.; Çopur, M.; Yartaşı, A. *Can. Metall. Quat.* **2005**, 44(1), 53-58.
6. Tekin, G. Kalsine Üleksitin Amonyum Klorür Çözeltileri İçinde Çözünürleştirilmesi Kinetiği, BAÜ Fen Bilimleri Enstitüsü Dergisi, **2004**, 6.1, 100-114 (in Turkish).
7. Künkül, A.; Demirkıran, N.; Baysar, A. *Ind. Eng. Chem. Res.* **2003**, 42 (5), 982-986.
8. Demirkıran, N. *Chem. Eng. J.* **2008**, 141, 180-186.
9. Alper, D.; Anbar, A. Küresel ısınmanın Dünya Ekonomisine ve Türkiye Ekonomisine Etkileri. Dokuz Eylül Üniversitesi Sosyal Bilimler Enstitüsü Dergisi, **2007**, 9(4), 15-54 (in Turkish).
10. <https://www.consilium.europa.eu/uedocs/cms.../110634.pdf>
11. Anonim, Chemanager Europe.October 2008, Page 29.
12. Graham, L. A.; Rideout, G.; Rosenblatt, D.; Hendren, J.. *Atmos. Environ.* **2008**, 42, 4665-4681.
13. Grande, C. A.; Rodrigues, A. E. *Int. J. Greenh. Gas Con.* **2008**, 2, 194-202.
14. Lee, S.; Filburn, T. F.; Gray, M.; Park, J. W.; Song, H. J. *Ind..Eng. Chem. Res.* **2008**, 47,7419-7423.
15. Hariharan, S.; Werner, M.; Hänchen, M.; Mazzotti, M. *Chem. Eng. J.* **2014**, 241, 314-326.
16. Çakal, G.; Çelen, E.; Soylu, F. Sodyum Pentaborat ve Üretim Yöntemi, Türk Patenti, Patent No: 2006/04991, Ulusal Bor Araştırma Enstitüsü, Ankara. 2006 (in Turkish).
17. Alsaran, A. Dupleks Yüzey İşlemi Uygulanmış AISI 5140 Çeliğinin Yapısal Mekanik ve Tribolojik Özelliklerinin Belirlenmesi. Atatürk Üniversitesi, Fen Bilimleri Enstitüsü, Makine Mühendisliği Anabilim Dalı, PhD Thesis, Erzurum. 2001 (in Turkish).

ORCID

ID 0000-0002-3375-1842 (V. Selimoglu)

ID 0000-0003-3276-6097 (M. M. Kocakerim)



Investigation of improvement of thermal and mechanical properties of polypropylene/nanoclay composites

Sameer A. AWAD*, Eman M. KHALAF

on the last page

Department of Chemistry, College of Education for Pure Science, University of Anbar, Iraq

Received: 08 October 2018, Revised: 10 November 2018; Accepted: 12 November 2018

*Corresponding author e-mail: Sameer.msc1981@gmail.com

Citation: Awad, S. A.; Khalaf, E. M. *Int. J. Chem. Technol.* 2018, 2 (2), 129-134.

ABSTRACT

This work aims to study the characterizations and modifications of systems based on polypropylene (PP) and nanoclay (NC). In this context, the effects of thermal and mechanical properties of the composites of nanoclays with different loading of 1, 3, and 6% incorporated in PP matrix were investigated. The influences of thermal and mechanical properties on the preparation of polypropylene/nanoclay (PPNC) composite were investigated. The results of the thermogravimetric analysis (TGA) showed that thermal stability increased with higher loadings of nanoclay. The tensile properties of PP and PPNC were also studied. The tensile strength of PP with the higher loading of nanoclay increased by 24.40% compared to that of the pure PP matrix (27.5MPa). The modulus of elasticity of PPNC with higher loading of 6% NC was higher by 17.32% than that of pure PP. The elongation at break of PPNC reduced by 53%, by comparing with pure PP. The Tg of PNCC with higher loading of NC were higher by 8.6%. The degree of crystallinity of PPNC was higher by 27% than pure PP.

Keywords: Polypropylene, nanoclay, composite, thermal-mechanical properties.

Polipropilen/nanokil kompozitlerinin termal ve mekanik özelliklerinin iyileştirilmesinin incelenmesi

ÖZ

Bu çalışma polipropilen (PP) ve nanokil (NK) bazlı sistemlerin karakterizasyonlarını ve modifikasyonlarını incelemeyi amaçlamaktadır. Bu bağlamda, PP matrisine katılan % 1, 3 ve 6 oranında farklı yüklemelerle nanokil kompozitlerinin termal ve mekanik özelliklerinin etkileri araştırıldı. Polipropilen/nanokil (PPNK) kompozitin hazırlanmasının üzerine termal ve mekanik özelliklerin etkileri araştırıldı. Termogravimetrik analiz (TGA) sonuçları, termal kararlılığın daha yüksek nanokil yüklenmesiyle arttığını gösterdi. PP ve PPNK'nin gerilme özellikleri de incelendi. PP'nin daha yüksek yükleme oranı ile PP'nin gerilme mukavemeti, saf PP matrisine (27,5 MPa) kıyasla % 24,40 artmıştır. Daha yüksek % 6 NK yüklü PPNK'nin esneklik modülü, saf PP'ninkinden % 17,32 oranında daha yüksekti. PPNK'nin kopma uzaması, saf PP'ye kıyasla % 53 oranında azaldı. Daha yüksek NK yüklemesiyle PPNK'nin Tg'si % 8,6 daha yüksekti. PPNK'nin kristallik derecesi, saf PP'ninkinden % 27 daha yüksekti.

Anahtar Kelimeler: Polipropilen, nanokil, kompozit, termal-mekanik özellikler.

1. INTRODUCTION

Polypropylene is an appropriate thermoplastic, and it is one of the most widely used polymers in injection-moulded products with a suitable balance between processing and performance. Also, it has been utilized widely for different applications such as packaging, technical automotive parts and compounds due to its low cost, thermal stability and corrosion resistance.¹⁻³

Fusion temperature of polypropylene is about 162-165°C and is high enough to resist hot water. It is not easy to make thermoforming. It is used highly for different applications due to its low cost, low density and high thermal stability, and corrosion resistance.⁴⁻⁶ Nanoclays consist of the nanoparticles of layered mineral silicates with layered structural units that can form complex clay crystallites.⁷⁻⁹ An individual layer unit is composed of octahedral and tetrahedral sheets. Nanoclay particle is

one of the essential nanoparticles utilized in polymeric materials as polymer nanocomposites with a wide variety. Also, the improvement of mechanical properties for thermoplastics due to the reinforcement by the clay nanolayers makes them significance to be investigated.¹⁰⁻

¹² Nanoclays have a great research interest due to its unique features which are including very high aspect ratio, and its ability to be dispersed within the polymer matrix.¹³⁻¹⁵ The thermoplastic polymer-inorganic nanocomposites have been studied abundantly, and one of the characteristics in obtaining them is that they significantly enhance the thermal and mechanical properties of the polymer.¹⁶⁻¹⁸ The influence of nanoclay additives on the properties of PP has been investigated by a few earlier studies.¹⁹⁻²⁴ Continual studies have showed the improvements in overall properties for final products of polymer reinforced nanoclay with lower contents 0.5 wt % compared to conventional composites with a large amount of micron size fillers such as wood particles, glass, and metals.²⁵ Some of the recent studies showed that polypropylene-nanoclay (PPNC) nanocomposites had gained a significant attention for their improvement on high modulus, strength, and heat resistance. The addition of nanoclay in PP and PP increases the melt flow viscosity and also enhances the improvements of the rate of crystallinity and thermal stability.²⁷ This work aims to investigate the effect of nanoclay with different concentrations on the thermal, mechanical, morphology properties of PP/nanoclay composites.

2. MATERIALS AND METHODS

2.1. Materials

Polypropylene particles were provided by Saudi Polymer Company (HGZ-120SP). Polypropylene polymer has a melt flow index of 4g·30 min⁻¹ at 237°C with the density of 0.921 g·cm⁻³. The nanoclay utilized was type Calsite 30B and was procured from Southern Clay Products (USA). Nanoclay (Calsite30B) consists of organically modified nanometer scale which layered by magnesium aluminium silicate platelets. Moisture content is ≤ 2%, particle size is about 2 μm.

2.2. PPNC preparation

The PPNC films were prepared by adding the PP with different ratios of 1, 3, and 6% of nanoclay using an internal mixer type (Haake HBI system 90, 300 cc, fill factor 0.8). Before melt mixing, the PP and the NC were preheated in a vacuum oven at 80°C for 8 hours. PP was fed into the twin screw extruder at the rate of 8 kg per hour and the NC was added regularly at the melting zone

The samples were then continuously mixed for 15 minutes at 170°C with a rotor speed of 50 rpm. The PP nanocomposite was pressed under 30 MPa at 190°C for 8 min and then cooled down at room temperature for 4 hours.

2.3. Characterization

2.3.1. DSC tests

Thermal properties were analyzed using the differential scanning calorimeter (model JADE, Perkin Elmer, USA). The weights of the samples used in this study were about ±7.9 mg. The samples were assessed with a thermal scan with temperatures from 30 to 300°C at a heating rate of 10°C·min⁻¹, under a nitrogen atmosphere. In the process, heat flow versus temperature change was monitored. The degrees of crystallinity (X_c) of PP and PPNC were calculated from the heat of fusion (ΔH_m) of the second heating cycle from the following equation:²⁸

$$X_c = \frac{\Delta H_m}{(1-\phi)\Delta H_m^0} \times 100\%$$

where, ΔH_m^0 is the fusion heat for 100% crystalline PP, which is 209 J·g⁻¹. ϕ is the weight fraction of NC filler in PPNC composites.

2.3.2. Thermal analysis

Thermogravimetric analysis (TGA) and differential thermal analysis (DTG) measurements were carried out using a Perkin-Elmer thermal analyzer (Waltham, MA, USA). The mass of the samples was between 5 to 10 mg. The samples were heated in the range 30-500°C with a flow heating rate 10°C·min⁻¹ under a nitrogen atmosphere.

2.3.3. Scanning Electron Microscopy (SEM)

Scanning electron microscopy (SEM) analyses were carried out to test the surface modification of PP and PPNC samples using SEM device (JCM-6000PLUS NeoScope). The samples were synthesized and coated with a gold coating.

2.3.4. Tensile tests

Tensile measurements of the samples were carried out at the room temperature using a device equipped with a 10 KN load cell (a Universal Instron Machine, UK. Model AT/CT M500). Dog-bone-shaped samples with overall dimensions of 16.3 × 1.9 × 0.5 cm were prepared, the tests were done according to the American Society

DOI: 10.32571/ijct.430058

E-ISSN:2602-277X

for Testing and Materials (ASTM) standard D638. Tensile tests were performed by a crosshead pulling at a rate of $2 \text{ mm} \cdot \text{min}^{-1}$ until the failure of the samples. Four samples were tested for each analysis of samples.

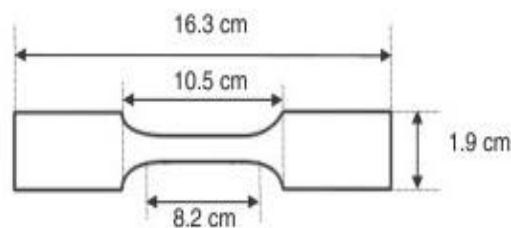


Figure. 1 The Dog-bone-shaped specimens of tensile samples.

2.3.5. Hardness test

Hardness tests were carried out using a Shimadzu testing machine (G21 series). Rockwell R method was used for the tests. Three samples with dimensions of $12.6 \text{ cm} \times 1.2 \text{ cm} \times 0.4 \text{ cm}$ were measured for each composite. The samples were dipped by utilizing a steel sphere with a load of 90 kg. The average of recorded data was stated as the Rockwell R hardness and the measurements made according to the standard ASTM E18.

3. RESULTS AND DISCUSSION

3.1. Differential Scanning Calorimetry (DSC)

Table 1 summarizes the DSC heating and cooling curves for PP and the PP/nanoclay composites. The melting temperatures of the PP composites are higher than that of pure PP (Table 1). The melting temperature with higher loading of 6% nanoclay ($172.8 \pm 0.7^\circ\text{C}$) is higher than that of pure PP ($159.5 \pm 0.8^\circ\text{C}$). The glass transition temperature (T_g) shifted toward the higher temperature with PPNC in comparison with the PP matrix. While T_g values were $63.7 \pm 0.5^\circ\text{C}$ for PP, for PP/nanoclay composites were $64.4 \pm 0.2^\circ\text{C}$, $65.1 \pm 0.3^\circ\text{C}$, and $69.2 \pm 0.2^\circ\text{C}$ with nanoclay loading 1, 3, and 6%, respectively. Furthermore, all crystallization degree of PPNC is slightly higher than that of PP. The crystallization degree with higher loading of nanoclay (6%) in PP was 48.9% once compared with PP (38.5%). Moreover, the melting temperature (T_m) values of PPNC shifted slightly toward the higher temperature, compared to that of pure PP. The crystallized temperature (T_c) of PPNC with higher loading showed a higher value ($120.6 \pm 0.8^\circ\text{C}$), compared to that of pure PP ($114.5 \pm 0.7^\circ\text{C}$). Previous study shows the glass transition temperature increases as the NC loadings increased in the PP matrix. ²⁹⁻³¹

Table 1. DSC results of all the investigated PP and PP/NC composite samples

Samples	T_g ($^\circ\text{C}$)	T_m ($^\circ\text{C}$)	T_c ($^\circ\text{C}$)	X_c %
Pure PP	63.7 ± 0.5	159.5 ± 0.8	114.5 ± 0.7	38.5
PP/1%NC	64.4 ± 0.2	162.7 ± 0.6	114.7 ± 0.5	41.2
PP/3%NC	65.1 ± 0.3	166.4 ± 1.2	120.6 ± 0.8	43.5
PP/6%NC	69.2 ± 0.2	172.8 ± 0.7	130.5 ± 1.1	48.9

3.2. Thermal analysis (TGA/DTG)

Pure PP and PP nanocomposites showed a single degradation step. The increase in thermal stability of the PP nanocomposites is occurred probably because of the presence of the nanoclay additives. TGA thermograms of pure PP and PP nanocomposites are displayed in Figure 2. The onset of degradation (T_i) gives more information according to TGA curves in Figure 2. The maximum temperature was calculated from the DTG curves in Figure 3. The summary of the thermal stability for each samples explaining the onset temperature (T_{ons}), the temperature at 50% weight loss (T_{50}), the maximum temperature (T_{max}), and residue for each sample are exhibited in Table 2.

Table 2. TGA results of PP and PP/nanosilica composites

Samples %	T_{onset} (± 0.1 $^\circ\text{C}$)	T_{50} (± 0.1 $^\circ\text{C}$)	T_{max} (± 0.1 $^\circ\text{C}$)	Residual yield %
PP	355	370	383.6	5.5
PP/1% nanoclay	368	373	385.7	6.8
PP/3% nanoclay	375	388	388.1	7.2
PP/6% nanoclay	382	391.5	390.5	9.5

The decrease in mass loss between $300\text{-}500^\circ\text{C}$ was observed with increasing the nanoclay content. The onset temperature (T_{ons}) and the maximum temperature (T_{max}) increased by 27°C and 7°C , respectively, compared to that of pure PP. The residual yield of PPNC with higher 6% NC loading was higher (9.5%) than that of lower loading of NC (1% and 3%), and pure PP that were 6.8 and 7.2%, and 5.5%, respectively. When compared to early studies that we performed on the thermal stability of PNCC, these studies showed that thermal decomposition of nanoclay incorporated in PP polymer

was shifted the decomposition to a higher temperature by comparing with PP.^{10,12,22,29,32}

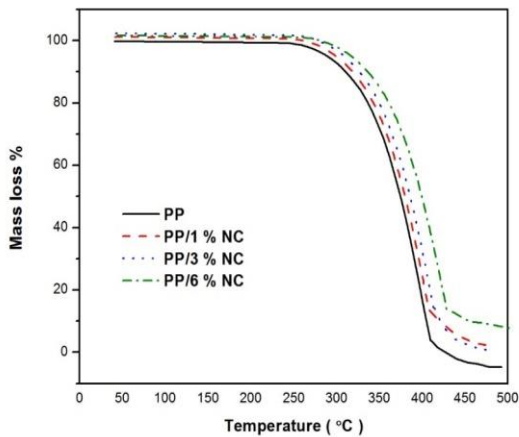


Figure 2. TGA thermograms of PP/nanoclay composites recorded at different loading ratios of 1, 3, and 6 % of nanoclays.

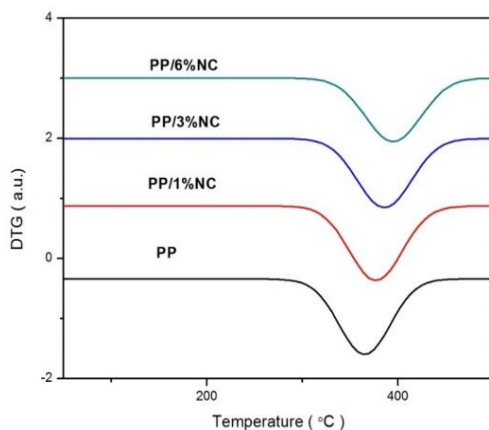


Figure 3. DTG thermograms of PP/nanoclay composites recorded at different loading ratios 1, 3, and 6 % of nanoclays.

3.3. Mechanical properties of PPNC

To further analyze the influence the content of nanoclay filler on the mechanical properties of the PP, the composite samples were tested by the tensile instruments. The summary of tensile tests for PP and PP nanocomposites is exhibited in Table 3. Accordingly, nanoclay content in PP increased tensile strength and reduced elongation at break.

The addition of nanoclay fillers of 1 wt. %, 3 wt. %, and 6 wt. % to the PP composite induced a rise in tensile strength 29.2 ± 0.2 MPa, 31.8 ± 0.4 MPa, and 34.2 ± 0.2 MPa, respectively, once compared with the tensile strength of pure PP (27.5 ± 0.3 MPa) (Table 3). The modulus increased upon nanoclay addition to the PP. The modulus with higher loading of nanoclay in PP was higher by 17.32% than pure PP. The elongation exhibited a slight reducing with nanoclay incorporated in PP. The elongation at break of PP/6% nanoclay composite was decreased by 53%, compared to that of pure PP (Table 3). The results of mechanical properties indicated that the higher dispersion with the addition of nanoclay (6 wt. %) improved the mechanical properties of the PP. The interfacial properties between PP and nanoclay fillers were enhanced in tensile strength and contributed to the slight increase in average tensile strength of their corresponded composites. As seen from Table 3, the hardness values increased by 16.2% compared to that of pure PP. Previous study on the propylene-clay nanocomposite exhibited significant improvement in the tensile properties. The improvement of tensile strength for PPNC is up to 50%.³¹

Table 3. Mechanical properties of PP and PPNC

Samples	Tensile strength MPa	Young's modulus MPa	Elongation %	Hardness
PP	27.5 ± 0.3	1480 ± 25	15 ± 1.2	66.8 ± 5.7
PP/1 % NC	29.2 ± 0.2	1510 ± 33	14.5 ± 0.9	67.6 ± 4.82
PP/3% NC	31.8 ± 0.4	1602 ± 35	12.2 ± 0.7	73.8 ± 5.92
PP/6% NC	34.2 ± 0.2	1790 ± 40	9.8 ± 0.9	79.5 ± 7.2

3.4. Morphology properties of PPNC

Figure 4a and 4b show SEM micrographs of pure PP and PPNC with 6% NC loading. Figure 4b showed that the NC with higher loading (6%) has well saturated dispersed in PP by comparing with PP matrix (Figure 6a) that exhibited little voids and nets on the surface random heterogeneous agglomerates.

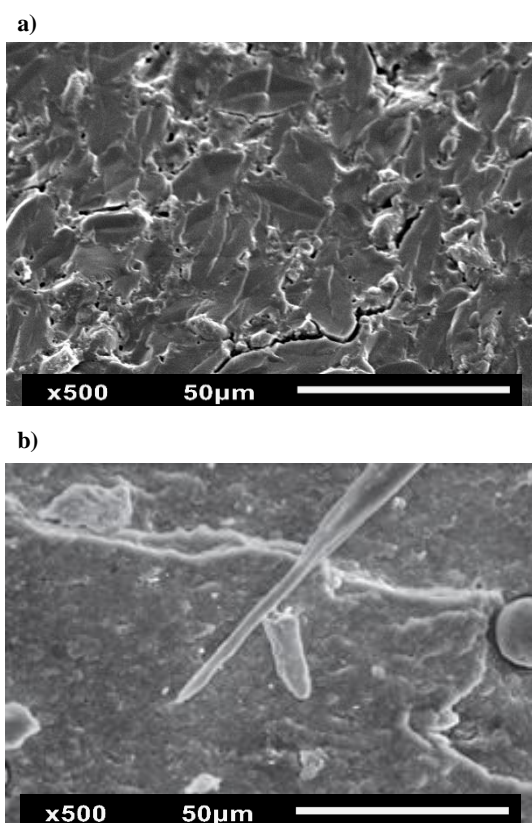


Figure 4. SEM micrographs of a) pure PP, b) PPNC with 6% NC loading.

4. CONCLUSIONS

Addition of NC to PP matrix has significant improvements in the properties of PPNC composites. The results of DSC showed that T_g of PNCC increased by 19.5%, compared to that of PP that exhibited no significant changes in T_g value and PPNC displayed the highest degree of the crystallinity (48.9%) compared to that of PP. The results of TGA displayed that the PPNC exhibited higher thermal stability as the NC loading increased in PP matrix. The maximum decomposition showed a higher resistant of thermal decomposition with a higher temperature ($390.5 \pm 0.1^\circ\text{C}$). The residual yield of PPNC (9.5%) was higher than that of pure PP (5.5%). The results of mechanical tests showed significant improvements as the NC content increased. Tensile strength and modulus of elasticity increased with the addition of nanoclay up to 6 wt%, and elongation at break reduced. The hardness of PPNC also increased with increasing nanoclay content. The morphology results showed good and homogenous dispersion on the surface of PPNC with higher loading.

Conflict of interest

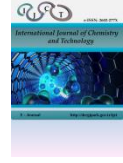
Authors declare that there is no conflict of interest to declare.

REFERENCES

- Hegde, R. R.; Bhat, G. S. *J. Appl. Polym. Sci.* **2010**, 118 (6), 3141-3155.
- Asl, D. H.; Abdouss, M.; Angaji, T. M.; Haji, A. *Chem. Ind. Chem. Eng.* **2013**, 19 (3), 441-448.
- Awad, S.; Khalaf, E. *Eng. Technol. J.* **2017**, 35, 845-848.
- Yuan, Q.; Awate, S.; Misra, R. *Eur. Polym. J.* **2006**, 42 (9), 1994-2002.
- Awad, S.; Khalaf, E. *Usak University J. Eng. Sci.* **2018**, 1 (1), 38-46.
- Hedayatnasab, Z.; Eslami-Farsani, R.; Khalili, S.; Soleimani, N. *Fiber Polym.* **2013**, 14 (10), 1650-1656.
- Khalaf, E.; Awad, S. *J. Adv. Chem.Sci.* **2017**, 3(1), 426-427.
- Komatsu, L.; Oliani, W.; Lugao, A.; Parra, D. *Radiat. Phy. Chem.* **2014**, 97, 233-238.
- Abareshi, M.; Zebarjad, S. M.; Goharshadi, E. K. *J. Vinyl. Addit. Technol.* **2016**, 22 (3), 285-292.
- Kumar, V.; Singh, A. *Rev. Chem. Eng.* **2013**, 29 (6), 439-448.
- Awad, S. A.; Khalaf, E. M. *Usak University J. Mater. Sci.* **2017**, 6 (1/2), 15-25
- Soleimani, N.; Khalili, S. M.; Farsani, R. E.; Nasab, Z. H. *J. Reinf. Plast. Compos.* **2012**, 31 (14), 967-976.
- Morales, A. R.; Paiva, L. B. d.; Zattarelli, D.; Guimarães, T. R. *Polímeros* **2012**, 22 (1), 54-60.
- Stoeffler, K.; Lafleur, P. G.; Perrin-Sarazin, F.; Bureau, M. N.; Denault, J. *Compos. A: Appl. Sci. Manufactur.* **2011**, 42 (8), 916-925.
- Awad, S. A.; Khalaf, E. M. *Bull. Mater. Sci.* **2018**, 41 (3), 67.
- Yuan, Q.; Misra, R. *Polymer* **2006**, 47 (12), 4421-4428.


17. Zhu, S.; Chen, J.; Li, H.; Cao, Y. *J. Appl. Polym. Sci.* **2013**, 128 (6), 3876-3885.
18. Khalaf, E.; Awad, S. *Int. J. Mater. Sci. Applications* **2016**, 5, 297-301.
19. Sharma, B.; Mahajan, S.; Chhibber, R.; Mehta, R. *Procedia Chem.* **2012**, 4, 39-46.
20. Picard, E.; Vermogen, A.; Gérard, J.-F.; Espuche, E. *J. Member. Sci.* **2007**, 292 (1-2), 133-144.
21. Wang, K.; Zhao, P.; Yang, H.; Liang, S.; Zhang, Q.; Du, R.; Fu, Q.; Yu, Z.; Chen, E. *Polymer* **2006**, 47 (20), 7103-7110.
22. Dimitry, O. I.; Abdeen, Z. I.; Ismail, E.; Saad, A. *J. Polym. Res.* **2010**, 17 (6), 801-813.
23. Awad, S. A.; Khalaf, E. M. *J. Thermoplast. Compos. Mater.* **2018**, 0892705718804585.
24. Xie, S.; Zhang, S.; Zhao, B.; Qin, H.; Wang, F.; Yang, M. *Polym. Int.* **2005**, 54 (12), 1673-1680.
25. Hegde, R. R.; Spruiell, J. E.; Bhat, G. S. *Polym. Int.* **2014**, 63 (6), 1112-1121.
26. Hegde, R. R.; Bhat, G. S.; Spruiell, J. E.; Benson, R. *J. Polym. Res.* **2013**, 20 (12), 323.
27. Saminathan, K.; Selvakumar, P.; Bhatnagar, N. *Polym. Test.* **2008**, 27 (3), 296-307.
28. Lertwimolnun, W.; Vergnes, B. *Polymer* **2005**, 46 (10), 3462-3471.
29. Taşdemir, M.; Caneba, G. T.; Tıwarı, R.; Wang, B. *Polymer-Plast. Technol. Eng.* **2011**, 50 (10), 1064-1070.
30. Ramsaroop, A.; Kanny, K.; Mohan, T. *Mater. Sci. Appl.* **2010**, 1 (05), 301.
31. Rane, A.; Abitha, V. *J. Mater. Environ. Sci.* **2015**, 6 (1), 60-69.
32. Fitaroni, L. B.; de Lima, J. A.; Cruz, S. A. ; Waldman, W. R. *Polym. Degrad. Stabil.* **2015**, 111, 102-108.

 ID 0000-0002-9194-719X (S. A. Awad) ID 0000-0001-7887-6158 (E. M. Khalaf)



Flow analyses of highly concentrated xanthan gum fluid

Guler Bengusu TEZEL

 at end page

Department of Chemical Engineering, Faculty of Engineering and Architecture, Bolu Abant İzzet Baysal University, 14280, Bolu, Turkey

Received: 09 October 2018, Revised: 12 November 2018; Accepted: 15 November 2018

*Corresponding author e-mail: gulerbengusutezel@ibu.edu.tr

Citation: Tezel, G. B. *Int. J. Chem. Technol.* **2018**, 2 (2), 135-140.

ABSTRACT

The concentration effect of Xanthan gum (XG) solutions (1.0, 1.5, 2.0, 2.5% w/v) on the rheological flow parameters are examined using stress controlled rheometer and gravity driven flow set-up measurement at 25°C. Concentrated XG solutions has yielding behavior obtained by fitting results through Herschel-Bulkley (HB) model with highest regression coefficient $R^2 = 0.995$ and $R^2 = 0.993$ respectively by rheometer and set-up measurement. The results agreed well each other from these measurements. Increasing the concentration of XG solutions promote dynamic and static yield stresses due to increase of entanglement structure density of XG solutions. Also, the magnitudes of consistency index, K , have increasing trend with XG concentration as a result of increasing entanglement density of XG structure. Static yield stress values are much closely dynamic stress values getting from under gravity dynamic flow indicating that supplies undisturbed molecular structure of XG due to nature of creeping flow.

Keywords: Xanthan Gum, dynamic yield stress, static yield stress, rheometer.

Yüksek derişimli ksantan gam sıvısının akış analizleri

ÖZ

Bu çalışmada, %1.0, %1.5, %2.0, %2.5 w/v derişimine sahip Ksantan gum (XG) sulu çözeltilerinin reolojik akış parametreleri 25°C de stress kontrollü rheometre ve yerçekimi güdümlü akış düzeneđi ile incelenmektedir. Akış için eşik streslerine sahip olan yüksek derişimli XG çözeltileri, reometrede $R^2 = 0.995$ ile akış düzeneđinde ise $R^2 = 0.993$ olmak üzere yüksek regresyon katsayıları ile Herschel-Bulkley akış modeline uyum göstermektedir. Ayrıca, her iki deneysel yöntem için sonuçlar birbirleri ile tutarlıdır. XG derişimi arttıkça, XG çözeltilesindeki dolanıklık yapı yoğunluğu arttığı için dinamik ve statik eşik stresleri de artmaktadır. Aynı zamanda, viskositenin ölçüsü olan, K , akış parametresi de artış göstermektedir. Yerçekimi güdümlü akış düzeneđi, çok düşük hıza sahip akış sağladığından ve de XG moleküler yapısını bozmadığından durağan eşik stres değerleri, akış düzeneđi ölçümlerinden elde edilen dinamik eşik stres değerlerine oldukça yakın bulunmuştur.

Anahtar Kelimeler: Ksantan Gam, dinamik eşik stresi, statik eşik stresi, reometre.

1. INTRODUCTION

For pipe line design considerations of non-Newtonian fluid flows, rheological investigation is a critical issue especially in getting constitutive equations for given viscosity information.^{1,2} Main difference between Newtonian and non-Newtonian fluids comes from non-linearity relation with shear rate and shear stress data.³ Hence, viscosity is variable based on applied steady shear rate on the fluid. Using a strain or stress controlled rheometer, the steady shear flow properties of solutions can be measured over a wide range of shear rates.⁴ There are many several inelastic and viscoplastic flow models

consisting yield stress parameter to get quantitative evaluation of steady shear flow of non-Newtonian flow models in the literature.⁵ Bingham, Casson, Herschel-Bulkley models are used frequently to describe the yield and viscosity behaviour of flows.⁶ For industrial applications, non-Newtonian fluids have been used widely because of their shear thinning or thickening rheological properties.⁷ Herein, Xanthan gum fluid has been chosen as a non-Newtonian fluid model for the identification of rheological parameters. Xanthan gum (XG) is a naturally occurring polysaccharide consisting primarily chain of glucose.⁸ It is used widely as a thickening and stabilizing agent especially in food and

pharmaceutical industries because of high solubility in water, low cost, biodegradable, and non-toxic.⁹ Xanthan aqueous solutions have a non-Newtonian rheology, with a shear-thinning and yielding behavior under increasing shear rate. Yielding behavior is related to the hydrogen bridging between xanthan molecules networks when mixed with water due to hydrophilic nature.^{8,9} If the applied stress reaches above the yield stress, entanglement structure is broken down and chains align through the flow generally for yielding fluids as in Figure 1.

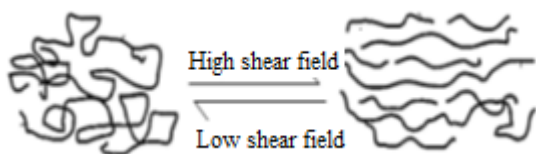


Figure 1. Non-Newtonian structure variation during the flow.

It is expected that entanglement density increases with the increased concentration of the fluid. Applied shear rate or the flow time decides the flow structure. Microstructure and rheology of XG solutions differ with respect to XG concentration. It also produces high viscosity solution with yield stress even at low concentrations.⁸ Rheological properties of XG solutions have been performed using dynamic shear tests and small amplitude oscillation test using conventional rheometers.^{10,11} However, obtained results from these conventional tests need to be verified with empirical equations.^{12,13} Analytical equations are derived from basic momentum conservation equations with pipeline design considerations based on flow profile of flowing fluid.^{13,14} The objective of the current study is to investigate the rheological flow properties as dynamic and static yield stress, consistency and flow index of highly concentrated Xanthan solutions using stress controlled rheometer and gravity driven flow set-up.

2. MATERIALS AND METHODS

2.1. Materials

The XG powders were dissolved in distilled water at 25 °C for 6 h using a magnetic stirrer with gentle shaking (400 rpm) in order to prepare 1, 1.5, 2 and 2.5% (w/v) stock solutions of XG. The solutions to be studied were left to stand overnight at 4°C to get complete hydration of XG remove the bubbles of the solutions.

2.2. Rheological and flow measurements

To get flow behavior of XG solutions, dynamic shear tests measurements were performed by a stress

controlled rheometer (Malvern Kinexus Pro, UK) fitted by a cone-and-plate system at 25°C. Diameter and angle of the cone were chosen as 40 mm and 4°, respectively. The gap between the cone-and-plate was fixed at 0.15 mm for all measurements. A peltier plate assembly was used for temperature controlling purpose during the measurements with ±0.1°C precision. Dynamic flow measurements were performed with the supply of gravity driven flow loop as in Figure 2. Test fluid was recirculated using peristaltic pump to move high concentrated XG solutions. Pressure drop was measured at the ends of the pipe with a constant length of 1.50 m using pressure transducer. To get the gravity flow, the storage tank height between 50-100 cm was also adjusted.

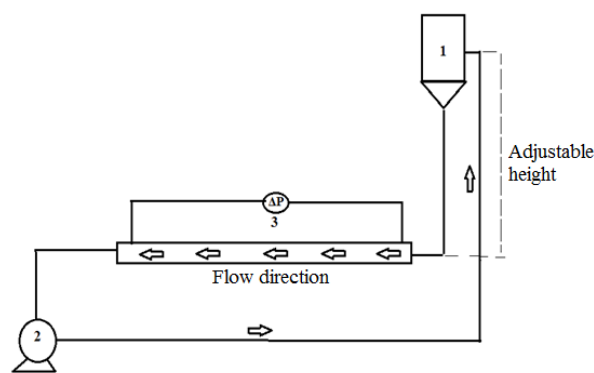


Figure 2. Flow system: 1. Storage tank, 2. Pump 3. Pressure Transducer.

2.3. Theoretical considerations of pipe flow

To evaluate shear viscosity in pipe flow, an incompressible fluid undergoes steady pressure-driven flow. There are many assumptions: laminar flow, no slip on the pipe wall, end effects are negligible.^{15,16} The conservation of linear momentum, which equates pressure forces to viscous forces, provides the relationship between the shear stress, σ , and radial position, r is as in Eq. (1).

$$\sigma(r) = \frac{-\Delta Pr}{2L} \quad (1)$$

Shear stress at the maximum at the pipe wall, radius r , $r = R$, σ_w is written as in Eq. (2);

$$\sigma_w = \frac{-\Delta PR}{2L} \quad (2)$$

To evaluate the shear rate, volumetric flow rate, Q can be given as in Eq. (3);

$$dQ = u2\pi r dr \quad (3)$$

Where u is linear velocity at r ; the total volumetric rate is found as integration of velocity over the flow area (Eq. (4));

$$Q = -\pi \int_0^R r^2 du \quad (4)$$

u can be expressed as in Eq. (5) as function of shear stress with changing radius, r ;

$$du = -f(\sigma)dr \quad (5)$$

Where r is $r = \frac{\sigma}{\sigma_w} R$ (6)

When Eq. (6) is substituted into Eq. (5), we get Eq. (7);

$$du = -f(\sigma) \frac{R}{\sigma_w} d\sigma$$

$$r^2 = \frac{\sigma^2 R^2}{\sigma_w^2} \quad (7)$$

After mathematically rearrangement, Eq. (8) is obtained as

$$Q = -\pi \int_0^{\sigma_w} \frac{\sigma^2 R^2}{\sigma_w^2} (-f(\sigma) \frac{R}{\sigma_w} d\sigma)$$

$$\frac{Q}{\pi R^3} = \frac{1}{\sigma_w^3} \int_0^{\sigma_w} \sigma^2 f(\sigma) d\sigma \quad (8)$$

According to rheological measurements, Herschel-Bulkley (HB) model gives best fit as in Eq. (9)

$$\sigma = K(\gamma^n) + \sigma_0$$

$$f(\sigma) = \gamma = \left(\frac{\sigma - \sigma_0}{K}\right)^{1/n} \quad (9)$$

After the substitution Eq. (9) into Eq. (8), Eq. (10) can be written as;

$$\frac{Q}{\pi R^3} = \frac{1}{\sigma_w^3} \int_0^{\sigma_w} \sigma^2 \left(\frac{\sigma - \sigma_0}{K}\right)^{1/n} d\sigma \quad (10)$$

When Eq. (10) is integrated over the wall stress, Eq. (11) gives volumetric flow rate;

$$Q = \left(\frac{\pi R^3}{256}\right) \left(\frac{4n}{3n+1}\right) \left(\frac{\sigma_w}{K}\right)^n \left(1 - \frac{\sigma_0}{\sigma_w}\right)^{\frac{1}{n}} \left[1 + \frac{2n}{n+1} \left(\frac{\sigma_0}{\sigma_w}\right) \left(1 + \frac{n\sigma_0}{\sigma_w}\right)\right] \quad (11)$$

If the definition of H.B model is;

$$\sigma = K\left(-\frac{du}{dr}\right)^n + \sigma_0 \quad (12)$$

The velocity profile is also found after integration of Eq. (5) over the radius yields (Eq. (13));

$$u = f(r) = \frac{2L}{\Delta P \left(1 + \frac{1}{n}\right) K^{1/n}} \left[(\sigma_w - \sigma_0)^{1 + \left(\frac{1}{n}\right)} - \left(\frac{(\Delta P)r}{2L} - \sigma_0\right)^{1 + \left(\frac{1}{n}\right)} \right] \quad (13)$$

3. RESULTS AND DISCUSSION

3.1. Steady shear measurements

Dynamic shear measurements were carried out using stress controlled rheometer (Malvern Kinexus Pro, UK). Different XG solution with 1.0, 1.5, 2.0, 2.5 w/v % concentration was processed using shear rate ramp measurements. Figure 3 depicts rheological data (shear stress and shear rate) to capture flow behavior of XG solutions over a shear rate range 0.1-100 s⁻¹ at 25°C. Plot of shear stress versus shear rate for XG solutions shows non-Newtonian behavior with yield stress due to non-linearity relation between shear stress and shear rate. The apparent shear stress values are increased with increase the XG concentration as expected.

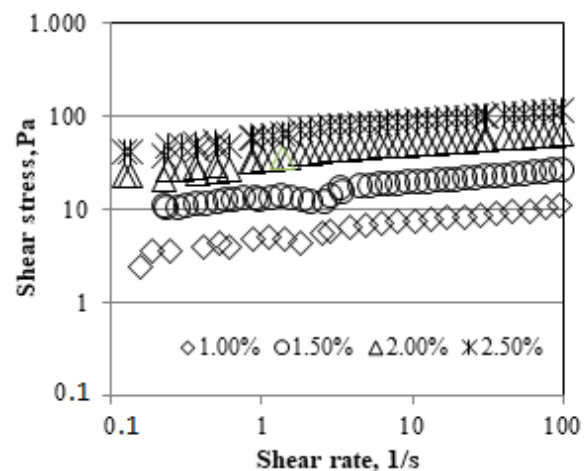


Figure 3. Experimental shear stress v.s shear rate data.

The results in Figure 3 suggest that steady properties can be modelled by Herschel-Bulkley (HB) model. The rheological model parameters predicted by HB model are listed in Table 1. The coefficient determination (R^2) is in the range of 0.985-0.995. R^2 values show that model perfectly fits to experimental data. Predicted dynamic yield stress rises with increasing XG concentrations.

Flow behavior index, n also gives the tendency of shear viscosity changing ratio with respect to shear rate. Lower n values at higher XG concentration indicate highly more non-Newtonian and shear thinning behavior of solutions.

Table 1. Fitting flow characteristics of XG solutions using rheometer

XG (w/v%)	Rheometer Measurement Results			
	Dynamic Yield Stress, σ_0 (Pa)	Consistency index, K (Pa.s ^{n})	Flow index, n	R^2
1.00%	3.842	0.5678	0.264	0.989
1.50%	5.451	1.2451	0.210	0.985
2.00%	7.656	3.2725	0.189	0.992
2.50%	9.852	5.8010	0.164	0.995

The magnitudes of consistency index, K , have increasing trend with XG concentration as a result of increasing viscosity of XG solutions. Another important parameter for yielding fluid is static yield stress value. Shear stress ramp results give static yield stress as seen in Figure 4. Static stress is which initiate the flow notations as in Figure 4 and they get higher value than the dynamic stress values as listed in Table 2. These Herschel-Bulkley flow parameters of XG solutions have similar trend as earlier reported by Bobade co-workers¹⁷ They analyzed between the range of 0.3%-0.6% (w/v) of XG solutions. Maximum dynamic yield stress was found as 1.729 Pa for 0.6% of XG solution.

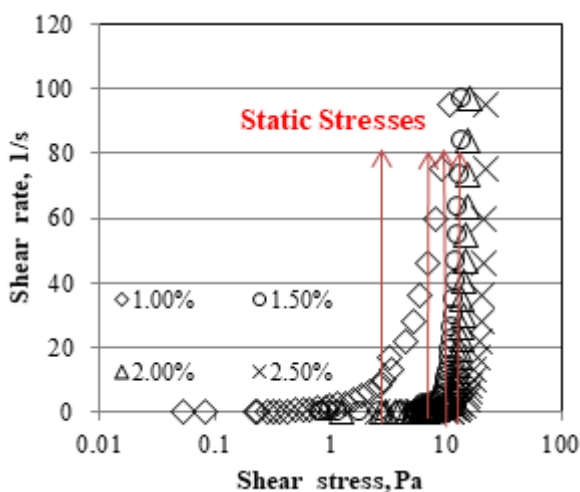


Figure 4. Static Stresses of XG solutions.

3.2. Dynamic flow measurements

In order to investigate the dynamic flow of XG solutions under gravity flow, the flow set-up were used as seen in Figure 2. By measuring volumetric flow rate

and pressure drop of XG flow and using Equations (11 and 12), wall shear stress and wall shear rate values are derived at the channel wall ($r = R$). Wall shear stress over wall shear rate gives the viscosity information of XG solutions as seen in Figure 5. For gravity flow of highly concentrated XG solutions,

Table 2. Static yield stresses of XG solutions

XG (w/v%)	Rheometer Measurement Results
	Static Yield Stress (Pa)
1.00%	4.890
1.50%	7.920
2.00%	10.123
2.50%	13.021

Table 3. Fitting flow characteristics of XG solutions using flow set-up

XG (w/v%)	Dynamic Flow Measurement Results			
	Dynamic Yield Stress, σ_0 (Pa)	Consistency index, K (Pa.s ^{n})	Flow index, n	R^2
1.00%	4.184	0.712	0.277	0.952
1.50%	6845	1.026	0.202	0.982
2.00%	9.865	4.325	0.171	0.992
2.50%	12.108	6.231	0.158	0.993

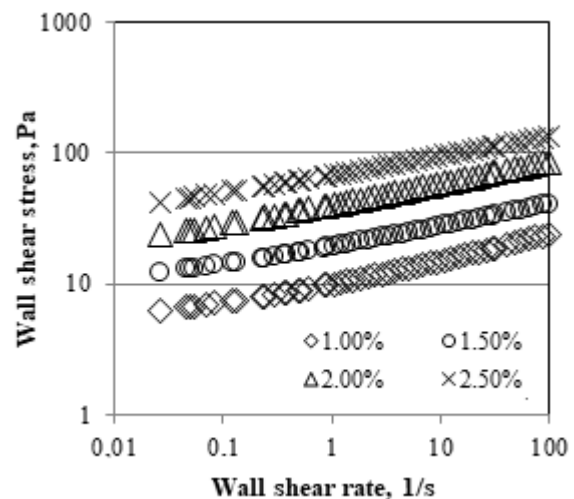


Figure 5. Wall shear stress versus wall shear rate.

Reynolds number (Re) changes the range of order 10^{-7} and 10^{-3} for this flow system. It can be said that it is creeping flow due to $Re \ll 1$. Table 3 shows fitting flow characteristics of XG solutions by using flow set-up. Herein obtained dynamic yield stress values are close to

static ones compared to the rheological results. Static yield stress emerges at the undisturbed fluid situation in such a creeping or very slow flow conditions. However, during shear test measurements, microstructure of XG solutions can be easily interrupted by increasing shear rates and so dynamic yield stress obtained from rheological measurements has lower values compared to the flow measurements. The flow curves were obtained from Eq. (13). Flow profile or flow field explains the way in which the flow of a fluid behaves or is likely to behave in a pipeline or channel based on its velocity and viscosity. The velocity profiles for the flow of non-Newtonian fluids are given as in Figure 6.

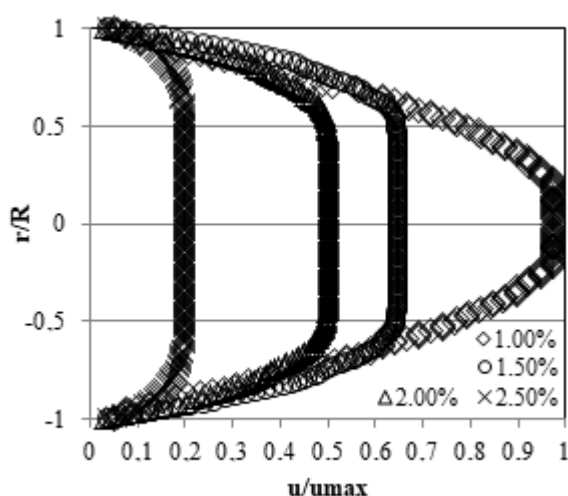


Figure 6. Laminar velocity profile of XG solutions.

These velocity profiles illustrate that with increasing the yield stress enlarges the radius of flowing down the center of pipe due to changing of viscosity variation of XG solutions. Flow profile reaches more plug-flow shape. The slope of flow curves gives the shear rate of the flow. %1 of XG solutions has more velocity changing with respect to radius at channel wall (at $r = 1$ and $r = -1$). Hence, maximum wall shear rate is achieved for 1% XG solution. Due to shear thinning nature of XG solutions, as shear rate increases, the viscosity decreases through the center of the channel. Hence, the fluid velocity profile changes over the cross section of the channel. Non-dimensional velocity (u/u_{max}) based on maximum velocity has shifted to lower values as increasing XG solutions owing to more viscous solutions as expected.

4. CONCLUSIONS

Inspection of flow behavior of highly concentrated of XG solutions is analyzed using rheometer and dynamical flow set-up measurements. Dynamic shear stress test and flow measurement results proved that dynamical and static yield stresses increased with concentration which is

an indication of more entanglement of structure of XG. The steady shear and flow experimental results are obtained by Herschel-Bulkley model with high R^2 values. Static yield stress values are found to be higher than dynamic stresses. This may be due to molecular structure deformation of XG during shear tests. On the other hand, flow measurements occurs creeping flow conditions which means undisturbed bulk flow and the dynamic yield results obtained from flow measurements are so close to static those. Further fundamental studies including highly concentrated XG systems in oscillation and creep-relaxation tests with the verification of the experimental measurements will create a part of future work.

ACKNOWLEDGEMENTS

Author is grateful to YENIGIDAM research center of Bolu Abant Izzet Baysal University (BAIBU) for supply of the rheometer and BAIBU Scientific Research Project Unit (Grant No: 2018.09.09.1316) for financial support.

Conflict of interest

Author declares that there is no a conflict of interest with any person, institute, company, etc.

REFERENCES


1. Barnes, H. A. *J. Non-Newton Fluid* **1997**, 70, 1-33.
2. Barnes, H. A.; Hutton J. F.; Walters, K. *An introduction to rheology*, Elsevier, Amsterdam, 1989.
3. Bird R.B.; Dai G.C.; Yarusso, B. J. *Rev. Chem. Eng.* **1983**, 1, 1-83.
4. Tanner, R.I. *Engineering rheology*, 2nd edn. Oxford university press, London, 2000.
5. Barnes, H.A.; Walters, K. *Rheol. Acta* **1985**, .24, 323-326,
6. Chhabra, R.P.; Richardson, J.F. *Non-Newtonian flow and applied rheology*, 2nd edn. Butterworth-Heinemann, Oxford, 2008.
7. Dullaert, K.; Mewis, J. *J. Rheol.* **2005**, 49, 1213-1230.
8. Alquraishi, A.A.; Alsewailem, F.D. *Carbohydr. Polym.* **2012**, 88, 859-863.
9. Anna, S. L.; McKinley, G.H. *J. Rheol.* **2001**, 45 (1), 115-138.

DOI: 10.32571/ijct.468529

E-ISSN:2602-277X

10. Cuvelier, G.; Launay, B. *Carbohydr. Polym.* **1986**, 6, 321-333.
11. Lim, T.; Uhl, J. T.; Prudhomme, R.K. *J. Rheol.* **1984**, 28, 367-379.
12. Nguyen, Q.D.; Boger, D.V. *Annu. Rev. Fluid* **1992**, 24, 47-88.
13. Yapici, K.; Cakmak, K. N.; Ilhan, N.; Uludag, Y. *Korea-Aust. Rheol. J.* **2014**, 26, 1-9
14. Tozzi, E.J.; Bacca, L.A.; Hartt, W.H.; McCarthy, K.L.; McCarthy M. J. *J. Rheol.* **2012**, 56, 1464-1499.
15. Callaghan, P.T. *Rep. Prog. Phys.* **1999**, 62, 599-670.
16. Bird, R.B.; Stewart, W. E.; Lightfoot, E. N. *Transport phenonema*, 1st ed., John Wiley and Sons Inc., New York, USA, 1960.
17. Bobade, V.; Cheetham, M.; Hashim, J.; Eshtiaghi, N. *Water Res.* **2018**, 134, 86-91.

 ORCID

 0000-0002-0671-208X (G. B. Tezel)



Molecular structure of Zn (II) compound containing 8-hydroxyquinoline and 2-picoline ligands [I], theoretical HF and DFT studies [II]

Kani ARICI^{1,*}, Özkan GÜL²

on the last page

¹Department of Physics, Faculty of Sciences and Arts, Kilis 7 Aralık University, Kilis, Turkey

²Anatolian High School Tatvan / Bitlis, Turkey

Received: 10 October 2018, Revised: 15 November 2018; Accepted: 16 November 2018

*Corresponding author e-mail: arici@kilis.edu.tr

Citation: Arici, K.; Gül, Ö. *Int. J. Chem. Technol.* 2018, 2 (2), 141-152.

ABSTRACT

In this study, Zn (II) compound containing 8-hydroxyquinoline (L1:8-Hq) and 2-picoline (L2: 2P) ligands was prepared and its elemental analysis was recorded. Infrared spectra of the ligands and the compound were obtained. The structure of the prepared compound was determined approximately based on the spectroscopic and analytical results. The infrared vibration frequencies of the prepared compound were calculated theoretically employing the ab-initio Hartree-Fock (HF) and density functional theory (DFT) methods with 6-311G(dp) basis set. Finally, the vibrational frequency values of the compound obtained both experimentally and theoretically were compared in details. It was observed that all the experimental and theoretical results are in good agreement with the literature.

Keywords: 8-hydroxyquinoline, 2-picoline, HF, DFT.

8-hidroksikinolin ve 2-pikolin ligandları içeren Zn (II) bileşiğinin moleküler yapısı [I], teorik HF ve DFT çalışmaları [II]

ÖZ

Bu çalışmada, 8-hidroksikinolin (L1: 8-Hq) ve 2-pikolin (L2:2P) ligandlarını içeren Zn (II) bileşiği hazırlandı ve elemental analizi yapıldı. Ligandların ve bileşiklerin infrared spektrumları elde edildi. Hazırlanan bileşiğin yapısı yaklaşık olarak spektroskopik ve analitik sonuçlara dayanarak belirlendi. Hazırlanan bileşiğin titreşim frekansları teorik olarak 6-311G (dp) temel seti ile ab-initio Hartree-Fock (HF) ve yoğunluk fonksiyon teorisi (DFT) yöntemleri kullanılarak hesaplandı. Son olarak, bileşiğin deneysel ve teorik olarak elde edilen titreşim frekans değerleri detaylı olarak karşılaştırıldı. Tüm deneysel ve teorik sonuçların literatürle iyi bir uyum içinde olduğu gözlemlendi.

Anahtar Kelimeler: 8-hidroksikinolin, 2-pikolin, HF, DFT.

1. INTRODUCTION

8-hydroxyquinoline and its derivatives are known to have activities against bacteria, fungi and amoebic¹ and they also exhibit therapeutic properties.² When 8-Hq lose a proton, they acquire the ability to compound with transition metals.³ Merrit and co-workers have investigated crystal structures of 8-Hq aqueous compounds.⁴ Magee and co-workers have obtained infrared spectra of some bivalent and trivalent metal chelate compounds of 8-Hq and they have given some vibrational modes of 8-Hq.⁵⁻⁷ Ohkaku and Nakamoto later Engelter and co-workers^{8,9} have reported the infrared spectra of $M(8-Hq)_2(H_2O)_2$ [M = Mn, Co, Zn,

Ni, Cu] compounds over the range 700-50 cm⁻¹ and they have determined the metal-ligand vibrations. Yurdakul and Arici¹⁰ have reported the IR spectra of the $M(8-HOq)_2X_2$ type complexes (where M=Zn, Co; X=Cl, Br, I and 8-HOq=8-hydroxyquinoline) and they approximated the geometric structures of the compounds via ligand and metal vibration bands.

Picoline derivatives have hypolipidemic, antineoplastic and anti-inflammatory effects. They also show activity against glioblastoma and leukemia cells.¹¹ The Picoline derivatives prepared from aminopyridine derivatives have been shown to have cholesterol lowering properties, anticancer and anti-inflammatory agents.¹²

Numerous studies have been carried out on pyridines and metal compounds of the derivatives.

Mutton and Thornton¹³ have reported the infrared spectra of $Zn(Py)_2X_2$ [$X = Cl, Br$ and I] compounds over the range $650-145\text{ cm}^{-1}$ and they have identified the metal-ligand and metal-halogen vibrations. Steffen and Palenik have determined the structure of the $Zn(Py)_2Cl_2$ (Py: pyridine) compound as tetrahedral.¹⁴ The crystal structure of $Cu(l)L_2$, ($L = 2\text{-methylpyridine}$ or 2-picoline) have been determined by single-crystal X-ray diffraction methods.¹⁵ Greenwood and Wade have prepared boron compounds with pyridine and piperidine.¹⁶ Many authors have obtained transition metal compounds with mixed ligands and studied their properties. Shaker and co-workers¹⁷ have obtained Fe(II), Co(II), Ni(II) and Cu(II) transition metal compounds with mixed 8-hydroxyquinoline and *o*-hydroxybenzylidene-1-phenyl-2,3-dimethyl-4-amino-3-pyrazolin-5-on ligands. They have used their infrared and UV-Vis spectroscopy to characterize the materials. In 2013, Kindel and co-workers¹⁸ have prepared Mn (I), Co (II), Ni (II), Cu (II), Zn (I), Cd (II), and Hg (II) compounds with 2-picoline and 8-hydroxyquinoline ligands. Using elemental analysis and M-N and M-O vibrations, they have determined the structure of the compound.

In the literature, both experimental transition metal compounds and theoretical vibrational calculations of 8-hydroxyquinoline and 2-picoline ligands have been studied. However, there is no study of mixed ligands both experimentally and theoretically. The aim of this study, for the first time, is to provide description of the molecular structure and infrared vibrations spectra of the Zn (II) compound containing 8-hydroxyquinoline and 2-picoline ligands.

2. MATERIALS AND METHODS

2.1. Experimental details

All chemical substances were purchased from Sigma Aldrich Company and used without further purification. Firstly, 1 mmol $ZnCl_2$ was dissolved in 10 ml absolute ethanol. Secondly, 2 mmol of both 8-hydroxyquinoline and 2-picoline ligands were dissolved separately in 20 ml of absolute ethanol. Finally, $ZnCl_2$ solution was added to the obtained solutions, and the mixture was stirred magnetically at room temperature for 24 hours. The precipitated complex was filtered, washed with ether and dried. The freshly prepared compound was analyzed by a Leco CHNS-932 for C, H and N and by a ICPS-OES analyzer for Zn (Table 1), but single crystal of the $ZnL^1_2L^2_2$ compound could not be obtained.

Table 1. Analytical data for the compound prepared

Compound	(%C)		(%H)		(%N)		(%Zn)	
$ZnL^1_2L^2_2$	Calculation	Found	Calculation	Found	Calculation	Found	Calculation	Found
	57.981	51.012	4.002	3.986	9.019	8.692	10.871	11.960

Infrared spectra of 8-Hq and 2P ligands and the compound ($ZnL^1_2L^2_2$) prepared were recorded between $4000-400\text{ cm}^{-1}$ and $700-30\text{ cm}^{-1}$ with ATR technical by Perkin Elmer Spectrum 400 FT-IR/FT-FIR spectrometer. In the free state, the infrared spectra of 8-Hq and 2P ligands at $4000-400\text{ cm}^{-1}$ are given in Figure 1 and 2, respectively. The infrared spectra of the prepared $ZnL^1_2L^2_2$ compound between $4000-400\text{ cm}^{-1}$ and $700-30\text{ cm}^{-1}$ are given in Figure 3 and 4, respectively. Also, the bands observed in the infrared spectrum of the 8-Hq ligand, 2P ligand and the prepared $ZnL^1_2L^2_2$ compound are given in Table 2.

2.2. Computational details

The infrared vibrations frequencies of the prepared $ZnL^1_2L^2_2$ compound were calculated quantum mechanically using the 6-311G(dp) basis set in HF and DFT methods. Therefore, the ligands and the compound were optimized using the same basis set at HF and DFT methods. Thus, our calculations make sure that there are not imaginary frequencies at the lowest energy state. In general, theoretical calculations show systematic deviations from experimental results. Therefore, all the

calculated vibrational frequencies are scaled by 0.9024 for HF/6-311G(dp) and 0.9602 for DFT/6-311G(dp) basis sets¹⁹ in order to determine the vibrational spectra of the molecule accurately. Molecular structures of $ZnL^1_2L^2_2$ compound was optimized at C_1 symmetry and was not restricted. All the calculations were performed by using Gauss View molecular visualization program²⁰ and GAUSSIAN09 program package on the personal computer.²¹ The infrared vibration frequencies obtained from the calculations and the experimental data are given in Table 3.

3. Results and discussion

3.1. Molecular structure of $ZnL^1_2L^2_2$ compound

It is known from the literature that 8-Hq and 2P ligands in a free state are linked via the N and O-H groups to form complexes with metals.

When the infrared spectrum of the prepared $ZnL^1_2L^2_2$ compound is compared with the spectra of 8-Hq and 2P ligands in the range of $4000-400\text{ cm}^{-1}$, it is observed that some bands are down or up, and some are missing or split (see Figures 1-4).

Table 2. The observed wavenumbers of the 8-hydroxyquinoline ligand, the 2-Picoline ligand and the prepared ZnL_1L_2 compound in the infrared spectrum

8-hydroxyquinoline(8-Hq)		2-Picoline (2P)		ZnL ₁ L ₂ compound		Assignment
3046	m.	3050	w. br.	3051	w. sh.	ν(C-H)
-----	-----	3012	w. sh.	-----	-----	ν(C-H)
-----	-----	2967	w.	-----	-----	ν(C-H) in CH ₃
1619	m. sh.	1590	m.	1603	m.	ν(C=N)
1576	m.	1569	m.	1577	s.	ν(C-C)
1499	s.	-----	-----	1498	s.	β(C-H)
1469	m.	1477	m.	1464	v.s.	β(C-H)
1433	m.	-----	-----	-----	-----	β(C-H)
-----	-----	1432	m.	1428	w.	Methyl As. Bending
1405	m.	-----	-----	-----	-----	β(O-H)
1375	s.	1377	w. sh.	1378	w. s.	β(C-H)
-----	-----	-----	-----	1316	w. s.	β(C-H)
1272	s.	1295	m.	1270	s.	ν(C-N)
1243	m.	-----	-----	-----	-----	ν(C-O)
-----	-----	1237	w.	1235	m.	ν(C-CH ₃)
1201	s.	-----	-----	-----	-----	β(C-H)
1138	m.	1147	m.	1137	w.	β(C-H)
1091	m.	1099	w.	1107	w. s.	ν(C-C)
1054	m.	1049	m.	1035	m.	Ring Breathing
971	m.	998	m.	972	v.w	γ(C-H)
893	m.	-----	-----	878	w. sh.	γ(C-H)
842	m. br.	-----	-----	-----	-----	-----
812	m.	806	v. w.	826	s.	γ(C-H)
-----	-----	-----	-----	790	s.	γ(C-H) + γ(C-C)
776	v.s.	750	v. s.	755	s.	γ(C-H) + γ(C-C) + γ(C-N)
738	v.s.	730	s.	734	v.s.	γ(C-H)
704	v. s.	-----	-----	-----	-----	γ(O-H)
633	m.	628	m.	646	m.	γ(C-C)
573	s.	-----	-----	589	s.	β(C-C-C)
542	m.	547	m.	553	w.	β(C-C-C)
480	m.	475	s.	484	s.	γ(C-C)
463	s.	-----	-----	-----	-----	-----
				398	br.	β ring
				364	br.	β(C-CH ₃)
				283	w.	ν(Zn-N)
				246	m.	ν(Zn-O)
				216	br. w.	ν(Zn-N)
				187	br.	2P Butterfly
				148	w.	2P Rocking
				124	m. br.	2P Rocking
				102	s.	ν(Zn-2P)
				77	m. sh.	β(Z-Zn-N)

As.: asymmetric, Br.: broad, m.: medium, s.: strong, sh.: shoulder, v.: very, w.: weak, ν: stretch, β: in plane bending, γ: out of plane bending.

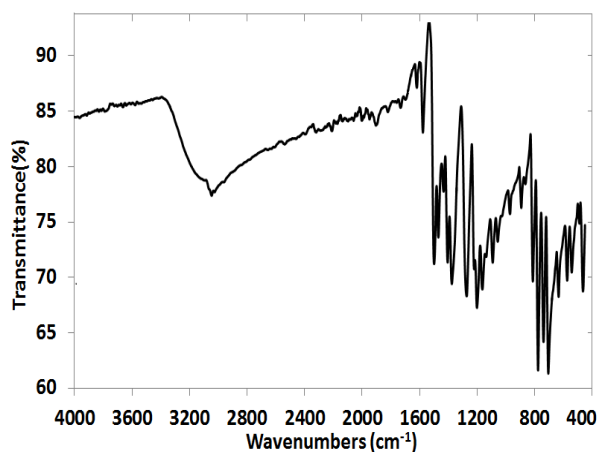


Figure 1. Infrared spectrum of 8-Hq ligand between 4000-400 cm^{-1} .

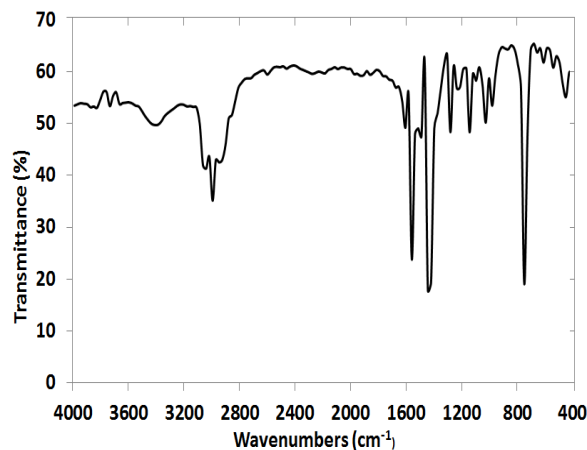


Figure 2. Infrared spectrum of 2P ligand between 4000-400 cm^{-1} .

As seen in Table 2, the C=N stretching band was observed at 1619 cm^{-1} with medium intensity for the 8-Hq ligand and at 1590 cm^{-1} with medium intensity for 2P ligand. We observed medium intensity band at 1603 cm^{-1} in the infrared spectra of the prepared $\text{ZnL}^1_2 \text{L}^2_2$ compound. This C=N stretching vibration band was observed at a frequency of 17 cm^{-1} lower than the 8-Hq ligand and at a frequency of 29 cm^{-1} higher than 2P ligand. In the literature, this C=N stretching vibration band is observed at 1630 cm^{-1} ,²² at 1600 cm^{-1} ,²³ at 1625 cm^{-1} ²⁴ for 8-Hq, at 1595 cm^{-1} ²⁵ for picoline, 1600 cm^{-1} ²⁶ for pyridine and at 1556 cm^{-1} ²⁷ for 2-aminopicoline. The C-N stretching band was observed as intensity band at 1272 cm^{-1} in the free 8-Hq ligand and as strong intensity at 1295 cm^{-1} in the free 2P ligand. We observed the C-N band at 1270 cm^{-1} in the prepared $\text{ZnL}^1_2 \text{L}^2_2$ compound. The C-N band appears to be shifted down compared to both ligands. All these shifts indicate that they are attached to the zinc atom via the nitrogen atoms in the ligands.

The C-O stretching band was observed at 1243 cm^{-1} with middle intensity in the 8-Hq ligand and at 1237 cm^{-1} with weak intensity in the 2P ligand. It is observed that this band shifted down at 1235 cm^{-1} in the prepared $\text{ZnL}^1_2 \text{L}^2_2$ compound. The C-O stretching band was also observed at 1222 cm^{-1} by Khaled and co-workers.²⁸

The O-H in-plane bending band is observed at 1405 cm^{-1} in the free 8-Hq ligand but does not appear in the spectrum of the $\text{ZnL}^1_2 \text{L}^2_2$ compound. In the literature, the OH in-plane bending band has been observed at 1407 cm^{-1} ,²⁹ 1408 cm^{-1} ³⁰ and 1380 cm^{-1} .²² Similarly the O-H out-of-plane twist band is observed to have middle intensity at 704 cm^{-1} but does not appear in the spectrum of the $\text{ZnL}^1_2 \text{L}^2_2$ compound. According to the results from the infrared spectra, it can be said that 8-Hq (L^1) ligand binds to both the N atom and the O atom of OH group and the 2P (L^2) ligand only binds to the metal from the nitrogen atom.

Metal ligand vibration bands can help determine the molecular structure around metal ions and generally, metal ligand vibrations are observed below 400 cm^{-1} in the infrared spectrum.

In this context, there are Zn-O, Zn-N₁ vibration bands for the L^1 ligand and Zn-N₂ vibration bands for the L^2 ligand below 400 cm^{-1} of the infrared spectrum of the $\text{ZnL}^1_2 \text{L}^2_2$ compound. From Table 2 and 4, it is observed that the Zn-O vibration band formed by the zinc metal with oxygen of the 8-Hq ligand at 246 cm^{-1} shows middle intensity. This band was observed at 241 cm^{-1} in an anhydrous $\text{Zn}(8\text{-Hq})_2$ compound by Engelter and co-workers⁹ and also at 315 cm^{-1} in $\text{Zn}(8\text{-Hq})_2 \text{Cl}_2$ compound with middle intensity by Yurdakul and co-workers.¹⁰ Ohkako and co-workers have observed the Zn-O band at $330\text{-}310 \text{ cm}^{-1}$ ¹⁸ in the compounds of 8-Hq ligand with Ni, Cu and Zn.

The vibration of the Zn-N bond formed by the N atom of the 8-Hq ligand with Zn atom were observed at 193 cm^{-1} by Engelter and co-workers,⁹ at 380 cm^{-1} by Mabrouk and co-workers³¹ and at 276 cm^{-1} by Yurdakul and co-workers¹⁰ with medium intensity. In this study, we observed moderate intensity of Zn-N stretch vibration band at 283 cm^{-1} .

We also observed that 2P ligand cause to Zn-N bond vibration with weak intensity at 216 cm^{-1} . This band was observed at 310 cm^{-1} by Ahmet-El-Toukhy,³² at $288\text{-}256 \text{ cm}^{-1}$ by Dimitra Kovala and co-workers³³ as in compounds made with pyridine and its derivatives at 213 cm^{-1} by Mutton and Thornton¹³ and at $222\text{-}203 \text{ cm}^{-1}$ by WLSteffen and co-workers observed.³⁴

It can be said that all the experimental values discussed above are in accordance with the literature. According to Table 1, it can be said that $\text{ZnL}^1_2 \text{L}^2_2$ compound has one Zn atom and two 8-Hq and 2P ligands. In Figure 3, it is shown that the absence of the expected O-H band at $3400\text{-}4000 \text{ cm}^{-1}$ in the infrared

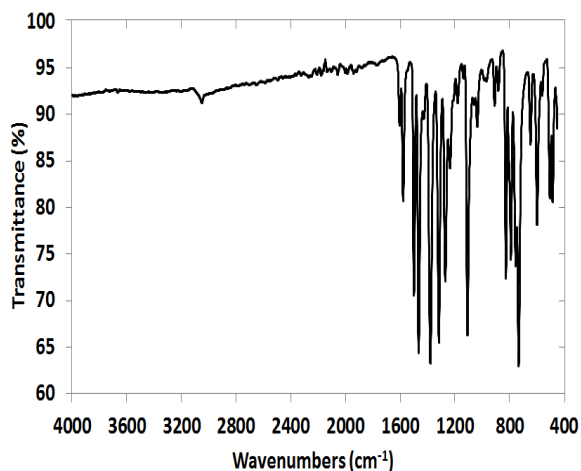


Figure 3. Infrared spectrum of $ZnL^1_2L^2_2$ compound between 4000-400 cm^{-1} .

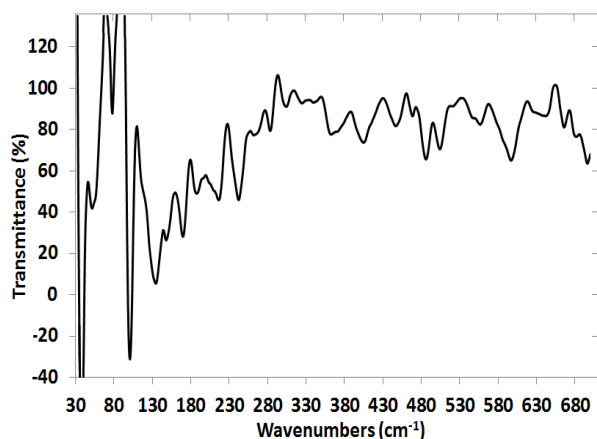


Figure 4. Infrared spectrum of $ZnL^1_2L^2_2$ compound between 700-30 cm^{-1} .

spectrum suggests that there is no water in the prepared $ZnL^1_2L^2_2$ compound. According to the Jan Teller theorem, the splitting of bands around 730 cm^{-1} and 750 cm^{-1} in the infrared spectrum of the $ZnL^1_2L^2_2$ compound indicates that the molecular geometry is slightly distorted.

According to the results obtained from the spectrum and elemental analysis, it can be deduced that $ZnL^1_2L^2_2$ compound is in a distorted octahedral structure. The molecular structure of the considered $ZnL^1_2L^2_2$ compound is given in Figure 5.

3.2. Theoretical HF and DFT calculations of the considered $ZnL^1_2L^2_2$ compound and fundamental vibrational assignments

As is known, it is difficult to make theoretical calculations of large compounds containing metals and to assign their infrared vibration bands.

The theoretically calculated number of vibrations is considerably greater than observed experimentally. This means that the compound is large and the calculations are done in gas phase. The compound does not have exact symmetry because it has a distorted octahedral structure. Thus all vibrations are active in both infrared spectroscopy and Raman spectroscopy.

Molecular symmetry was not considered in calculations. All the frequencies are assigned in terms of fundamental, overtone and combination bands. As shown in Figure 5, the compound has 63 atoms and 183 fundamental vibrations.

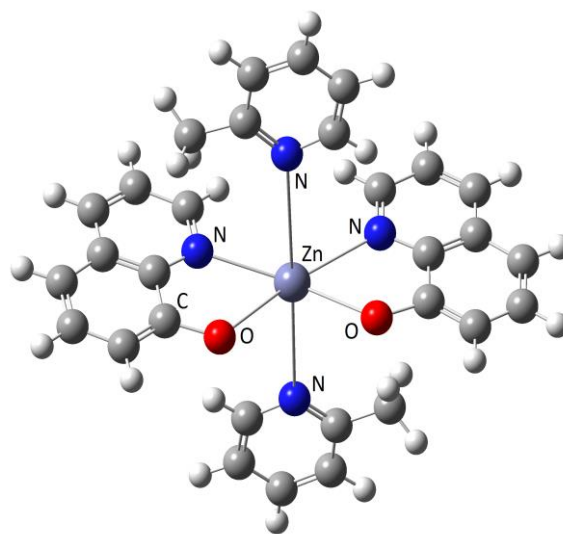


Figure 5. Molecular structure of the considered $ZnL^1_2L^2_2$ compound.

3.2.1. C-H vibrations

Usually, the bands observed in the infrared spectrum between 3000 and 3250 cm^{-1} are C-H stretching vibration bands³⁵ and they are pure. The weak band observed at 3051 cm^{-1} in the spectrum is assigned to C-H vibration band which shows good correlation with computed wave number at 3022.16 cm^{-1} by HF and at 3058.51 cm^{-1} by B3LYP methods (see Table 3).

Other the C-H stretching bands which are not visible in the infrared spectrum of the compound was calculated at (3008.20 cm^{-1} - 3087.90 cm^{-1}) at HF and (3048.82 cm^{-1} - 3121.68 cm^{-1}) at DFT as the theoretical.

In-plane and out-of-plane C-H bending vibrations are observed at 1000-1300 cm^{-1} and 950-800 cm^{-1} , respectively.³⁶⁻³⁸ We observed very strong bands at 1498 cm^{-1} and 1316 cm^{-1} in the infrared spectra of the $ZnL^1_2L^2_2$ compound and they are determined as $\beta(C-H) + \nu(C=C)$ and $\beta(C-H) + \nu(C-C)$ in Table 3. These bands arise from the coupling between the in-plane C-H bending and ring C-C stretching vibrations.

DOI: 10.32571/ijct.469000

E-ISSN:2602-277X

Table 3. The infrared vibration frequencies of $ZnL^1_2L^2_2$ compound obtained from the calculations and the experimental data, approximately assignment

No:	HF/6-311G(dp)			DFT/B3LYP/6-311G(dp)			Exp. IR (cm^{-1})	Approximately Assignment
	IR in.	(cm^{-1})	Scaled ^a	IR in.	(cm^{-1})	Scaled ^b		
1	0.021	5.04	4.57	0.023	6.50	6.28	----	Molecule Torsion
2	0.519	18.08	16.42	0.183	19.74	19.08	----	Molecule Butterfly
3	0.311	22.81	20.72	0.000	23.60	22.81	----	Molecule Torsion
4	0.002	25.26	22.94	1.083	27.45	26.54	----	Molecule Torsion
5	1.127	28.54	25.92	0.418	33.12	32.02	----	Molecule Torsion
6	0.581	32.37	29.40	0.547	33.58	32.46	----	Molecule Butterfly
7	0.069	56.46	51.29	0.616	55.44	53.60	----	Molecular Fluctuation
8	0.009	57.23	51.99	0.002	60.54	58.53	----	8Hq Fluctuation
9	9.422	61.81	56.15	0.288	69.28	66.98	----	ν (Zn-2P)
10	0.477	67.35	61.18	3.214	74.47	72.00	----	2P Fluctuation
11	1.207	75.41	68.50	0.005	77.71	75.13	----	Skeleton Vibration
12	0.015	77.05	69.99	0.248	80.96	78.28	77 m.	β (N-Zn-N)
13	0.460	97.24	88.34	0.342	97.99	94.74	----	Methyl Torsion
14	17.818	100.59	91.38	17.102	113.70	109.93	102 s.	ν (Zn-2P)
15	0.912	114.90	104.38	0.247	121.62	117.59	----	2P Waking
16	1.544	119.12	108.22	0.704	125.74	121.57	124 br.	2P Rocking
17	0.027	133.45	121.23	0.010	140.35	135.70	----	Methyl Torsion
18	2.365	134.97	122.62	6.069	142.32	137.60	----	Skeleton Vibration
19	0.028	149.37	135.70	5.543	145.30	140.49	----	Molecular Vibration
20	7.819	151.21	137.37	5.393	157.27	152.06	148 w.	2P Rocking
21	15.845	161.91	147.09	0.750	161.53	156.18	----	Fluctuation
22	0.049	186.09	169.06	0.029	182.92	176.86	----	Fluctuation
23	67.198	201.08	182.68	17.460	192.08	185.72	----	8-Hq Butterfly
24	0.007	207.40	188.42	0.160	192.81	186.42	187 br.	2P Butterfly
25	24.878	211.66	192.29	66.814	202.66	195.95	----	8-Hq Butterfly
26	1.717	233.01	211.68	1.075	210.73	203.75	----	2P Butterfly
27	7.339	234.98	213.47	5.690	221.57	214.23	----	ν (Zn-N) with 2P
28	0.532	241.50	219.40	0.362	221.90	214.55	216 w.	ν (Zn-N) with 2P
29	118.316	288.44	262.04	110.555	268.67	259.77	246 m.	ν (Zn-O) with 8Hq
30	0.113	302.31	274.64	0.232	277.62	268.43	----	ν (Zn-O) with 8Hq
31	13.540	307.72	279.56	17.366	282.72	273.36	283 w.	ν (Zn-N) with 8Hq
32	4.326	396.88	360.56	5.568	373.31	360.95	-----	ν (Zn-N) with 8Hq
33	11.147	408.71	371.31	0.088	382.76	370.09	364 br.	β (C-CH ₃)
34	0.048	409.69	372.20	11.329	386.26	373.47	----	β (C-CH ₃)
35	16.843	418.91	380.57	17.945	395.16	382.08	----	β ring
36	3.003	471.15	428.03	0.017	432.58	418.26	402 br.	γ (C-C)
37	30.748	475.38	431.88	42.649	437.96	423.46	----	γ (C-C)
38	0.071	493.29	448.15	0.049	453.08	438.08	----	γ (C-C)
39	3.101	494.71	449.44	5.161	455.17	440.10	----	γ (C-C)
40	0.000	520.14	472.54	0.000	476.97	461.18	----	γ (C-C)
41	0.382	524.58	476.58	0.059	481.75	465.80	----	γ (C-C)
42	7.326	527.94	479.63	4.643	483.23	467.23	----	γ (C-C)
43	1.592	529.60	481.14	1.405	492.60	476.29	----	β (C-C-C)
44	1.307	533.40	484.59	1.362	494.02	477.66	477 s.	β (C-C-C)
45	1.907	536.42	487.33	0.163	497.41	480.94	----	γ (C-C)
46	76.958	546.77	496.74	61.944	508.44	491.61	----	β (C-C-C)
47	1.238	550.74	500.34	0.055	513.09	496.10	----	β (C-C-C)
48	1.540	592.23	538.04	0.580	558.02	539.54	----	β (C-C-C)
49	0.602	593.44	539.14	0.127	558.53	540.04	----	β (C-C-C)
50	1.255	611.88	555.89	0.170	571.59	552.67	553 w.	β (C-C-C)
51	0.987	615.04	558.76	0.941	573.99	554.99	----	β (C-C-C)
52	14.898	659.14	598.82	0.087	603.56	583.58	589 s.	β (C-C-C)
53	6.616	662.41	601.79	0.372	603.60	583.62	----	β (C-C-C)
54	0.002	664.12	603.35	7.108	617.39	596.95	----	γ (C-C) + γ (C-N)
55	0.410	664.43	603.63	2.728	621.60	601.02	----	γ (C-C) + γ (C-N)
56	6.747	691.36	628.10	6.297	649.45	627.95	----	β (C-C-C)
57	4.653	697.96	634.09	3.270	655.01	633.32	----	β (C-C-C)
58	0.264	725.68	659.28	0.045	663.33	641.37	----	γ (C-C)

DOI: 10.32571/ijct.469000

E-ISSN:2602-277X

Table 3. Continuation

59	33.493	731.46	664.53	16.010	669.93	647.75	646 m.	$\gamma(\text{C-C})$
60	99.429	792.47	719.95	60.926	739.12	714.65	----	$\beta(\text{C-C-C})$
61	3.712	797.87	724.86	0.655	743.53	718.52	----	$\beta(\text{C-C-C})$
62	30.557	809.06	735.03	1.164	746.94	722.21	----	$\gamma(\text{C=C}) + \gamma(\text{C-N})$
63	44.465	813.16	738.75	63.609	747.50	722.75	----	$\gamma(\text{C=C}) + \gamma(\text{C-N})$
64	0.488	824.23	748.81	26.790	749.07	724.27	----	$\gamma(\text{C-H}) + \gamma(\text{C=N})$
65	98.686	824.63	749.17	40.647	752.76	727.84	734 v.s.	$\gamma(\text{C-H}) + \gamma(\text{C=N})$
66	22.443	848.13	770.52	8.254	770.48	744.97	755 s.	$\gamma(\text{C-H}) + \gamma(\text{C=C})$
67	34.820	849.12	771.42	26.449	772.71	772.71	----	$\gamma(\text{C-H}) + \gamma(\text{C=C})$
68	40.723	863.63	784.60	0.207	794.19	767.90	----	$\beta(\text{C-C-C}) + \beta(\text{N=C-C})$
69	19.221	865.69	786.47	96.071	799.62	773.15	----	$\beta(\text{C-C-C}) + \beta(\text{N=C-C})$
70	0.706	868.41	788.95	20.530	812.68	785.78	----	$\beta(\text{C-C-C}) + \beta(\text{N=C-C})$
71	0.188	871.94	792.15	12.501	814.41	787.45	----	$\beta(\text{C-C-C}) + \beta(\text{N=C-C})$
72	1.275	878.60	798.20	4.091	817.58	790.51	790 v.s.	$\gamma(\text{C-H}) + \gamma(\text{C=C})$
73	85.925	881.86	801.16	0.883	818.93	791.82	----	$\gamma(\text{C-H}) + \gamma(\text{C=C})$
74	0.3177	915.20	831.45	0.023	828.99	801.55	----	$\gamma(\text{C=C}) + \gamma(\text{C=N})$
75	63.144	916.43	832.57	31.821	831.24	803.72	----	$\gamma(\text{C=C}) + \gamma(\text{C=N})$
76	0.079	956.19	868.69	0.282	869.20	840.42	826 s.	$\gamma(\text{C-H})$
77	23.414	956.75	869.20	15.622	869.54	840.75	----	$\gamma(\text{C-H})$
78	0.156	978.56	889.02	0.619	896.07	866.41	----	$\gamma(\text{C-H})$
79	0.489	981.15	891.37	0.230	896.16	866.49	----	$\gamma(\text{C-H})$
80	0.382	981.70	891.87	0.350	916.80	886.45	878 w.	$\gamma(\text{C-H}) + \gamma(\text{C=C})$
81	0.236	987.32	896.98	0.002	919.46	889.02	----	$\beta(\text{C-C-C})$
82	0.151	1055.66	959.06	0.010	922.81	892.26	----	$\gamma(\text{C-H}) + \gamma(\text{C=C})$
83	0.337	1070.28	972.34	0.216	934.97	904.02	909 w.	$\gamma(\text{C-H}) + \gamma(\text{C=C})$
84	4.072	1073.83	975.57	0.104	974.62	942.36	----	$\gamma(\text{C-H})$
85	3.897	1078.96	980.23	0.023	975.26	942.97	----	$\beta(\text{C-N-C})$
86	18.928	1085.98	986.61	0.200	975.29	943.00	----	$\beta(\text{C-N-C})$
87	0.013	1089.62	989.91	4.912	979.65	947.22	----	$\gamma(\text{C-H})$
88	0.640	1089.67	989.96	0.004	994.16	961.25	----	Methyl Wagging
89	3.613	1091.53	991.65	1.035	994.82	961.89	962 w.	Methyl Wagging
90	0.000	1096.24	995.93	3.185	1002.34	969.16	----	$\gamma(\text{C=C})$
91	7.748	1097.82	997.36	0.460	1013.57	980.02	----	$\beta(\text{C-C-C}) + \beta(\text{C-N=C})$
92	12.078	1099.92	999.27	0.045	1014.78	981.19	----	$\beta(\text{C-C-C}) + \beta(\text{C-N=C})$
93	2.515	1102.09	1001.24	3.037	1015.47	981.85	----	$\gamma(\text{C-H})$
94	0.001	1115.54	1013.46	8.509	1028.31	994.27	----	Methyl Rocking
95	0.297	1116.22	1014.08	6.980	1035.13	1000.86	----	Methyl Rocking
96	0.017	1125.73	1022.72	0.039	1058.86	1023.81	----	$\gamma(\text{C-H})$
97	0.318	1129.41	1026.06	6.619	1066.30	1031.00	1029 m.	Ring Breathing
98	0.060	1151.65	1046.27	13.383	1068.78	1033.40	----	$\gamma(\text{C-H})$
99	13.851	1153.43	1047.89	8.954	1075.16	1039.57	----	Ring Breathing
100	2.180	1155.21	1049.50	9.732	1082.74	1046.90	----	$\gamma(\text{C-H})$
101	15.184	1158.24	1052.26	2.133	1084.14	1048.25	----	Ring Breathing
102	7.410	1167.15	1060.35	15.787	1085.28	1049.35	----	Ring Breathing
103	20.340	1169.70	1062.67	0.358	1090.08	1053.99	----	$\beta(\text{C-C-C})$
104	7.454	1175.63	1068.05	79.428	1132.13	1094.65	----	$\gamma(\text{C-H})$
105	1.570	1179.53	1071.60	9.766	1132.90	1095.40	----	$\nu(\text{C-C})$
106	18.227	1181.49	1073.38	7.907	1133.49	1095.97	----	$\beta(\text{C-H})$
107	3.852	1186.01	1077.49	5.288	1136.05	1098.44	1107w.v	$\nu(\text{C-C})$
108	133.510	1214.41	1103.29	1.572	1158.22	1119.88	----	$\beta(\text{C-C-C}) + \beta(\text{C-N=C})$
109	1.053	1215.59	1104.36	0.056	1158.95	1120.58	1129 w.	$\beta(\text{C-H})$
110	25.387	1217.18	1105.80	5.631	1179.91	1140.85	----	$\beta(\text{C-C-C}) + \beta(\text{C-N=C})$
111	5.179	1221.04	1109.31	6.609	1180.21	1141.14	----	$\beta(\text{C-H})$
112	0.514	1277.16	1160.29	16.879	1193.84	1154.32	----	$\beta(\text{C-H}) + \nu(\text{C-C})$
113	8.087	1277.89	1160.96	6.561	1194.39	1154.85	----	$\beta(\text{C-H}) + \nu(\text{C-C})$
114	27.263	1283.09	1165.68	6.306	1239.36	1198.33	----	$\nu(\text{C-C})$
115	6.504	1284.07	1166.57	0.028	1239.85	1198.81	----	$\nu(\text{C-C})$
116	0.670	1299.38	1180.48	59.906	1247.53	1206.23	1179 w.	$\beta(\text{C-H})$
117	1.026	1299.70	1180.77	13.474	1256.32	1214.73	----	$\beta(\text{C-H})$
118	96.965	1341.67	1218.90	0.512	1262.37	1220.58	----	$\beta(\text{C-H}) + \nu(\text{C-C})$
119	6.241	1351.10	1227.47	2.533	1263.34	1221.52	----	$\beta(\text{C-H}) + \nu(\text{C-C})$
120	0.696	1354.26	1230.34	0.404	1277.81	1235.51	1235 m.	$\nu(\text{C-CH}_3)$
121	0.744	1355.53	1231.49	0.702	1279.16	1236.81	----	$\nu(\text{C-CH}_3)$
122	0.323	1387.63	1260.66	16.917	1315.22	1271.68	1270 s.	$\nu(\text{C-N})$

DOI: 10.32571/ijct.469000

E-ISSN:2602-277X

Table 3. Continuation

123	10.075	1388.83	1261.75	2.134	1316.88	1273.29	-----	β (C-H)
124	20.748	1438.31	1306.70	19.705	1330.92	1286.86	-----	ν (C-N)
125	55.965	1453.34	1320.35	30.829	1346.04	1301.48	-----	ν (C-C) + ν (C-N)
126	60.476	1455.02	1321.88	77.155	1361.79	1316.71	1316 v.s.	β (C-H) + ν (C-C)
127	169.307	1459.20	1325.68	29.566	1367.61	1322.34	-----	ν (C-C)
128	153.805	1470.33	1335.79	5.524	1385.11	1339.26	-----	β (C-H)
129	7.494	1475.33	1340.33	138.363	1386.02	1340.14	-----	β (C-H)
130	187.148	1529.95	1389.95	1.396	1415.17	1368.32	-----	β (C-H)
131	0.434	1538.89	1398.08	82.227	1417.87	1370.93	-----	ν (C-C)
132	97.124	1542.13	1401.02	62.649	1425.33	1378.15	1378 v.s.	Methyl Umbrella (Sy. Bend.)
133	0.723	1553.55	1411.40	1.196	1430.57	1383.21	-----	Methyl Umbrella (Sy. Bend.)
134	41.235	1575.05	1430.93	15.828	1456.75	1408.53	-----	β (C-H)
135	2.653	1575.89	1431.69	40.227	1458.34	1410.06	-----	β (C-H)
136	14.165	1580.00	1435.43	3.352	1460.22	1411.18	-----	β (C-H)
137	18.213	1581.58	1436.86	7.627	1462.63	1414.21	-----	ν (C-N)
138	207.078	1592.14	1446.45	70.558	1464.96	1416.46	-----	ν (C-C)
139	0.042	1600.20	1453.78	0.175	1479.60	1430.62	1428 w.	ν (C=C)
140	822.243	1611.49	1464.03	641.313	1495.02	1445.53	-----	ν (C=C)
141	25.405	1616.19	1468.30	119.797	1498.73	1449.12	-----	Methyl As. Bending
142	112.106	1617.36	1469.37	34.534	1500.60	1450.93	-----	Methyl As. Bending
143	22.221	1633.17	1483.73	27.651	1514.21	1464.08	-----	Methyl As. Bending
144	27.500	1648.89	1498.01	46.694	1514.99	1464.84	1464 v.s.	Methyl As. Bending
145	183.769	1651.51	1500.39	17.476	1522.72	1472.31	-----	β (C-H) + ν (C-C)
146	9.989	1653.13	1501.86	62.992	1533.36	1482.60	-----	β (C-H) + ν (C=C)
147	21.062	1655.80	1504.29	8.173	1534.04	1483.26	1498 v.s.	β (C-H) + ν (C=C)
148	47.513	1759.16	1598.19	129.412	1601.91	1549.85	-----	ν (C=C)
149	316.464	1762.22	1600.95	2.240	1606.68	1553.49	-----	ν (C=C)
150	39.101	1764.43	1602.98	10.913	1610.59	1557.27	-----	ν (C=C)
151	6.580	1765.73	1604.16	124.586	1612.63	1559.25	-----	ν (C=N)
152	3.925	1765.93	1604.34	7.359	1613.40	1559.99	-----	ν (C=C)
153	29.491	1771.36	1609.28	11.075	1616.60	1563.09	-----	ν (C=N) + ν (C=C)
154	56.764	1796.02	1631.68	198.690	1633.99	1579.90	1577 s.	ν (C=C)
155	80.605	1796.32	1631.95	9.183	1638.89	1584.64	-----	ν (C=N) + ν (C=C)
156	26.565	1799.38	1634.73	33.845	1645.23	1590.77	-----	ν (C=C)
157	68.328	1802.88	1637.91	53.597	1648.29	1593.73	1603 m.	ν (C=N)
158	17.523	3188.44	2896.69	45.255	3038.71	2938.12	-----	Sy. ν (C-H) in methyl
159	38.174	3192.08	2900.00	12.039	3045.17	2944.37	-----	Sy. ν (C-H) in methyl
160	28.154	3256.57	2958.59	53.597	3100.30	2997.67	-----	As. ν (C-H) in methyl
161	16.636	3257.51	2959.44	45.255	3108.85	3005.95	-----	As. ν (C-H) in methyl
162	10.418	3269.24	2970.10	12.039	3117.97	3014.76	-----	As. ν (C-H) in methyl
163	0.327	3278.05	2978.10	9.858	3123.14	3019.76	-----	As. ν (C-H) in methyl
164	25.934	3311.18	3008.20	24.884	3153.16	3048.79	-----	ν (C-H)
165	8.110	3311.22	3008.24	8.458	3153.20	3048.82	-----	ν (C-H)
166	10.193	3325.55	3021.26	3.933	3162.93	3058.23	-----	ν (C-H)
167	0.713	3326.54	3022.16	1.743	3163.22	3058.51	3051 w.	ν (C-H)
168	0.278	3327.69	3023.20	6.166	3168.06	3063.19	-----	ν (C-H)
169	7.278	3329.27	3024.64	3.854	3170.18	3065.24	-----	ν (C-H)
170	1.415	3336.60	3031.30	34.854	3175.14	3070.04	-----	ν (C-H)
171	4.742	3337.40	3032.02	12.387	3178.34	3073.13	-----	ν (C-H)
172	117.183	3338.80	3033.29	43.484	3178.35	3073.14	-----	ν (C-H)
173	41.553	3346.98	3040.73	6.957	3180.78	3075.49	-----	ν (C-H)
174	16.881	3347.07	3040.81	13.836	3184.13	3078.73	-----	ν (C-H)
175	3.917	3349.62	3043.12	15.133	3186.16	3080.69	-----	ν (C-H)
176	21.744	3349.75	3043.24	16.629	3186.29	3080.82	-----	ν (C-H)
177	10.785	3350.31	3043.75	17.070	3186.73	3081.24	-----	ν (C-H)
178	12.693	3358.39	3051.09	17.843	3191.18	3085.55	-----	ν (C-H)
179	1.223	3358.58	3051.26	0.063	3194.33	3088.59	-----	ν (C-H)
180	22.350	3359.01	3051.66	10.002	3196.20	3090.40	-----	ν (C-H)
181	6.442	3370.25	3061.87	15.309	3200.34	3094.40	-----	ν (C-H)
182	30.576	3374.43	3065.66	22.335	3201.28	3095.31	-----	ν (C-H)
183	2.451	3398.91	3087.90	5.260	3228.55	3121.68	-----	ν (C-H)

As.: asymmetric, a: 0.9024, b: 0.9602 Br.: broad, m.: medium, s.: strong, sh.: shoulder, Sy.: symmetric, v.: very, w.: weak, ν : stretch, β : in plane bending, γ : out of plane bending.

This indicates that during this normal mode the total dipole moment changes substantially, and this is consistent with the large IR intensity of this mode. These in-plane C-H bending vibrations were observed at 1510 cm^{-1} for *p*-Fluorophenol-OH, at 1508 cm^{-1} for *p*-Fluorophenol-OD,³⁹ *p*-chloro and *p*-bromophenol, respectively.⁴⁰ As seen in Table 3, we observed a very intense in-plane (C-H) bending band at 1316 cm^{-1} . This band was observed weakly at 1310 cm^{-1} in the *p*-Fluorophenol-OH molecule by Zierkiewicz and Michalska.³⁹ Also, the bands observed at 1179 and 1129 cm^{-1} in the infrared spectrum of the compound were assigned as C-H in-plane bending vibrations. These observed C-H in-plane bending vibrations were calculated as 1180.48 and 1104.36 cm^{-1} via HF method, 1206.23 and 1120.58 cm^{-1} via DFT method, respectively. However, the C-H in plane bending vibrations not visible in the spectrum are theoretically calculated and given in Table 3.

The C-H out-of-plane bending vibrations are observed at 878, 826, 790, 755 and 734 cm^{-1} . While the 826 cm^{-1} band was assigned as pure, the other bands were assigned in combination with the $\gamma(\text{C}=\text{C})$ and $\gamma(\text{C}=\text{N})$ bands. These bands were calculated as 891.87, 798.20, 770.52 and 749.17 cm^{-1} via HF, 886.45, 840.42, 790.51, 744.97 and 727.84 cm^{-1} via DFT methods respectively.

According to the literature, the in-plane and out-of-plane bending vibrational frequencies have been found to be well within their characteristic regions.

3.2.2. Ring vibrations

The C=N stretching band generally seems between 1645 and 1575 cm^{-1} .⁴¹ This band has been observed at 1630 cm^{-1} ²² at 1600 cm^{-1} ²³, at 1625 cm^{-1} ²⁴ for 8-hydroxyquinoline, at 1595 cm^{-1} ²⁵ for picoline, at 1600 cm^{-1} ²⁶ for pyridine in the literature. In the spectrum of the compound we have indicated the medium intensity band at 1603 cm^{-1} as the C=N stretching vibration which calculated as 1637.91 cm^{-1} by HF and 1593.73 cm^{-1} by DFT methods. The other three C=N stretching vibrations not visible in the spectrum are calculated and given in Table 3. The C-N stretching usually lies in the region 1400–1200 cm^{-1} .⁴² The C-N stretching vibration is assigned at 1270 cm^{-1} with very strong intensity. This band is calculated as 1260.66 cm^{-1} by HF and 1271.68 cm^{-1} by DFT methods. As mentioned above, we assigned the band $\gamma(\text{C-H}) + \gamma(\text{C}=\text{N})$, which appears to be very strong at 734 cm^{-1} .

Arjuna and co-workers have observed the C=C ring stretching vibration for the 7-bromo-5-chloro-8-hydroxyquinoline and 5-aminoquinoline molecules in the range 1611 to 1412 cm^{-1} .^{43,44} The C=C stretching vibrations are assigned at 1577, 1498 and 1428 cm^{-1} with strong, very strong and weak intensity, respectively. These bands are calculated as 1631.68, 1504.29 and 1453

cm^{-1} by HF and 1579.90, 1483.26 and 1430.62 cm^{-1} by DFT method, respectively. The stretching vibrations bands for C-C bond are assigned at 1316 cm^{-1} with very strong and at 1107 cm^{-1} with weak intensity. The experimentally observed bands are found to be at 1321.88 and 1077.49 cm^{-1} via HF method and 1316.71 and 1098.44 cm^{-1} via DFT method, respectively. These theoretically calculated values are in agreement with both the intensity and the spectrum of the bands. This result is also consistent with the literature.⁴⁵ We assigned the band $\gamma(\text{C}=\text{C})$ as a combination of $\gamma(\text{C-H})$ which appears to be weak at 878, very strong at 790, strong at 755 cm^{-1} and medium at 646 cm^{-1} . In addition, the band we have observed with medium intensity at 646 and broad at 402 cm^{-1} are determined as the pure out-of-plane C-C vibration.

In the spectrum, we labeled the bands that were strong at 598, weak at 553, and strong at 477 cm^{-1} as $\beta(\text{C-C-C})$ in-plane angle bending. These bands are calculated at 598.82, 555.89 and 484.59 cm^{-1} by HF and 583.58, 552.62 and 477.66 cm^{-1} by DFT method, respectively. This result is in consistent with the literature.⁴⁴

We observed a medium intensity band at 1029 cm^{-1} and assigned the band as ring breathing. This band is calculated at 1026.06 cm^{-1} by HF and 1031.00 cm^{-1} by DFT method and it is in consistent with the literature.⁴⁶

3.2.3. Methyl group vibrations

The CH_3 methyl group is known to have nine types of vibrations. These are one symmetric stretch, two asymmetric stretches, one symmetrical bending, two asymmetric bendings, two rocks and one torsion vibration. Symmetrical and asymmetric vibrations in the methyl group are observed in the range of 3000-2900 cm^{-1} . Symmetrical and asymmetric bending vibrations are observed in the range of 1465-1370 cm^{-1} and rocking vibrations are observed in the range of 1040-990 cm^{-1} .²⁵ Symmetrical and asymmetric stretching vibrations frequencies are not observed in the infrared spectra but asymmetric bending modes at methyl CH_3 are assigned at 1464 cm^{-1} to be very strong. The experimentally observed band is found at 1504.29 cm^{-1} via HF and 1483.26 cm^{-1} via DFT method. The methyl symmetric bending vibration is obtained at 1378 cm^{-1} with very strong intensity. We calculated this band at 1401.02 cm^{-1} with HF and at 1378.15 cm^{-1} with DFT method. In this study, we could not observe the methyl rocking and methyl torsion vibrations, but we observed the methyl wagging vibration at 962 cm^{-1} with weak intensity. We also observed the stretching vibration between the methyl groups and the ring as a broad band at 364 cm^{-1} . It is calculated as 371 cm^{-1} , 370.09 cm^{-1} with HF and DFT methods, respectively. These values are given in Table 3. It can be said that the assignments made for methyl are in good agreement with the literature.

3.2.4. Zn-N, Zn-O and other vibrations

As mentioned above, these vibration bands are assigned in more detail in Table 3. The Zn-N stretching band between the zinc atom and the nitrogen atom in 8-Hq was calculated at 279.56 cm^{-1} with HF method and 273.36 cm^{-1} with DFT method. Also, the band between the zinc atom and the nitrogen atom in 2P was calculated at 219.40 cm^{-1} with HF method and 214.55 cm^{-1} with DFT method. Zn-O bands between 8-hq ligand and zinc

were calculated as 274.64 cm^{-1} and 262.04 cm^{-1} with HF and 259.77 cm^{-1} and 268.43 cm^{-1} with DFT methods.

We observed a broad band at 364 cm^{-1} and assigned the band as $\beta(\text{C-CH}_3)$. This broad band observed at 187 cm^{-1} was assigned as a butterfly of the 2P ligand. The weak band observed at 148 cm^{-1} and broad band at 124 cm^{-1} were assigned as a rocking of the 2P ligand. In addition, the bands observed at 102 cm^{-1} and 77 cm^{-1} in the spectrum were assigned as $\nu(\text{Zn-2P})$ and $\beta(\text{N-Zn-N})$ vibrations, respectively. Table 3 shows that these observed bands are in good agreement with the calculations.

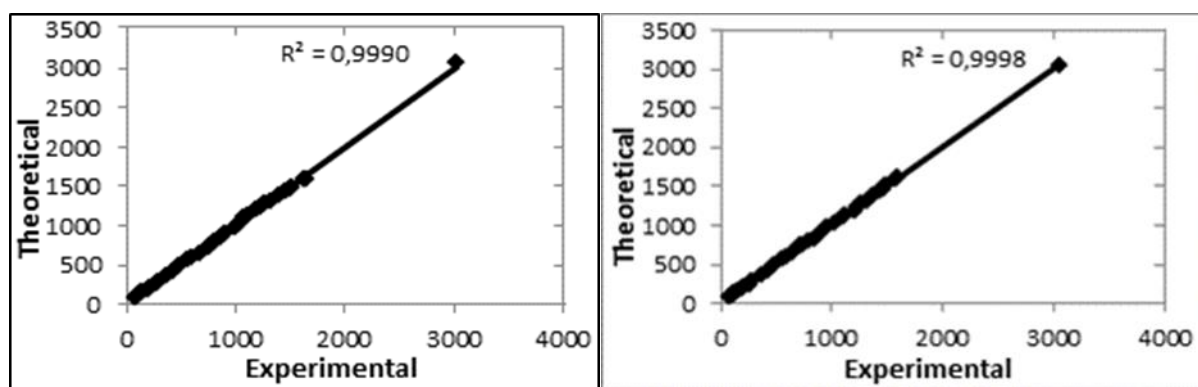


Figure 6. Correlation graphs of theoretical and experimental vibration frequencies.

Correlation diagrams for comparison of the experimental and theoretical infrared vibration frequencies of the prepared $\text{ZnL}^1_2\text{L}^2_2$ compound are shown in Figure 6.

As can be seen from Figure 6, the experimental vibration frequencies are in better agreement with the scaled vibration frequencies and are found to have a better correlation for DFT/B3LYP/6-311G(dp) than and HF/6-311G(dp).

4. CONCLUSIONS

The structure of the prepared $\text{ZnL}^1_2\text{L}^2_2$ compound was determined with the help of analyzing C, H, N and Zn via observed infrared spectra. The geometry of $\text{ZnL}^1_2\text{L}^2_2$ compound were optimized using the HF and DFT/B3LYP methods with 6-311G(dp) basis set. Then, using this optimized data, the vibration frequencies of the compound were calculated and compared with the experimental values one by one. It has been shown that the results are in perfect agreement and these results are supported by correlation graphics.

ACKNOWLEDGEMENTS

In this study, we used the Gaussian09 program which was obtained from the BAP project number 2010/02/08 supported by Kilis 7 Aralık University.

Conflict of interest

We declare that there is no a conflict of interest with any person, institute, company, etc.

REFERENCES

- Bambury, R. E.; Wolff, M. E. *Burger's Medicinal Chemistry, Part II*, John Wiley, (New York), 1979, p 41.
- Buchmann, G.; Proffit, E.; *Arzneimittelforsch*, **1960**, 10, 181.
- Hamada, Y.; Sano, T.; Fijujita, M.; Fujii, Y.; Nishio, Y.; Shibata, K. *Jpn. J. Appl. Phys.* **1993**, 32, L512.

DOI: [10.32571/ijct.469000](https://doi.org/10.32571/ijct.469000)

E-ISSN:2602-277X


4. Merritt, L. L. *Anal. Chem.* **1953**, 25, 718-721.
5. Magee, R. J.; Gordon, L. *Talanta* **1963**, 10 (8), 851-859.
6. Magee, R. J.; Gordon, L. *Talanta* **1963**, 10 (9), 961-966.
7. Magee, R. J.; Gordon, L. *Talanta* **1963**, 10 (9), 967-970.
8. Ohkaku, N.; Nakamoto, K. *Inorg. Chem.* **1971**, 10 (4), 798-805.
9. Engelter, C.; Jackson, G. E.; Knight, C. L.; Thornton, D. A. *J. Mol. Struct.* **1989**, 213, 133-144.
10. Yurdakul, Ş.; Arıcı, K. *J. Mol. Struct.* **2004**, 691 (1-3), 45-49.
11. Das, M. K.; Maiti, P. K.; Roy, S.; Mittakanti, M.; Morse, K. W.; Hall, I. H. *Arch. Pharm-Weinheim.* **1992**, 325 (5), 267-272.
12. Saravanan, S. P.; Sankar, A.; Parimala, K. *IJSRM*, **2017**, 7 (3), 74-82.
13. Mutton, A. T.; Thornton, D. A. *Spectrosc. Lett.* **1977**, 10 (1), 57-65.
14. Steffen, W. L.; Palenik, G. J. *Acta Cryst.* **1976**, B32, 298-302.
15. Healy, P. C.; Pakawatchai, C.; White, A. H. *J. Chem. Soc. Dalton Trans.* **1983**, 9, 1917-1927.
16. Greenwood, N. N.; Wade, K. *J. Chem. Soc.* **1960**, 1130-1141.
17. Shayma, A. S.; Farina, Y.; Salleh, A. A. *Euro. J. Sci. Res.* **2009**, 33 (4), 702-709.
18. Kindeel, A.S.; I.; Dawood, I. J.; Aziz, M. R. *Baghdad Sci. J.* **2013**, 10, 396-403.
19. Irikura, K. K.; Johnson, R. D.; Kacker, R. N. *J. Phys. Chem.* **2005**, A 109 (37), 8430-8437.
20. Frisch, A.; Nielsen, A. B.; Holder, A. J. *Gauss 09 View User Manual (Pittsburg: Gaussian Inc.)* 2009.
21. Frisch, M.J et al, GAUSSIAN 09: Revision C.02 (Pittsburg, PA: Gaussian Inc.) 2009.
22. Ramakrishnan, L.; Soundararajan, S. *Indian. Acad. Sci.* **1977**, 86A, 59-64.
23. Krishnakumar, V.; Ramasamy, R. *Spectrochim. Acta* **2005**, 61 (4), 673-683.
24. EI-Asmy, A.A.; EI-Sonbati, A.Z., Ba-Issa, A.A. *Transit. Metal Chem.* **1990**, 15, 222-225.
25. Arenas, J.F.; Tocon, I.L.; Otero, J.C.; Marcos, J.I. *J. Mol. Struct.* **1997**, 410-411, 443-446.
26. Greenwood, N.N.; Wade, K. *J. Chem. Soc.* **1960**, 1130-1141.
27. Sujin, P.J.; Mohan, S.; *Spectrochim. Acta* **2006**, 64 (1), 240-25.
28. Bahgat, K.; Ragheb, A. G. *Cent. Eur. J. Chem.* **2007**, 5 (1), 201-220.
29. Srivastava, S.L.; Rohitashava, M.P. *Spectrochim. Acta* **1984**, 40 (7), 681-685.
30. Arıcı, K.; Yurdakul, M.; Yurdakul, S. *Spectrochim. Acta* **2005**, 61 (1-2), 37-43.
31. Mabrouk, H.E.; EI-Asmy, A.A.; Mounir, M. *Transit. Metal Chem.* **1993**, 18 (6), 573-575.
32. El Toukhy, A. *Qatar Univ. Sci. Bull.* **1990**, 10, 83-97.
33. Kovala-Demertzi, D.; Yadav, P. N.; Wiecek, J.; Skoulika, S.; Varadinova, T.; Demertzis, M. *A. J. Inorg. Biochem.* **2006**, 100 (9), 1558-1567.
34. Steffen, W. L.; Palenik, G. J. *Inorg. Chem.* **1977**, 16 (5), 1119-1127.
35. Sharma, A.; Gupta, V.P.; Viridi, A. *IJPAP*, **2004**, 42, 251-257.
36. Krishnakumar, V.; Prabavathi, N. *Spectrochim. Acta* **2008**, 71 (2), 449-457.
37. Altun, A.; Golcuk, K.; Kumru, M. *J. Mol. Struct. THEOCHEM.* **2003**, 637 (1-3), 155-169.
38. Singh, S. J.; Pandey, S. M. *Indian J. Pure Ap. Phy.* **1974**, 12, 300-304.
39. Zierkiewicz, W.; Michalska, D. *J. Phys. Chem. A.* **2003**, 107, 4547-4554.
40. Zierkiewicz, W.; Michalska, D.; Zeegers-Huyskens, T. *J. Phys. Chem. A.* **2000**, 104 (50), 11685-11692.
41. Gunasekaran, S.; Natarajan, R.K.; Syamala, D.; Rathikha, R. *Indian J. Pure Ap. Phy.* **2006**, 44 (04), 315-319.


DOI: [10.32571/ijct.469000](https://doi.org/10.32571/ijct.469000)

E-ISSN: [2602-277X](https://www.issn.org/issn/2602-277X)

42. Prabhakaran, M.; Prabakaran, A.R.; Srinivasan, S.; Gunasekaran, S. *Spectrochim. Acta* **2015**, 138, 711-722.
43. Arjunan, V.; Mohan, S.; Ravindran, P.; Mythili, C. V. *Spectrochim. Acta* **2009**, 72 (4), 783-788.
44. Arjunan, V.; Mohan, S.; Balamourougane, P.S.; Ravindran, P. *Spectrochim. Acta* **2009**, 74, 1215-1229.
45. Srivastava, A.; Singh, V. B. *Indian Pure Appl. Phys.* **2007**, 45, 714-720.
46. Varsányi G. *Vibrational spectra of benzene derivatives*, Academic Press New York and, London, 1969, P. 215.

[ORCID](https://orcid.org/)


 ID 0000-0001-7947-0766 (K. Arıcı)

 ID 0000-0001-7204-7957 (Ö. Gül)



Determination of aflatoxin and some trace element contents in black pepper samples

Fevzi KILIÇEL^{*1}, Hacer Sibel KARAPINAR²

 on the last page

¹Department of Chemistry, Kamil Özdağ Sciences Faculty, Karamanoğlu Mehmetbey University, Karaman, Turkey

²Scientific and Technological Research Center, Karamanoğlu Mehmetbey University, Karaman, Turkey

Received: 26 September 2018, Revised 26.11.2018, Accept: 29.11.2018

*Corresponding author e-mail: fevzi@kmu.edu.tr

Citation: Kılıçel, F.; Karapınar, H. S. *Int. J. Chem. Technol.* 2018, 2 (2), 153-160.

ABSTRACT

Concentrations of the total aflatoxin (AF), aflatoxin G1 (AFG1), aflatoxin G2 (AFG2), aflatoxin B1 (AFB1), aflatoxin B2 (AFB2) and some trace elements such as lead, cobalt, nickel, arsenic, copper, zinc, manganese, magnesium, iron, calcium and chromium in black pepper samples were determined. Four black pepper samples were collected from markets in Karaman/Turkey. Detection of toxins were performed using HPLC instruments after pre-separation using immunoaffinity columns working through a solid phase extraction. The heavy metal contents in black peppers were determined by flame atomic adsorption methods. Also, quantities of trace elements were determined in 4 samples collected during summer and winter months. The total AF was determined below the maximum limits in pepper samples. Quantities of Co, Ni, Cr, Cu, Zn, Pb, Mn, Fe, Mg and Ca were detected in the samples. When the results were evaluated, the values found for Cu, Zn and Mg were seen to be at normal levels. Co, Ni, Cr, Pb, Mn, Fe, Ca trace element concentrations were obtained above the normal limit but Co, Pb and Mn were found below the toxic limits.

Keywords: Aflatoxin, heavy metals, HPLC, FAAS.

Karabiber örneklerinde aflatoksin ve bazı eser element içeriklerinin belirlenmesi

ÖZ

Karabiber örneklerinde toplam aflatoksin (AF), aflatoksin G1 (AFG1), aflatoksin G2 (AFG2), aflatoksin B1 (AFB1), aflatoksin B2 (AFB2) ve kurşun, kobalt, nikel, arsenik, bakır, çinko, manganez, magnezyum, demir, kalsiyum ve krom gibi bazı eser elementlerin konsantrasyonları belirlenmiştir. Dört adet karabiber örneği Karaman/ Türkiye'nin pazarlarından toplanmıştır. Toksinlerin belirlenmesi, bir katı faz ekstraksiyonu ile çalışan immünoafinite kolonları kullanılarak ön ayırma işleminden sonra HPLC cihazı kullanılarak gerçekleştirilmiştir. Karabiberlerdeki ağır metal içerikleri alevli atomik adsorpsiyonmetodu ile belirlenmiştir. Ayrıca, yaz ve kış aylarında toplanan 4 örnekte eser element miktarları belirlenmiştir. Biber örneklerinde toplam AF, maksimum sınırların altında belirlenmiştir. Örneklerdeki Co, Ni, Cr, Cu, Zn, Pb, Mn, Fe, Mg ve Ca miktarları tespit edilmiştir. Sonuçlar değerlendirildiğinde Cu, Zn ve Mg için bulunan değerler normal seviyelerde olduğu görülmüştür. Co, Ni, Cr, Pb, Mn, Fe, Ca eser element konsantrasyonları normal sınırın üzerinde elde edilmiştir, ancak Co, Pb ve Mn toksik sınırların altında bulunmuştur.

Anahtar Kelimeler: Aflatoksin, ağır metaller, HPLC, FAAS.

1. INTRODUCTION

Mycotoxins are types of compound that can be found everywhere by fungal spores known to have harmful

influences on human and animal health. Mycotoxins that can occur in cereals, nuts, fruits and green coffee beans endanger food safety.¹ The most widespread mycotoxins are aflatoxin G1 (AFG1), aflatoxin G2 (AFG2), aflatoxin B1

DOI: 10.32571/ijct.464189

E-ISSN:2602-277X

(AFB1), aflatoxin B2 (AFB2).² The presence of mycotoxins causes serious problems in human health.³ Therefore, the presence of mycotoxins should be eliminated or reduced.³ The most important factors causing aflatoxin formation in foods are temperature, humidity, drying and storage conditions.^{4, 5} Aflatoxins are strongly influenced by ultraviolet light throughout the ring structure. Aflatoxin B1 gives blue fluorescent light (425 nm) under UV light.⁶ Since heavy metals are present in the soil, in the air and in the water, they can also be found in all foodstuffs. The amount of metal deposited in food depends on the conditions at which food is produced and processed. Also, it has nutritional value in many metals and is essential for human health. Some elements such as lead, cadmium, mercury, arsenic and thallium have no nutritional value and these elements are taken into the body, causing health problems.⁷ The contents of trace elements that can be found in foodstuffs are mostly determined by spectrometric techniques such as ICP-OES or AAS.^{8,9} The relationship between heavy metals and mycotoxin compounds that can be found in food products is not mentioned in the literature. In this study, concentrations of the total aflatoxin, aflatoxin G1, aflatoxin G2, aflatoxin B1, aflatoxin B2, lead, cobalt, nickel, arsenic, copper, zinc, manganese, magnesium, iron, calcium and chromium in black pepper samples were determined.

2. MATERIALS AND METHODS

4 samples were analysed for AFs and trace element contents. The samples were obtained from Karaman province in Turkey. Samples were collected winter and summer seasons and checked for AFs levels. At least 100 g of the sample was collected and transported to the laboratory in containers that do not cause pollution.

2.1. Sample preparation for aflatoxins analyses

All samples were ground with a mixer to obtain the appropriate particle size. It was stored in a glass container in a refrigerator until analysis. The AOAC Official Method 999.31 was used to detect AFs in black pepper samples.¹⁰ In this method, extraction with methanol-water mixture, cleaning with IAC and post-column derivatization with kobra cell were performed. The aflatoxins were detected in the liquid chromatography device coupled with the fluorescence detector. 125 g of methanol-water mixture (70:30, v/v) and 5 g of NaCl were added 25 g of finely ground sample. The mixture was stirred at high speed for 2 minutes using a Waring stirrer. The mixture was filtered through filter paper. 15 ml of the resulting filtrate was diluted with 30 ml of water, shaken well and filtered through a microfiber filter (Wicam). It was then passed through an AflaPrep column, which was attached to a vacuum manifold at a flow rate of about 1 ml per minute,

taking from a 15 ml diluted filtrate. The column was washed twice in succession with 10 ml of ultrapure water. AFs bound to the certain antibody were eluted by passing 1ml of methanol through the column and collected in HPLC vials. The solution was stored at 2-8°C until HPLC analysis and diluted with 1 ml of ultrapure water just before analysis.

2.2. Sample preparation for heavy metals analyses

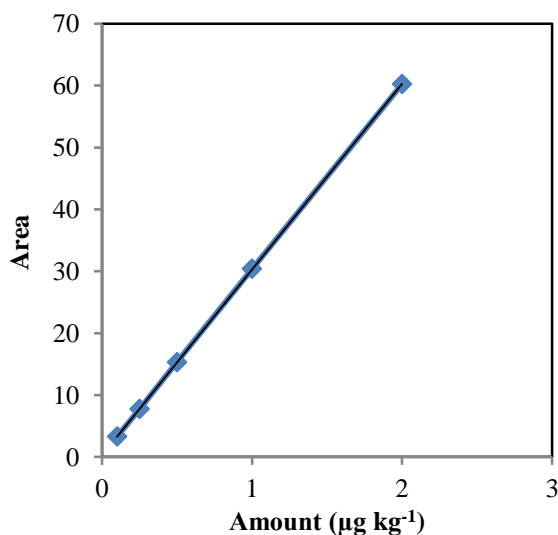
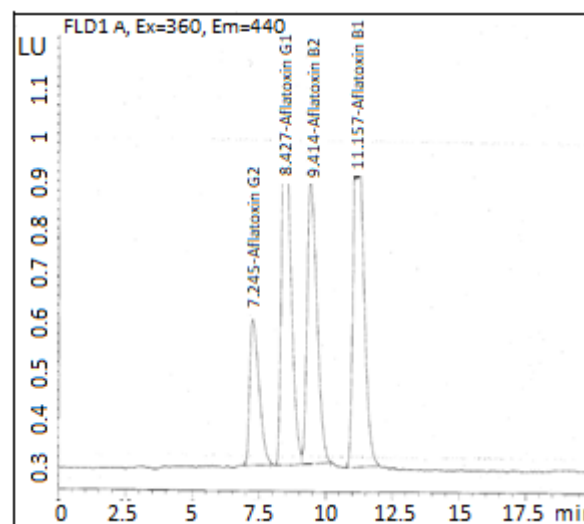
All samples were prepared for the analysis using the wet burning method to be parallel to 2 samples each sample. For this purpose, one gram of washed, dried and ground-sized powder sample is weighed. 16 ml of HNO₃ (65%, w/w) and 4 ml of HClO₄ (70-72%, w/w) were added. The solution is slowly heated on the heater for about 5-6 hours. The heating process close to the last of the acids was cut off and the solutions were cooled. Then 5 ml of H₂O₂ (30%, w/w) was added the solution and heating was continued until a clear liquid was obtained. After the heating was released, the solutions were allowed to cool. The cooled mixtures were filtered through blue band filter paper and mixed with purified water to make 30 ml solution for analysis. The concentrations of the selected elements were determined by Flame Atomic Absorption Spectrometry. Quantity and field data of aflatoxin standards and calibration curve of aflatoxin B1 standard are given Table 1 and Figure 1, respectively. HPLC-FLD chromatograms of aflatoxin standards and chromatographic parameters used in HPLC analysis are given Figure 2 and Table 2, respectively.

2.3. Chromatographic separations

The fluorescence detector was set to an excitation and emission wavelengths of 360 and 430 nm, respectively. The retention times were around 7.245, 8.427, 9.414 and 11.57 min for AFG2, AFG1, AFB2 and AFB1, respectively. Linearity, recovery, accuracy, and sensitivity were detected to appraise the performance of analytic method used for aflatoxins (AFs). To define linearity, five-point calibration graphs were drawn over the concentration range of 0.1-2 µg l⁻¹ for each AF. Linear lines were plotted using the peak area against the standard concentration. The linearity was defined by linear regression analysis and expressed as coefficient of determination (R²). The detection limits of analytical methods (LOD) and quantitative limits (LOQ) were determined according to the EURACHEM Guide recovery test.¹¹ Blank black pepper samples were spiked with 0.1 mg kg⁻¹ for each analyte and measured in 6 independent replicates. LODs and LOQs were calculated according to some equations. These equations: LOD = X + 3s, LOQ = X + 10s in which, "X" is the mean concentration of fortified sample blank values, and "s" is the sample standard deflection.

Table 1. Quantity and field data of aflatoxin standards

	Ref. Amount	RT	Signal	Compound	Lvl	Amt($\mu\text{g kg}^{-1}$)	Area	ISTD
1	2.5000e-2	7.379	FLD1A	Aflatoxin G2	1	2.5000e-2	8.0166e-1	No
	6.2500e-2				2	6.2500e-2	2.027	
	1.2500e-1				3	1.2500e-1	4.007	
	0.250				4	0.250	8.084	
	0.500				5	0.500	16.225	
2	0.100	8.652	FLD1A	Aflatoxin G1	1	0.100	2.643	No
	0.250				6	0.250	6.534	
	0.500				7	0.500	13.042	
	1.000				8	1.000	25.965	
	2.000				9	2.00	51.656	
3	2.5000e-2	9.663	FLD1A	Aflatoxin B2	1	2.5000e-2	1.697	No
	6.2500e-2				2	6.2500e-2	4.15	
	1.2500e-1				3	1.2500e-1	8.129	
	0.250				4	0.250	16.47	
	0.500				5	0.500	32.679	
4	0.100	11.532	FLD1A	Aflatoxin B1	1	0.100	3.29	No
	0.250				6	0.250	7.735	
	0.500				7	0.500	15.326	
	1.000				8	1.000	30.405	
	2.000				9	2.00	60.234	

**Figure 1.** Calibration curve of aflatoxin B1 standard.**Figure 2.** HPLC-FLD chromatograms of aflatoxin standards.

Linearity data and method performance characteristics for aflatoxins and standard mixing solution concentrations which have been prepared for calibration curves are given [Tables 3 and 4](#).

Table 2. Chromatographic parameters used in HPLC analysis

	Method
Column temperature	33
Column flow (ml dk ⁻¹)	1.0
Injection volume (µl)	20
Detection wavelength (nm)	202, 212, 219, 222, 263, 265, 279
Mobile phase A	Water/Acetonitrile/Methanol+KBr+HNO ₃
Column	C18 (250 × 4.6mm, 5µm)
Dedector	Fluorescence (ex: 360 nm, em: 435)

Table 3. Linearity data and method performance characteristics for aflatoxins

Aflatoxins	Linearity Range (µg kg ⁻¹)	Lineer Regression Equation	R ²	LOD (µg kg ⁻¹)	LOQ (µg kg ⁻¹)
AFB1	0.1-2	y = 4.67x + 0,17	0.9999	0.11	0.13
AFB2	0.1-2	y = 6.86x + 0,11	0.9997	0.11	0.13
AFG1	0.1-2	y = 3.89x + 0,14	0.9998	0.12	0.14
AFG2	0.1-2	y = 2.96x + 0,12	0.9996	0.12	0.14

R²: Coefficient of determination. LOD: Detection limit of the chromatographic method. LOQ: Quantification limit of the chromatographic method.

Table 4. Standard mixing solution concentrations which have been prepared for calibration graphics (mg kg⁻¹)

ELEMENT	STANDART NO								
	1	2	3	4	5	6	7	8	9
Ca	1.0	2.0	4.0	8.0	12.0	16.0	32.0	64.0	72.0
Pb	1.0	2.0	4.0	6.0	12.0				
Co	1.0	2.0	3.0	4.0	5.0	6.0	12.0		
Cr	1.0	2.0	3.0	4.0	5.0	6.0			
Cu	1.0	2.0	3.0	4.0	5.0	6.0			
Fe	1.0	3.0	5.0	7.0	9.0	18.0	36.0	54.0	72.0
Mg	0.5	1.0	2.0	4.0	6.0	12.0	24.0		
Mn	1.0	2.0	3.0	4.0	5.0	10.0	20.0		
Ni	1.0	2.0	3.0	4.0	5.0	6.0			
Zn	1.0	2.0	3.0	4.0	5.0	10.0	20.0	40.0	

3. RESULTS AND DISCUSSION

Aflatoxin concentrations in black pepper collected in winter and summer are given in [Tables 5](#) and [6](#).

Table 5. Aflatoxin concentrations in black pepper collected in winter ($\mu\text{g kg}^{-1}$)

Sample	B1	B2	G1	G2
1	0.012	-	0.157	-
2	0.011	0.009	0.145	-
3	0.013	0.008	0.143	0.016
4	0.012	-	-	0.014
Average \pm SD	0.012 ± 0.0008	0.085 ± 0.007	0.148 ± 0.007	0.0015 ± 0.001

Table 6. Aflatoxin concentrations in black pepper collected in summer ($\mu\text{g kg}^{-1}$)

Sample	B1	B2	G1	G2
1	-	-	0.043	0.015
2	-	-	0.042	0.016
3	-	-	0.045	0.014
4	0.003	-	0.048	0.013
Average \pm SD	0.003	-	0.044 ± 0.002	0.014 ± 0.001

Aflatoxin levels in black pepper collected in winter and summer, and aflatoxin and total aflatoxin levels in samples are given in [Figures 3-5](#). The average concentrations of trace elements in the black peppers are given in [Table 7](#). Average trace element concentrations in black pepper samples are given in [Figures 6-8](#). Average element contents and assessment in foodstuffs are given in [Table 8](#).

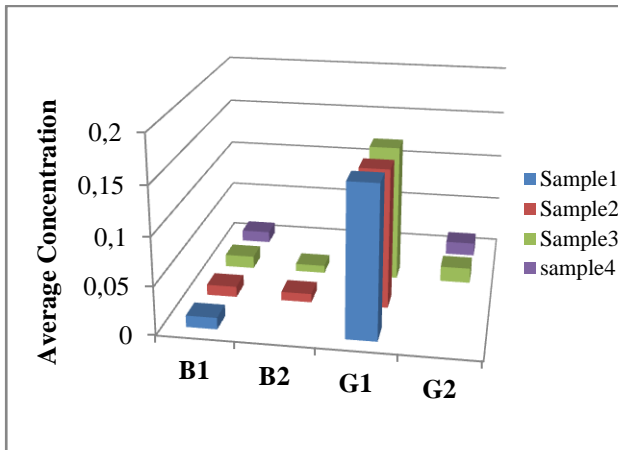


Figure 3. Aflatoxin levels in black pepper collected in winter ($\mu\text{g kg}^{-1}$).

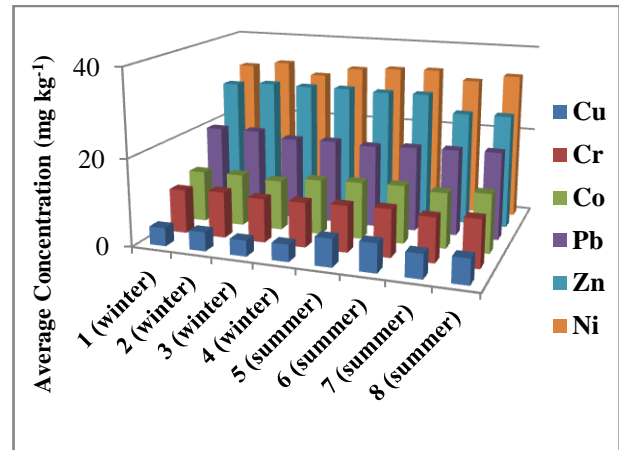


Figure 6. Average trace element (Cu, Cr, Co, Pb, Zn, Ni) concentrations in black pepper samples (mg kg^{-1}).

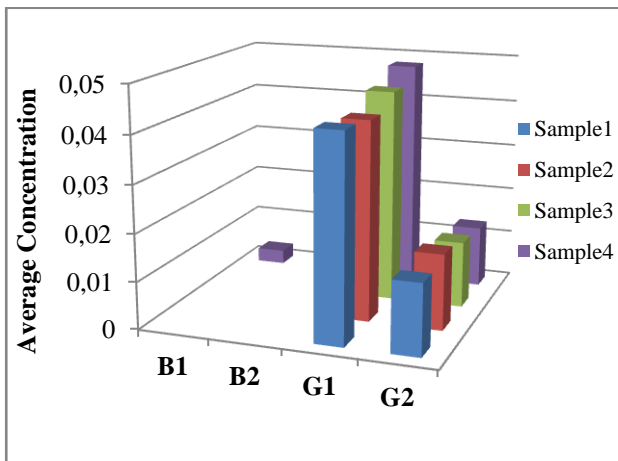


Figure 4. Aflatoxin levels in black pepper collected in summer ($\mu\text{g kg}^{-1}$).

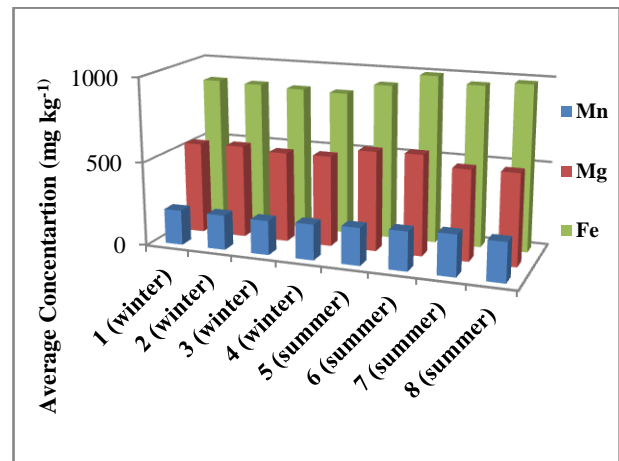


Figure 7. Average trace element (Mn, Mg, Fe) concentrations in black pepper samples (mg kg^{-1}).

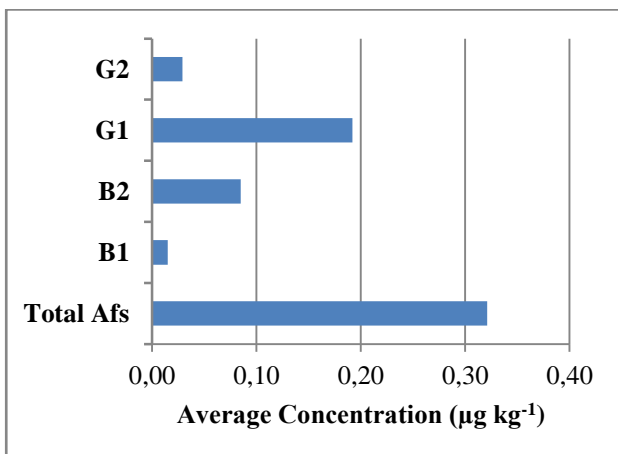


Figure 5. Aflatoxin levels and total aflatoxin in samples ($\mu\text{g kg}^{-1}$).

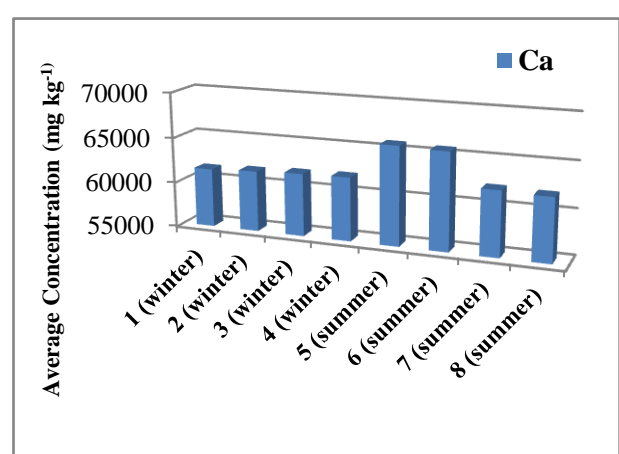


Figure 8. Average trace element (Ca) concentrations in black pepper samples (mg kg^{-1}).

Table 7. The average trace element concentrations in the black peppers (mg kg⁻¹)

	Co	Ni	Cr	Cu	Zn	Pb	Mn	Mg	Fe	Ca
Black Pepper										
Winter	11.81	32.41	10.03	4.17	29.34	20.09	208.3	544	882	61480
	11.96	33.61	10.55	4.32	29.97	20.19	206.7	552	875	61690
	11.47	31.03	10.04	3.60	29.87	19.01	203.5	535	864	61910
	12.62	33.16	10.21	3.90	29.99	19.31	211.9	539	857	62010
Summer	13.03	33.72	10.57	6.37	29.73	18.96	222.1	591	922	65860
	13.27	33.99	10.88	6.55	29.91	19.48	232.1	597	996	65710
	12.62	32.02	10.16	5.49	25.99	19.77	245.3	537	958	62160
	13.44	33.68	10.85	5.73	26.14	20.07	234.2	542	983	62000
Average	12.53	32.95	10.41	5.016	28.86	19.61	220.5	554.6	917.1	62852
±SD	± 0.718	± 1.037	± 0.347	± 1.157	± 1.742	± 0.491	± 15.32	± 24.89	± 55.67	± 1822

Table 8. Average element contents and evaluation in foodstuffs (mg kg⁻¹)^{9,12}

Element	Range Found	Normal Concentration	Toxic Concentration	Evaluation
Co	11.47 – 13.44	0.05 -0.50	30 - 40	High
Ni	31.03 - 33.99	0.10 -5.00	30.0	High
Cr	10.03 – 10.88	0.10 -1.00	2.00	High
Cu	3.60 - 6.55	3.00-15.0	20.0	Normal
Zn	25.99 – 29.99	15.0 - 150	200	Normal
Pb	18.96 – 20.19	1.00- 5.00	20.0	High
Mn	203.5 – 245.3	15.0 - 100	400	High
Fe	857 – 996	50.0 - 250	500	High
Mg	535– 597	250 - 3500	--	Normal
Ca	61480 - 65860	90 - 12000	--	High

DOI: 10.32571/ijct.464189

E-ISSN:2602-277X

When the results were evaluated, Cu, Zn and Mg were found to be normal in the determined limits. Co, Ni, Cr, Pb, Mn, Fe, Ca element concentrations were found above the normal range, but Co, Pb and Mn below the toxic limits. European quantification limits were 0.11, 0.11, 0.12 and 0.14 $\mu\text{g kg}^{-1}$ for AFB1, AFB2, AFG1 and AFG2, respectively. AFs are present in 100% of black pepper at total AFs levels ranging. Four black pepper samples were found below the European maximum tolerable limit (MTL) for AFB1 and total AFs concentration.

4. CONCLUSIONS

In this study, concentrations of the total aflatoxin, AFG1, AFG2, AFB1, AFB2, lead, cobalt, nickel, arsenic, copper, zinc, manganese, magnesium, iron, calcium and chromium in black pepper samples were determined. Minerals should be taken less than 100 mg per day. These elements make up less than 0.01% of body weight. The basic trace elements required for human health are silicon, zinc, manganese, iron, copper, chromium, fluoride and iodine. Basic minerals function as structural components of textures.¹⁰ In addition, these elements are active in cellular and basal metabolism, water and acid-base balance in the human body.¹⁰ Prevention of heavy metal contamination, sources of contamination should be identified. These resources should be eliminated or reduced. Inspections of potentially dangerous sources should be carried out continuously. Codex Alimentarius has developed various application codes to prevent and reduce the formation of AFs in foods. Producers should produce food according to the rules, taking into account the Good Agricultural Practices (GAP). Good Storage Practices (GMP) and Good Food Production (GMP) rules should be applied during the processing and storage of food after production.¹³

ACKNOWLEDGEMENTS

The authors are grateful for the financial support of the Karamanoğlu Mehmetbey University Scientific Research Project for trace element analysis (Project Number 27-M-15 / 2017).


Conflict of interest


Authors declare that there is no a conflict of interest with any person, institute, company, etc.

REFERENCES

1. D'Mello, J. P. F. *Food safety: Contaminants and toxins*. 2003, pp 65.
2. Kwiatkowski, A.; De Faria Alves, A. P. *SaBios-Revista de Saúde e Biologia*. 2007, 2(2).
3. Creppy, E. E. *Toxicol. Lett.* 2002, 127(1-3), 19-28.
4. Solis-Sánchez, L. O.; Castañeda-Miranda, R.; García-Escalante, J. J.; Torres-Pacheco, I.; Guevara-González, R. G.; Castañeda-Miranda, C. L.; Alaniz-Lumbreras, P. D. *Comput. Electron. Agric.* 2011, 75(1), 92-99.
5. Strosnider, H.; Azziz-Baumgartner, E.; Banziger, M.; Bhat, R. V., Breiman, R.; Brune, M. N.; Henry, S. H. *Environ. Health Persp.* 2006, 114(12), 1898.
6. Razzaghi-Abyaneh, M.; Shams-Ghahfarokhi, M.; Peng-Kuang, C. Aflatoxins: Mechanism of inhibition by antagonistic plants and bacteria; Eds., www. *Intechopen.com/boks*. 2010; pp 586-304.
7. Merian, E.; Clarkson, T. W. *Metals and their compounds in the environment*, 1991. <http://agris.fao.org/agris-search/index.do> (accessed May 10, 2017).
8. Hongxing, Z.; Yu-Kui, R. *J. Chem.* 2011, 8(2), 782-786.
9. Singh, A.; Sharma, R. K.; Agrawal, M.; Marshall, F. M. *Food Chem. Toxicol.* 2010, 48(2), 611-619.
10. Macrae, R.; Robinson, R.K.; Sadler, M.J. *Encyclopaedia of Food Science. Food Technology and Nutrition*, Academic Press INC, San Diego, 1993, pp 3126 -3131.
11. Guide, E. *A laboratory guide to method validation and related topics, LGC, Teddington, Middlesex, UK*, 1998.
12. Stanojkovic-Sebic, A.; Pivic, R.; Josic, D.; Dinic, Z.; Stanojkovic, A. *Tarım Bilimleri Dergisi*. 2015, 21(3), 317-325 (in Turkish).
13. Kilicel, F.; Karapinar, H. S.; Cimen, A. *Science J. Anal. Chem.* 2017, 5(6), 90.

ORCID

 0000-0002-5454-5597 (F. Kılıçel)

 0000-0002-0123-3901 (H. S. Karapinar)



Promising bay laurel (*Laurus nobilis* L.) genotypes for fruit production

Filiz AYANOĞLU^{1,*}, Durmuş Alpaslan KAYA¹, Oğuzhan KOÇER²

on the last page

¹ Field Crops Department, Faculty of Agriculture, Mustafa Kemal University, Antakya, Hatay, Turkey

² Field Crops Department, Institute of Science, Mustafa Kemal University, Antakya, Hatay, Turkey

Received: 21 November 2018, Revised: 19 December 2018; Accepted: 20 December 2018

*Corresponding author e-mail: filizayanoglu@gmail.com

Citation: Ayanoglu, F.; Kaya, D. A.; Koçer, O. *Int. J. Chem. Technol.* 2018, 2 (2), 161-167.

ABSTRACT

Bay laurel (*Laurus nobilis* L.) is an evergreen and dioecious tree or shrub plant with a small black fruit. This study was conducted to determine bay laurel genotypes with high-quality characteristics which grown intensively in Hatay. 149 female trees were preselected and then 49 laurel genotypes were used as material according to Turkish Standards (TS-5205) for fatty acid compositions. In the study, berry weights (0.77-1.76 g), kernel weights (0.49-1.12 g), kernel ratios (51.73-77.44%), dry matter ratios (44.89-69.44%), berry oil ratios (18.92-37.85%), berry flesh oil ratios (20.76-53.98%) and kernel oil ratios (11.75-27.49%) of genotypes were determined. The content of fatty acid compositions ranged between 12.74-31.19% for lauric acid, 12.35-19.91% for palmitic acid, 30.35-44.43% for oleic acid and 15.93-26.75% for linoleic acid. Genotype K9 has attracted attention with high lauric acid and low palmitic acid ratio. On the other hand, genotype ER6 for berry weight, B30 for kernel weight and ER14 for kernel oil ratio were found to be promising genotypes.

Keywords: Fatty acid compositions, Lauric acid, Selection, Hatay

Meyve üretimi için ümitvar defne (*Laurus nobilis* L.) genotipleri

ÖZ

Defne (*Laurus nobilis* L.), küçük siyah meyvesi olan herdem yeşil ve iki evcikli bir ağaç veya çalı formunda bir bitkidir. Bu çalışma, Hatay'da yoğun olarak yetişen yüksek kaliteli defne genotiplerini belirlemek için yürütülmüştür. Öncelikle 149 dişi ağaç önseçim yapılmıştır ve daha sonra yağ asitleri bileşimleri için Türk Standartlarına (TS-5205) göre 49 defne genotipi materyal olarak kullanılmıştır. Çalışmada, defne genotiplerinin meyve ağırlıkları (0.77-1.76 g), çekirdek ağırlıkları (0.49-1.12 g), çekirdek oranları (% 51.73-77.44), kuru madde oranları (% 44.89-69.44), meyve yağı oranları (% 18.92-37.85), meyve eti yağı oranları (% 20.76-53.98) ve çekirdek yağı oranları (% 11.75-27.49) belirlenmiştir. Yağ asidi bileşimlerinin içeriği, laurik asit için% 12.74-31.19, palmitik asit için% 12.35-19.91, oleik asit için% 30.35-44.43 ve linoleik asit için% 15.93-26.75 arasında değişmiştir. K9 genotipi yüksek laurik asit ve düşük palmitik asit oranıyla dikkat çekmiştir. Öte yandan, meyve ağırlığı için genotip ER6, çekirdek ağırlığı için B30 ve çekirdek yağı oranı için ER14'ün umut verici genotipler olduğu bulunmuştur.

Anahtar Kelimeler: Yağ asiti bileşimleri, Laurik asit, Seleksiyon, Hatay

1. INTRODUCTION

Bay laurel (*Laurus nobilis* L.) is an evergreen, dioecious plant in the form of a pyramidal-shaped tree or large bush of the *Laurus* genus of the Lauraceae family.^{1,2} *Laurus nobilis* L., also known as Mediterranean bay laurel, is widely grown in Turkey,

Greece, Italy, Spain, Portugal, France, Syria, Morocco, Algeria, Mediterranean Islands, and California³⁻⁶

Bay laurel is one of the most important medicinal plants of Turkey and grows naturally starting from the province of Hatay along the Mediterranean, Aegean, and the Black Sea coasts and up to 1200 m in the inner parts of these coastal areas.⁷⁻⁹ In Turkey, 5500 tons of bay La-

DOI: 10.32571/ijct.485896

E-ISSN:2602-277X

urel seeds are produced.⁹⁻¹¹ In addition, when the medicinal and aromatic plant exports values of recent years are examined, it is seen that bay laurel is one of the important plants as quantity and economic value.^{11,12}

The olive-like berries of bay laurel are green in color firstly, when it matures, it becomes a bright bluish black color. Bay laurel berries reach physiological maturity in October-November and are collected at about 40% moisture.¹³ In studies conducted with soxhlet extraction and supercritical CO₂ extraction of bay laurel berries, it was determined that bay berries contained 15-35.87% fixed oil.¹⁴⁻¹⁸ However, the fixed oil content obtained by the traditional boiling method is about 10%. The berry flesh of bay laurel contains 26% and the kernel contains 18% fixed oils.^{15,19} There are more than 20 fatty acids in the bay laurel oil.²⁰ The main components of bay laurel fixed oil are lauric acid, oleic acid, linoleic acid, and palmitic acid. Lauric acid is found only in the bay laurel berry kernel. The oil obtained from laurel berry is used in soap making, medicine, and cosmetics industry. In recent years, parallel to the demand for natural products the demand for bay laurel soap is increasing day by day, and bay laurel berries are used as a natural anthocyanin instead of synthetic dyes in the food, pharmaceutical, and cosmetic industries.¹⁸

There are no registered bay laurel species in Turkey yet. Laurel berries are collected from naturally grown trees. Naturally grown trees have a wide variation in berry yield, berry characteristics, fixed oil content, and components of berries.^{18,21} For this reason, problems may occur from time to time in compliance with the standardization of oils. This study was carried out to develop new varieties in accordance with standards for oil components with high berry and oil yield and superior berry characteristics.

2. MATERIALS AND METHODS

In the experiment, bay laurel trees in the flora of Hatay with different characteristics were selected, and the coordinates and altitudes of them were registered. Berry oils of pre-selected genotypes were extracted and oil content and fatty acids composition were determined. The obtained data were evaluated according to TSE standards and 48 genotypes were determined to be in compliance with standards for fatty acids composition. Berries of 48 genotypes were examined for their pomological and chemical properties. In the experiment, berry samples were collected when they completely blackened period. Some of the characteristics examined in barires of 48 female genotypes are berry weight (g), ovality coefficient, kernel weight (g), kernel ratio (%), dry matter ratio (%), berry oil ratio (%), berry flesh oil ratio (%) and kernel oil ratio (%). Pomological features

were determined in 50 bay barriers. Oil extraction: Soxhlet extracts were obtained in 100 g dried and grounded samples from each genotype. Oil samples were kept at 4°C until chemical analysis, which was duplicated.

Fatty acids composition: The components of the oils obtained from the berries of each genotype were analyzed by Hewlett Packard 6890 N model GC/MS. After esterification of the oils, the composition of fatty acids was determined on GC/MS. For this purpose, firstly 0.5 g of the oil sample is taken and methanolic NaOH was added and boiled under reflux for 10 minutes. With the disappearance of the oil droplets, 10 ml of B3 methanol complex was added, boiled for 10 minutes and then added with hexane.²² Upper phase was taken into 2 ml vial bottle and read in GC/MS. Capillary column, HP-Innowax 60 meters diameter 0.25 micrometer, helium was used as carrier gas.

3. RESULTS AND DISCUSSION

In preselection studies 48 genotypes were selected according to fatty acid compositions. The altitude of the areas where 48 genotypes were collected ranged from 42 m to 985 m. The results of the researches carried out on the berries are given below.

3.1. Fixed oil contents

The dry matter and fixed oil ratios of the berries of bay laurel genotypes varied considerably compared to the genotypes. The values of the dry matter and fixed oil ratios of 48 genotypes berries are given in Table 1. The lowest value for the dry matter content of the berries was taken from the genotype O10 with 44.89% and the highest value was taken from the genotype B13 with 69.44%. The average dry matter content of the berries gathered from the pre-selected genotypes was 61.80%. The lowest value for whole berries (together with the kernel and berry flesh) oil content was obtained from the genotype SK3 with 18.92% while the highest value was obtained from genotype ER16 with 37.85%. The average of fixed oil percentage of the berries of examined genotypes was 27.73%. As in other features, there is a considerable variation in the fixed oil ratios among genotypes (Table 1). When we examined the previous studies; in studies conducted in Turkey, Yazıcı²³ reported that the fatty oil ratio of bay laurel berry was between 13.05% and 18.11%; found that the ratio of fatty oil of bay laurel berry varied between 17.52% and 28.14% in their study in Lebanon. Marzouki and co-workers¹⁶ reported that the ratio of fatty oil of bay laurel berry was between 17.1% and 27.6% in Tunisia. Beis and Dunford¹⁵ found between 14-28% in their study. The result that we obtained showed similarities with

Table 1. Dry matter ratio and fixed oil contents of bay laurel genotypes (%)

Genotypes	Dry Matter Ratio	Berry Oil Ratio	Berry Flesh Oil Ratio	Kernel Oil Ratio	Genotypes	Dry Matter Ratio	Berry Oil Ratio	Berry Flesh Oil Ratio	Kernel Oil Ratio
YY5	64.28	24.30	20.76	11.75	ER17	59.47	37.05	41.92	26.49
YY8	61.04	25.90	35.53	16.26	ER21	62.98	30.68	37.15	20.92
ŞK3	65.21	18.92	21.91	18.92	ER27	65.85	33.47	44.53	22.91
ŞK5	62.48	26.49	36.32	16.66	ER41	51.95	32.07	44.86	21.91
ŞK6	52.18	27.29	21.12	17.33	ER44	60.17	28.88	44.02	20.72
O4	65.73	24.70	33.93	15.46	ER46	57.78	26.10	43.91	22.31
O10	44.89	27.09	32.07	16.14	ER47	63.70	30.88	40.64	22.31
E5	65.76	32.87	35.66	25.10	ER48	63.33	24.30	38.61	22.31
E6	63.33	28.88	37.72	25.30	B3	58.42	27.49	41.09	18.92
E8	63.93	22.31	47.01	17.33	B5	63.00	24.90	44.02	16.73
E9	60.60	31.67	48.02	25.70	B13	69.44	28.06	41.09	19.07
HB4	64.25	24.50	33.66	15.33	B21	54.48	21.51	48.90	12.55
K2	65.02	23.90	44.62	15.94	B30	57.79	26.10	43.82	18.92
K5	62.60	29.68	36.36	16.93	B33	61.79	26.69	39.84	16.14
K8	62.14	23.90	28.49	17.13	B34	69.25	25.10	34.46	15.73
K9	64.41	22.31	33.86	16.33	D2	64.19	33.07	49.30	23.71
K10	61.45	26.69	39.04	19.72	D4	64.91	30.68	52.67	20.72
K12	60.25	24.50	48.61	18.13	D13	65.54	30.28	44.91	21.31
K15	64.44	22.71	42.97	16.53	H2	56.10	33.27	40.36	19.92
BA7	64.22	24.50	33.53	16.14	H10	65.54	33.07	34.92	13.73
ER6	57.31	34.06	39.64	21.71	SY2	58.93	25.70	42.97	13.75
ER10	61.53	27.09	45.80	22.31	SY3	60.09	25.70	38.25	18.13
ER14	63.09	34.26	47.01	27.49	S6	66.45	21.71	31.27	17.53
ER16	67.73	37.85	53.98	22.51	S8	66.79	26.49	42.23	14.34

Dry Matter: Min: 44.89; Max: 69.44; Mean: 61.80; STD: 4.63; CV: 7.49, Berry Oil Ratio: Min: 18.92; Max: 37.85; Mean: 27.73; STD: 4.28; CV: 15.43, Berry Flesh Oil Ratio: Min: 20.76; Max: 53.98; Mean: 39.56; STD: 7.42; CV: 18.76, Kernel Oil Ratio: Min: 11.75; Max: 27.49; Mean: 19.05; STD: 3.76; CV: 19.74.

these values in some point of view and all of these results indicate that the fatty oil content of the bay laurel berry has changed according to genotypes, growing region, climatic differences the time of collection and the morphological and physiological structure of the collected plant.

In the analysis to determine the fixed oil ratios contained only in the berry flesh of bay laurel berry, the lowest value for the ratio of flesh fixed oils was determined in genotype YY5 with 20.76% and the highest value of 53.98% in genotype ER16. The average berry flesh fixed oil ratio of the genotypes was 39.56% (Table 1). The lowest value obtained in the analysis of fixed oils in the kernels of bay laurel berries was taken from the genotype YY5 with 11.75% and the highest value with 27.49% from the genotype ER14. The average

fixed oil content of the berry kernels of pre-selected bay laurel genotypes grown in Hatay region was determined as 19.05% (Table 1). Genotypes with high kernel fixed oil should be taken into consideration when evaluating future work. Because lauric acid is found in the kernel rather than berry flesh.

3.2. Fatty acids compositions

In the analysis of the fixed oils obtained from the berries of each genotype, the fatty acids compositions were determined and given in Table 2. The genotype with the highest lauric acid ratio in the study was K9 with 31.19% and the genotype with the lowest value was H10 with 12.74%. The genotype K9 has also attracted attention with a low palmitic acid ratio (12.35%). The genotype

the highest rate of palmitic acid was B21 with 19.91%. The average oleic acid content of the genotypes was determined to be 37.08% and the highest value was determined in the genotype H2 with 44.43% and the lowest value was found in the genotype O10 with 30.35%. The mean of the linoleic acid content of the genotypes was 23.09%, and the K2 genotype was the lowest with 15.93% and the SY3 genotype was the highest with the linoleic acid ratio of 26.75%. As can be understood from Table 2, the most common fatty acid in bay laurel berry is oleic acid. However, the characteristic of bay laurel fixed oil is that it is originated from lauric acid. Lauric acid is only present in the kernel of the berry

and according to Turkish Standardization (TS-5205), bay laurel oil cannot be exported if lauric acid is less than 12.5%. For this reason, the amount of lauric acid is the foreground for bay laurel oil. As a matter of fact, genotypes containing about 30% of lauric acid were determined in the study. Especially, K2 and K9 have become genotypes that attract attention in this respect. As regards to fixed oil composition, the results showed similar variations with¹⁵ that studied in flora of Turkey. These results were also within the range of fatty acids composition previously reported in literature.^{16, 24,25}

Table 2. Fatty acids compositions of bay laurel genotypes (%)

Genotypes	Lauric Acid	Palmitic Acid	Oleic Acid	Linoleic Acid	Genotypes	Lauric Acid	Palmitic Acid	Oleic Acid	Linoleic Acid
YY5	15.83	18.73	41.40	24.04	ER17	18.09	17.63	37.71	22.87
YY8	17.57	19.58	35.28	25.03	ER21	12.75	19.60	38.32	25.99
ŞK3	19.35	17.79	33.44	26.64	ER27	18.09	17.92	34.59	25.09
ŞK5	25.20	14.55	36.51	19.49	ER41	22.22	17.28	37.08	23.43
ŞK6	20.74	17.00	37.98	20.30	ER44	15.87	17.58	39.26	23.18
O4	16.20	17.33	39.89	23.26	ER46	15.24	17.89	38.80	24.68
O10	22.01	19.61	30.35	24.08	ER47	21.69	18.48	36.73	19.60
E5	25.03	14.78	31.62	24.99	ER48	18.66	16.26	38.71	22.88
E6	19.41	16.10	35.49	26.29	B3	18.88	18.86	37.86	20.71
E8	16.59	17.59	37.98	24.72	B5	12.79	18.98	38.86	26.33
E9	18.39	16.47	37.92	23.88	B13	17.55	19.03	38.45	23.16
HB4	21.79	16.32	34.49	23.38	B21	20.08	19.91	33.14	23.68
K2	31.17	14.93	37.97	15.93	B30	18.98	17.83	39.94	21.69
K5	25.55	14.27	36.80	19.65	B33	13.65	18.46	39.01	24.41
K8	24.24	16.48	35.58	21.35	B34	26.70	16.48	33.71	23.10
K9	31.19	12.35	34.22	19.20	D2	19.87	18.29	33.17	25.23
K10	22.02	15.05	40.21	22.71	D4	18.90	18.83	36.54	23.73
K12	17.55	19.70	34.79	24.83	D13	21.51	19.63	32.67	23.99
K15	23.77	14.87	32.79	24.50	H2	14.67	15.95	44.43	21.89
BA7	15.98	16.22	41.35	21.97	H10	12.74	19.28	40.08	23.84
ER6	16.57	18.57	38.08	23.90	SY2	16.20	17.35	37.62	25.54
ER10	20.29	15.08	40.22	21.63	SY3	15.00	14.60	39.80	26.75
ER14	15.32	14.49	36.77	18.42	S6	23.35	15.81	34.85	19.70
ER16	17.50	16.98	39.81	22.53	S8	16.28	18.39	37.74	24.26

Lauric acid: Min: 12.74; Max: 31.19; Mean: 19.35; STD: 4.27; CV: 22.07, Palmitic acid: Min: 12.35; Max: 19.91; Mean: 17.19; STD: 1.80; CV: 10.47, Oleic acid: Min: 30.35; Max: 44.43; Mean: 37.08; STD: 2.86; CV: 7.71, Linoleic acid: Min: 15.93; Max: 26.75; Mean: 23.09; STD: 2.34; CV: 10.13.

3.4. Pomological characteristics

The weights in bay laurel berry revealed quite large variations among genotypes (Coefficient of Variation 19.08). The values of the berry weights of 48 female genotypes are given in Table 3.

The lowest berry weights of the genotypes were taken from D13 with 0.77 g and the highest value from ER6 with 1.76 g. The average weight of the berries was found to be 1.31 g. The distribution of berry weight generally appears to be concentrated between 1.00 g and 1.50 g. The average fruit weight was higher than that of the

values obtained by Karik and co-workers (1.06 g)¹⁸, Baytöre (0.93 g)¹⁷ and Boza (1.04 g).²⁶ This is an expected result as the genotypes selected for pre-selection studies.

In order to obtain information about the berry shape of the bay laurel plants growing in the region, round or long shape, ovality coefficients were determined by calculating the ratio of the berry length and berry width of berries. Genotypes with 1 ovality coefficient are round form berry types. The genotype with the highest ovality coefficient of the berry was genotype D13 with 0.89, while the lowest ovality coefficient was obtained from

Table 3. Pomological characteristics of bay laurel genotypes

Genotypes	Berry weight	Ovality Coef.	Kernel Weight	Kernel Ratio	Genotypes	Berry weight	Ovality Coef.	Kernel Weight	Kernel Ratio
YY5	1.41	0.76	1.02	72.48	ER17	1.24	0.76	0.71	57.58
YY8	1.45	0.77	0.91	62.74	ER21	1.53	0.72	1.03	67.32
ŞK3	1.27	0.61	0.90	70.98	ER27	1.21	0.81	0.78	64.30
ŞK5	1.18	0.75	0.74	62.75	ER41	1.62	0.61	0.99	60.99
ŞK6	1.01	0.63	0.66	65.82	ER44	1.46	0.72	0.86	58.77
O4	1.12	0.71	0.70	62.75	ER46	1.44	0.83	0.89	61.94
O10	1.17	0.73	0.73	61.98	ER47	1.25	0.67	0.82	65.92
E5	0.97	0.78	0.65	66.80	ER48	1.12	0.74	0.67	60.00
E6	1.00	0.74	0.68	68.20	B3	1.10	0.78	0.65	59.45
E8	1.58	0.78	1.04	65.95	B5	1.40	0.75	1.06	75.73
E9	1.54	0.80	0.98	63.38	B13	0.83	0.73	0.49	59.13
HB4	1.17	0.70	0.73	62.75	B21	1.33	0.73	0.78	58.86
K2	1.35	0.60	1.05	77.44	B30	1.67	0.68	1.12	67.26
K5	0.98	0.67	0.53	54.23	B33	1.08	0.82	0.78	72.17
K8	1.58	0.62	0.97	61.34	B34	1.61	0.72	1.01	62.71
K9	1.33	0.87	0.94	71.04	D2	0.99	0.83	0.62	63.03
K10	1.45	0.82	0.80	55.30	D4	1.29	0.80	0.79	60.93
K12	1.50	0.72	0.78	51.73	D13	0.77	0.89	0.51	66.75
K15	1.10	0.86	0.70	63.43	H2	1.65	0.74	1.02	61.94
BA7	1.31	0.84	0.94	72.00	H10	1.21	0.67	0.75	61.98
ER6	1.76	0.61	0.93	52.90	SY2	1.52	0.62	0.85	55.59
ER10	1.32	0.70	0.89	67.58	SY3	1.74	0.75	0.98	56.07
ER14	1.06	0.76	0.68	64.34	S6	1.67	0.58	1.02	61.15
ER16	1.07	0.74	0.65	60.37	S8	1.47	0.62	0.88	59.55

Berry weight: Min: 0.77; Max: 1.76; Mean: 1.31; STD: 0.25; CV: 19.08, Ovality Coefficient: Min: 0.58; Max: 0.89; Mean: 0.73; STD: 0.08; CV: 10.96

Kernel Weight: Min: 0.49; Max: 1.12; Mean: 0.82; STD: 0.16; CV: 19.51, Kernel Ratio: Min: 51.73; Max: 77.44; Mean: 63.33; STD: 5.65; CV: 8.92

DOI: 10.32571/ijct.485896

E-ISSN:2602-277X

the genotype ER14 with 0.58. According to these results, the most rounded genotype is D13 and the longest genotype is genotype ER14. Average ovality coefficient of laurel trees grown in the region was determined as 0.73.

It has been determined that there are also quite large variations among kernel weights of bay laurel genotypes. The values for the kernel weights of the 48 female bay laurel genotypes are given in Table 3. The lowest value for the kernel weights was taken from B13 with 0.49 g and the highest value with 1.12 g from genotype B30. The average kernel weight of the berries was found to be 0.82 g.

In the study, the lowest value for kernel ratios of genotypes was obtained from the genotype K12 with 51.73% and the highest value from genotype K2 with 77.44%. The average kernel ratios of the berries were determined as 63.33%.

The kernel ratios and kernel weight of the berry appear as an important criterion in bay laurel selection. Because, lauric acid is only present in the kernel of bay laurel berries. For this reason, in order to obtain genotypes with the high lauric acid ratio, genotypes with higher kernel ratio and kernel oil contents should be given priority in selection.

4. CONCLUSIONS

The result that we obtained indicates that the fatty oil content of the bay laurel berry has changed according to genotypes, growing region, climatic differences the time of collection and the morphological and physiological structure of the collected plant. It can be concluded that there is a great variation among the genotypes in the flora. In the study, the K9 genotype has attracted attention with a high lauric acid and low palmitic acid ratio. On the other hand genotype ER6 for berry weight, B30 for kernel weight and ER14 for kernel oil ratio were found to be promising genotypes. Studies should be continuing on this genotype.

ACKNOWLEDGMENTS

This study was supported by TÜBİTAK (Project number 108O878).

Conflict of interest

We declare that there is no a conflict of interest with any person, institute, company, etc.

REFERENCES

1. Heywood, V. H. *Flowering Plants of the World*. Oxford University Press, 1978.

2. Christenhusz, M. J. M.; Byng, J. W. *Phytotaxa* 2016 261 (3), 201–217.

3. Baytop, T. *Türkiye'de Bitkiler ile Tedavi, Geçmişte ve Bugün*, 2. Baskı, Nobel Tıp Kitabevi, 1999 (in Turkish).

4. Ross, I. A. *Springer Science Business Media*, 2001.

5. Kumar, S.; Singh, J.; Sharma, A.; *Bay Leaves*. In: Peter, KV, Editor. *Handbook of Herbs and Spices*. Vol. I. Abington Woodhead Publishing Limited, 2003; pp 52-61.

6. Rodriguez-Sanchez, F.; Guzman, B.; Valido, A.; Vargas, P. *J. Biogeogr.* 2009, 36, 1270-1281.

7. Kayacık, H. İstanbul Üniversitesi, Orman Fakültesi, 1977, Yayın No: 247 (in Turkish).

8. Davis, P. H. *Flora of Turkey and East Aegean Islands*. Vol. 7. Edinburgh University Press, 1982.

9. Anonymous: Defne Eylem Planı 2016-2020. Orman ve Su İşleri Bakanlığı. Orman Genel Müdürlüğü, 2016 (in Turkish).

10. Anonymous: Ormancılık İstatistikleri, T.C. Orman ve Su İşleri Bakanlığı, Türkiye İstatistik Kurumu Matbaası, 2014 (in Turkish).

11. Kurt, R.; Karayılmazlar, S.; İmren, E; Çabuk, Y. *BAROFD* 2016, 18(2), 158-167.

12. Şafak, İ.; Okan, T. *J. DOA*, 2004, 10, 101-129.

13. Anonymous: T.C. Hatay Valiliği, 2012, Yayın No: 14 (in Turkish).

14. Erden, Ü. Akdeniz Defnesi'nde (*Laurus nobilis* L.) Mevsimsel Varyabilite ve Optimal Kurutma Yöntemlerinin Araştırılması. Master Thesis, Çukurova Üniversitesi, Fen Bilimleri Enstitüsü, Adana, 2005 (in Turkish).

15. Beis, S. H.; Dunford, N. T. *J. Am. Oil Chem. Soc.* 2006, 83(11), 953-957.

16. Marzouki, H.; Piras, A.; Marongiu, B.; Rosa, A; Dessi, M. A. *Molecules* 2008, 13, 1702-1711.




17. Baytöre, F. Yalova ilinde farklı yüksekliklerde doğal olarak yetişen defne (*Laurus nobilis* L.) populasyonlarında bazı morfolojik ve kalite özellikleri ile ontogenetik varyabilitenin belirlenmesi. Master Thesis, Namık Kemal Üniversitesi, Fen Bilimleri Enstitüsü, Tekirdağ, 2014 (in Turkish).

DOI: [10.32571/ijct.485896](https://doi.org/10.32571/ijct.485896)

E-ISSN:2602-277X

18. Karık, Ü.; Çiçek, F.; Ođur, E.; Tutar, M; Ayas, F. *J. AARI*, **2016**, 26 (1),1-16.
19. Yazıcıođlu, T.; Karaali, A. *Eur. J. Lipid Sci. Tech.* **1983**. 85 (1), 23–29.
20. Hafizoglu, H.; Reunanen, M. *Fett. Wiss. Technol.* **1993**, 95, 304-308.
21. Ayanođlu, F.; Mert, A; Kaya, D. A.; Köse, E. Tübitak Project No: 108O878, Final report, 2010.
22. Öztekin, L.; Bařođlu, F.; *J. Food*, **1998**, 23 (1), 27-35.
23. Yazıcı, H. Batı Karadeniz Bölgesinde yetişen defne (*laurus nobilis* L.) yaprak ve meyvelerinden faydalanma imkanlarının araştırılması. Ph.D. Thesis, Zonguldak Karaelmas Üniversitesi, Fen Bilimleri, Zonguldak, 2002 (in Turkish).
24. Said, C.M.; Kanaan Hussein, K. *ESJ*. **2014**, 10 (15), 412-419.
25. Castilho, P. C.; Costa, M. C.; Rodrigues, A.; Partidário, A. *J. Am. Oil Chem. Soc.* **2014**, 82 (12), 863-868.
26. Boza, A. Karaburun, Çeşme ve Dilek Yarımadası'nda bulunan doğal defne (*Laurus nobilis* L.) populasyonları üzerinde arařtırmalar. Ph.D. Thesis, Ege Üniversitesi, Fen Bilimleri Enstitüsü, İzmir, 2011 (in Turkish).

[ORCID](https://orcid.org/)

-  0000-0002-3704-0829 (F. Ayanođlu)
-  0000-0003-3544-9214 (D. A. Kaya)
-  0000-0002-0104-7586 (O. Koçer)



Development of calcium-selective potentiometric electrode using 10,19-Bis[(octadecylcarbamoil)methoxyacetyl]-1,4,7,13,16-pentaoxa-10,19-diazacycloheneicosane compound as ionophore

Omer IŞILDAK*

at end page

Tokat Gaziosmanpaşa University, Faculty of Science and Education, Chemistry, Tokat, Turkey

Received: 17 October 2018, Revised: 21 December 2018, Accepted: 23 December 2018

*Corresponding author e-mail: omer.isildak@gop.edu.tr

Citation: Işıldak, O. <i>Int. J. Chem. Technol.</i> 2018 , 2 (2), 168-172.
--

ABSTRACT

This work deals with the development of micro-size potentiometric calcium-selective electrode. A simple and rapid potentiometric method of determining calcium concentration, based on 10,19-Bis[(octadecylcarbamoil) methoxyacetyl]-1,4,7,13,16-pentaoxa-10,19-diazacycloheneicosane, is described. For this aim, calcium-selective polyvinylchloride (PVC) membrane was prepared by coating on the surface of solid-contact. Calcium-selective PVC membrane electrode does not contain internal reference electrode and solution. The potentiometric performance of calcium-selective PVC membrane electrode (selectivity constant, liner working range, detection limit, response time, pH working range, repeatability, lifetime, and time dependent potential decay) was determined using computer controlled measurement system in static conditions. The results showed that the calcium-selective electrode exhibited good reproducibility in calcium determination.

Keywords: Potentiometric electrode, ionophore, calcium selective electrode.

İyonofor olarak 10,19-Bis [(oktadesilkarbamoil) metoksiasetil]-1,4,7,13,16-pentaoxa-10,19-diazasikloheniikosan bileşiğini kullanarak kalsiyum seçici potansiyometrik elektrotun geliştirilmesi

ÖZ

Bu çalışma mikro boyutta potansiyometrik kalsiyum-seçici elektrotun geliştirilmesi ile ilgilidir. 10,19-Bis [(oktadesilkarbamoil) metoksiasetil] - 1,4,7,13,16 - pentaoksa - 10,19-diazasikloheniikosan temelli kalsiyum konsantrasyonunu belirleyen basit ve hızlı potansiyometrik bir yöntem tarif edilmiştir. Bu amaçla, kalsiyum seçici polivinilklorid (PVC) membran katı hal kontak yüzeyi üzerine kaplanarak hazırlanmıştır. Kalsiyum-seçici PVC membran elektrot, iç referans elektrot veya çözelti içermemektedir. Kalsiyum-seçici PVC membran elektrotun (seçicilik sabiti, liner çalışma aralığı, tayin sınırı, cevap süresi, pH çalışma aralığı, tekrarlanabilirlik, ömür ve zamana bağlı potansiyeldeki değişim) potansiyometrik performansı, statik koşullarda bilgisayar kontrollü ölçüm sistemi kullanılarak belirlenmiştir. Sonuçlar, kalsiyum seçici elektrotun kalsiyum tayininde iyi tekrarlanabilirlik sergilediğini gösterdi.

Anahtar Kelimeler: Potansiyometrik elektrot, iyonofor, kalsiyum seçici elektrot.

1. INTRODUCTION

Calcium is the fifth element in the earth's crust and the third most abundant metal. This element is vital for the life of plants and animals because it is found in animal skeletons, dentistry, egg shells, corals and many

other soils. Calcium is the most common metal in the human body. It is an important component of a healthy diet and a mineral necessary for life. It is also very important for other physical functions, such as blood circulation and muscle control. Calcium deficiency is one of the main causes of osteoporosis.¹ Osteoporosis is a

disease that causes the bones to become excessively porous and to be exposed to the fracture. The calcium requirement of the human body varies with age. The recommended diet amount for calcium by the Food and Nutrition Committee is approximately 1100 mg per day for adults.^{2,3} Calcium is an important component of the diet, and its monitoring and analysis in biological fluid, food and environmental samples is important.

Several techniques have been used to determination of calcium in biologic liquids, foods and environment samples. These techniques consist essentially of flame atomic absorption spectrometry (FAAS),⁴ titrimetry,⁵ inductively couple plasma-optical emission spectrometry (ICP-OES)⁶ and inductively couple plasma mass spectrometry (ICP-MS).⁷ However, these developed methods are expensive, time-consuming and not sufficiently selective and sensitive and can be used with too many solvents.

This work deals with preparation of micro-size potentiometric PVC membrane calcium-selective electrode. For this aim, calcium-selective electrode membrane was prepared by coating of cocktail on the surface of solid-state-contact.⁸ The electrode does not contain an internal reference electrode or solution. The potentiometric performance of calcium-selective PVC membrane electrode (linear working range, response time, detection limit, selectivity, repeatability, and pH working range, lifetime, and time dependent potential decay) was determined using computer controlled measurement system in static conditions.

2. MATERIALS AND METHODS

2.1. Reagents

The solid-contact components and graphite was obtained from Sigma-Aldrich Company. Hardener (Desmodur RFE) and epoxy resins (Macroplast Su 2227) were supplied Henkel and Bayer Company, respectively. The polymer membrane components, the plasticizers and high molecular weight polyvinylchloride (PVC), bis(2-ethylhexyl) sebecate (DOS), bis-(2-ethylhexyl) phtalate (DOP), bis-(2-ethylhexyl) adipate (DOA), 2-nitrophenyloctyl ether (NPOE) and lipophilic anionic additive reagent potassium tetrakis-(p-chlorophenyl) borate (KTCIPB), were from Fluka company. Tetrahydrofuran (THF) was from Merck Company. Calcium-selective ionophore (10,19 - Bis[(octadecylcarbamoil) methoxyacetyl] - 1,4,7,13,16 - pentaoxa - 10,19 - diazacycloheneicosane) was from Sigma-Aldrich Company (Figure 1). Standard metal salts were of analytical grade (Merck). All solvents were used after purification. The other reagents used were of analytical reagent grade. All solutions were prepared with twice-distilled deionize water. All of the experiments were operated at room temperature, 25±1 °C.

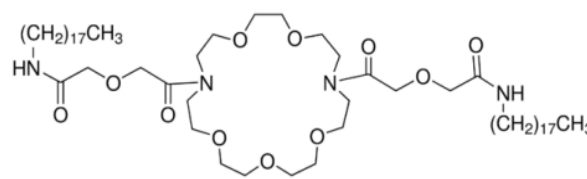


Figure 1. 10,19 - Bis[(octadecylcarbamoil) methoxyacetyl]-1,4,7,13,16 – pentaoxa - 10,19 – diazacycloheneicosane.

2.2. Preparation of solid state contact

Solid state contact mixture composed of 50.0 mg of graphite, 35.0 mg of epoxy and 15.0 mg of hardener was dissolved in THF and was stirred thoroughly until a suitable viscosity provided. The surface of the copper wire (about 0.5-1 mm thickness, 5-15 cm long) was coated by dipping into this mixture 4-5 times. It was allowed to stand overnight at room temperature.

2.3. Preparation of membrane cocktail

The membrane cocktail was prepared using a mixture of 3.0 mg of ionophore, 32.0 mg of PVC, 64.0 mg of plasticizer and 1.0 mg of KTpCIPB. The components were dissolved in dried THF and were stirred thoroughly until a suitable viscosity provided and the solid-state contact surface is coated in a specific thickness. Calcium-selective electrode, then allowed to dry for 3-4 hours and 10^{-2} M Ca^{2+} was conditioned for 24 hours at room temperature.

2.4. Preparation of solution

A stock Ca^{2+} solutions (1.0×10^{-1} mol l^{-1}) were prepared in deionize water. The diluted solutions (1.0×10^{-1} to 1.0×10^{-5} mol l^{-1}) of Ca^{2+} were prepared by dilution of the stock solution. The stock solutions of metals (1.0×10^{-1} mol l^{-1}) were obtained by dissolving salts of the corresponding metals.

2.5. Apparatus

Potentiometric measurements were performed at room temperature (25±1 °C) using a computer-controlled multichannel potentiometric system. All potential measurements were made with a micro-sized silver/silver chloride reference electrode and the calcium-selective membrane electrode. The potentiometric characteristics of the calcium-selective PVC membrane electrode were investigated with measurements of the potential differences between two points which is the cause of electrical currents. Measurements were taken in the following cell assembly:

Micro-sized solid silver/silver chloride reference electrode/test solution/calcium-selective electrode/solid-state contact/Cu wire.

3. RESULTS AND DISCUSSION

3.1. Optimization of membrane composition

The response characteristics of electrode such as working range and response time depend on optimum membrane composition.⁹ The electrode membrane while preparing cocktails, each of the different plasticizers (DOS, DOP, DOA, and NPOE) were used separately and the best potentiometric behavior was detected which exhibits the plasticizer. Of these plasticizers, DOP exhibited the best sensitivity in the linear working range. Good compatibility with ionophore-based PVC membrane electrodes is explained by the high polarity of DOP.¹⁰ 10,19-Bis [(octadecylcarbamoyl) methoxyacetyl]-1,4,7,13,16-pentaoxa-10,19-diazacikloheniikosan based PVC membrane electrodes were prepared in different amounts and potential measurements were performed. The results are summarized in Table 1.

One of the other parameters of the PVC membrane composition to be investigated is the ionophore concentration. For this purpose, PVC membrane electrodes were prepared and tested using the different ratio of 10,19-Bis[(octadecylcarbamoyl)methoxyacetyl]-1,4,7,13,16-pentaoxa-10,19-diazacycloheneicosane.

Optimum ionophore ratio was determined as 3.0%. From the data shown in Table 1, the membrane composition with optimized PVC: DOP: ionophore: KTpCIPB weight percentage ratio of 32:64:3.0:1.0 was selected for further studies.

3.2. Working concentration range and slope

The potential behavior of calcium-selective PVC membrane electrode was determined in calcium nitrate solutions of the concentration 1×10^{-1} to 1×10^{-5} mol l⁻¹. The potential changes of the electrode are shown in Figure 2 and the calibration curve is shown in Figure 3.

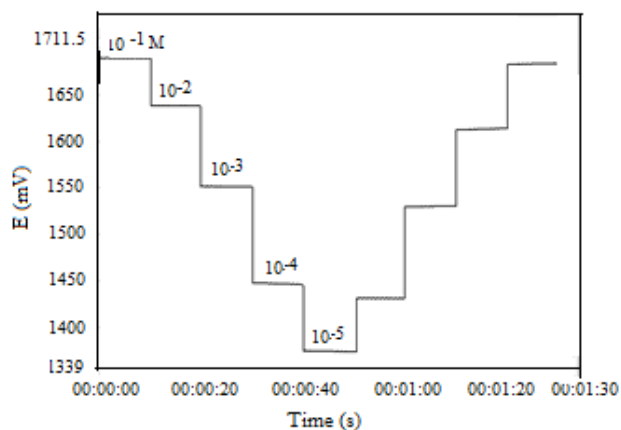


Figure 2. Potentiometric response of all-solid-state PVC membrane Ca²⁺-selective electrode.

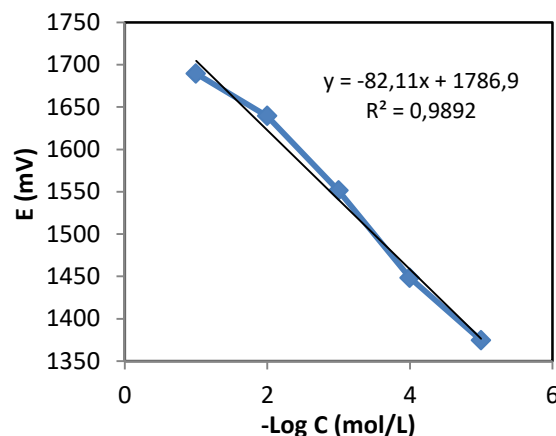


Figure 3. Calibration curve of all-solid-state PVC membrane Ca²⁺-selective membrane electrode obtained over Ca²⁺ concentration range of 1×10^{-1} to 1×10^{-5} mol l⁻¹.

As shown in Figure 1, the calcium-selective PVC membrane electrode showed a good potential change against the concentration change of the calcium ions. The calcium-selective electrode has a good concentration of working range and appears to exhibit Nernst behavior. It was also observed that the response time of the electrode was shorter than 15 s. The response time is defined as the time when the potential is balanced and unchanged after the ion is added to the sample. Electrodes were held in Ca²⁺ solution before measurement, and then measurements were taken.

3.3. pH effect

The pH working range of the electrode was determined by measuring the potential values of 0.01 M Ca solutions ranging between pH 2 and 7. The pH of the solutions used in the measurements was adjusted with HNO₃. We did not take measurements after pH 7 because Ca(OH)₂ precipitated in basic medium. As shown in Figure 4, the electrode was able to operate between pH 2 and 7 without being affected by the pH.

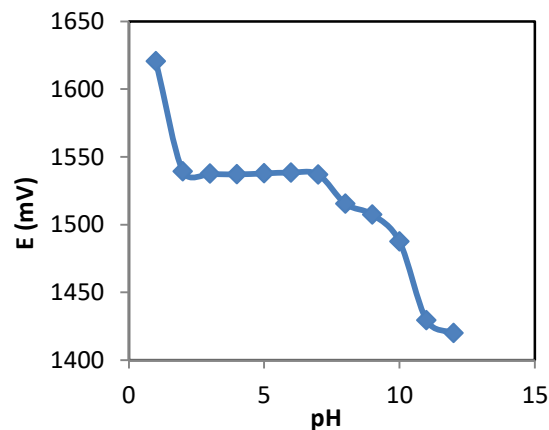


Figure 4. The dependence of the all-solid-state contact Ca²⁺-selective membrane electrode response in pH.

Table 1. The membrane compositions of all-solid-state PVC membrane Ca²⁺-selective electrode

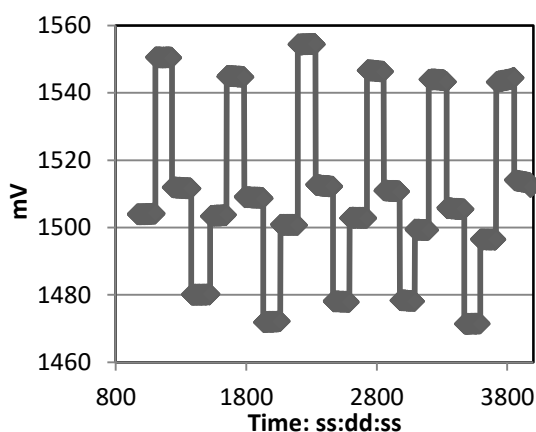
(Active ingredient) Ionophore	Composition (%) (w/w)					
	PVC	Plasticizer				(Conductivity enhancer) KTCIPB
		NPOE	DOS	DOP	DOA	
2.0	30	-	67	67	-	1.0
2.5	31	65	-	65	65	0.5
3.0	32	64	64	64	64	1.0
3.5	33	62	62	62	-	1.5
4.0	34	61	-	-	61	1.0
5.0	34	65	-	65	-	1.0

3.4. Selectivity

Selectivity is one of the most important parameters of PVC membrane electrode and determines whether reliable measurement is possible. Selectivity of calcium selective PVC membrane electrode was determined according to the separate solution method proposed by IUPAC. The selectivity coefficient values of the calcium-selective PVC membrane electrode are shown in Table 2. According to the values in Table 2, the existence of interfering ions seems to be selective against the Ca²⁺ ions of the PVC membrane electrode.

3.5. Repeatability

Measurements made with calcium-selective PVC membrane electrode have shown that the electrode gives reproducible results. Figure 5 shows repeat measurements of the sensor against calcium concentrations of 10⁻², 10⁻³, and 10⁻⁴ mol l⁻¹.

**Figure 5.** Potentiometric repeatability of all-solid-state PVC membrane Ca²⁺-selective electrode.

4. CONCLUSIONS

The proposed calcium-selective PVC membrane electrode is a sensitive, low cost, precise and highly selective method for determination of Ca²⁺ ion, based on the 10,19 – Bis [(octadecylcarbamoyl) methoxyacetyl] –

1,4,7,13,16 – penta-oxa – 10,19 – diazacycloheneicosane entrapped in PVC matrix. The electrode produced a linear response for calcium concentration range of 1.0x10⁻¹ – 1.0x10⁻⁵ M. As a result of this study, we will provide a contribution to the existing methods in the literature as an alternative method for the determination of calcium ion.

Table 2. Selectivity coefficient values of all-solid-state PVC membrane Ca²⁺-selective electrode.

Interfering ion	k _{Ca²⁺} ^{pot} , M	Log k
Na ⁺	5.88x10 ⁻³	-2.23
K ⁺	3.38x10 ⁻⁴	-3.47
Cu ²⁺	5.24x10 ⁻³	-2.28
Cd ²⁺	1.51x10 ⁻⁴	-3.82
Co ²⁺	3.71x10 ⁻⁴	-3.43
Mg ²⁺	7.24x10 ⁻²	-1.14
Pb ²⁺	7.07x10 ⁻³	-2.15
Mn ²⁺	3.01x10 ⁻³	-2.52
Ba ²⁺	6.76x10 ⁻⁵	-4.17
Ni ²⁺	4.57x10 ⁻⁶	-5.34
Al ³⁺	1.44x10 ⁻⁴	-3.84
Cr ³⁺	1.86x10 ⁻³	-2.73

Conflict of interest

Author declares that there is no a conflict of interest with any person, institute, company, etc.

REFERENCES

1. Mardas, N.; Buseti, J.; de Figueiredo, J. A. P.; Mezzomo, L.A.; Scarparo, R.K.; Donos, N. *Clin. Oral Impl. Res.* **2017**, 28, 362-371.
2. Mahan, L. K.; Stump, S.E.; Alimentos, nutrição and dietoterapia. 10. ed. São Paulo, , Roca, 2002.
3. Petrovich, M. B.; Filho, V. R. A.; Neto, J. A.G. *Ecl. Quím. São Paulo*, **2007**, 32(3), 25-30.
4. De la Fuente, M. A.; Juárez, M. *Analyst* **1995**, 120, 107-111.
5. Baccan, N.; Andrade, J. C.; Godinho, O. E. S.; Barone, J. S. *Química analítica quantitativa elementar*. 3.ed. São Paulo, Edgard Blücher, 2001.
6. Murcia, M. A.; Vera, A.; Tomé, M. M.; Muñoz, A.; Córdoba, M.H.; Gonzalez, R.O. *Lebensm.-Wiss. u-Technol.* **1999**, 32, 175.
7. Nobrega, J. A.; Gelinas, Y.; Krushevska, A.; Barnes, R.M. *J. Anal. At. Spectrom.* **1997**, 12, 1239-1242.
8. Isıldak, I.; Covington, A. K. *Chimica Acta Turcica*, **1998**, 26, 49-56.
9. Eugster, R.; Gehrig, P.M.; Morp, W.E.; Spichiger, U.; Simon, W. *Anal. Chem.* **1991**, 63, 2285-2289.
10. Seiler, K.; Simon, W. *Anal. Chim. Acta*, **1992**, 266 (1), 73-87.

ORCID



0000-0003-4690-4323 (O. Isıldak)